

UNIVERSITY OF SHEFFIELD
Department of Civil and Structural Engineering



HYDROMECHANICAL FACTORS INFLUENCING
SEEPAGE-INDUCED SUFFUSION IN
INTERNALLY UNSTABLE SOILS.

February 2024

Author:

ROWENA E STEVENSON

Supervisors:

DR. ELISABETH BOWMAN

PROF. COLIN SMITH

A thesis submitted in fulfillment of the requirements for the
degree of

DOCTOR IN PHILOSOPHY

ABSTRACT

Internal erosion, and in particular suffusion, poses an escalating threat to the stability of water-retaining earth structures such as embankment dams and levees globally, due to increased pressures from climate change and growing populations. While it is well-established that the hydromechanical regime within the soil body influences this process, existing studies conducted under varying testing configurations have come to conflicting conclusions on the exact mechanisms in process. This study addresses this knowledge deficit by introducing a novel rigid-walled centrifuge permeameter, purpose-built for investigating a wide range of seepage path lengths and effective stress conditions. This apparatus facilitates the manipulation of established centrifuge scaling laws via a parametric modelling of models approach, allowing the spatial onset and progression of suffusion to be tracked through interstitial pore pressure measurements and post-test particle size analysis.

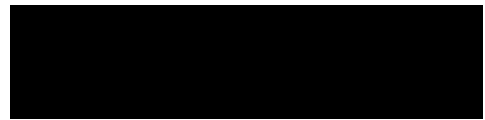
In total, seven centrifuge permeameter tests are conducted, accompanied by a 1-g test undertaken in the same cell. An under-filled, gap-graded soil comprising of a mixture of silt and sand is used in all tests. The suite of tests allows for the influence of both macroscale and granular seepage path length to be considered, as well as the effective stress gradient across the specimens. Notably, the hydraulic loading history emerges as a paramount factor governing the spatial progression of suffusion. This insight underscores the importance of considering not just the initiation of fine particle migration but, more crucially, the ongoing evolution of suffusion.

The results of this study reveal that suffusion is a phenomenon characterised by substantial spatial variability, thereby challenging conventional modelling approaches based on macroscale assumptions of homogeneity and Darcy's flow. Through a mesoscale interpretation of the results, it becomes evident that variations in hydraulic loading regimes, boundary conditions, and measurement point locations have historically contributed to the discrepancies observed between tests conducted in different apparatuses. Moving forward, a more unified approach between particle scale and element scale modelling is needed, so that suffusion can be accurately characterised within real structures.

DECLARATION

I, the author, confirm that the Thesis is my own work. I am aware of the University's Guidance on the Use of Unfair Means (www.sheffield.ac.uk/ssid/unfair-means). This work has not been previously been presented for an award at this, or any other, university.

Sheffield, UK, February 2024



Rowena E Stevenson

ACKNOWLEDGMENTS

I would like to express my gratitude to my supervisor, Elisabeth Bowman, for her support, guidance, and mentorship throughout the course of my research. Her expertise and dedication have been invaluable in the shaping of this thesis.

I am also deeply appreciative of the technical knowledge and expertise provided by Alex Cargill and Mark Foster, as well as the rest of the technical staff in the Department. Their efforts were crucial in facilitating the smooth progression of my experiments and data collection.

Finally, I would like to extend my acknowledgement to family and friends, in Sheffield, London, and further afield. This would have not been possible without you.

CONTENTS

List of Figures	x
List of Tables	xviii
List of Symbols and Acronyms	xx
1 Introduction	1
1.1 Aims and objectives	2
1.2 Thesis outline	3
2 Literature Review	4
2.1 Background	4
2.2 Definitions	7
2.2.1 Internal erosion	8
2.2.2 Internal or material instability	10
2.2.3 Under-filled, over-filled and transitional materials	10
2.2.4 Fines and the finer fraction	12
2.2.5 Suffusion and suffosion	13
2.2.6 Internal and external fines migration	14
2.2.7 Permeameters	15
2.2.8 Seepage path length	15
2.2.9 Micro-, macro- and mesoscale	16
2.3 The geotechnical centrifuge as an investigative tool	17
2.3.1 Principles of centrifuge modelling	17
2.3.2 Understanding the scaling of hydraulic gradient	18
2.3.3 Errors and limitations of centrifuge modelling	21
2.3.4 Internal erosion testing in the centrifuge	24
2.3.5 Centrifuge facilities at the University of Sheffield	25
2.4 Material Instability	25
2.4.1 Geometric instability criteria	26
2.4.2 Pore network constrictions	29
2.4.3 Kozeny-Carman permeability	32
2.5 Onset of suffusion	34
2.5.1 Critical hydraulic gradient and the α factor	34
2.5.2 Hydromechanical envelopes	36
2.5.3 The influence of effective stress	42

2.5.4	Critical seepage velocity and hydraulic stress	45
2.6	Progression of suffusion	47
2.6.1	Hydraulic loading regime	47
2.6.2	Spatial development of internal fines migration	51
2.6.3	Influence of seepage path length	55
2.6.4	Fines migration from an energy perspective	57
2.7	A microscale understanding of fines migration	60
2.7.1	Force chains and the α factor	60
2.7.2	Initiation of particle migration	61
2.7.3	Representative elementary volumes (REV)	63
2.8	Summary	65
3	Methodology	67
3.1	Introduction	67
3.2	Materials tested	67
3.2.1	Constraints and requirements	67
3.2.2	Final soil design	68
3.2.3	Determining the particle size distribution	71
3.2.4	Maximum and minimum density tests	72
3.3	Developing a new centrifuge permeameter	73
3.3.1	Centrifuge permeameter apparatus	73
3.3.2	Water supply and flow control system	75
3.3.3	Permeameter cell	77
3.3.4	Data acquisition and PPTs	80
3.3.5	Influence of variation in g across the model	81
3.4	Preparation of sample for testing	82
3.4.1	Specimen preparation	82
3.5	Test procedure	85
3.5.1	Centrifuge tests	85
3.5.2	Test conducted at 1- g	86
3.6	Post-test dissection	88
3.7	Data interpretation	91
3.8	Experimental programme	94
3.8.1	Naming convention	95
3.8.2	Modelling-of-models	95
3.8.3	Other comparative tests	98
3.9	Summary	99
4	Validation of experimental methods	101

4.1	Introduction	101
4.2	Darcy's law assumption	101
4.3	Pre-erosion permeability of the soil	103
4.3.1	Kozeny-Carman permeability	103
4.3.2	Pre-erosion experimental permeability	104
4.4	Deairing water using nitrogen purging	105
4.5	Validating spatial fine particle content measurement	106
4.6	Influence of saturation stage of homogeneity	107
4.7	Summary	109
5	Tests conducted at 40-g	111
5.1	Introduction	111
5.1.1	Defining a suffusion event	113
5.1.2	Interpreting results	113
5.2	T ₄₀ L _{2.5}	115
5.2.1	Test description	115
5.2.2	Permeability response during centrifuge testing	117
5.2.3	Post-test dissection	120
5.3	T ₄₀ L _{2.5} (R)	122
5.3.1	Test description	122
5.3.2	Permeability response during centrifuge testing	122
5.4	T ₄₀ S _{2.5}	126
5.4.1	Test conditions	126
5.4.2	Permeability response during centrifuge testing	127
5.4.3	Post-test dissection	131
5.5	T ₄₀ LCH	132
5.5.1	Test conditions	132
5.5.2	Permeability response during centrifuge testing	133
5.5.3	Post-test dissection	135
5.6	Summary	137
6	Tests at lower g-levels	139
6.1	Introduction	139
6.2	T ₃₀ L _{2.5/5}	141
6.2.1	Test description	141
6.2.2	Permeability response during testing	143
6.2.3	Post-test dissection	145
6.3	T ₂₀ L ₅	147
6.3.1	Test description	147

6.3.2	Permeability response during testing	149
6.4	T10L10	152
6.4.1	Test description	152
6.4.2	Permeability response during centrifuge testing	154
6.5	T1LCH	157
6.5.1	Test description	157
6.5.2	1-g permeameter testing	158
6.5.3	Post-test dissection	163
6.6	Summary	164
7	Analysis and discussion: centrifuge perspectives	166
7.1	Modelling-of-models 1: T40L2.5, T30L2.5/5, T20L5 and T10L10	166
7.1.1	Initial observations: whole specimen behaviour	167
7.1.2	Initial observations: top layer behaviour	171
7.1.3	Onset of suffusion: hydromechanical envelopes	172
7.1.4	Summary of modelling-of-models 1	176
7.2	Modelling-of-models 2: T40S2.5 and T20L5	177
7.2.1	Comparison of two tests under the same effective stress conditions	177
7.2.2	The difference between seepage path length and specimen height	182
7.2.3	Summary of modelling-of-models 2	183
7.3	Modelling-of-models 3: T40LCH and T1LCH	184
7.3.1	Initial observations	184
7.3.2	Outcome of suffusion: mass of fines lost	186
7.3.3	Summary of modelling-of-models 3	191
7.4	Summary	191
8	Analysis and discussion: factors influencing suffusion	193
8.1	Comparison 1: Repeatability and microscale variation	193
8.1.1	Summary	197
8.2	Comparison 2: Hydraulic loading regime	198
8.2.1	Particle scale conceptual framework of the evolution of suffusion under the two loading conditions	201
8.2.2	Summary	204
8.3	Comparison 3: Seepage path length and boundaries	204
8.3.1	Summary	207
8.4	Linking permeability readings to final fines distribution	207
8.5	Summary	213

9	Conclusions and recommendations	214
9.1	Conclusions	214
9.1.1	The development of a centrifuge permeameter	214
9.1.2	The relationship between tested parameters and the onset and progression of suffusion and clogging	215
9.1.3	Threshold conditions for suffusion onset and erosion resistance as an inherent soil property	219
9.1.4	Suffusion as a microscale phenomenon and the disconnect between permeability and fines distribution	220
9.2	Recommendations	221
9.2.1	Recommendations for further exploration of the suffusion phenomenon	221
9.2.2	Lessons learnt during the development of a centrifuge permeameter	222
	Reference list	226

LIST OF FIGURES

Figure 2.1	Three conditions for internal erosion, from Garner and Fannin (2010)	5
Figure 2.2	Fines particles do not fill the void spaces in under-filled soils, in contrast to over-filled soils	6
Figure 2.3	Progression of suffusion with time in a soil body subjected to seepage flow	7
Figure 2.4	Transition between a matrix-supported and clast-supported bimodal granular material based on fines content, from Skempton and Brogan (1994)	11
Figure 2.5	The role of fine particles in stress transfer depending on fines content (i = under-filled, ii = transitional, iv = over-filled), from Thevanayagam et al. (2002)	12
Figure 2.6	Conceptual framework for suffusion and suffosion under upwards seepage flow, adapted from Fannin and Slangen (2014)	13
Figure 2.7	A 0.4 m tall model experiences a significant variation in g-level across its height at 40-g, even when the effective radius is chosen to minimise stress variation	22
Figure 2.8	An error in calculated acceleration is introduced across the width of a centrifuge model due to the slight difference in radius to the payload centre compared to the payload extremities	23
Figure 2.9	View of the 50gT geotechnical beam centrifuge at the University of Sheffield	26
Figure 2.10	Graphical representation of the Kenney and Lau (1985) method, from Li (2008)	27
Figure 2.11	Particle size distributions of internally unstable soil A and and internally stable soil C from the experimental study of Skempton and Brogan (1994)	28

Figure 2.12	Internal instability boundaries in $H - F$ space from Li and Fannin (2008), modified to include unstable soil A and stable soil C from Skempton and Brogan (1994) . . .	30
Figure 2.13	Determining controlling constriction size along the seepage path, from Kenney et al. (1985)	31
Figure 2.14	Assessment of internal instability by constriction size distribution, from Indraratna et al. (2015)	32
Figure 2.15	Hydromechanical boundaries calculated by Moffat (2005) for the four real soils tested in the large UBC permeameter, plotted in $\sigma' - i$ space	37
Figure 2.16	Particle size distributions of the soil gradations tested in the small and large permeameters at UBC, † indicates a gradation that comprised of spherical glass beads (Crawford-Flett, 2014; Li, 2008; Moffat, 2005)	38
Figure 2.17	Hydromechanical boundary for suffusion onset and hydromechanical paths for different flow directions, modified from Li and Fannin (2022). Case A indicates a soil under its own self-weight, whilst Case B has some additional applied vertical stress.	41
Figure 2.18	Conceptual model of the development of elongated pores under triaxial loading, from Chang and Zhang (2013a)	44
Figure 2.19	Interpreting critical hydraulic gradients from a series of triaxial suffusion tests, from Liang et al. (2019)	44
Figure 2.20	Critical hydraulic shear stress in the pore network of a suffusive soil, from Bonelli and Marot (2011)	46
Figure 2.21	Hydraulic conductivity of specimens comprising of two soil mixes (A and R) under two multi-stage seepage flow regimes (a and b), from Rochim et al. (2017)	49
Figure 2.22	Onset of suffusion is characterised by the increase in rate of change of flow velocity with hydraulic gradient across the specimen, from Annapareddy et al. (2023)	50
Figure 2.23	Fines content during suffusion from X-ray CT scans, from Nguyen et al. (2019)	53
Figure 2.24	Pre- and post-test particle size distributions for specimens subjected to downwards seepage flow (Layer 1 = top), from Zhong et al. (2018)	53

Figure 2.25	Development of hydraulic conductivity for three centrifuge permeameter tests, from Marot et al. (2012)	55
Figure 2.26	Critical hydraulic gradient for different specimen lengths, from Zhong et al. (2018)	56
Figure 2.27	Erosion resistance index boundaries and test results, from Zhong et al. (2018)	59
Figure 2.28	Relationship between the fines content and α factor for loose and dense materials according to numerical simulations (Kawano et al., 2018)	61
Figure 2.29	Fine particles (rattlers) provide structural support in under-filled materials, from Wautier (2018)	62
Figure 2.30	Forces affecting the sliding or strengthening of a particle contact, from Ma et al. (2021)	63
Figure 2.31	Distribution of angle between flow direction and particle displacement at time of particle detachment, from Ma et al. (2021)	64
Figure 3.1	Particle size distribution of the tested material	70
Figure 3.2	H/F diagram for tested material	70
Figure 3.3	Microscope images of the coarse and fine soils tested	71
Figure 3.4	Mastersizer 3000 used to ascertain the silt particle size distribution	72
Figure 3.5	Schematic of centrifuge payload components	74
Figure 3.6	Centrifuge payload	74
Figure 3.7	Centrifuge payload with water supply system highlighted, labelling consistent with the schematic in Figure 3.5	75
Figure 3.8	Linear actuator with stepper motor to lower the outlet CHT whilst the centrifuge is in flight	76
Figure 3.9	Configurations of the permeameter cell for different sample lengths	78
Figure 3.10	Schematic of the permeameter cell	78
Figure 3.11	Base sections of the centrifuge permeameter	79
Figure 3.12	Pore pressure transducer used in centrifuge tests	81
Figure 3.13	Particle size distribution of the component soils used in the unstable specimen alongside the Leighton Buzzard fraction A sand used in the overburden and free-draining base layer	82

Figure 3.14	Pre-portioned layers of silt-sand soil mix are moist-tamped to their desired height in the cell	83
Figure 3.15	Sample is overlain with a coarse free-draining sand and a layer of permeable mesh	84
Figure 3.16	GDS advanced pressure controller used to saturate the sample	85
Figure 3.17	Permeameter cell measurement points modified for 1-g constant head test	87
Figure 3.18	1-g constant applied head test configuration	88
Figure 3.19	Layers of the sample for both specimen dissection and interstitial permeability measurements compared to PPT locations, with the cardinal directions used to define quadrants indicated	89
Figure 3.20	Photographs of the sample dissection process	90
Figure 3.21	Calibration graph for PPTs located within the permeameter cell	91
Figure 3.22	Example of post-processing of the outlet tank PPT data and Chebyshev polynomial fit for Stage 1 of <i>T40L2.5</i> used to calculate the flowrate through the specimen during testing	92
Figure 4.1	Dissolved oxygen content of 15 L of water over time during nitrogen purging	105
Figure 4.2	Wet sieving method applied to prepared test samples accurately captures the fine particle content of a 100g sample	107
Figure 4.3	Post test spatial fine particle content for a saturated, untested sample	108
Figure 5.1	Colour scales used to aide interpretation and comparison of tables of results in Chapters 5 and 6	115
Figure 5.2	Energy gradient applied to <i>T40L2.5</i> and cumulative energy expended by the seepage flow over the 3 stages of testing	116
Figure 5.3	Effective stress profile in <i>T40L2.5</i> at the beginning and end of the centrifuge seepage flow test	117
Figure 5.4	Global permeability of <i>T40L2.5</i>	118
Figure 5.5	Permeability and timeline of suffusion events for each layer of <i>T40L2.5</i>	119

Figure 5.6	Effective stress profile in $T_{40L2.5(R)}$ at the beginning and end of the centrifuge seepage flow test	123
Figure 5.7	Energy gradient applied to $T_{40L2.5R}$ and cumulative energy expended by the seepage flow over the 2 stages of testing	123
Figure 5.8	Global permeability of $T_{40L2.5(R)}$	124
Figure 5.9	Permeability and timeline of suffusion events for each layer of $T_{40L2.5(R)}$	125
Figure 5.10	$T_{40S2.5}$ used only three of the permeameter segments to allow testing of a shorter seepage path	126
Figure 5.11	Energy gradient applied to $T_{40S2.5}$ and cumulative energy expended by the seepage flow over the 4 stages of testing	127
Figure 5.12	Effective stress profile in $T_{40S2.5}$ at the beginning and end of the centrifuge seepage flow test	128
Figure 5.13	Global permeability of $T_{40S2.5}$	128
Figure 5.14	Permeability and timeline of the suffusion events for each layer of $T_{40S2.5}$	130
Figure 5.15	Energy gradient applied to T_{40LCH} and cumulative energy expended by the seepage flow over the 2 stages of testing	133
Figure 5.16	Global permeability variation of T_{40LCH} during centrifuge testing	134
Figure 5.17	Permeability variation and timeline of suffusion events for each layer of T_{40LCH}	135
Figure 6.1	Energy gradient applied to $T_{30L2.5/5}$ and cumulative energy expended by the seepage flow over the 3 stages of testing	142
Figure 6.2	Effective stress profile in $T_{30L2.5/5}$ at the beginning and end of the centrifuge seepage flow test	142
Figure 6.3	Global permeability of $T_{30L2.5/5}$	143
Figure 6.4	Permeability and timeline of suffusion events for each layer of $T_{30L2.5/5}$	145
Figure 6.5	For T_{20L5} , the top layer of the permeameter contained coarse sand, the specimen layers are numbered 1-5. . .	147

Figure 6.6	Energy gradient applied to T_{20L5} and cumulative energy expended by the seepage flow over the 2 stages of testing	148
Figure 6.7	Effective stress profile in T_{20L5} at the beginning and end of the centrifuge seepage flow test	149
Figure 6.8	Global permeability of T_{20L5}	150
Figure 6.9	Permeability and timeline of suffusion events for each layer of T_{20L5}	152
Figure 6.10	Energy gradient applied to T_{10L10} and cumulative energy expended by the seepage flow over the 2 stages of testing	153
Figure 6.11	Effective stress profile in T_{10L10} at the beginning and end of the centrifuge seepage flow test	154
Figure 6.12	Global permeability of T_{10L10}	155
Figure 6.13	Permeability and timeline of suffusion events for each layer of T_{10L10}	156
Figure 6.14	Permeability of each layer and whole specimen during 1-g constant head permeameter testing of T_{1LCH} , with the time of the images in Figure 6.15 and Figure 6.16 indicated	158
Figure 6.15	A front of externally eroded fine particles moving through the downstream constant head tank at the start of 1-g permeameter testing, T_{1LCH}	160
Figure 6.16	Cloudiness in downstream constant head tank indicates fine particles eroded from sample throughout 1-g permeameter testing, T_{1LCH}	161
Figure 6.17	Settling velocities of the fine silt particles based on Stoke's Law compared to the upwards flow velocity in the downstream CHT tank for test T_{1LCH}	162
Figure 7.1	Global permeabilities of each of the tests $T_{40L2.5}$, $T_{30L2.5/5}$, T_{20L5} and T_{10L10} in time (centrifuge spin-down breaks marked with coloured triangles)	168
Figure 7.2	Local permeabilities of the top layer of each of the tests $T_{40L2.5}$, $T_{30L2.5/5}$, T_{20L5} and T_{10L10} in time (centrifuge spin-down breaks marked with coloured triangles)	172

Figure 7.3	Global permeabilities of two tests conducted to model the same prototype, $T_{40S2.5}$ and T_{20L5} (centrifuge spin-down breaks marked with coloured triangles)	179
Figure 7.4	The total mass of fines lost per unit volume against the cumulative energy expended energy from the seepage flow for the dissected tests of this study (shown with blue crosses) alongside data reported in previous studies by Le et al. (2018), Marot et al. (2012), Rochim et al. (2017) and Zhong et al. (2018)	187
Figure 7.5	Comparison of the range in masses of fine particles eroded in this study and previous studies using the erosion resistance index approach.	190
Figure 8.1	Global permeabilities of two repeat tests $T_{40L2.5}$ and $T_{40L2.5}(R)$ plotted against time (centrifuge spin-down breaks marked with coloured triangles)	194
Figure 8.2	Global permeabilities of two repeat tests plotted against the cumulative energy expended by the seepage flow .	196
Figure 8.3	Global permeabilities of two 40-g tests conducted under different loading regimes, $T_{40L2.5}$ and T_{40LCH} (centrifuge spin-down breaks marked with coloured triangles)	199
Figure 8.4	Step-wise diagram of the particle scale conceptual framework, with the left branch leading to continual fines migration and suffusion, and the right branch leading to particle deposition and clogging	203
Figure 8.5	Global permeabilities of the tests $T_{40L2.5}$ and $T_{40S2.5}$ in time (centrifuge spin-down breaks marked with coloured triangles)	206
Figure 8.6	Phase diagram for the uneroded soil representative volume	209
Figure 8.7	Phase diagram for the eroded soil representative volume, where the fine fraction is located in the bottom portion of the soil	210
Figure 9.1	Permeability of soil layer at the initiation of either suffusion or clogging behaviour compared to the energy gradient applied to the whole specimen at that time . .	216

Figure 9.2	Effective stress at the midpoint of the soil layer at the initiation of either suffusion or clogging behaviour compared to the energy gradient applied to the whole specimen at that time	217
Figure 9.3	Relative energy gradient (EG) in the soil layer which exhibited suffusion or clogging behaviour, compared to the energy gradient applied to the specimen, in relation to the seepage flow velocity through the whole specimen	218
Figure 9.4	Gravity analogue turbidity sensor (SKU SEN0189) from DFRobot, with a modified casing on the centrifuge payload	223

LIST OF TABLES

Table 2.1	Centrifuge scaling laws relating to the phenomenon of internal fines migration (for quantities marked †, see Section 2.3.2)	18
Table 2.2	Local (i_{cr}) and average (i_{av}) hydraulic gradients reported by Li (2008) at the onset of suffusion for all tests conducted on the FR7 glass bead gradation	39
Table 3.1	Soil properties	69
Table 3.2	Summary of the key parameters of each test in the permeameter testing programme	95
Table 5.1	Summary of parameters for centrifuge permeameter tests at 40-g	111
Table 5.2	Variation in permeability for each layer of test $T_{40L2.5}$	118
Table 5.3	Ultimate spatial distribution of fine particles from specimen dissection for test $T_{40L2.5}$ (some data lost)	121
Table 5.4	Variation in permeability for each layer of test $T_{40L2.5}(R)$	124
Table 5.5	Variation in permeability for each layer of test $T_{40S2.5}$	129
Table 5.6	Ultimate spatial distribution of fine particles from specimen dissection for test $T_{40S2.5}$	131
Table 5.7	Variation in permeability for each layer of test T_{40LCH}	136
Table 5.8	Ultimate spatial distribution of fine particles from specimen dissection for test T_{40LCH}	136
Table 6.1	Summary of parameters for centrifuge and 1-g permeameter tests at lower g-levels	139
Table 6.2	Increments of applied head difference and fluid velocity for multi-stage centrifuge tests at different g-levels . . .	140
Table 6.3	Variation in permeability for each layer of test $T_{30L2.5/5}$	144
Table 6.4	Ultimate spatial distribution of fine particles from specimen dissection for test $T_{30L2.5/5}$	146
Table 6.5	Total mass of the silt fraction lost over the duration of permeameter testing calculated from the dissected specimens	146
Table 6.6	Final global permeability of centrifuge permeameter tests	150

Table 6.7	Variation in permeability for each layer of test T_{20L5}	151
Table 6.8	Variation in permeability for each layer of test T_{10L10}	156
Table 6.9	Ultimate spatial distribution of fine particles from specimen dissection for test T_{1LCH}	164
Table 7.1	Comparison of the key testing parameters in the four centrifuge tests conducted as part of modelling of models comparison 1.	167
Table 7.2	Testing conditions at the onset of the four global suffusion events for test $T_{40L2.5}$ and three events for $T_{30L2.5/5}$	170
Table 7.3	Scaled seepage path length and initial effective stress in the top layers of the four tests conducted as part of modelling of models comparison 1, along with their net permeability change across the test duration.	171
Table 7.4	Observed critical hydraulic conditions for the onset of the first suffusion even in the top layer of each test in modelling-of-models comparison 1 alongside the critical hydraulic gradient calculated from Li and Fannin (2022). The top layer of T_{20L5} was located between PPT1 and 2, rather than PPT0 and 1 as in the other tests, explaining the higher effective stress and layer number.	175
Table 7.5	Comparison of the testing parameters for the two tests conducted to achieve the same prototype, $T_{40S2.5}$ and T_{20L5} . The same effective stress at the midpoint is achieved by adjusting the height of coarse sand used as overburden	178
Table 7.6	Testing conditions at the onset of global suffusion events in test $T_{40S2.5}$	179
Table 7.7	Results of two tests conducted to the same prototype conditions from the centrifuge study of Marot et al. (2012)	181
Table 8.1	Comparison of the testing parameters for the two tests conducted at 40-g with different model heights, $T_{40L2.5}$ and $T_{40S2.5}$	205

LIST OF SYMBOLS AND ACRONYMS

α	Skempton and Brogan (1994) stress reduction factor
$\Delta z_M, \Delta z_P$	Seepage path length at model and prototype scale (m)
$\gamma, \gamma_w, \gamma'$	Unit weight of soil, water, and submerged unit weight (kg/m ²)
μ	Dynamic fluid viscosity (Pa.s)
ω	Angular centrifuge velocity (rad/s)
$\bar{\sigma}'_{vm}$	normalized mean vertical effective stress (-)
ρ, ρ_w	Density of soil, water (kg/m ³)
$\sigma'_{vm}, \sigma'_{vm0}$	Mean vertical effective stress, mean vertical effective stress under hydrostatic conditions (kPa)
τ	Critical hydraulic shear stress
D_{c35}^c	35 th percentile of the CSD of the coarse fraction
$d_{85,SA}^f$	85 th percentile of the fine fraction by surface area
D'_{15}	15 th percentile of the coarse fraction by particle size
d'_{85}	85 th percentile of the fine fraction by particle size
D_h^c	Kozeny Carman effective grain diameter
e	soil void ratio
E_{exp}	Cumulative energy expended by the seepage flow (J)
EG	Energy gradient, a similar concept to hydraulic gradient but more applicable in centrifuge testing (kPa/m)
$EG_{app}, EG_{app,max}$	Applied energy gradient, maximum applied energy gradient during experimental testing (kPa/m)
F_n	Fines percentage
g	Earth's gravitational acceleration (9.81 m/s ²)

H/F_{min}	Kenney and Lau (1985) geometric instability criteria
i	Hydraulic gradient (-)
$i_{app}, i_{app,max}$	Applied hydraulic gradient, maximum applied hydraulic gradient during experimental testing
$i_{cr}, i_{cr,d}, i_{cr,u}$	Critical hydraulic gradient, modified for downwards and upwards flow
I_{α}	Erosion resistance index
K	Intrinsic soil permeability (m^2)
$k, \Delta k$	Darcy's permeability coefficient and change in permeability respectively, (m/s)
k_{kc}	Kozeny Carman permeability (m/s)
N	Centrifuge scaling factor
n, n_c	soil porosity, porosity of the coarse fraction
O_{50}	Effective diameter of the coarser fraction's pore constrictions
P_w	Probability of fine particle transport
Q	Volumetric flow rate (m^3/s)
Re	Reynold's number
SF	Shape factor, used in Kozeny-Carman approximation for permeability
v, v_{max}	Seepage flow velocity based on Darcy's permeability, and maximum seepage velocity (m/s)
v_s	Stoke's settling velocity (m/s)
W_{flow}	Instantaneous seepage flow power
CFD-DEM	Coupled numerical model, combining DEM for the solids, and computational fluid dynamics (CFD) for the fluid phase
CHT	Constant head tank
DEM	Discrete element modelling, a numerical method for modelling granular structures

DEM-PFV	Coupled numerical model, combining DEM for the solids, and pore-scale finite volume (PFV) analysis for the fluid phase
HCHG	Higher critical hydraulic gradient for skeleton deformation, from Liang et al. (2019)
LBD-DEM	Coupled numerical model, combining DEM for the solids, and a Lattice Boltzmann method for the fluid phase
LCHG	Lower critical hydraulic gradient for suffusion onset, from Liang et al. (2019)
PPT	Pore pressure transducer
PSD	Particle size distribution
REV	Representative elementary volume

INTRODUCTION

The seepage of water through earth structures such as embankment dams and levees can cause internal erosion, a process responsible for almost 50% of historical embankment dam failures (Foster et al., 2000). In the UK alone, there are over 2000 embankment dams identified by the Reservoirs Act of 1975, with an average age of over 100 years (Bridle, 2008). If these dams were to fail, it could lead to costly damage and potential loss of life. The problem faced by engineers is that, as the name suggests, internal erosion occurs within the body of the structure and may not be discovered for many months or years, by which time the damage is extensive. Suffusion, the selective erosion of the finer soil particles of a gap-graded soil, in particular, is difficult to identify as it is characterised by no volumetric change of the soil body. For the UK's dams, each year there are an estimated 1600 unreported dam failures for every one reported failure (Brown and Gosden, 2004). Increasing demands on existing infrastructure due to climate change and growing populations suggests that the rate of failure of these structures is likely to increase in the coming years.

Despite being a well-acknowledged problem, the factors controlling suffusion erosion are not fully understood. It is generally accepted that suffusion is controlled by both the intrinsic instability of the material, and the combination of hydraulic and stress conditions within that soil (Garner and Fannin, 2010). The loading history of the soil has also been identified as playing a significant role in how this internal erosion progresses through the material. Although many studies have been conducted to explore the influence of various parameters on the onset and progression of suffusion, there is a disconnect between the granular-scale results obtained in numerical models and the macroscale observations in conventional permeameter-style element testing. Although this gap has started to close in recent years due to advances in both computing power and experimental imaging techniques, the current guidelines for the onset and progression of suffusion are exclusively informed by continuum-based assessment methods, despite the well-accepting fact that suffusion is, at its core, a particle-scale phenomenon.

In this study, the results of a series of centrifuge permeameter tests are presented. These have been conducted in order to explore the influence of macroscale parameters used in existing assessment approaches, for example seepage path length and effective stress, by the manipulation of the centrifuge scaling laws. A gap-graded, internally unstable soil is tested under a series of hydraulic loading regimes and specimen configurations. The local and global permeabilities of the specimens are recorded, and samples are dissected post-testing to confirm the final spatial distribution of fine particles within the specimen. These results are analysed using existing suffusion assessment methods, including the concepts of critical hydraulic gradient and erosion resistance index, and a particle-scale conceptual framework for the observed macroscale variation in results is presented.

1.1 AIMS AND OBJECTIVES

This study aims to use a centrifuge modelling perspective to address some of the knowledge gaps in relation to suffusion identified in the literature review. This is achieved by the following objectives:

- To design and develop a centrifuge permeameter that allows the fundamental physics of the suffusion process to be examined by using the centrifuge scaling laws. The apparatus will also facilitate the tracking of the spatial development of suffusion via interstitial pore pressure measurements and post-test particle size analysis.
- To undertake a series of centrifuge tests under a selection of seepage path lengths, effective stress gradients, and hydraulic loading conditions to explore the onset and progression of suffusion using a parametric modelling-of-models approach.
- To impartially examine existing models for suffusion by pushing the boundaries of their macroscale assumptions using the unusual experimental boundary conditions presented by the enhanced gravity environment of the centrifuge.
- To develop a mesoscale approach for considering internal erosion, which may help to explain the discrepancy between existing models that are based on different measurement scales and boundary conditions.

1.2 THESIS OUTLINE

This thesis comprises of nine chapters, the contents of which can be summarised as follows:

- *Chapter 1* briefly introduces the phenomenon of internal erosion, and specifically suffusion, and highlights the aims and objectives of the current study.
- *Chapter 2* defines the terminology used in this study, summarises the key principles of centrifuge modelling, and provides a detailed review of the existing experimental and numerical studies related to suffusion.
- *Chapter 3* presents the materials and methods used in the study, as well as a description of the new centrifuge permeameter.
- *Chapter 4* validates the experimental techniques and data interpretation methods used in this study, where they are non-standard in the context of internal erosion testing.
- *Chapter 5* details the results of the four permeameter tests conducted at 40-g in the centrifuge, including the temporal variation in permeability across the specimens and, where applicable, the results of the post-test particle size analysis.
- *Chapter 6* follows the same structure as the previous chapter, but in this case presenting the results of the four tests conducted at lower than 40-g, including a permeameter test conducted at 1-g outside of the centrifuge environment.
- *Chapter 7* interprets the results of the tests undertaken in this study from a centrifuge modelling-of-models perspective and interrogates existing approaches to classifying suffusion erosion.
- *Chapter 8* takes a more particle-scale approach to interpreting the results of the study, focussing on the impact of hydraulic loading conditions and spatial variation in fines content on the progression and outcomes of suffusion.
- *Chapter 9* summarises the findings of this study and suggests recommendations for future research.

LITERATURE REVIEW

2.1 BACKGROUND

Internal erosion has caused many fatal dam collapses throughout history. In 1989, the Gouhou Dam in China catastrophically failed, killing 400 people. The dam had been built of an internally unstable material and, on its first filling, water seeped into the body of the dam through cracks in the parapet walls. This caused unexpectedly high flow rates in the soil embankment, enough to initiate internal erosion and eventually lead to total collapse (Zhang and Chen, 2006). More recently the near-failure of the Toddbrook Reservoir dam in Derbyshire, UK, captured the attention of the public, in part due to the arresting images of an RAF helicopter airlifting bags of aggregate to plug the gaping hole in the embankment. Although the near-failure of this structure was caused by a poorly designed and maintained spillway, forensic examination of the structure revealed that internal erosion had been occurring unnoticed for some time (Balmforth, 2020; Hughes, 2020).

Sheffield, as well, has a history marred by the collapse of an embankment dam due to internal erosion. In 1864, workers at the newly built Dale Dyke dam on the outskirts of the city noticed water rushing out of the face of the dam. Within a few hours, the dam had completely collapsed and a huge wave of water and debris rushed down the valley into the city centre, killing 244 people in the event still remembered as the Great Sheffield Flood. A hydraulic fracture in the dam's core allowed for an increased flowrate through the dam, leading to catastrophic internal erosion. The problem was only noticed a few hours before collapse, although it is likely that the internal erosion had been progressing for some time (Blight, 1997; Machan, 1999).

It is not just catastrophic structural failure that must be guarded against, internal erosion can also reduce the effectiveness of water-retaining structures. The flow through the soil can cause a redistribution of soil grains, creating areas of higher and lower permeability. This heterogeneity alters the flow

path, meaning the structure does not perform as expected. Increasing the permeability of a dam through loss of some soil particles in turn increases the volume flowing through the body of the dam. For a hydroelectric company, for example, every litre of water flowing through the dam, rather than through the turbines, represents a loss of profits and waste of resources.

According to the model from Garner and Fannin (2010) in Figure 2.1, several criteria must be met for internal erosion to occur. The material must have the intrinsic potential for internal instability, and both the hydraulic and stress conditions must be such that they facilitate the initiation and continuation of that erosion (Garner and Fannin, 2010). A structure with a potentially unstable composition may be completely safe for decades, until some hydromechanical change is made, for example by increasing the height of retained water behind a dam. In the coming years, dams and levees can expect increased water levels due to climate change (increased occurrence of extreme weather events, melting of glaciers) and growing population (greater demands on supplies of drinking water). It is clear that globally, the ageing dam infrastructure may expect to experience more internal erosion incidents in the near future.

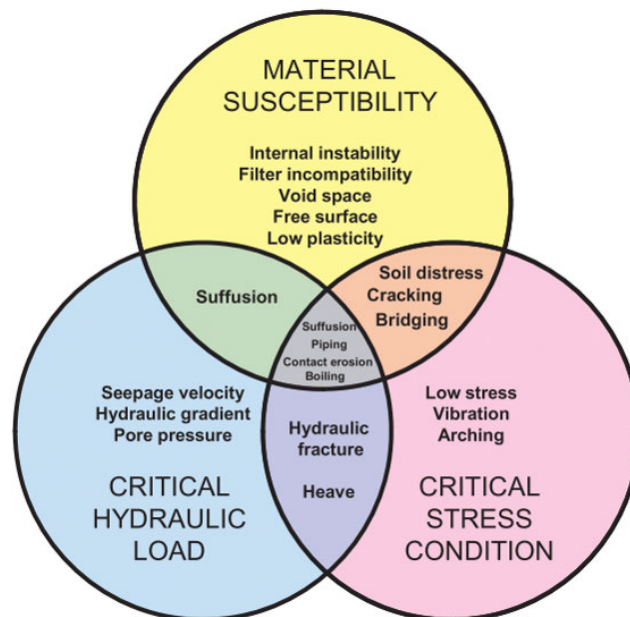


Figure 2.1: Three conditions for internal erosion, from Garner and Fannin (2010)

Of the above mentioned criteria, perhaps the best understood is the material susceptibility. Many studies have found and verified methods to assess instability potential, for example the work of Burenkova (1993), Kenney and

Lau (1985), Kezdi (1979), Li and Fannin (2008) and Wan and Fell (2008) which are discussed further in Section 2.4.1.

So far in this thesis, only the term internal erosion has been used, but this is an all-encompassing phrase for four different processes: concentrated leak erosion, contact erosion, piping, and suffusion (ICOLD, 2017). This study is focused primarily on suffusion, which occurs in gap-graded soils with less than 24% fines (Skempton and Brogan, 1994), also known as under filled soils - Figure 2.2. The flow of water selectively erodes the finest particles of the soil from the voids of the stable coarse matrix. In this model, stress is considered to be entirely transferred by the coarse stable matrix, leaving the fine particles free to move within the soil. Section 2.2.9 gives specific definitions for each of the internal erosion processes, as well as the concepts of fines and under-filled soils.

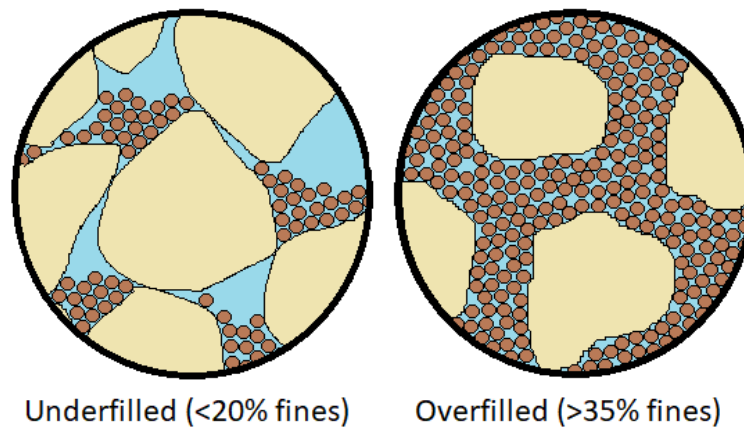


Figure 2.2: Fines particles do not fill the void spaces in under-filled soils, in contrast to over-filled soils

Suffusion is arguably the hardest internal erosion process to identify via external observations, as it is characterized by little or no change in overall soil volume. Luo et al. (2013) describe suffusion as a complex, iterative process. Fines particles are picked up by the flow, migrate through the network of pore spaces, reach a too-small constriction and cause clogging. This increases the local hydraulic gradient up to a level that is able to dislodge the clogged particles, facilitating fines re-migration. Figure 2.3 shows the progression of suffusion when the void spaces are large enough to allow the fines to migrate out of the sample, meaning no clogging occurs.

Another facet of suffusion that has garnered interest in recent years is the influence of heterogeneities in the soil body on the initiation and progression

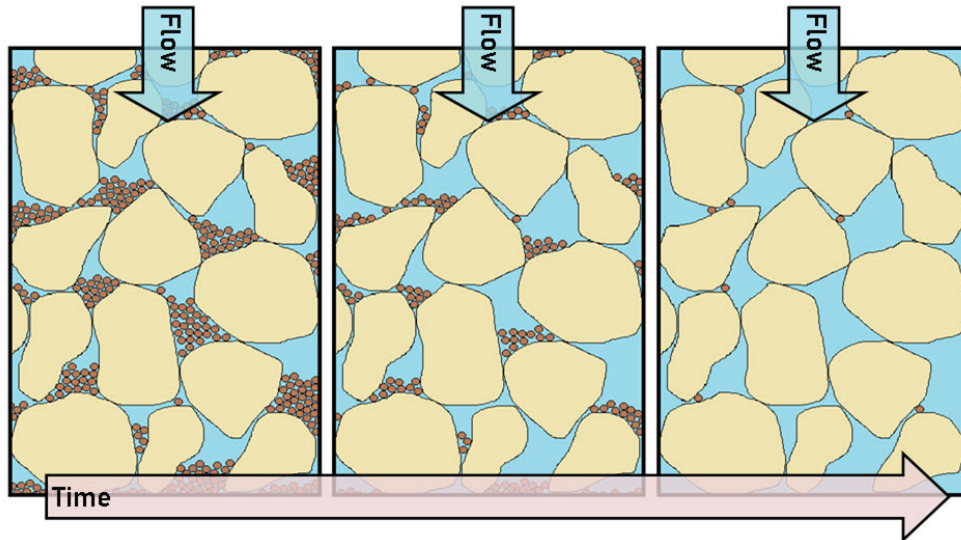


Figure 2.3: Progression of suffusion with time in a soil body subjected to seepage flow

of erosion. Because it is a local process, internal fines migration is more likely to initiate at an area of ‘weakness’, like a zone of less dense material (Shire et al., 2014). This spatial variation can be due to segregation during the dam construction process (ICOLD, 2013) or induced by the naturally tortuous pore fluid flow within the soil. The redistribution of fine particles through a structure by suffusion also creates heterogeneity, changing the material response of the soil (Muir Wood et al., 2010).

2.2 DEFINITIONS

Within this thesis, the terms and concepts defined in this section will be used extensively. Some of these terms share their names with other processes within soil mechanics and geotechnical engineering. Even within internal erosion research, different interpretations for each term are possible, with terms like suffusion and suffosion historically having been used interchangeably. To avoid confusion, their definitions as used in this body of work are given below. In general, the terms ‘fines migration’ will be used to encompass all internal erosion processes, and ‘suffusion’ will be used to describe the erosion witnessed in this study’s experimental work.

2.2.1 *Internal erosion*

Internal erosion is a general term for processes that involve soil particles being detached and transported by seepage flow within the body of a water-retaining earth structure. The eroded particles can be redistributed within the body of the material, or be transported out of the structure by the action of the fluid. As defined by the research-driven bulletin for engineering practitioners released by ICOLD (2017), there are four stages to an internal erosion event, which are as follows:

- *Initiation* - The initial perturbation of soil grains by the seepage flow. There are four distinct forms of internal erosion, defined below.
- *Continuation* - Once soil particles are migrating, erosion will continue unless their passage is physically blocked, or a change in the hydraulic regime causes them to be deposited within a short distance. Structures are designed to prevent continuation by the use of filter layers and material zoning.
- *Progression* - The method of progression varies depending on the type of internal erosion, but in all causes the hydraulic regime within the structure is altered. This can be due to the formation of a pipe or sinkhole. For suffusion, progression manifests as an increase in permeability for areas with depleted fine particles, or decreased permeability where particle deposition occurs.
- *Breach* - If left unchecked, the progression of internal erosion can lead to structural failure of the dam or levee. This can have devastating consequences for the environment and human life. Through monitoring of properties such as pore pressures and surface settlements, practitioners aim to detect internal erosion and intervene before this stage can be reached.

There is a clear spatial scale variation between these stages, from the microscale initiation on a granular level, to the macroscale structural response. This study focusses on the first three stages of the internal erosion process, as understanding the material behaviour at this smaller scale defines the intrinsic mechanics behind the internal erosion process. Structural breach is less of a soil mechanics problem and more related to the specific design of an individual dam or levee. A clear understanding of the factors affecting the earlier stages of

erosion would allow practitioners to make judicious design choices, preventing the latter stage from being reached.

ICOLD (2017) defines four distinct forms of internal erosion initiation, dependent on the granular material present in the structure and the geometry of the problem. This study focusses on suffusion, which is defined in more detail later in this section. A brief summary of the remaining three forms of internal erosion are given below for completeness. At the microscale, the individual movements of fine particles are governed by local forces, and consequently there is a lot of similarity between the four erosion types, a fact that is often overlooked by the separate branches of internal erosion researchers.

- *Concentrated leak erosion* - This occurs when an existing crack within a soil structure is enlarged by seepage flow. The initial crack may be formed by differential settlement, hydraulic fracture, or desiccation. This usually occurs in plastic soils, for example in the clay core of a dam or levee.
- *Contact erosion* - When there is flow parallel to a boundary between a coarse and fine soil, contact erosion can occur. The finer soil is eroded into the granular matrix of the coarse material. In this way, there are many similarities between the transportation processes in suffusion erosion. Contact erosion is a concern at interfaces and boundaries, for example between the core and foundation of a water-retaining structure.
- *Backward erosion* - Occurring in uniform sands, backward erosion can be subdivided into two categories, piping and global backward erosion. The first describes a process of a pipe forming at the downstream side and progressing backwards towards the upstream side of the structure. If left unchecked, this can form a direct channel from the reservoir to the dam or levee toe. Similarly, global backwards erosion progresses backwards along the seepage path. The pipe created is unable to hold itself open and collapses, leading to general movement of the soil above. If this occurs under the core it can cause cavities and sinkholes, or if under the downstream side, it can cause unravelling of the downstream face of the structure.
- *Suffusion* - This fourth process is the focus of this study and is defined by ICOLD (2017) as the transportation of fine particles by seepage flow through a matrix of coarser, stress-carrying particles. In the bulletin, no

distinction is made between suffusion occurring in under-filled compared to suffusion in over-filled materials (sometimes referred to as suffusion in other texts).

According to the often-cited model shown in Figure 2.1 proposed by Garner and Fannin (2010), internal erosion only occurs when at least two of the three criteria are met. The material must have the intrinsic potential for instability, and then either the critical hydraulic or stress conditions (or combination of the two) must be met for erosion to initiate.

2.2.2 *Internal or material instability*

The term internal or material instability can be used to describe a soil that fails to meet the "material susceptibility" criteria in Figure 2.1 from Garner and Fannin (2010). A soil is classed as internally unstable if it has the potential for its fine particles to be transported under the application of sufficient seepage flow. For erosion to occur in an internally unstable soil, the hydromechanical conditions must also be met.

In the case of suffusion, gap- and widely graded soils are usually the most internally unstable. There are many different methods based on the geometric properties of the soil that can be used to assess the internal instability, including those by Kezdi (1979), Kenney and Lau (1985) and Burenkova (1993). These are discussed in detail later in this thesis in Section 2.4.

2.2.3 *Under-filled, over-filled and transitional materials*

A bimodal granular material, in other words one made out of two different scale particles, can be classified as under-filled, transitional or over-filled. In an under-filled soil, also known as a clast-supported structure, the amount of fine particles is small enough that they fit within the void spaces of the coarse particle matrix. They take very little part in the stress transfer through the soil. If the fine particles are eroded by seepage flow, very little settlement occurs as the coarse matrix remains largely unaffected. Skempton and Brogan (1994) found that for a dense packing, to be under-filled a soil needs $< 24\%$ fines

content, which rises to 29% for loosely packed soils, shown schematically in Figure 2.4.

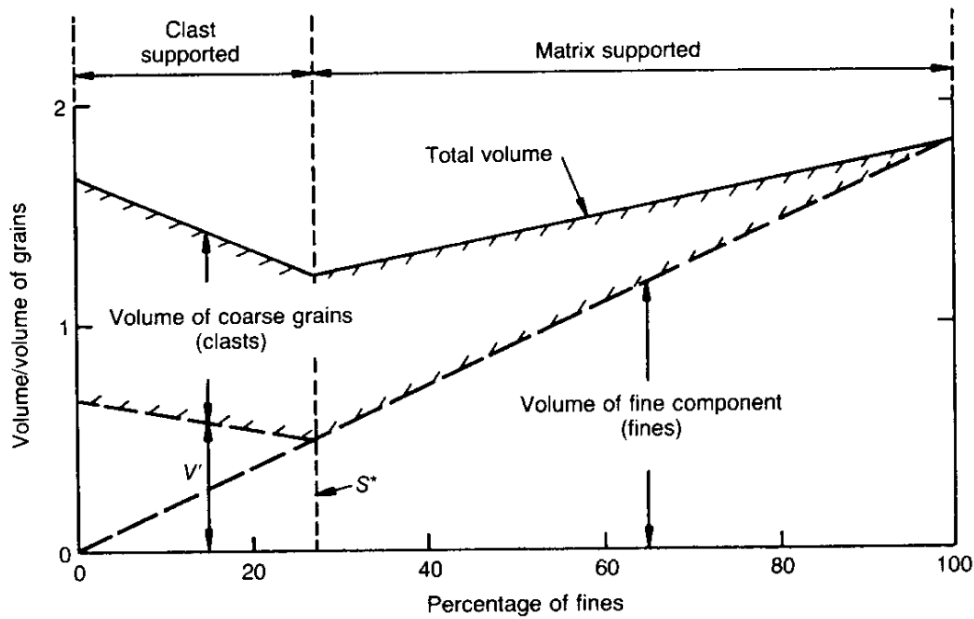


Figure 2.4: Transition between a matrix-supported and clast-supported bimodal granular material based on fines content, from Skempton and Brogan (1994)

Above fines contents of 24 – 29%, the pore spaces are filled and some of the fine particles play a part in the force-chain network alongside the coarse particles, providing lateral support in what can be referred to as a matrix-supported structure. Up until a fines content of around 35% the material is known as a transitional material. Above 35% fines content, the coarse particles are essentially isolated within a sea of fine particles and the both sizes are equally likely to take part in the force chain network. This is shown visually in Figure 2.5. These fines content boundaries, whilst theoretically supported, are not clear distinctions, and the soil behaviour under seepage flow also depends on grain angularity of the coarse fraction (Marot et al., 2016) and the size difference between the two fractions (Chang and Zhang, 2013b). Discrete element modelling of internally unstable soil gradations has been used to explore the role of the finer fraction in transmitting stresses through the soil, for example the work of Shire et al. (2014), and this is discussed in more detail in Section 2.7.1.

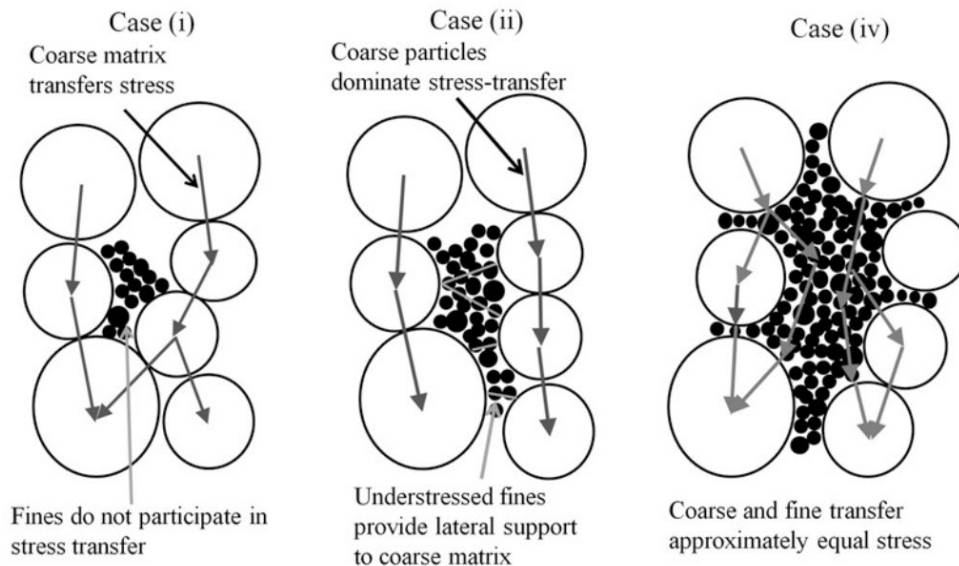


Figure 2.5: The role of fine particles in stress transfer depending on fines content (i = under-filled, ii = transitional, iv = over-filled), from Thevanayagam et al. (2002)

2.2.4 *Fines and the finer fraction*

Conventionally in geotechnical engineering, the term fines refers to silt and clay particles which can pass through a 63 micron sieve, the finest mesh in the standard set of sieves used in the UK (Powrie, 1997). Within the suffusion research community, the term fines is used in a more general way to refer to the finer fraction of a bimodal material, the portion of the soil which is able to migrate through the stable coarse matrix due to the seepage flow. This is a relative term compared to the whole gradation of the soil, rather than an absolute particle diameter. For example, in a gravel/sand mix, the sand portion can be referred to as the finer fraction, or fines, whilst the gravel constitutes the coarse granular matrix.

This distinction is relatively simple in a gap-graded material, but the boundary between the finer and coarser fraction can be harder to define in an internally unstable widely-graded material. For the internally unstable material tested in this study detailed in Section 3.2.2, the term fines is used to refer to the silt fraction, which has a particle diameter up to 90 microns. The sand, despite being very fine with a maximum particle size of 300 microns, is referred to as the coarse fraction, as it has a larger particle sizes relative to the silt.

2.2.5 Suffusion and suffosion

Suffusion is one of the four initiation processes for internal erosion, as identified by ICOLD (2017). It is defined as the selective erosion of fine particles through a matrix of coarse, stress-carrying particles due to the action of seepage flow, shown in Figure 2.3. In some studies, suffusion is the name given to only the transportation of fine particles in an under-filled material. This is characterised by no change in overall volume as the coarse matrix is not disturbed. In contrast, suffosion occurs in transitional and over-filled soils, where the fine particles take part in the force transfer network and their removal causes settlement as the force chains rearrange.

Moffat and Fannin (2011) used the term suffosion to define a second stage of suffusion accompanied by a significant change in total soil volume, whereas other studies state that soils can be either suffusive or suffosive depending on their initial fines content (Fannin and Slangen, 2014). It is widely agreed that both processes are accompanied by mass loss and change in hydraulic conductivity, but only suffosion sees a change in the soil volume, as shown in the conceptual framework adapted from Fannin and Slangen (2014) in Figure 2.6.

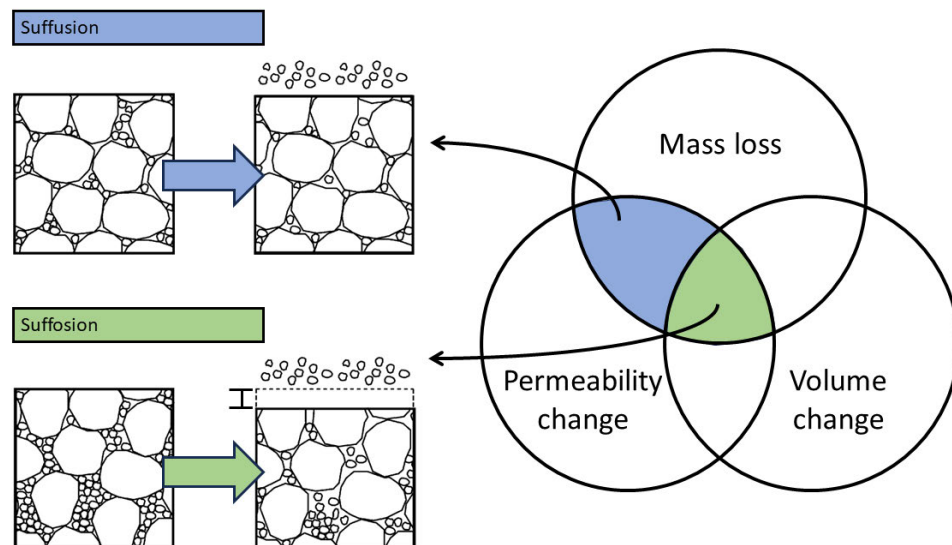


Figure 2.6: Conceptual framework for suffusion and suffosion under upwards seepage flow, adapted from Fannin and Slangen (2014)

In this study, only an under-filled soil gradation is experimentally tested, and so the process will be referred to as suffusion in relation to these results. However, comparisons will be made between this study and the results and frameworks based on studies that were conducted on a range of materials, including transitional and over-filled materials. Although this could be defined as suffusion, the two processes are not necessarily distinct phenomena, with an abrupt transition as soon as the fines content reaches a certain percentage. Over the course of a seepage test, the redistribution of fines within the sample can cause an area to change from under-filled to transitional due to deposition, or from over- to under-filled as fines are eroded.

In general, when making comparisons between studies, the terms internal and external fines migration, as defined in the next section, will be used to avoid the semantic issue of suffusion versus suffosion.

2.2.6 *Internal and external fines migration*

Fines migration is a more general term, preferred by some in the internal erosion community, to describe the transportation and potential deposition of particles through the soil body by the seepage flow. This encompasses both suffusion and suffosion, as well as contact erosion, the progression of which arguably shares many similarities with the first two processes.

Internal fines migration refers to the transportation and deposition of a fine particle within the area of interest (the soil element in a laboratory permeameter test). This local deposition occurs due to the inability of a particle to pass through a constriction, or due to a change in the hydraulic forces acting on the particle, a process that is referred to as clogging. When the migration of the fine particle is not impeded along the seepage path and it can be fully removed from the soil block, the process is termed external fines migration, and specifically external suffusion for under-filled materials.

Whilst fines loss is generally locally destabilising, clogging can have a stabilising effect (Wautier, 2018). However, this particle deposition does change the flow and stress regime within the soil, which can have consequences at other points along the seepage path. This redistribution of fine particles spatially within the soil, without necessarily being externally eroded, is a large focus of the current study, and will be discussed in depth in Section 2.6.2.

2.2.7 *Permeameters*

The permeameter is a traditional piece of equipment used to find the permeability of a soil from laboratory tests by employing Darcy's law (Section 2.3.2) to interpret the flow rate through the specimen under a known applied hydraulic head (Head, 1982). By following these principles, researchers have modified the classic permeameter set-up to investigate the process of internal erosion. Usually developed internally in each institution, there is a lot of variability between different permeameters, but they can broadly be split into two categories.

The most common type of apparatus for the investigation of suffusion is the modified rigid-walled permeameter. Although each device has a slightly different design, the basic components remain the same. The soil sample is housed in a cylindrical rigid-walled cell, with pore pressure measurements taken along its length to calculate the changing permeability of the soil as suffusion occurs. Seepage flow is either applied upwards against gravity or downwards through the sample, and the amount of eroded material is often quantified. This can be done by using turbidity measurements (Le et al., 2018), catching and weighing eroded fines (Horikoshi and Takahashi, 2015), or by characterising the post-test particle size distribution (Wan and Fell, 2008).

For more complex stress states, a device based on an adapted triaxial cell can be used. This stress-controlled apparatus can be used to explore the influence of shear stress on the initiation and progression of suffusion. The flexible walls of the cell allow the soil to volumetrically deform without creating preferential flow channels at a rigid boundary, letting the force chains rearrange into a more stable configuration (Slangen and Fannin, 2017). These devices are more commonly used to investigate suffosion which, unlike suffusion, is characterised by a significant volume change. Triaxial cells can also be used to investigate the mechanical consequences of erosion on a soil sample, for example in the work of Chitravel et al. (2022), Ke and Takahashi (2014a) and Muir Wood et al. (2010).

2.2.8 *Seepage path length*

The seepage path length of a soil is a parameter that has previously linked to influencing both the onset and progression of the suffusion phenomenon,

as discussed in Section 2.6.3. Within a granular material such as a soil, the actual route that water takes through the pore void spaces is tortuous and very difficult to measure. Consequently, this has been simplified to a continuum-scale distance in a similar manner to the assumptions made when discussing Darcy's flow (Section 2.3.2). In permeameters, the 1-D flow is typically vertical, and the seepage path length is taken as the height of the cylindrical specimen. In 2-D models, the seepage path and realistic 3-D conditions the seepage path is more complicated, but can be found using flow nets and other analytical approaches.

In the centrifuge, the specimen height is scaled by a factor of N (Section 2.3.1), and so in the initial analysis in Chapter 5, the scaled specimen height is used as the seepage path length. The implications and limitations of this approach are discussed in Section 7.2.2. When reporting results of centrifuge tests in this study, typically both the actual (model) specimen height and the scaled (prototype) height are quoted.

2.2.9 *Micro-, macro- and mesoscale*

The connection between microscale and macroscale understandings of internal erosion processes is at the forefront of current research efforts, being an issue that was frequently highlighted at the 29th annual meeting of the European Working Group on Internal Erosion, held in Lyon in 2023. The key question being, how can we bridge the gap between the granular scale observations in DEM simulations, laboratory scale element tests, and processes occurring in in-situ water-retaining structures?

In this thesis, the term macroscale is used to refer to observations and studies undertaken based on continuum assumptions for the soil behaviour. This approach is typically used when designing modelling-of-models tests in the centrifuge (Section 2.3.1) and is also the basis of the majority of existing frameworks for understanding suffusion. (Section 2.5.2). Common continuum assumptions include Darcy's Law (Section 2.3.2) and Kozeny-Carman permeability (Section 2.4.3). At the opposite end of things, the term microscale is used here to talk about the behaviour of individual particles due to the hydromechanical forces acting on them. This is typically examined by DEM simulations, sometimes coupled with seepage flow forces, which are currently

limited by computational power to only a few thousand, typically spherical, particles.

In very recent years, steps have been taken to examine a scale in between these two extremes both using numerical and experimental methods. The doctoral work of Wautier (2018), as well as the CFD-DEM simulations of Hu et al. (2019) (both discussed in Section 2.7.3), both blurred the distinction of micro- and macroscale by simulating enough particles to consider a representative elementary volume (REV). In experimental testing, recent use of X-ray tomography by Nguyen et al. (2019) (Section 2.6.2) has allowed a visualization of suffusion progression at a granular level, if only at discrete intervals, using a 'real' soil gradation, something that was previously only possible in laser-illuminated glass beads (e.g. Hunter and Bowman, 2018). In this study, this intermediate scale of testing is referred to as the mesoscale.

2.3 THE GEOTECHNICAL CENTRIFUGE AS AN INVESTIGATIVE TOOL

2.3.1 *Principles of centrifuge modelling*

Using a centrifuge to replicate large-scale geotechnical problems with much smaller models has become a widely accepted technique since its inception in the middle of the last century. By subjecting a model to an enhanced g-field many times Earth's gravity, the stresses and strains of a full sized structure (called a prototype) can be generated.

$$Ng = R\omega^2 \tag{2.1}$$

Although the stresses and pressures in the model and prototype will be the same, other properties are scaled with the centrifuge acceleration factor, symbolised by the letter N . The relationship between centrifuge angular velocity, ω , and enhanced g-level, Ng , is given in Equation 2.1 and is dependent on the centrifuge radius, R . The key scaling factors used in this study are summarised in Table 2.1. The scaling factor is applied to the model value to find the prototype value and given in terms of N . For example, for length the scaling factor is N , so a model with a height of 0.1 m at $N = 100$ times Earth's gravity would have a prototype height of 10 m. There are conflicting interpretations

of the scaling of hydraulic gradient versus permeability, which are discussed further in the following section.

Table 2.1: Centrifuge scaling laws relating to the phenomenon of internal fines migration (for quantities marked †, see Section 2.3.2)

Parameter	Scaling factor (prototype / model)
Length	N
Pressure	1
Stress σ	1
Density ρ	1
Gravitational acceleration g	N
Seepage velocity v	N
†Darcy's permeability k	N
†Hydraulic gradient i	1

The technique of modelling-of-models is used in geotechnical centrifuge modelling to assess similarities and scaling conflicts when scaling laws are not immediately apparent, for example in problems with complex geometries of multiple processes occurring (Taylor, 1994). The basic principle involves preparing models of varying model dimension and accelerating them at different g -levels to achieve the same prototype conditions. For example, the vertical stress at base of a 0.2 m column of soil in a model at 50-g would be the same as the vertical stress at base of a similar column 0.1 m high at 100-g. To truly achieve similitude in seepage flow problems, the pore fluid used should also be varied to keep the viscosity similar between models. In practice, this is complex and inconvenient to achieve in the laboratory, and this step is often omitted in models with laminar flow, due to the limited impact of viscosity at these low flows (Goodings, 1994).

2.3.2 Understanding the scaling of hydraulic gradient

As alluded to in Table 2.1, the scaling laws surrounding hydraulic gradient and Darcy's law are somewhat contested, with some scaling the hydraulic

gradient, i (Madabhushi, 2013; Marot et al., 2012), whilst others apply the scale factor to the permeability, k (Garnier et al., 2007; Taylor, 1994). To understand where this discrepancy arises, Darcy's law for seepage must be clearly defined as follows (adapted from Powrie, 1997).

$$q = Aki \quad (2.2)$$

where:

q is the volumetric flowrate of the water (L^3T^{-1} in dimensional analysis)

A is the cross-sectional area of the flow (L^2)

k is Darcy's coefficient of permeability, alternatively termed hydraulic conductivity (LT^{-1})

and i is the hydraulic gradient (dimensionless)

When the cross-section is constant across the seepage path, q/A can be simplified to the Darcy's seepage velocity, v , as shown in Equation 2.3. This property v is an average velocity across the whole soil cross section. In reality, the fluid velocity within the pores of the granular material (termed tortuous velocity) will be significantly higher. At an even smaller scale, there will be a gradient in fluid velocity across each individual pore. Consequently, this parameter is based on macroscale assumptions.

$$v = ki \quad (2.3)$$

The hydraulic gradient, i , is the decrease in total fluid head, Δh (L in dimensional analysis), across the length of the seepage path, Δz (L), and is calculated using Equation 2.4.

$$i = \frac{\Delta h}{\Delta z} \quad (2.4)$$

Darcy's coefficient of permeability, referred to hereafter as permeability, k , is a function of both the soil structure and the properties of the permeant fluid, specifically its unit weight, γ_f in kN/m^3 ($ML^{-2}T^{-2}$), and dynamic viscosity, μ_f in kNs/m^2 ($ML^{-1}T^{-1}$). The soil structure is represented by the intrinsic permeability, K , which is purely a property of the soil matrix and has the units m^2 (L^2).

$$k = K \times \frac{\gamma_f}{\mu_f} \quad (2.5)$$

In the centrifuge, when the fluid and soil are kept constant, the permeability, k , scales with g -level (Garnier et al., 2007). The hydraulic gradient is dimensionless and does not scale, leading to the seepage velocity, v , scaling by N . This was verified experimentally by Khalifa et al. (2000).

Whilst this all makes sense from a continuum perspective, this does not capture how the concept of hydraulic gradient is used within the internal erosion community. Hydraulic gradient is an easy to calculate parameter that can be compared between different studies, used as a catch-all for describing the hydraulic regime within a soil body. At 1- g , to move between fluid head and pressure is simply a matter of multiplying head by the fluid's unit weight, and the seepage path is the distance between the two measurement points.

Intrinsically, the hydraulic gradient reflects the energy dissipated across a seepage path due to frictional losses and elevation potential energy in laminar flow through a soil. The changes in i reported in suffusion studies are due to a change in intrinsic permeability, K , caused by work done in the migration of fine particles, which is a much more complex to quantify than Darcy's coefficient of permeability. This microscale variation in K is captured within the changing macroscale parameter of i , and the coefficient of permeability, k , is inferred from this. In the centrifuge, this simple relationship breaks down because of the varying scales on the different parameters.

Thusyanthan and Madabhushi (2003) modified Darcy's law to calculate the 1- g permeability of a soil, k_{1g} , from the potential energy gradient across a model, and its unscaled model seepage path length. This is shown in Equation 2.6.

$$v = \frac{k_{1g}}{\gamma_{1g}} \times \frac{\Delta(P + z\rho g)}{\Delta L} \quad (2.6)$$

where:

v = Darcy's seepage flow velocity for laminar flow

k_{1g} = Darcy's permeability at 1- g

γ_{1g} = unit weight of the fluid at 1- g

ΔP = pore pressure difference across the soil

$\Delta z\rho g$ = elevation pressure difference across the soil

ΔL = model seepage path length

The benefits of using this formulation for this study are twofold. Firstly, it allows for easy comparison between permeabilities of specimens tested at different g -levels as it calculates the 1- g permeability. Secondly, using the potential energy gradient captures the fact that there is greater energy dissipation over the same granular matrix at the microscale for an identical model conducted at a higher g -level. In contrast the continuum interpretation of Darcy's law in Equation 2.2 would imply that the same hydraulic conditions were present in both models.

In the discussion of hydromechanical envelopes in Section 7.1, the critical hydraulic gradients, i_{cr} , from the 1- g study of Li and Fannin (2022) are converted to critical potential energy gradients, EG_{cr} , for comparison with the results of this study. This is achieved by multiplying them by the unit weight of the pore fluid, γ_f .

$$EG_{cr} = i_{cr}\gamma_f = i_{cr} \times \rho_f \times g \quad (2.7)$$

2.3.3 Errors and limitations of centrifuge modelling

Due to the relatively small radius of the centrifuge (compared to the radius of the Earth), there can be a significant variation in g -level across the height of a model. In a tall model, this effect is particularly pronounced and needs to be corrected for when analysing centrifuge data. Although a scale factor, N , is usually quoted for centrifuge tests, this is specifically at the effective radius of the centrifuge, R_e , from the centre of rotation, CoR. Typically, this is chosen to minimise stress variation across the sample height (Taylor, 1994), as shown graphically in Figure 2.7.

In a simple column of soil, if the radius to the soil surface is R_{top} , the vertical stress at a depth of z , σ_{vm} , can be found using Equation 2.8, where ρ is the bulk density and ω is the angular velocity of the centrifuge.

$$\sigma_{vm} = \int_0^z \rho\omega^2 (R_{top} + z) dz = \rho\omega^2 z \left(R_{top} + \frac{z}{2} \right) \quad (2.8)$$

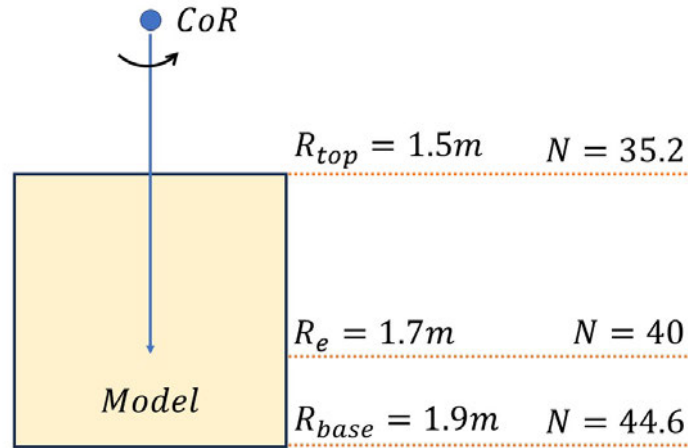


Figure 2.7: A 0.4 m tall model experiences a significant variation in g-level across its height at 40-g, even when the effective radius is chosen to minimise stress variation

The same principle must also be used when evaluating hydraulic heads, which include both an elevation and pressure head component, following Bernoulli's principle. It is not appropriate to consider the elevation head at the top of the sample as just the length of the seepage path, rather Anderson et al. (2015) formulates it as a potential energy difference across a model height, $P(d)$, at any distance from the datum, d in Equation 2.9. The radius to the base of the sample is given by r_b . This corresponds directly to the modified Darcy's law approach presented in Equation 2.6.

$$P(d) = \rho\omega^2 \left(r_b d - \frac{d^2}{2} \right) \quad (2.9)$$

As well as the variation in acceleration in the radial direction, an error across the width of the model is also introduced due to the slightly different radii to the centre of the payload, compared to the outside edge, as shown in Figure 2.8. This error, E_{width} is calculated from the two radii shown in the figure using Equation 2.10.

$$E_{width} = \left(1 - \frac{R_1}{R_2} \right) \quad (2.10)$$

Conventionally in centrifuge modelling, the particle size of the soil is not scaled to match the prototype. Scaling a gravel in the field down to a sand in

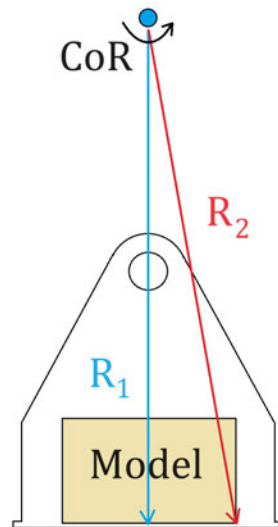


Figure 2.8: An error in calculated acceleration is introduced across the width of a centrifuge model due to the slight difference in radius to the payload centre compared to the payload extremities

the centrifuge may be a valid approach, but scaling a sand down to a clay in the centrifuge would not give compatible results, due to their very different stress-strain results (Taylor, 1994). Additionally, centrifuge modelling can be undertaken on undisturbed samples from a site, where the grain size cannot be scaled. Instead, the ratio of the particle size to the dimensions of the model must be designed to be large enough to minimise the particle size affects.

Although not undertaken in a centrifuge, the scales of the two permeameters in the internal erosion study of Li (2008) prompted an examination of the ratio of particle size to permeameter diameter. Following the ASTM:D5101 (2017) advice for gradient ratio tests suggests a minimum ratio of the largest particle size, D_{100} , to the internal diameter of the cell of 10 to prevent soil arching. This was also the minimum ratio used the Kenney and Lau (1985) study, a foundation of suffusion testing. For a footing problem, Taylor (1994) cites a minimum particle to footing ratio of 15 in the centrifuge, below which there was deviation from the classic stress-strain response in the soil. Marot et al. (2012) used a ratio of D_{100} to cell diameter of 160 for their centrifuge study, and Ovalle-Villamil and Sasanakul (2020) had a ratio of >500 .

2.3.4 *Internal erosion testing in the centrifuge*

To the author's knowledge, there have been very few centrifuge studies of internal erosion processes to date, with only the study of Marot et al. (2012) focussing on suffusion specifically. This study investigated the length scale effect on suffusion progression by testing a range of specimen lengths in a rigid-walled centrifuge permeameter at g-levels between 10- and 40-g. The methods and results of this study are discussed in Section 2.6.3 as they formed a large part of the initial motivation for this current study. An important point to note about the study is that the authors chose to apply a scaling factor to the hydraulic gradients reported in the paper, scaling the head difference across the specimen, H_{WM} , but using the model rather than the prototype specimen height, Δz_M . This is shown in Equation 2.11, taken directly from Marot et al. (2012).

$$i = \frac{H_{WM}N}{\Delta z_M} \quad (2.11)$$

For the reasons stated in Section 2.3.2, the hydraulic gradient is not scaled in this study, and, apart from where necessary for comparison with existing studies, the energy gradient approach is preferred.

Ovalle-Villamil and Sasanakul (2020) also published an assessment of centrifuge modelling of internal erosion under upwards flow conditions, with a series of centrifuge tests conducted between 10- and 30-g. These experiments focussed on backwards erosion piping, but highlighted the complexity of scaling parameters that are crucial to the interpretation of suffusion, including hydraulic and pressure gradients. The tests were performed without scaling particle size, pore fluid and model dimensions, instead testing the same model under a variety of hydraulic conditions by manipulating the centrifuge scaling laws. This approach, a similar one to Marot et al. (2012), varies from the traditional modelling-of-models approach described above, but still allows for a parametric study of the influence of scaling the stress and hydraulic loading. Accordingly, this approach is used in this current study and is detailed in Section 3.8.

2.3.5 *Centrifuge facilities at the University of Sheffield*

The 50gT geotechnical beam centrifuge at the University of Sheffield has a radius of 2 m and the capability of accelerating a 500 kg payload at 100 g. The centrifuge is shown in Figure 2.9 and was designed and manufactured by Broadbent Ltd. A full specification is given in Black et al. (2014). The mass of the payload and centrifuge cradle is counterbalanced by a counterweight at the opposite end of the beam. This is adjusted pre flight based on the weight of the payload, and there is also an in-flight autobalance capability to counteract the effects of fluid drainage and movement of equipment during the test.

The centrifuge has a maximum rotational speed of 280 RPM, however in this study tests are undertaken at a maximum of 145 RPM. Slip rings for power, control and hydraulics allow the centrifuge test to be monitored and controlled from the centrifuge control room located adjacent to the beam chamber. A webcam on the cross bar of the beam gives a live feed in the control room of the plan view of the payload whilst in flight. Another camera with a live feed to the control room can be attached to the payload to monitor elements of the apparatus in flight. In this study, the camera was used to verify the water level in the upstream constant head tank.

Data acquisition is accomplished with a National Instruments solution programmed through LabView. The beam is equipped with a NI cDAQ 9188XT compact DAQ chassis, which allows up to seven DAQ modules to be connected. For the tests in this study, three NI 9237 bridge input modules are used for the pore pressure transducers. A NI 9205 voltage input module allows for the control of the linear actuator, which adjusts the height of the downstream constant head tank, as well as providing power for the payload lights and turbidity sensor.

2.4 MATERIAL INSTABILITY

As mentioned previously, there are many different methods for assessing material instability in a soil. These are typically based on geometric characteristics of either the particle size- or constriction size distribution (PSD and CSD respectively) and work on the concept of a soil's ability to self-filtrate migrating particles within a short particle transport difference. Dassanayake et al. (2022)

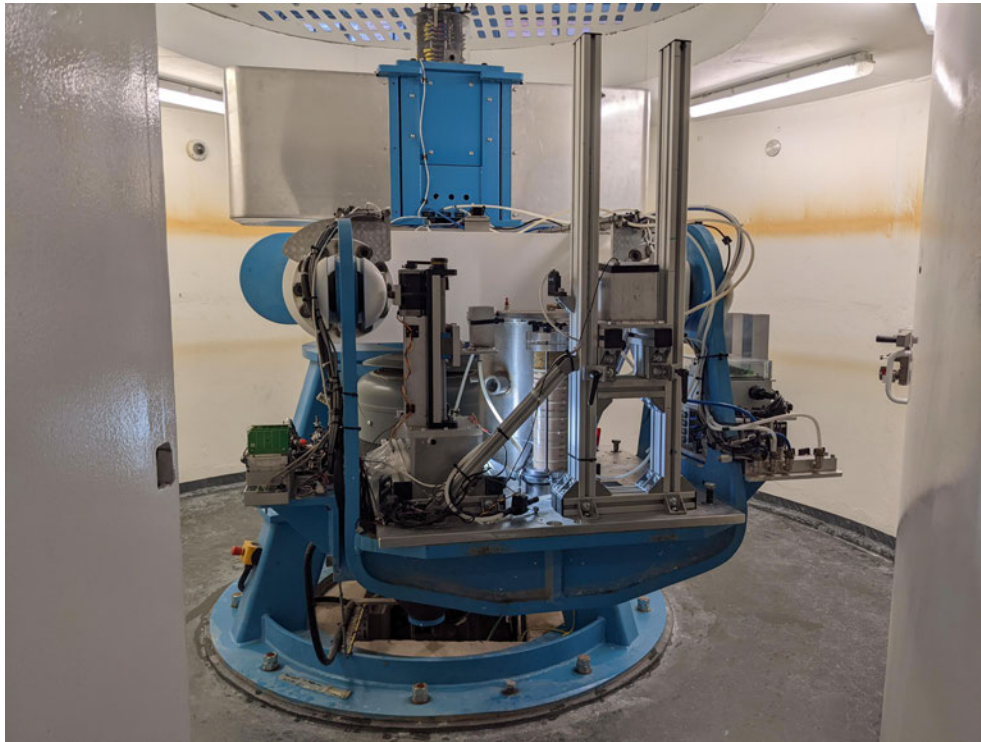


Figure 2.9: View of the 50gT geotechnical beam centrifuge at the University of Sheffield

provides a comprehensive review of the various assessment methods proposed in literature, and the following section gives a detailed review of the methods chosen to assess the materials in this study.

2.4.1 *Geometric instability criteria*

In this section, two of the most common geometric instability criteria, Kenney and Lau (1985) and Li and Fannin (2008), are discussed in detail, as they are later used to assess the internal stability of the soil gradation used in this study (Section 3.2.2). The justification of using these methods over other geometric criteria is also mentioned.

Kenney and Lau (1985) method

The Kenney and Lau (1985) method of assessing material instability stems from the ability of the loose particles to block the pore constrictions and prevent the passage of fine particles through the system. The material can be considered as a coarse matrix of particles carrying the stress, and loose particles that sit

un-stressed in the pores of the matrix. Some, but not all, of these loose particles are able to move through the material when a seepage flow is applied.

When this flow is applied, the loose particles are picked up and transported through the coarse matrix until they either leave the sample or reach a constriction smaller than their size. When this happens, they are deposited and that constriction is then blocked. If the soil is missing a certain size range of particles, constrictions of a smaller size cannot be blocked, leaving an open passage for fine particles to continue being transported through the sample. This characterises an internally unstable material.

It is clear from this that the internal instability is related to the proportion of grains of each size. The absolute value of size is not important; it is the relative sizes within the particle size distribution. In this method, the increase in cumulative mass percentage between an initial grain diameter and the grain diameter four times its size is measured. The cumulative percentage at grain size D is termed F , and the increase in percentage is termed H . This process is repeated for many grain sizes along the PSD to capture the curvature of the distribution. Figure 2.10 from Li (2008) shows this method graphically.

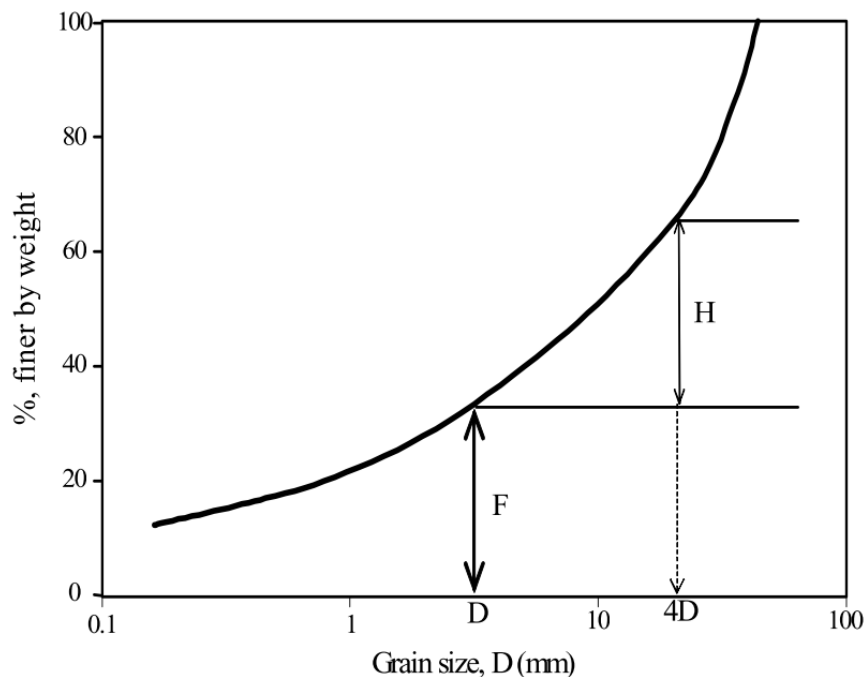


Figure 2.10: Graphical representation of the Kenney and Lau (1985) method, from Li (2008)

This range is chosen with reference to Kenney et al. (1985), who found that a particle size D can pass through a constriction made by particles with size $4D$. If there is a relatively small number of grains contained in the range H , a particle of size D would be able to pass relatively uninhibited through the sample.

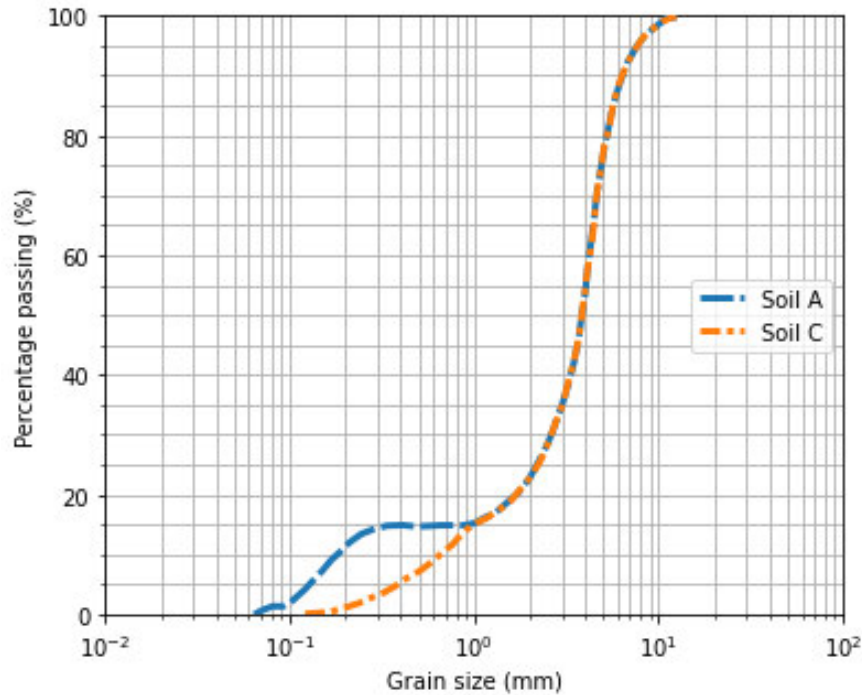


Figure 2.11: Particle size distributions of internally unstable soil A and internally stable soil C from the experimental study of Skempton and Brogan (1994)

To perform this analysis, many different values of D are used and the results are plotted as a soil curve in $H - F$ space. A material is classified as unstable according to Kenney and Lau (1985) if the soil curve dips below the threshold $H/F = 1.0$ in the region of $F < 0.3$. Figure 2.11 shows the particle size distributions of materials A and C used in the permeameter tests of Skempton and Brogan (1994) (Section 2.5.1). A is a gap-graded soil which was shown to be internally unstable when subjected to one dimensional downwards seepage flow, whereas C was stable against internal erosion. In Figure 2.12, which shows both the Kenney and Lau (1985) and Kezdi (1979) (discussed in the following section) instability boundaries, the H/F line for material A dips below the $H = F$ boundary line with a minimum $H/F = 0.14$. In contrast, the H/F line for material C is constantly above the Kenney and Lau (1985) stability boundary ($H/F_{min} = 1.6$).

Li and Fannin (2008) and the Kezdi (1979) method

A method based on a similar approach to the Kenney and Lau (1985) method detailed above is from Kezdi (1979), with the fraction of the mass between D and $4D$ having to be greater than 15% for the material to be stable. This threshold is based on the Terzaghi (1939) semi-empirical filter criterion $D'_{15}/d'_{85} = 4$ used in practice for its simplicity, where the soil is split into a coarse component, D , and a fine component, d . The particle size curve for the border between stable and unstable in this case is linear on a semi-logarithmic plot, whereas for Kenney and Lau (1985) it is upwardly concave.

Li and Fannin (2008) undertook a comparison of the two methods and proposed using a combination of the two to assess material stability. Figure 2.12 illustrates the modified $H - F$ diagram, including the two soils A and C previously discussed from Skempton and Brogan (1994). Li and Fannin (2008) found that the Kezdi method is more successful at identifying instability in gap-graded soils, whereas the Kenney and Lau method is favoured for widely-graded soils. Using a combination of the two, Kezdi at $F < 0.15$ and Kenney and Lau at $0.15 < F < 0.3$, proves to be the most conservative option.

As an alternative to this method, Wan and Fell (2008) also proposed extension of the Burenkova (1993) method, which considers the probability of internal instability. This is more suitable for very widely graded materials such as glacial tills, although the boundary between stable and unstable is not as clear-cut. However, this method does allow for the inclusion of some cohesive (plastic) fines, which is a key advantage when compared to the Kezdi (1979) and Kenney and Lau (1985) methods which are only applicable to non-plastic materials. As this project considers only a silt/sand soil gradation with no cohesive fines, this method will not be further explored.

2.4.2 *Pore network constrictions*

Rather than using a particle size distribution to infer a soil's self-filtering potential, the ability of the fine particles to migrate through the pore network of the coarse matrix can be considered. This concept of a controlling constriction size for self-filtering was proposed by Kenney et al. (1985) and is based on the ability of a particle to infiltrate through a multilayer model representing

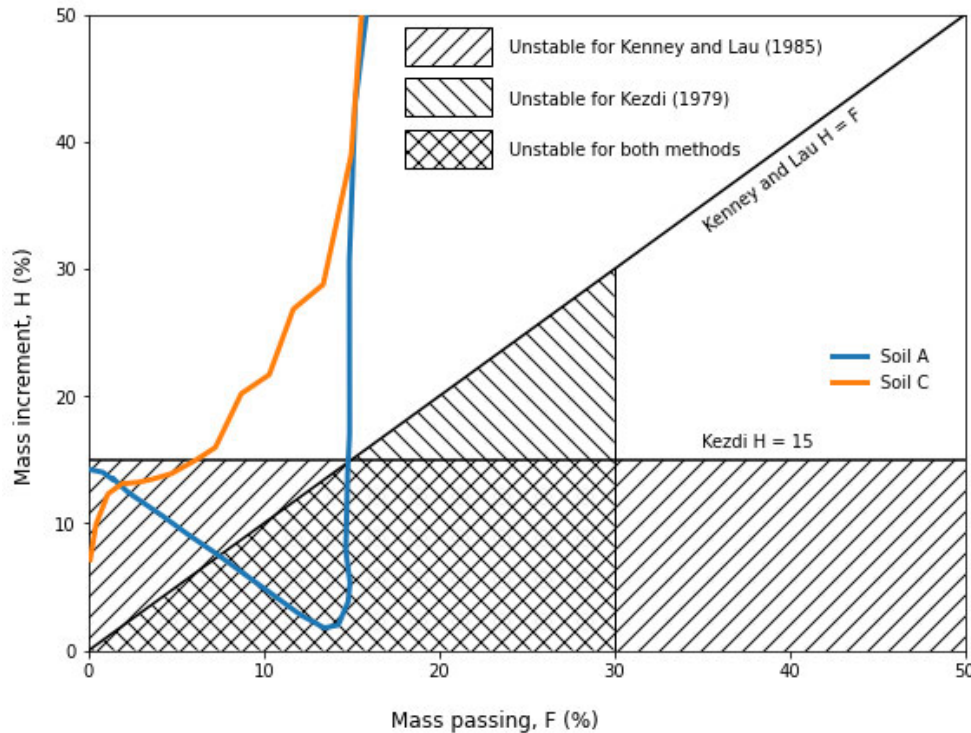


Figure 2.12: Internal instability boundaries in $H - F$ space from Li and Fannin (2008), modified to include unstable soil A and stable soil C from Skempton and Brogan (1994)

the constrictions of the coarse matrix (Figure 2.13). This can be measured experimentally using a series of mesh sieves, or inferred from a series of assumptions about the particle shape and packing.

By splitting a soil into its coarse and fine fraction, Indraratna et al. (2015) defined an optimum constriction size criterion for internal stability of the soil, given in Equation 2.12. In order for the soil to be stable, the diameter of the 85th percentile of the fine fraction, $d_{85,SA}^f$, must be larger than the 35th percentile of the constriction size distribution of the coarse fraction, D_{c35}^c . Rather than using the typical mass passing PSD for the fine fraction, which over-represents the influence of the largest particles, the PSD by surface area is used, as shown in Figure 2.14. This, as well as the constriction distribution, is calculated by making assumptions about the particle shape, usually that it is spherical. By using the constriction size, the relative density of the soil can be considered in the stability assessment criteria.

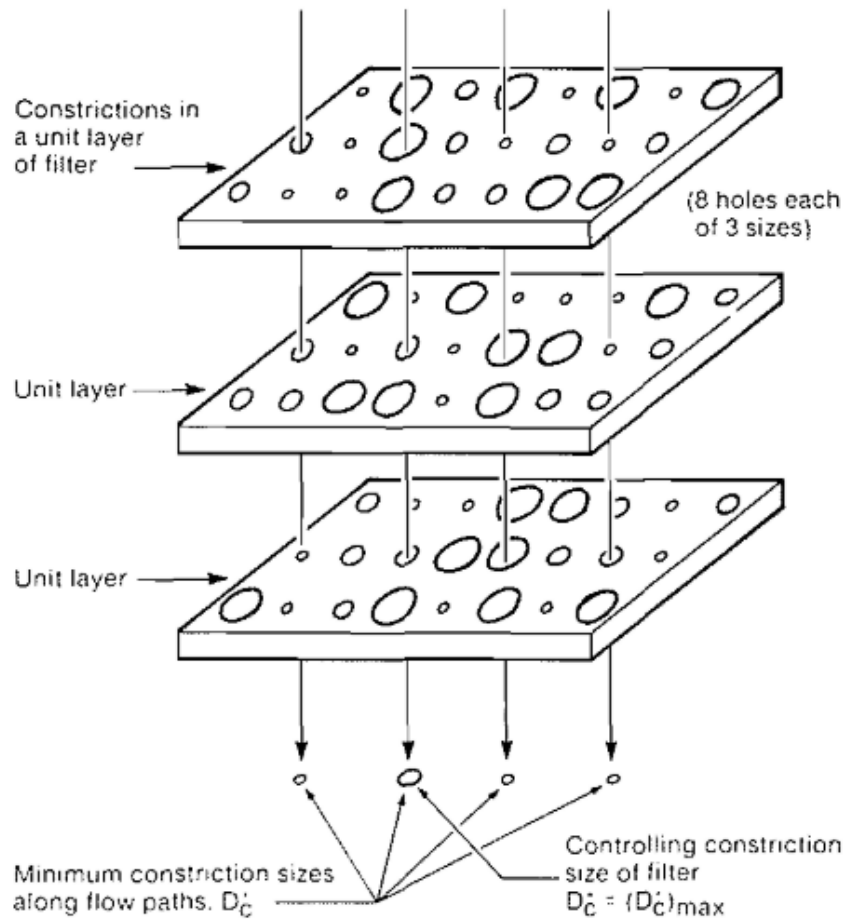


Figure 2.13: Determining controlling constriction size along the seepage path, from Kenney et al. (1985)

$$\frac{D_{c35}^c}{d_{85,SA}^f} \leq 1 \quad (2.12)$$

To account for the transportation potential of a migrating fine particle, To et al. (2016) introduced a probability of fine particle being transported to the next pore space. The total probability for all the loose particles being transported, P_w is calculated for each size of particle. Soils with P_w above 50% can be classified as unstable, but percentages below that show self-filtering potential, as the probability of a fine particle passing through successive constrictions compounds as the number of constrictions increases (Equation 2.13). Whilst this encompasses the full suffusion process in theory and would be very useful for assessing complex soil gradations, in practice it is currently only viable to calculate this at the microscale in a DEM model due to the computational

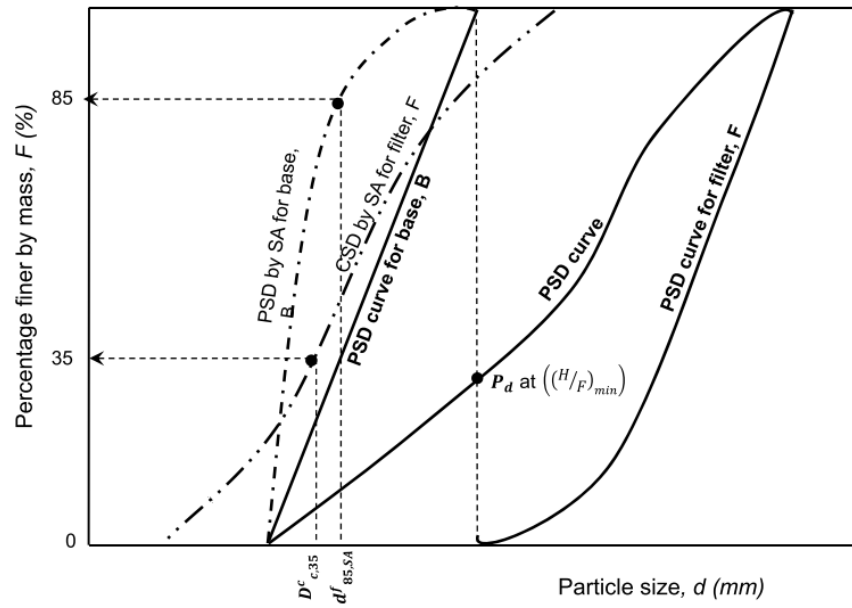


Figure 2.14: Assessment of internal instability by constriction size distribution, from Indraratna et al. (2015)

effort in calculating the CSD of even a granular matrix containing just spherical particles.

$$\begin{aligned}
 P_w < 20\% & \quad \text{soil is stable} \\
 20\% \leq P_w \leq 50\% & \quad \text{soil is in transitional zone} \\
 P_w > 50\% & \quad \text{soil is unstable}
 \end{aligned}
 \tag{2.13}$$

2.4.3 Kozeny-Carman permeability

Measuring permeability in field situations is often a complicated matter for soils where either the flow rate is too slow for a test to be practicable or disturbance to the soil structure should be limited. In this case, it would be beneficial to link a change in particle size distribution of a small sample to a change in permeability within the soil. This concept is explored in this study by comparing changes in permeability calculated from the post-test dissection of the specimen and observed permeability changes using the pore pressure data.

There are many different methods to estimate permeability using soil parameters, usually with combinations of particle size and shape, void ratio and grain size distribution. One of the simplest options is the Hazen method, which only uses the D_{10} grain size (Carrier, 2003). However, this is only applicable to uniform sands and is not suitable for tracking fines migration because the D_{10} value does not fully encompass the changing fines content, so a method based on the full particle size distribution must be used. Feng et al. (2019) found that when comparing several different permeability methods, both K-C and another PSD based approach called grading entropy had the highest correlation with experimental permeability, although the K-C method consistently underestimated the permeability. In contrast, Pap and Mahler (2019) found that the K-C approach overestimated permeability, suggesting that the shape factor used has a key impact on the accuracy of the results.

The shape factor accounts for the angularity of the grains when estimating the specific surface area of the soil (a parameter not commonly taken for soils) and is based on the engineer's judgement of the angularity of the grains on inspection. Liu and Jeng (2019) used numerical modelling to conclude that the basic K-C equation is good enough for 'not-too-rough' particles, like the sub-rounded particles used in this study, whilst more angular soils should use a formulation with more shape parameters. As the same soil is being used in each test, and a change in permeability rather than an absolute value is desired, the formulation of the K-C equation given by Carrier (2003) is implemented. The equation is as follows and is used to find the change in permeability of the dissected specimen quadrants based on their final and initial fines content:

$$k = 1.99 \times 10^4 \left(100\% / \left(\sum \frac{f_i}{D_{li}^{0.404} \times D_{si}^{0.595}} \right)^2 \left(\frac{1}{SF^2} \right) \left(\frac{e^3}{1+e} \right) \right) \quad (2.14)$$

where:

k = theoretical permeability (cm/s)

f_i = fraction of particles between two grain sizes (%)

$D_{li}^{0.404} \times D_{si}^{0.595}$ = average particle size between two grain sizes (cm)

SF = shape factor based on particle angularity, Carrier (2003) suggests 7.5 for a medium angularity grain

e = soil void ratio

2.5 ONSET OF SUFFUSION

In an experimental study exploring how applying long term hydraulic loading affects the onset and progression of suffusion, Luo et al. (2013) describes suffusion as complicated and iterative processes, starting with fine particle migration, followed by pores clogging, the pushing out of clogged pores, and leading to fine particle re-migration. A significant part of understanding the suffusion process is in understanding the factors that control the first stage, the initial instigation of fine particle movement. This section discusses the onset of suffusion and the models and frameworks that exist to quantify it, whilst Section 2.6 explores what influences the continued migration of the fine particles once they have been picked up by the seepage flow.

2.5.1 Critical hydraulic gradient and the α factor

For internally stable soils, Terzaghi (1939) expressed the a critical hydraulic gradient for heave under upwards flow. This is a function of the hydraulic pressure needed to overcome the self-weight of the soil and any overburden pressure acting on it. For a soil with no overburden, the critical hydraulic gradient for heave is expressed in Equation 2.15, and is approximately equal to 1. In Equation 2.15 γ , γ_w and γ' are the unit weight of the soil, water and buoyant unit weight respectively.

$$i_{cr(heave)} = \frac{\gamma - \gamma_w}{\gamma_w} = \frac{\gamma'}{\gamma_w} \quad (2.15)$$

In a soil susceptible to suffusion (under-filled, gap-graded - Section 2.4.1), the critical hydraulic gradient for the initiation of suffusion has been observed to be significantly lower than that for heave in stable soils. To reflect this, Skempton and Brogan (1994) introduced a stress reduction factor, α (Equation 2.16). This was based on a series of upwards flow tests undertaken on four different soil gradations in a rigid-walled permeamer. The study proposed that the finer fraction carry only a small proportion, α , of the effective stress imposed on the soil, and therefore can be migrated at a much lower hydraulic gradient. DEM simulations from Kawano et al. (2018), Shire et al. (2014) and Wautier (2018),

amongst others, corroborate this idea of relatively under-stressed 'free' fine particles, or 'rattlers', that are located within the pore network (Section 2.7.1).

$$i_{cr} = \alpha \frac{\gamma'}{\gamma_w} \quad (2.16)$$

In the next section, Section 2.5.2, the work of Li (2008) on hydromechanical envelopes to capture the onset of suffusion is discussed in detail, but that doctoral work also involved comparing results of 22 soil gradations tested in four different studies to assess different geometric instability criteria. The experimentally observed α factor in these tests was found to correlate well ($R^2 \approx 0.8$) with the simplified Kovacs (1981) criterion, d'_{85}/O_{50} to give the linear relationship in Equation 2.17, suggesting that α is an intrinsic soil property. The parameter O_{50} represents the effective diameter of the coarser fraction's pore constrictions, and is discussed in more depth in Section 7.1.3.

$$\alpha = 3.85 \left(\frac{d'_{85}}{O_{50}} \right) - 0.616 \quad (2.17)$$

Some studies take the approach of defining a critical hydraulic gradient for each stage of the erosion process. Liang et al. (2019) define a lower critical hydraulic gradient that is reached when the initiation of fines migration is observed and a higher one when global external suffusion occurs. The latter is experimentally easy to observe by monitoring the eroded fines in the effluent water, but the former is more difficult to identify because initiation is such a localised phenomenon. It may be hard to spot the initiation if it does not occur near one of the measurement points (Zhong et al., 2018). Chang and Zhang (2013a) also define suffusion by two hydraulic gradients: a 'skeleton deforming' value and a higher 'failure' value. Both of these studies were conducted in flexible-walled permeameters with over-filled soil gradations, allowing the rearrangement of force chains and therefore volume deformation of the specimen to occur. The results of these two studies in reference to effective stress are discussed in Section 2.5.3.

2.5.2 Hydromechanical envelopes

The concept of a hydromechanical envelope to define the onset of suffusion within a soil, based on the stress conditions and critical hydraulic gradient, has been developed over several years at the University of British Columbia (UBC). This interpretation approach started with the doctoral works of Moffat (2005) and Li (2008). The method has been modified and updated in a series of papers and technical notes in recent years, with the most recent publication being a technical note by Li and Fannin (2022). The experimental results predominantly originate from the theses of Moffat (2005) and Li (2008), and the hydromechanical envelopes from these studies are presented succinctly in Moffat and Fannin (2011) and Li and Fannin (2012) respectively.

The first of the studies by this group, the doctoral work of Moffat (2005), concerned a series of tests undertaken in a large, rigid-walled permeameter under both upwards and downwards flow. The permeameter had a diameter of 279 mm, and an average specimen length of 425 mm. Pore pressure measurement ports spaced along the sidewall of the permeameter (5 ports at 125 mm spacing) allowed the local hydraulic gradients in the specimen to be examined over the course of the tests. A selection of material gradations with between 5 and 30% fines content were tested at applied vertical stresses between 0 and 175 kPa to explore the influence of effective stress on suffusion and suffusion onset. The specimens were subjected to a multi-stage seepage flow regime. Each stage was maintained for approximately 90 minutes with the applied hydraulic gradient increasing in steps of $i=1$ from 0 to a maximum of 45. The tests were terminated at the onset of suffusion in one of the layers, characterised by a significant increase in flow rate through the sample.

The study observed that the onset of internal instability was triggered by either an increase in the hydraulic gradient, i , or by a decrease in the vertical effective stress, σ' . At the critical hydraulic gradient, there was a limited number of fines that could be eroded, and either i or σ' had to be changed to 'unlock' the next batch of fines. Figure 2.15 shows the hydromechanical boundaries for each of the soils tested, defined by the testing paths of between 2 and 5 tests at different confining stresses for each soil. The critical hydraulic gradient value was taken as the local value between two measurement ports, and onset was deemed to occur at a significant decrease in i over a relatively short period of time. The number suffix of each test, for example 5 for T-

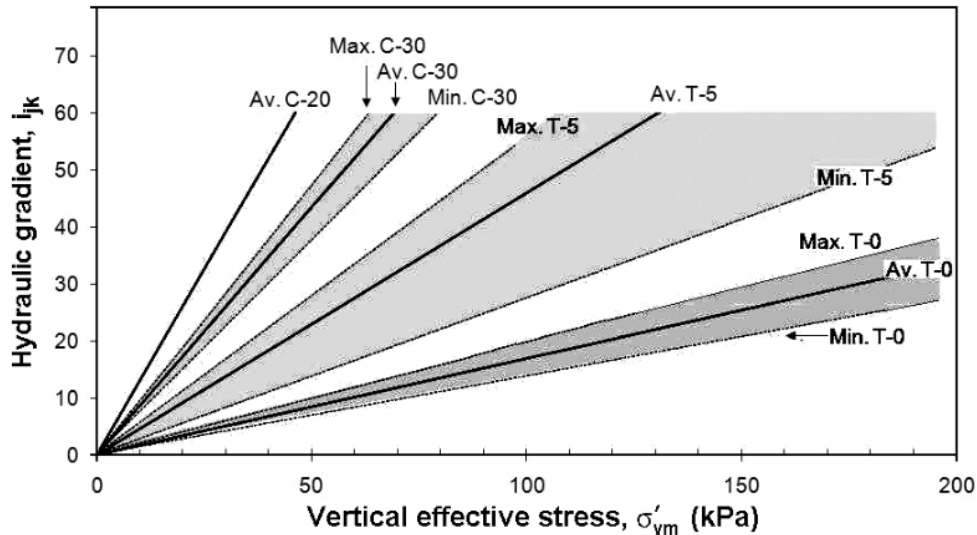


Figure 2.15: Hydromechanical boundaries calculated by Moffat (2005) for the four real soils tested in the large UBC permeameter, plotted in $\sigma' - i$ space

5, indicates the fines content of the material as defined in that study. The gradations of all of the soils tested in the studies undertaken at UBC discussed in this section are presented in Figure 2.16. In many cases these soils were designed to represent the in-situ material at the WAC Bennett dam in British Columbia.

The upper and lower bounds of the hydromechanical paths in Figure 2.15 show a much wider range in results for the under-filled materials, T-0 and T-5, whilst for the transitional materials C-20 and C-30, where the fine particles are assumed to take a more active part in the stress transfer matrix, there seems to be a much stronger relationship between effective stress and hydraulic gradient at onset. A repeat test conducted on soil T-5 with 50 kPa mean confining stress showed very different critical local hydraulic gradients of 18.2 and 57, these also occurred in different zones, although towards the base of the sample. Two specimens with the same flow direction and material yielded different hydromechanical boundaries, a difference that Moffat (2005) noted could not be explained by the geometric properties of the soil. However, from a more general observation of all the soils tested, the author concluded that the slope of the hydromechanical boundary depends partly on the shape of the soil's particle size distribution. Although Moffat (2005) classified T-5 as having a fines content of 5%, this was based on the traditional definition of fines <63 microns, and the soil in fact had a clear gap at a fine particle content of 40% (Figure 2.16).

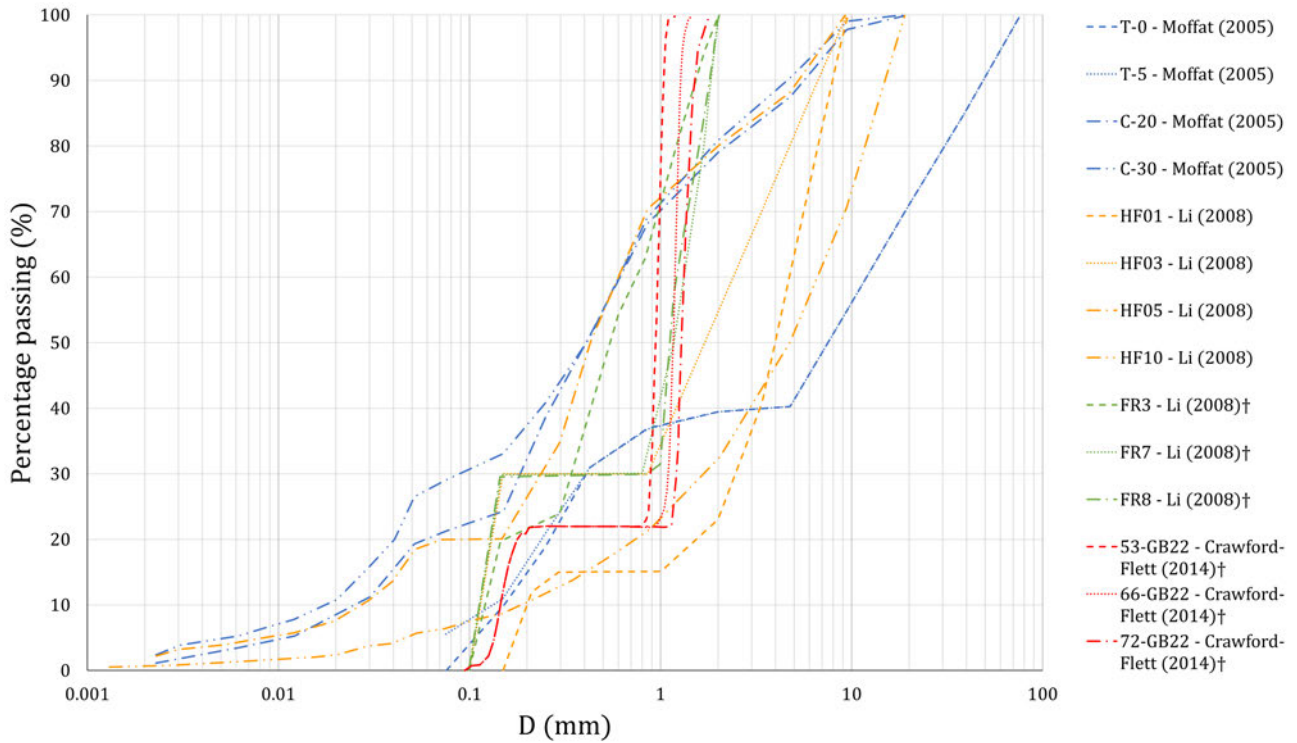


Figure 2.16: Particle size distributions of the soil gradations tested in the small and large permeameters at UBC, † indicates a gradation that comprised of spherical glass beads (Crawford-Flett, 2014; Li, 2008; Moffat, 2005)

Li (2008) expanded on this work by testing both reconstituted real soils from the WAC Bennett Dam and glass bead gradations under upwards and downwards seepage flow. The study used both the large permeameter of Moffat (2005), and a smaller permeameter, allowing the influence of the length scale to be explored, although only the FR7 glass bead gradation under downward flow was tested in both apparatuses. The materials tested are presented in Figure 2.16. This smaller permeameter had a diameter of 102 mm and an average specimen length of 100 mm. As with the larger device, there were interstitial pore pressure measurement ports along the sidewall, a total of 4 within the specimen at 25.4 mm centres. Mean vertical effective stresses of up to 150 kPa were applied to the samples and a similar multi-stage seepage flow approach was taken. The average applied hydraulic gradient was increased in steps of $i \approx 0.5$ for the small permeameter and $i \approx 1 - 2$ for the large permeameter until the onset of suffusion in one of the layers. The smaller permeameter was limited by a maximum applied hydraulic gradient of 15, whilst the larger permeameter could accommodate average gradients up to 65.

For the present study, the most relevant results from Li (2008) concern the glass bead gradation FR7, which was tested under downwards flow in both permeameters. This gradation had a fine particle content of 30% and a gap ratio of 7.1. Table 2.2, adapted from Li (2008), gives the critical hydraulic gradients and associated parameters for each of the tests on this gradation. The critical hydraulic gradients for the tests in the larger permeameter are significantly lower than those for the smaller device, suggesting that an increased seepage path length makes a soil more susceptible to internal instability, a finding that could cause serious concern in industry, as seepage paths in structures are orders of magnitude larger than those that can be tested in the laboratory. It is also interesting to note that the local hydraulic gradient in the layer that suffusion occurred was always higher than the average value applied to the specimen. Invariably under downwards flow, when a large reduction in hydraulic gradient signifying the onset of erosion was observed, the hydraulic gradient in the lower layers increased, sometimes to a value higher than the critical value, but suffusion did not occur. The effective stress was higher in these lower layers.

Table 2.2: Local (i_{cr}) and average (i_{av}) hydraulic gradients reported by Li (2008) at the onset of suffusion for all tests conducted on the FR7 glass bead gradation

Test	Device	σ'_{vm} (kPa)	Flow	i_{av}	i_{cr}
FR7-25-D	Small	25	↓	7.3	8.7
FR7-50-D	Small	50	↓	9.5	16.5
FR7-100-D	Small	100	↓	15.5	27.1
FR7-150-D	Large	150	↓	4.0	5.0
FR7-150-U	Large	150	↑	2.5	3.0

To account for this scale effect, Li (2008) proposed a hydromechanical envelope in $\bar{\sigma}'_{vm} - i$ space, where $\bar{\sigma}'_{vm}$ is the mean effective stress normalised by the seepage path length, Δz , shown in Equation 2.18. Clearly there was a different suffusion response between the two devices, but it is unclear whether this was due to a difference in boundary conditions rather than an intrinsically the seepage path length. The seepage path length referred to in Equation 2.18 is the length of the local failure zone i.e., the distance between the two measuring points. From a soil mechanics perspective, the points of observation should not influence the soil behaviour. Using this approach suggests that, if only

every other PPT were in use, the observed critical hydraulic gradient would be reduced. Although this does not seem to make physical sense, it is actually capturing the fact that the onset of suffusion is a very local phenomenon (Section 2.7.3), and although the local change in hydraulic gradient in the immediate vicinity of the initiation may be massive, the coarseness of the measurement points attenuates this peak value, making the critical value appear much lower.

$$\bar{\sigma}'_{vm} = \frac{\sigma'_{vm}}{\gamma_w \Delta Z} \quad (2.18)$$

Li and Fannin (2012) initially proposed a critical hydraulic gradient for upwards seepage flow, $i_{cr,u}$, shown in Equation 2.19 based on the proportion of effective stress transmitted by the finer fraction of the soil, represented by the α factor (Section 2.5.1). This was later updated in Li and Fannin (2022) to include the hydromechanical path for downwards flow and corresponding critical hydraulic gradient, $i_{cr,d}$ (Equation 2.20), and the hydromechanical envelope is shown in Figure 2.17. In the downwards flow case according to this model, the seepage flow has a stabilising effect by increasing the effective stress on the fine particles. According to this theoretical hydromechanical path, a marginally unstable soil with an alpha just below one, would have a critical hydraulic gradient of 10 if there was no external loading of the sample, which the author used to justify the magnitude of hydraulic gradients used in the UBC studies.

$$i_{cr,u} = \alpha \left(\bar{\sigma}'_{vm0} + 0.5 \frac{\gamma'}{\gamma_w} \right) \quad (2.19)$$

$$i_{cr,d} = \frac{\alpha}{1 - \alpha} \left(\bar{\sigma}'_{vm0} + 0.5 \frac{\gamma'}{\gamma_w} \right) \quad (2.20)$$

where:

α = stress reduction factor from Skempton and Brogan (1994),

$\bar{\sigma}'_{vm0}$ = normalised mean vertical effective stress for the soil element under hydrostatic conditions (Equation 2.18),

γ', γ_w = submerged unit weight of soil and unit weight of water.

Hydromechanical boundary for suffusion onset and hydromechanical paths for different flow directions, modified from Li and Fannin (2022). Case A

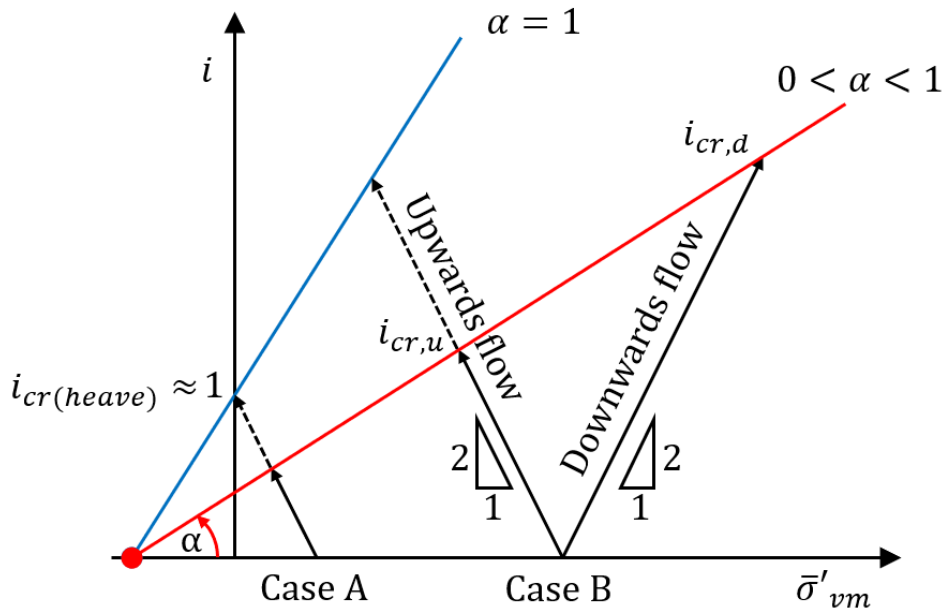


Figure 2.17: Hydromechanical boundary for suffusion onset and hydromechanical paths for different flow directions, modified from Li and Fannin (2022). Case A indicates a soil under its own self-weight, whilst Case B has some additional applied vertical stress.

indicates a soil under its own self-weight, whilst Case B has some additional applied vertical stress.

In contrast to the findings of Moffat (2005) and Li (2008), Crawford-Flett (2014) argues that basing the hydromechanical boundary purely on the effective stress transfer in the finer particles (quantified by the α factor) does not represent the true suffusion behaviour of under-filled soils. This conclusion was made from a series of upwards flow tests conducted on gap-graded glass bead gradations 66GB22 and 72GB22 (Figure 2.16) in the same large permeameter as the previous studies. These two soils had very large gap-ratios of 6.6 and 7.2 respectively, and consequently were deemed to be very internally unstable with $\alpha \approx 0$, at the hydromechanical lower bound, as it was termed in this study. These gradations had a fines content of 22%, in contrast to the 40% and 30% of T-5 and FR7 respectively (when the finer fraction is defined at the step in the gradation). As with the other studies, the specimens were subject to vertical effective stresses between 0 and 150 kPa, but in this case the hydraulic gradient applied to the specimen was increased in increments of $i = 0.05$.

In both soils, suffusion onset occurred at critical hydraulic gradients between 0.13 and 0.20, when both the local and global hydraulic conductivity was

observed to increase. Internal migration of fine particles was also observed in this study, shown by local fluctuations in hydraulic conductivity. The study concluded that in these under-filled, dense gradations, the occurrence of suffusion is based on three conditions. These are the availability of unstressed fine particles located in the voids; a critical hydraulic condition; and the transportation potential of a fine particle through the pore constrictions of the soil. In the upwards flow case, the critical hydraulic condition was found to be a seepage velocity greater than the sinking velocity of the fine particle.

2.5.3 *The influence of effective stress*

From the experimental results of Moffat (2005) and Li (2008), fully explored in Section 2.5.2, it was found that increasing the effective stress increased the hydraulic gradient needed to initiate suffusion, and resulted in a modified Equation 2.16 to include a vertical effective stress term. Later works in the same permeameter contradict these findings somewhat. Both Crawford-Flett (2014) and Slangen (2015) found that for an under-filled material - Moffat and Li were using some transitional soils - suffusion onset is completely independent of effective stress. They argue that in these gap-graded soils, the fine particles are located loose within the voids and take almost no part in the stress-transfer network.

Ke and Takahashi (2014a) undertook downwards-flow permeameter tests on a series of gap-graded soils (15%, 25% and 35% fines) isotropically confined at effective stresses between 50 and 200 kPa. They found that, not only did increasing effective stress increase the critical hydraulic gradient, it also decreased the mass of fine particles lost from 25% to 17% of the original value. They hypothesised that this was due to the relative density, which was very loose, at 30% for the tests and that the higher effective stress caused compression, resulting in smaller pores. They considered that the volume change observed may be due to initial densification on the application of seepage flow and effective stress, rather than fines migration-based volume change. It is likely that fines migrating through the soil were less able to move through the pore network unimpeded, and so clogging was more likely than external suffusion.

In a parametric study evaluating the influence of fines content, hydraulic gradient and confining pressure on internal erosion, Bendahmane et al. (2008) observed that the erosion rate increased with a decrease in effective stress. The tests were conducted in a flexible-walled permeameter on a mixture of sand and kaolinite (5-30%) at confining stresses between 100 and 250 kPa. Although the fines used were cohesive, the erosion mechanism in the lower fines content mixtures was deemed suffusion, as there was no change in sample volume, and none of the coarse particles were eroded. Reducing the confining pressure by a third doubled the rate of fines lost from the sample, suggesting effective stress influences not only the onset, but also progression of this mechanism.

Other experimental studies have explored the influence of more complex stress states on suffusion erosion. In a series of flexible-walled permeameter tests under isotropic, triaxial compression, and triaxial extension stress conditions, Chang and Zhang (2013a) explored the behaviour of a soil with 35% fines content as the specimen was subjected to an increasing hydraulic gradient up to $i = 9$. Once fine particles were observed to externally erode, the hydraulic gradient was kept constant at this critical value.

The triaxial compression tests, where the major principle stress is in the vertical direction, had much lower initiation hydraulic gradients than the extension tests, where the major principle stress is horizontal. This led to the conclusion that seepage flow in the direction of the major principle stress is more destabilising than flow perpendicular to it. A conceptual model was proposed where the pores are elongated in the direction of the major principle stress (Figure 2.18). This allows a less tortuous path for the seepage flow in the vertical flow conditions, and lowered the observed critical hydraulic gradient.

Liang et al. (2019) conducted a series of downward flow experiments under isotropic and anisotropic stress conditions in a flexible-walled permeameter. The results showed a linear increase in critical hydraulic gradient with increasing isotropic stress in an under-filled gap-graded soil. Under anisotropic stress states, the critical hydraulic gradient for the onset of fine particle migration was observed to increase with deviatoric stress, until $q = 20$ kPa, where the critical hydraulic gradient started to decrease. As mentioned in Section 2.5.1, Liang et al. (2019) proposed an alternative approach to i_{cr} from Li (2008), defining an empirical relationship for a lower critical value for the onset of fines migration (LCHG) and a higher skeleton deformation value (HCHG),

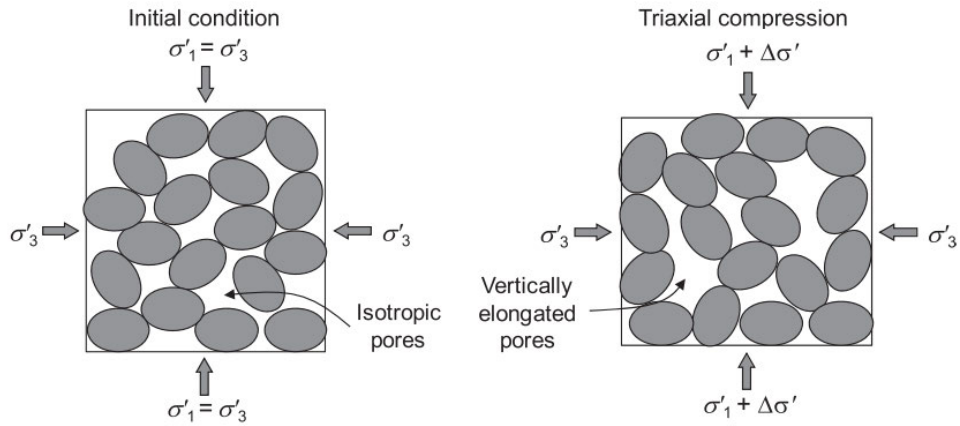


Figure 2.18: Conceptual model of the development of elongated pores under triaxial loading, from Chang and Zhang (2013a)

shown in Figure 2.19, based on their experimental results. They argue that Li's formulation does not differentiate between iso- and anisotropic stress states.

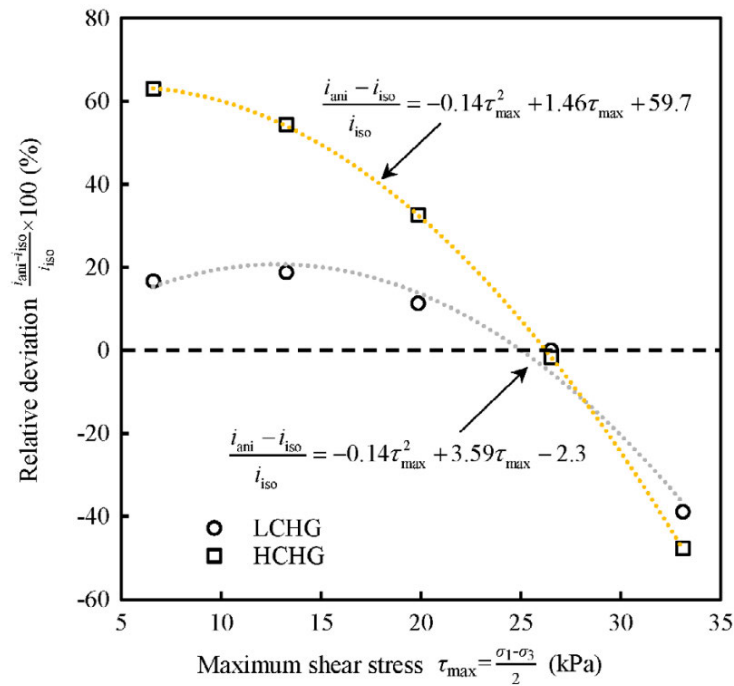


Figure 2.19: Interpreting critical hydraulic gradients from a series of triaxial suffusion tests, from Liang et al. (2019)

Tomlinson and Vaid (2000) is often referenced by stress-related suffusion papers as finding that increasing the confining pressure triggers erosion at a lower hydraulic gradient because the soil arching breaks down. However, this paper focusses on piping erosion in two distinct layers of different sized

glass beads (a ‘base’ and a ‘filter’ soil). Piping was defined in the study as “the free movement of soil particles through the movement of soil base particles through a granular filter, culminating in the formation of an open channel in the soil”. The first half of this definition shares some of similarities with the description of suffusion used in this report, but the initial configuration differs as the layer of erodible fines is located directly over the stable filter layer. Suffusion, as defined in Section 2.2.9, does not lead to the formation of open pipe structures.

2.5.4 Critical seepage velocity and hydraulic stress

An alternative way to quantify the initiation of particle migration is to consider the critical hydraulic shear stress or seepage velocity needed to move a fine particle by considering force equilibrium on that grain. Reddi et al. (2000) formulated the hydraulic shear stress within a soil body by conceptualising the pore voids as bundles of capillary tubes with a certain length and radius. The critical hydraulic shear stress, τ , to initiate erosion was found by noting the pressure gradient applied to the soil at the point of erosion onset, and using Equation 2.21 to calculate the hydraulic shear stress within the pores. Tian et al. (2020) investigated the variation of this critical seepage velocity with fines content with a series of experiments in a rigid-walled permeameter. For under-filled materials, the critical seepage velocity increased slightly with fines content. This method explicitly accounts for the porosity of the soil in its formulation, whilst formulations for hydraulic gradient do not take into account the constriction network and soil density, encompassing all the aspects of the soil structure in the α factor, which is often presumed constant for a soil gradation (Section 2.5.1).

$$\tau = 1.414 \left(\frac{\Delta p}{\Delta z} \right) \sqrt{\frac{K}{n}} \quad (2.21)$$

where:

$\frac{\Delta p}{\Delta z}$ = pressure gradient over the soil sample

K = intrinsic permeability

n = porosity of the sample

In Sato and Kuwano (2015), the critical seepage velocity and critical hydraulic gradient are used somewhat interchangeably, with the former being calculated from the latter using the soil porosity and flow rate. This critical velocity used in their framework does not consider the individual migration of the particle, rather that which allows for the “transportation of the maximum number of loose particles”. This acknowledges that at lower seepage flows, although a particle can be picked up by the flow, it is likely to be redeposited in a constriction close to its initial location and there will be no discernable suffusion across the sample.

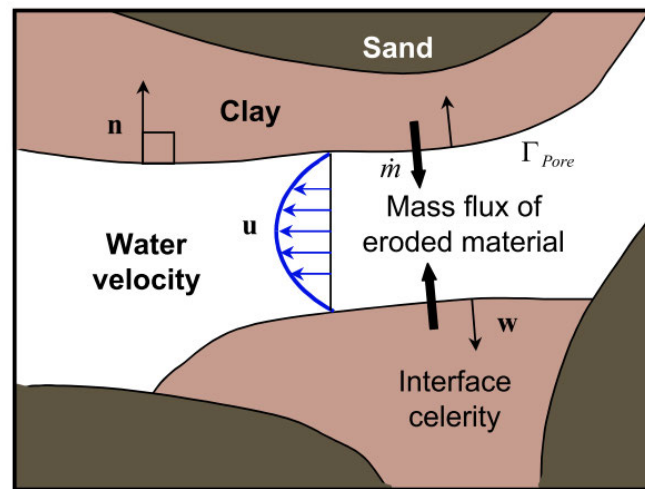


Figure 2.20: Critical hydraulic shear stress in the pore network of a suffusive soil, from Bonelli and Marot (2011)

Using critical seepage velocity, or the associated hydraulic shear stress in the pores is commonly used in continuum numerical modelling of suffusion as an erosion criteria for the phase exchange between from solid to fluidised particles. Bonelli and Marot (2011) uses the critical hydraulic shear from surficial erosion work to connect the micro-scale removal of fine particles with a bulk erosion property measured at the macro-scale. By considering a representative elementary volume (REV), individual pore channels can be considered as piping erosion problems, with a stable coarse sand matrix and erodible clay fines (Figure 2.20). Similarly Bi et al. (2021) also uses the REV concept and finds a critical seepage velocity at which the minimum particle diameter can be eroded in their continuum model taking into account soil gradation.

2.6 PROGRESSION OF SUFFUSION

Whilst it is important to understand the mechanisms controlling the onset of suffusion, it is perhaps more of a concern for dam and levee operators to understand how the process is likely to progress under the applied hydromechanical conditions. From a practical perspective, a small amount of fine particles being transported on the order of a few centimetres is not a pressing concern, but if that erosion progresses to the point of significantly modifying the hydraulic regime within a structure, then that is a cause for alarm. By understanding the factors controlling the transportation and potential deposition of fine particles, informed decisions can be made on whether potentially costly remediation measures need to be taken. These concerns at the structural scale cannot be understood without evaluating the influence of identified parameters within the controlled laboratory environment.

2.6.1 *Hydraulic loading regime*

There are essentially three ways that an experimental suffusion tests can be conducted. The first is by holding a specimen at a constant applied hydraulic condition. This can either be achieved through controlling the head difference applied across the specimen (such as Bendahmane et al., 2008; Moffat et al., 2011; Rochim et al., 2017), or by the less common method of controlling the flow velocity through the specimen (Ke and Takahashi, 2014b). Typically these tests are undertaken to investigate the progression or mechanical consequences of suffusion and apply a relatively high hydraulic loading to ensure the occurrence of suffusion, although in the studies of Luo et al. (2013) and Lee et al. (2021) the samples were held at hydraulic conditions below the critical values for suffusion that the authors had observed for those soils.

The second approach to testing is to steadily increase the applied hydraulic loading, holding each interval for a certain period of time, known as multi-stage seepage flow (e.g. Li, 2008; Moffat, 2005; Zhong et al., 2018). This process can be used to identify the onset of erosion and define the critical hydraulic gradient or seepage velocity. The progress of suffusion from this point onwards can also be examined. Both the rate of increase and the length of each

seepage interval have been found to influence the fines migration process (Annapareddy et al., 2023; Rochim et al., 2017).

The third and final approach is not explored in this thesis as it is used to define suffusion in specific loading scenarios such as in railway ballast and structures with fluctuating water levels. This involves the cyclical application of seepage flow through a specimen at a frequency in line with the specific problem being modelled. The following paragraphs explore how the choice of either multi-stage or constant seepage flow tests influences the suffusion response of the soil and how they provide insight into the controlling parameters for the fine particle migration process.

One of the first suffusion studies to explicitly state that the hydromechanical loading conditions influences the onset of suffusion was the work by Moffat and Fannin (2011), which discussed the concept of fines available to be eroded at a given hydromechanical conditions. To 'unlock' the next batch of erodible particles, either the hydraulic gradient must increase, or the effective stress decrease within the soil. They state that the combination of high applied hydraulic gradients (up to $i = 45$) and loose initial packing could be causing local rearrangement of force chains and pore void spaces upon the increase in hydraulic loading.

In order to study the effect of hydraulic loading history on suffusion susceptibility, Rochim et al. (2017) conducted a series of downwards flow tests on four cohesionless, gap-graded materials with fines contents between 20 and 30% in a rigid-walled permeameter. The specimens were subjected to two multi-stage (MS) and two constant head (CH) hydraulic loading regimes. Of the MS tests, testing regime *a* consisted of steadily increasing steps of i , initially increasing by 0.1 to $i = 2$, 0.5 when $2 < i < 4$, and steps of 1 until $i = 10$. Testing regime *b*, in contrast, had constant incremental increases of 1, to a maximum of $i = 13$. For both MS regimes, each interval lasted 10 minutes. Test *c* maintained an applied hydraulic gradient, i_{app} equal to 4 for 5.5 hours, which was assumed to be above the critical gradient predicted from Li and Fannin (2012), whilst test *k* was subject to a constant $i = 0.5$ for a total of 12 hours.

When comparing the two multi-stage regimes (*a* and *b*) the specimens were observed to decrease significantly in hydraulic conductivity before starting to erode, suggesting significant internal fines migration before any external suffusion was observed (Figure 2.21). Specimens loaded more rapidly with loading regime *b*, showed a much more rapid response, whilst loading regime

a exhibited a much longer and more pronounced stage of clogging before reaching almost a plateau in hydraulic conductivity. The initiation of global suffusion is then shown by the rapid increase in hydraulic conductivity. The erosion rate, calculated from the mass of fine particles eroded from the sample with time, was systematically higher for the soils tested under MS routine *b* compared to *a*.

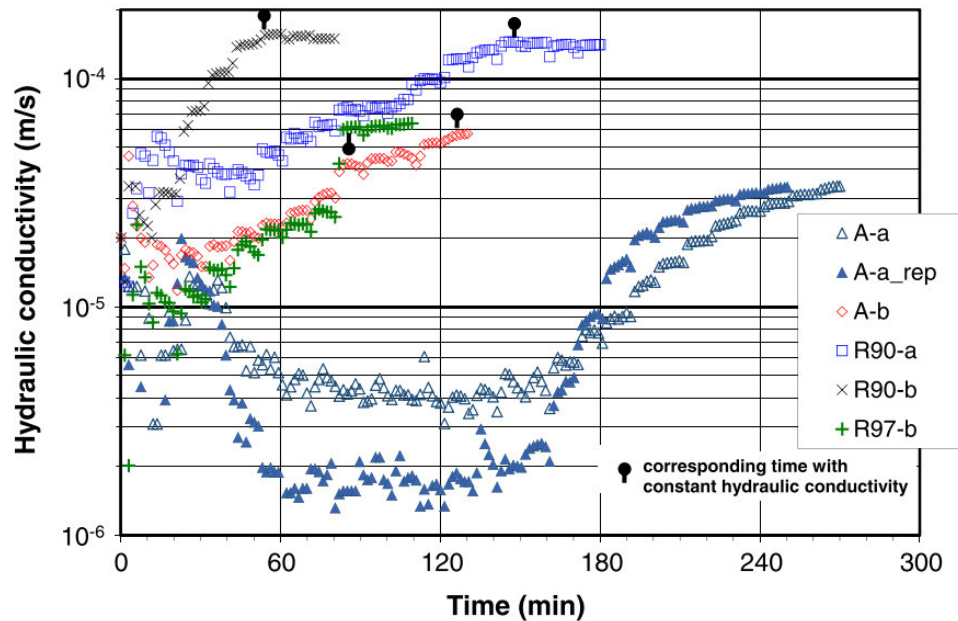


Figure 2.21: Hydraulic conductivity of specimens comprising of two soil mixes (A and R) under two multi-stage seepage flow regimes (a and b), from Rochim et al. (2017)

The study also observed a difference in the cumulative loss of fine particles over the course of the test for the different loading regimes. The multi-stage regime *a* experienced almost 10 times more mass lost than regime *c* with a constant $i = 4$ for the same soil prepared in the same way, despite having similar cumulative expended energies (Section 2.6.4). Interestingly, when the long-term low hydraulic regime *k* was applied to the same soil, the specimen experienced a similar loss of fines as the multi-stage regime *a*, representing approximately 9% of the total initial mass of fine particles.

Annapareddy et al. (2023) undertook a series of upwards flow seepage experiments on gap-graded mixtures of glass beads with fine particle contents between 15 and 25%. Two different hydraulic loading regimes were tested, one where the applied hydraulic gradient was initially taken to $i = 5$, then $i = 10$, and from there was increased by 1 in 5 minutes intervals to a maximum

$i_{app} = 30$ (LH2), and the other where the hydraulic gradients was increased in increments of 1 to a maximum of $i_{app} = 60$ (LH1). Each interval was maintained for a longer duration of 10 minutes. For the under-filled materials (15 and 20% fine particle content) the critical hydraulic gradient for the onset of suffusion was higher for the first, more rapidly loaded scenario, LH2. For the 25% fine particle content specimens, the hydraulic gradient at the onset of suffusion was similar for both loading regimes (Figure 2.22). The study attributes this variation to the cumulative energy applied to the sample by the time of erosion initiation.

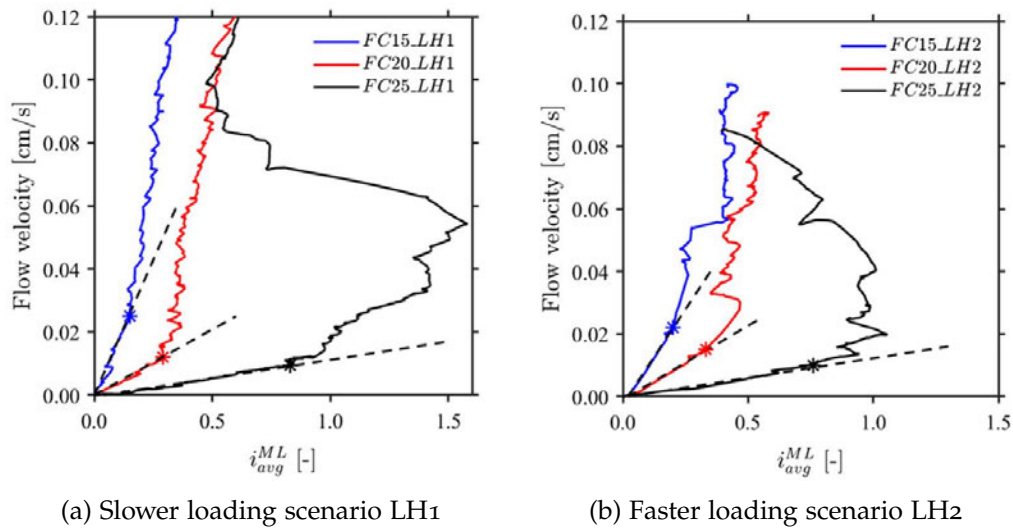


Figure 2.22: Onset of suffusion is characterised by the increase in rate of change of flow velocity with hydraulic gradient across the specimen, from Annapareddy et al. (2023)

Luo et al. (2013) conducted a series of downwards seepage flow tests in flexible-walled permeameter to explore the response of soils subjected to long term hydraulic gradients. To identify the critical hydraulic gradient for the gap-graded soil (fines content $\approx 20\%$), an initial multi-stage seepage regime was conducted at confining pressures of 0.2 and 0.4 MPa, to a maximum hydraulic gradient of ≈ 5 . Having identified critical hydraulic gradients for onset of suffusion of 0.35 and 0.435 for the confining pressures respectively, long-term constant head tests at $i_{app} = 0.5, 1.0$ and 2.0 were conducted lasting up to 8 days.

The specimens subjected to the long-term head 'failed' (defined by the study as a rapid decrease in hydraulic gradient and increase in mass eroded) at a lower hydraulic gradient than those loaded using the short-term MS regime.

The authors attributed this to the long-term flow through the soil allowing for the build up of regions of clogged particles, significantly altering the flow regime. They suggest that this would then create areas of locally high hydraulic gradients, not captured in the specimen-scale observations.

The specimens subjected to 0.4 MPa confining pressure and hydraulic gradients of 0.5 and 1.0 were deemed by the study not to have failed, and the tests were terminated after 33.1 and 14.4 hours respectively, as there had been no observed mass lost in the previous hours. They did, however, initially lose 0.4% and 0.8% of their initial fines content. This initial migration of fines is consistent with the short-term tests, where mass loss was observed at the very early stages, at hydraulic gradients less than 1.

Lee et al. (2021) also conducted a series of experimental tests to investigate the impact of long-term seepage flow on suffusion. Although focussing mostly on widely-graded materials in these downwards flow permeameter tests, a gap-graded material (fines content = 15%) was also tested under a short-term MS regime (maximum $i_{app} = 12$, duration of 11 hours) and a long-term constant head test ($i_{app} = 5$, duration of 11 days). The critical hydraulic gradient for the MS regime was taken as 10, which is when a significant increase in permeability of the specimen occurred. The long-term applied i was deliberately chosen to be half of this supposed critical value.

A significantly larger amount of soil was eroded out of the sample in the long-term test compared to the short term test, 12.4% of the initial fine particle mass compared to 4.1%. The study suggests that the incremental increase of applied downwards seepage flow has a stabilizing effect on the soil structure. Again, even at the very early stages of testing, when the hydraulic gradient was below the gradient needed for significant changes in permeability, fine particles were observed to be eroding from the specimen.

2.6.2 *Spatial development of internal fines migration*

In recent years there have been many studies that examine the spatial and temporal development of the fines migration within the soil structure. This variation occurs both parallel to the seepage flow and in the transverse direction, with boundary conditions significantly affecting suffusion evolution. These studies use developing experimental techniques such as X-ray/neutron

tomography (Bianchi et al., 2018; Nguyen et al., 2019) or spatial time-domain reflectometry (Annapareddy et al., 2023) to examine the local migration of particles during testing, rather than through macroscale observations (e.g. by inferring particle migration from permeability change).

Coupled CFD-DEM studies (Hu et al., 2019; Liu et al., 2023; Zou et al., 2020) have also explored the local variability in particle migration, although high computing costs limit the flow time that can be simulated (Section 2.7.3). Post-test dissection and particle size analysis of samples also provides valuable information on the ultimate distribution of migrated particles within a soil, although the temporal development of the process cannot be examined (Horikoshi and Takahashi, 2015; Ke and Takahashi, 2014b). The work by Yang et al. (2019) introduces spatial variability in porosity and fine particle content to the finite element macroscale approach of modelling suffusion in order to capture the migration and clogging process, trying to bridge the gap between the microscale observations and macroscale behaviour of the soil.

Experimental observations of suffusion tests show that the process does not develop evenly over the cross section of the soil, instead forming areas of preferential erosion - i. e. fine particle loss and increase in porosity. In rigid-walled permeameter tests, fines loss has been observed to occur preferentially at the permeameter walls (Israr et al., 2016; Luo et al., 2013; Nguyen et al., 2019; Sail et al., 2011). This is typically where pore pressure readings are taken in experimental suffusion tests.

Figure 2.23 shows the distribution of fine particles within a specimen initially and after three stages of increasingly strong seepage flow. The distribution was obtained from X-ray CT scans of a real gap-graded soil and shows clear erosion channels along the wall of the cell (Nguyen et al., 2019). The initial soil had a fines content 25%, but even after the second stage of applied flow there are areas with less than 10% fines content, and these develop significantly over the final stage.

Luo et al. (2013) also observed concentrated erosion channels in experiments on gap-graded soils subjected to long-term hydraulic head. These channels formed preferential flow paths from the inlet to the outlet, but this was not a direct line, with the cross sectional-distribution captured at different points along the seepage path. This tortuous development highlights that heterogeneities in the initial packing will influence the initiation and progression of suffusion erosion.

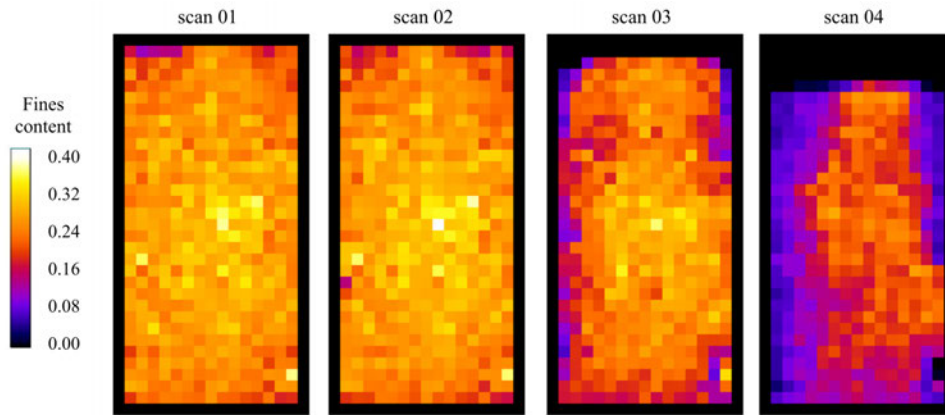


Figure 2.23: Fines content during suffusion from X-ray CT scans, from Nguyen et al. (2019)

An observation consistent across most experimental tests is that the fine particle content in the section at the start of the seepage path decreases more significantly than the other layers. Zhong et al. (2018) reported the spatial variation in particle size distribution across a sample tested under multi-stage downwards seepage flow in a rigid-walled permeaeter. In both a sample with an initial fines content of 16% (specimen 4-O) and one with 23% (1-O), the top layers exhibited the largest reduction in fine particles, as shown by the post test dissection in Figure 2.24. In specimen 1-O the bottom layer increased in fines content, meaning particles eroded from the overlying layers were redeposited, rather than being fully removed from the sample.

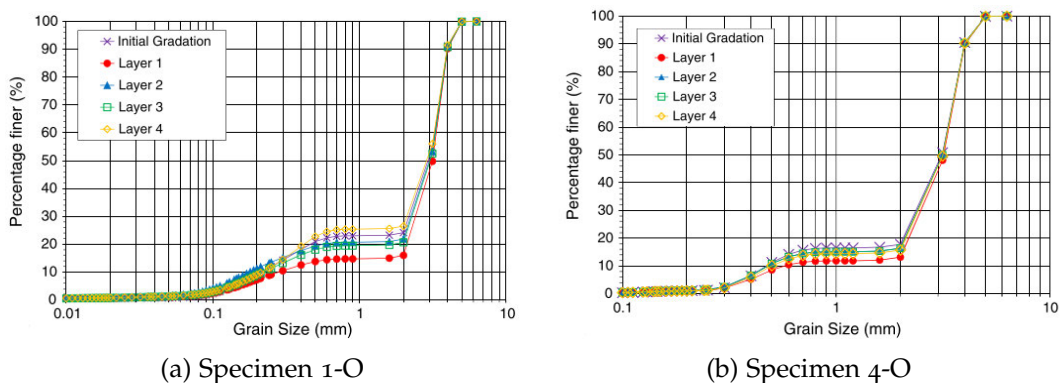


Figure 2.24: Pre- and post-test particle size distributions for specimens subjected to downwards seepage flow (Layer 1 = top), from Zhong et al. (2018)

This highlights the complexity of suffusion, as for specimen 1-O more particles were eroded overall, which perhaps suggests why more were deposited. When there is a smaller supply of fine particles from the layer above, the

influx may be smaller than the outflux from that layer. Just because a layer is clogging, does not mean that the particles originally in that layer were not transported from that layer by the seepage flow and then replaced by particles from further upstream.

Studies focussing on the post-suffusion mechanical behaviour of soils are also concerned with the spatial variation in fines content caused by erosion, but in this case for the opposite reason. There is a desire to end up with as homogeneous as possible sample after erosion for consistency in triaxial testing. Experimental observations in triaxial cells, usually by post-suffusion particle size distribution analysis also show this trend of higher erosion at the top of the sample compared to lower levels (Chang and Zhang, 2011; Chitravel et al., 2022; Ke and Takahashi, 2014b; Mehdizadeh et al., 2021). Both Chitravel et al. (2022) and Mehdizadeh et al. (2021) found that increasing the specimen height increased the possibility of clogging within the sample, towards the end of the seepage path.

This clear trend of decreasing erosion along the seepage path that is observed in flexible walled cells was not identified in the rigid walled cell of Nguyen et al. (2019). As Figure 2.23 shows, there was fairly homogeneous development of suffusion along the seepage path throughout the test, with only a thin layer of higher fines loss at the inlet and to a lesser degree at the outlet boundary. In this situation the transverse heterogeneity was much more pronounced than any variation longitudinally.

Post-test dissection of samples by Chang and Zhang (2013a), Ke and Takahashi (2014b) and Liang et al. (2019) also showed that more fines are lost at the top of the flow path, even when the hydraulic gradient is above the value theoretically needed to cause global migration (external suffusion) according to existing proposed hydromechanical envelopes (Section 2.5.2). Bianchi et al. (2018) used x-ray tomography to look at how the particles move through a column of soil. The study found that clogging could happen locally and tended to start in the bulk of the sample and move towards the upstream face with time, with a downstream region of erosion occurring in the previously clogged zone. This rearrangement of particles reorganised the flow path through the material.

The hydraulic conductivity of three specimens through time in the centrifuge permeameter study of Marot et al. (2012) are shown in Figure 2.25. The permeability, termed hydraulic conductivity in that study, decreased signi-

ificantly over the course of the test in all three cases, suggesting significant clogging within the specimen. This is despite the fact the tests were observed to experience external suffusion, with 0.12, 0.19 and 0.69 g of fine particles collected in the outflow containers for tests 14, 15 and 16 respectively. For all three tests, the maximum rate of erosion occurred within the first 400 seconds corresponding to a decrease, rather than the expected increase, in hydraulic conductivity. This centrifuge study is explored in more depth in Section 2.6.3.

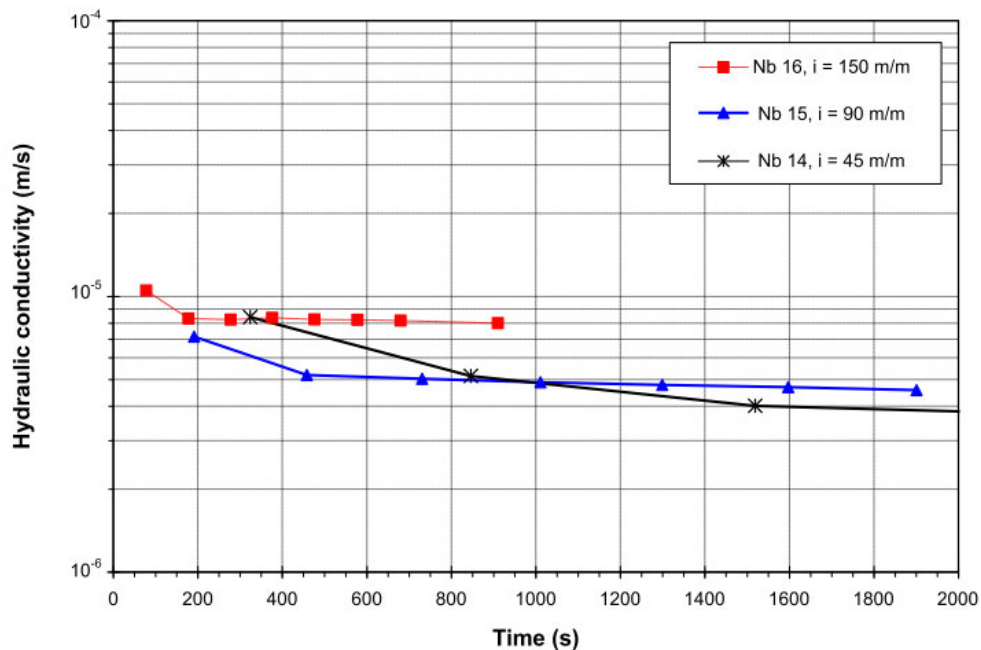


Figure 2.25: Development of hydraulic conductivity for three centrifuge permeameter tests, from Marot et al. (2012)

2.6.3 Influence of seepage path length

For piping erosion as defined by Tomlinson and Vaid (2000), Sellmeijer (1988) found that the critical hydraulic gradient is inversely proportional to the length of the seepage path. This could mean that the critical hydraulic gradient for a soil specimen in the laboratory may be many times larger than in the field case. Li (2008) found that, for the same effective stress, the critical hydraulic gradient was seven times higher in the small (102 mm diameter) permeameter compared to the large (279 mm). Both permeameters are rigid-walled and allow for specimen lengths of approximately 100 and 300 mm respectively. To account for the influence of seepage path length on the critical hydraulic

gradient, the specimen length term Δz was included in the denominator of Equation 2.18, as discussed in Section 2.5.2.

More recently, Zhong et al. (2018) also found that the critical hydraulic gradient decreased with seepage path length using two different sized permeameters, with the critical hydraulic gradient for a variety of specimens shown in Figure 2.26. The larger apparatus (suffix -O) used is a rigid walled permeameter which can accommodate 285 mm diameter specimens up to 600 mm long, whilst the smaller is a flexible walled triaxial device (suffix -T) for 50 mm diameter, 100 mm long specimens. It is important to note that the different boundary conditions between the two devices could also have influenced the observed variation in i_{cr} . The reduction in i_{cr} with seepage path length was more pronounced in Soil 4 (tests 4-O and 4-T for the rigid-walled and triaxial walled test respectively), which had a higher H/F_{min} value of 0.600 to 0.161 compared to soil 1 (tests 1-O and 1-T), as well as a smaller gap ratio (2.29 to 3.33).

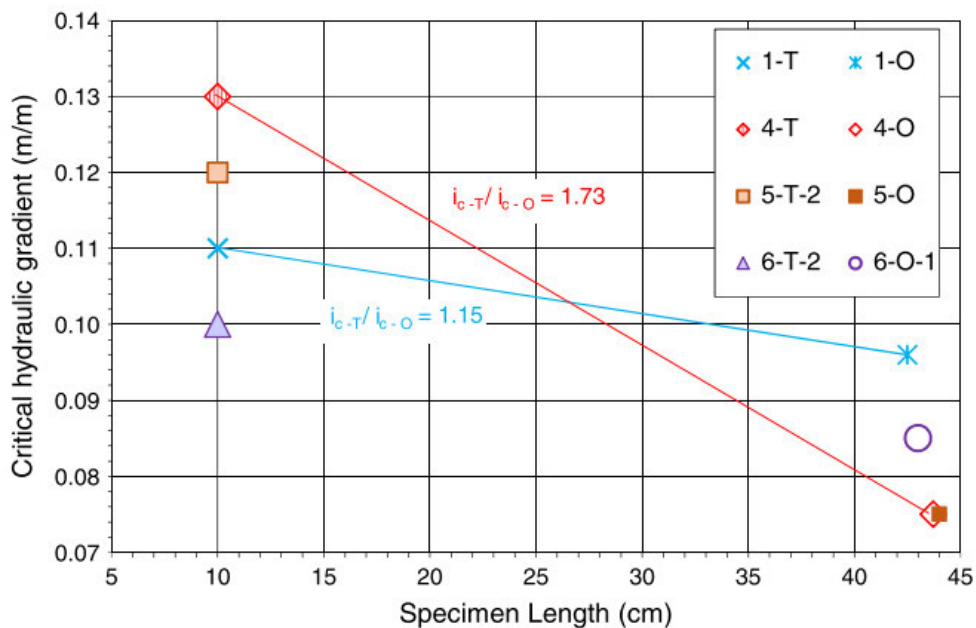


Figure 2.26: Critical hydraulic gradient for different specimen lengths, from Zhong et al. (2018)

The experimental work of Marot et al. (2012), which has been mentioned in passing already in this chapter, used centrifuge scaling laws to explore the relationship between seepage path length and an applied vertical stress on the initiation and progression of suffusion erosion. The study tested a gap-graded soil with 10% fines content under downwards flow at centrifuge accelerations

between 10- and 40-g. Specimens with a diameter of 73 mm were prepared to model lengths of between 60 and 120 mm and subjected to constant applied head difference at model scale of between 150 and 600 mm. Vertical effective stresses of between 14.2 and 42.5 kPa were also applied in this parametric study. The fine particle erosion rate and flow rate were measured by collecting the effluent water in discrete volumes using a rotating beaker system controlled remotely. The flow rate and applied difference was used to find the hydraulic conductivity of each sample with time (Figure 2.25).

Correlations between average erosion rate and applied hydraulic gradient for the tests of each specimen length was used to identify a critical hydraulic gradient as the lower limit at which an erosion rate could be detected, based on the accuracy of mass, test duration and device geometry measurements. The critical hydraulic gradient to cause fine particles to be externally eroded from the specimen was observed to decrease with decreasing model seepage path lengths. The study found that doubling the length of the specimen reduced the critical hydraulic gradient by 40% and doubled the rate of erosion. Instead of incorporating length into a hydromechanical boundary, an energy analysis was used to show a linear correlation between power of fluid flow and external suffusion rate, removing the length scale from the suffusion characteristics. This energy analysis approach is detailed in Section 2.6.4.

2.6.4 *Fines migration from an energy perspective*

An alternative to a Skempton and Brogan (1994) α factor-based approach of assessing suffusion is to use an energy-based approach. The benefit of this approach, as discussed by Gelet and Marot (2022), is that it considers the whole development of suffusion, rather than having to consider initiation and probability of progression with different criteria. The energy-based approach links the hydraulic loading to the mass of fines externally eroded from the specimen by considering the energy expended by the seepage flow.

This approach was first used for suffusion erosion in the centrifuge permeameter work of Marot et al. (2012). The power of the seepage flow is equal to the work done across the system and is a sum of the energy dissipated by pressure, viscosity, turbulence, and internal erosion. Because the flow is laminar,

the viscosity and turbulence components are negligible and the instantaneous power, W_{flow} , can be calculated using Equation 2.22.

$$W_{flow} = Q\rho g\Delta z + Q\Delta P \quad (2.22)$$

where:

Δz = length of the seepage path (m)

Q = volumetric fluid flow rate (m^3/s)

ΔP = change in fluid pressure across the sample (kPa)

The cumulative energy expended by the seepage flow, E_{exp} , can be calculated from the time integration of the instantaneous power, shown in Equation 2.23. Marot et al. (2012) found a linear correlation between the cumulative energy expended by the seepage flow and the total mass of fine particles externally eroded during their constant applied head tests. By considering the cumulative energy expended on the specimen over time, an element of hydraulic loading history is captured in this approach.

$$E_{exp} = \int_{t_0}^{t_1} W_{flow} dt \quad (2.23)$$

The concept of relating the eroded mass and expended energy within a parameter to categorise susceptibility to internal erosion was first introduced in the work of Marot et al. (2011) in relation to jet erosion and hole erosion tests (JET and HET) for surface erosion. The erosion resistance index, I_α , can be calculated from the experimental results and the soil can be classified into one of six categories, from highly resistant to highly erodible. Marot et al. (2016) then adapted this approach for suffusion resistance (initially using clayey soils), and proposed boundaries ranging from $I_\alpha < 2$ for highly erodible soils, to $I_\alpha > 6$ for greatly resistant soils. I_α can be calculated using Equation 2.24.

$$I_\alpha = -\log \left(\frac{\text{cumulative loss of dry mass, } m}{\text{expended energy, } E_{exp}} \right) \quad (2.24)$$

This approach has been used in several studies in recent years, including the work of Zhong et al. (2018), the results of which are shown in Figure 2.27, with each number prefix indicating a different soil, and each letter suffix

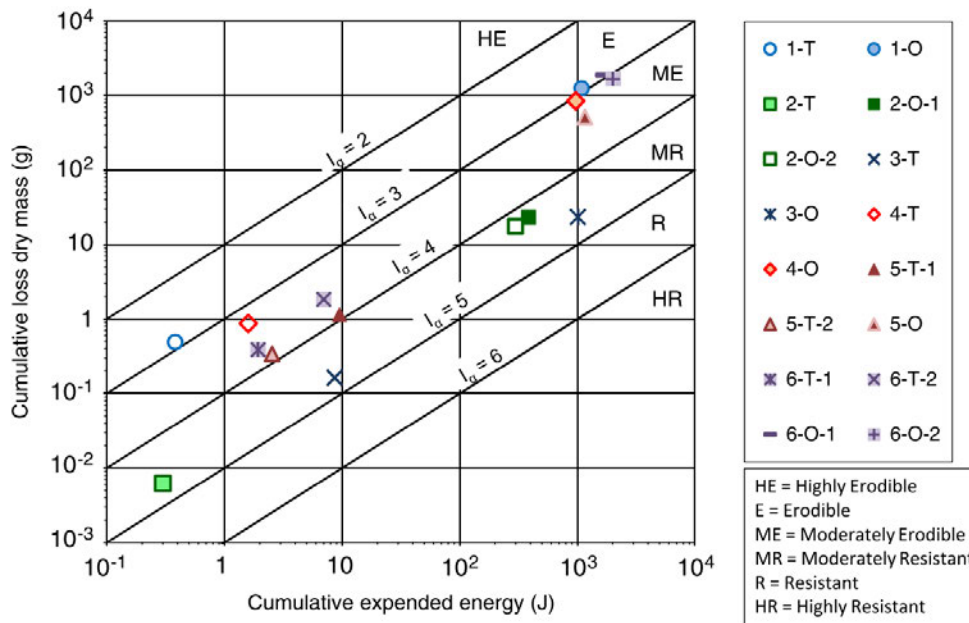


Figure 2.27: Erosion resistance index boundaries and test results, from Zhong et al. (2018)

denoting the testing apparatus (Section 2.6.3). The cumulative mass of soil lost is plotted against the energy expended by seepage flow within the sample, and the specimen falls within one of the I_α boundaries. I_α was found to be independent of the hydraulic loading regime (Rochim et al., 2017) and the seepage path length (Zhong et al., 2018). To compare tests across different apparatus and studies Le et al. (2018) normalised both axes by the volume of the sample and modified the I_α boundaries in accordance with this.

This method is based on the idea that the specimens have a fully-eroded state, observed in several studies, where further expended energy no longer causes any more fine particles to be eroded (Rochim et al., 2017; Zhong et al., 2018). Whilst the initiation of suffusion is consistently observed to be influenced by the hydraulic loading regime, and I_α and the cumulative expended energy needed to reach the fully eroded state, normalised by the specimen volume, are assumed to be intrinsic soil parameters (Gelet and Marot, 2022).

One of the main limitations of this approach is that it only considers the mass externally eroded, and not the particle transportation within the sample, although this is known to occur (Section 2.6.2). Whilst in element testing, this is not an issue, at full-scale it is not possible to quantify the mass lost from a zone, and there will potentially be a net influx of particles from upstream areas as well in addition to the particles transported out of the block. Connecting

the expended energy to a change in permeability instead, would have direct applicability to readings that can be made within earth structures.

2.7 A MICROSCALE UNDERSTANDING OF FINES MIGRATION

Due to their relatively sparse measurement points and typical assumptions made in geotechnical models, physical suffusion experiments on real soils must on the whole consider the soil as a continuum, rather than a granular structure. Experimental studies often propose hydromechanical laws that fit the observed macroscale behaviour, but an understanding of the micromechanical response of the soil is needed to ensure these laws are physically robust.

In addition, considering the individual particle interaction in the fines migration process allows a clearer understanding of why the soil exhibits the macroscale response that it does. At the microscale the detachment of fines and their transportation occurs at different length scales, allowing both processes to be investigated separately using discrete element modelling (DEM) (Wautier, 2018).

2.7.1 *Force chains and the α factor*

DEM is a numerical technique for modelling the interaction between individual idealised soil grains. The DEM model of Shire and O'Sullivan (2013) found a clear correlation between the Kezdi (1979) soil stability criterion and the number of inter-particle contacts for each grain. There was no clear transition between stable and unstable granular structures with increasing fines content, rather the structure became increasingly unstable as D_{15}/d_{85} increased.

The coupled CFD-DEM study of Kawano et al. (2018) also shows this trend of increasing α factor with fines content, as shown in Figure 2.28, also including the data from Shire and O'Sullivan (2013). There was not a clear distinction between the α factor for under-filled, transitional, and over-filled materials. The simulations of Shire and O'Sullivan (2013) suggested that the more contacts a particle has, the more involved it is in the force chain network. Ma et al. (2021) found that coarse-coarse contacts carried the majority of the stress applied

to a gap-graded soil structure, despite being the smallest proportion of the contacts.

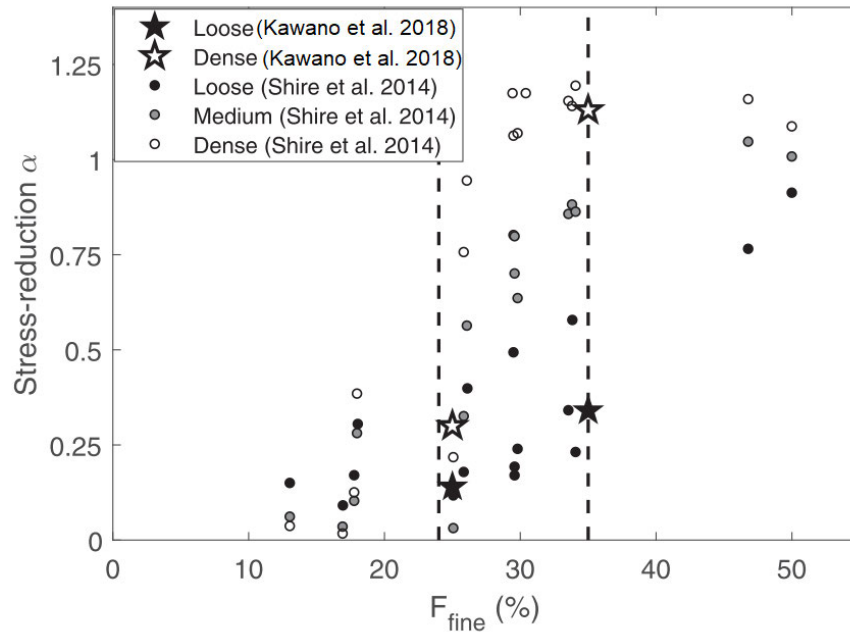


Figure 2.28: Relationship between the fines content and α factor for loose and dense materials according to numerical simulations (Kawano et al., 2018)

Fine particles with fewer than two contacts in the gravity-free simulation of Shire et al. (2014) took no part in the stress transfer. This gives a physical reasoning for the experimentally observed α factor reduction in critical hydraulic gradient observed by Skempton and Brogan (1994). In under-filled soils with less than 25% fines, the vast majority of the fine particles were located in the void spaces, with no inter-particle contacts. In a separate study, the X-ray tomography testing real soil by Fonseca et al. (2014) confirmed that the mean number of particle contacts decreased with increased instability, although real soils were found to have significantly more inter-particle contacts than the idealised spheres.

2.7.2 Initiation of particle migration

Using a DEM approach is very useful for considering the grain interactions, but suffusion is a two-phase process, where both the mechanical and hydraulic influence must be considered in tandem. Coupled DEM-fluid flow studies are limited by the immense computing power required, but in recent years

they have become a more feasible option. For example, coupled DEM-PFV (pore-scale finite volume) work by Wautier et al. (2019) shown in Figure 2.29 found that the transportation potential of loose particles (rattlers) is much higher when the flow is in the direction of the major principle stress because of force chain arrangements, echoing the experimental conclusions of Chang and Zhang (2013a) and Israr (2016).

Israr (2016) used a selection of relatively uniformly-graded real soils and Wautier et al. (2019) used a similar, although numerically generated, distribution. Although these soils are not classified as internally unstable, they can still give an understanding about the force distribution among differently sized particles. Wautier (2018) found an uneven distribution of load, with smaller particles being more likely to be more lightly loaded than larger particles.

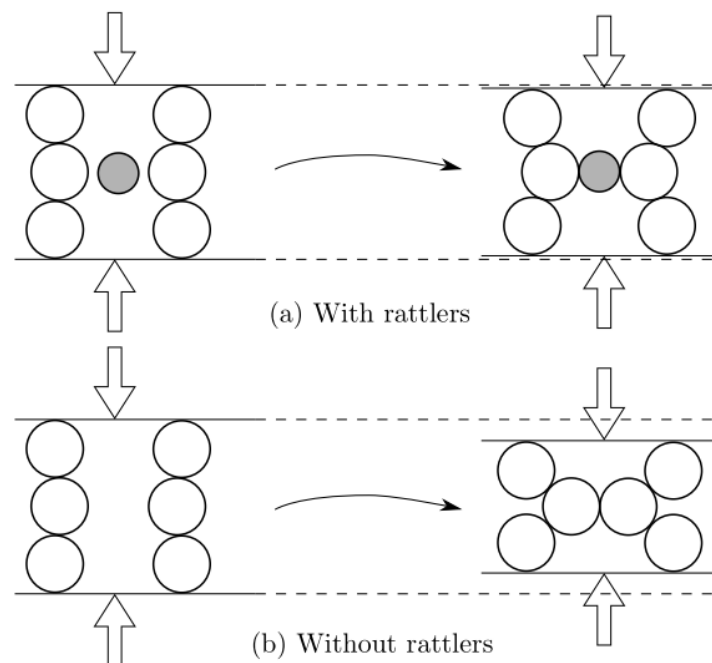


Figure 2.29: Fine particles (rattlers) provide structural support in under-filled materials, from Wautier (2018)

Ma et al. (2021) undertook a series of LBM-DEM simulations of suffusion on a gap-graded PSD and analysed the contact network and forces at particle contacts on the point of particle detachment. They proposed a sliding index for a particle contact to assess whether a contact will slide or strengthen under the action of the fluid force. If there is a stable particle with a contact with a neighbouring particle, as shown in Figure 2.30, at the point of contact there

will be a normal and a tangential force. If a perturbation gives a displacement that acts in the same direction as the tangential force the tangential force will decrease, reducing the risk of sliding, strengthening the contact. Conversely a force in the same direction as the tangential force increases the force. The risk of sliding P increases and the particle could become detached.

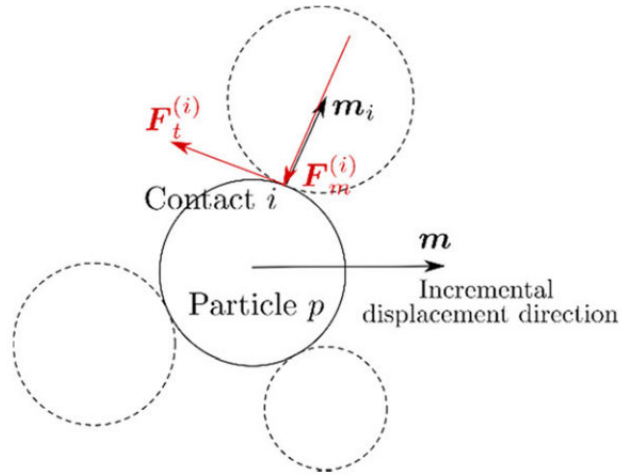


Figure 2.30: Forces affecting the sliding or strengthening of a particle contact, from Ma et al. (2021)

The LBM-DEM work of Ma et al. (2021) also showed higher erosion when the flow direction is parallel to the applied stress direction, compared to the perpendicular case. For horizontal flow, a higher proportion of the particle detachments move the particles in the macro fluid flow direction, whereas the detachment direction is much more varied for the vertical flow case (Figure 2.31).

2.7.3 Representative elementary volumes (REV)

Whilst DEM models can simulate inter-particle behaviours, it is important to simulate a sufficient number of particles to achieve results that can be directly compared between experimental and numerical results, at a scale known as the representative elementary volume (REV) (Wautier, 2018). Although constant advances in computing power allows for simulations of tens to hundreds of thousands of particles, this may only represent a small structure of an internally unstable material, due to the size difference between the fine and coarse particles. At REV scale, which can be referred to as the mesoscale

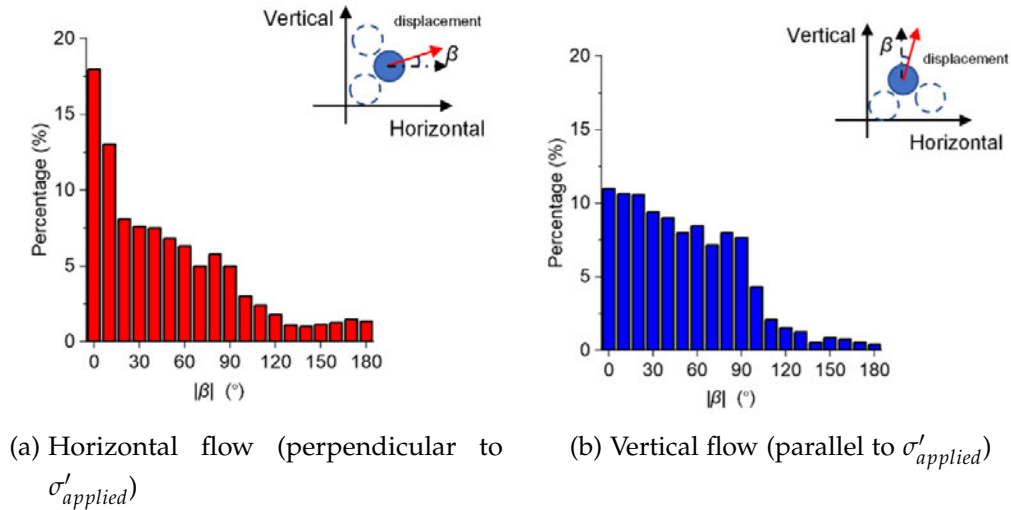


Figure 2.31: Distribution of angle between flow direction and particle displacement at time of particle detachment, from Ma et al. (2021)

(Section 2.2.9), the individual particle behaviours can be averaged across the model to achieve an approximation of the macroscale response to the same input.

In the doctoral work of Wautier (2018), a coupled DEM-PFV model of suffusion in gap-graded materials at the REV scale was proposed, allowing the author to explore how the microscale initiation and continuation of suffusion contributed to the mechanical instability of the 3D specimen. The detachment of individual grains was not explored in the simulation, instead focusing of the development of the force-chain network upon the removal of particles. Expected transportation distances of eroded fines were calculated using pore network model assumptions (Section 2.4.2).

Coupled CFD-DEM simulations allowed Hu et al. (2019) to investigate the erosion and clogging potential of a column of under-filled gap-graded soils (5, 10 and 15% fines) and one well-graded soil, bridging the gap between grain-scale and macroscale behaviour. Each simulation had 40,000 particles and a DEM time step of 5×10^{-7} seconds, for a total simulation time of 30 seconds. Gap-graded soils with higher fines content were found to be more susceptible to clogging than those with a lower initial fines percentage, and again the migration of fine particles with no inter-particle contacts through the pore network was observed. The removal of fines by the seepage flow was accompanied by a decrease in the number of particles with low inter-particle connectivity and weak particle contacts. Gravity was not applied to the solid

phase in this study, although it was considered for the upwards fluid seepage flow.

Zou et al. (2020) also used coupled CFD-DEM to model the migration of fine particles through under-filled gap-graded soils subjected to an upwards seepage flow regime. The influence of gravity on the migrating fine particles was considered. At higher hydraulic gradients, the erosion rate was higher and a greater total amount of eroded particles was observed. Even the samples classed as 'stable' experienced some minimal loss of fine particles. The paths of the migrating particles were tortuous and their velocities fluctuated greatly throughout their journey. The maximum velocity for particles from the end of the seepage path (upper layer) was lower than for the bottom layer and the beginning of the seepage path. The model was very computationally expensive so only 0.4 seconds of flow time could be modelled.

When investigating the influence of heterogeneity and inclusions on fines particle migration using coupled CFD-DEM, Liu et al. (2023) found that fine particles are likely to deposit at the interface between layers of different fines content. These developing areas of heterogeneity influence the flow regime within the soil as the fines migration progresses. The study found that the inclusion of cut-off walls increased the migration distance of the fine particles and certain configurations reduced fine particle loss, although these micromechanical observations cannot be extrapolated directly to predict macroscale responses. The study found that fine particles with low coordination numbers (number of inter-particle contacts) and little contact force were the most likely to be eroded by the seepage flow. As gravity was ignored in this study, fine particles could have coordination numbers equal to zero.

2.8 SUMMARY

In this chapter, a summary of the terminology used in this study is given, as, historically, different terms for the internal erosion process have been favoured by different research groups. The principles of geotechnical centrifuge modelling are also detailed, as very few internal erosion studies have been conducted in enhanced-g environments to date. The bulk of this chapter is dedicated to presenting the current understanding of the suffusion process, starting by discussing the material instability, and then moving onto the hydromechanical

factors affecting the onset and progression of suffusion. Particular focus is given to the hydromechanical envelope and expended energy-based suffusion assessment methods, as the scaling laws of the centrifuge allow the macroscale assumptions of these approaches to be challenged.

Factors such as hydraulic loading regime, effective stress and seepage path length are consistently observed to have an influence on the development of suffusion in experimental studies, but the variety in testing apparatuses and boundary conditions lead to different conclusions being reached on the exact influence of each parameter. This literature review also highlights the current disconnect between the microscale particle transportation process, typically modelled using numerical techniques, and the macroscale measurements taken in experimental work. An understanding of the spatially varying process of suffusion that is consistent between the two scales is needed, an area experiencing increasing interest in recent years due to the closing of the gap between numerical and experimental scales, at scale termed the representative elementary volume.

METHODOLOGY

3.1 INTRODUCTION

In this chapter the apparatus, materials and methods for the final suite of permeameter tests are presented. This includes the design of an internally unstable soil mix suitable for centrifuge testing, one of the key components of Garner and Fannin's (2010) Venn diagram (Figure 2.1). The details of the designing and commissioning of the centrifuge permeameter as part of this study, as well as the steps for sample preparation and post-test dissection are presented. The testing procedure for both centrifuge and 1-g permeameter tests are also given and the reasoning for the inclusion of each test and the centrifuge testing approach is also justified.

The details on processing and interpreting the data obtained by the data acquisition system are given. Many different approaches to analysing the suffusion phenomenon have been proposed in literature, as can be seen in Chapter 2, and the implementation of those used in this study, including critical hydraulic gradient and energy analysis, are explained in this chapter. The chapter finishes with a table summarising the experimental programme and key parameters for each test.

3.2 MATERIALS TESTED

3.2.1 *Constraints and requirements*

There are several considerations that need to be taken into account when designing an soil susceptible to suffusion erosion that will be tested in a centrifuge environment. The fluid velocity through the soil scales linearly with the centrifuge's acceleration and many of the methods for analysing suffusion erosion are based on the assumption of laminar flow, following Darcy's law. To ensure

that the laminar flow requirement is met, both the coarse matrix soil and the fine erodible soil need to be sufficiently fine-grained to keep the hydraulic conductivity low under centrifuge accelerations, as fluid flows can become turbulent even in relatively fine materials (Taylor, 1994).

The soil used for testing must be, first and foremost, susceptible to suffusion. The International Commission on Large Dams (ICOLD, 2013) identifies several methods to assess the suffusion potential of a material. These are predominantly based on the particle size gradation of the soil and are derived from experimental results, as well as conceptual ideas such as dividing a material into coarse and fine fractions, or considering the pore constrictions limiting the travel distance of loose fine particles.

Engineers are advised to choose the most appropriate method for their particular soil depending on the grading and presence of cohesive fines. This reliance on engineering judgement can also be seen in some of the proposed criteria, where the engineer is required to define the exact grain size where the curve transitions between coarse and fine materials. Whilst this is simple for a gap-graded soil, the issue becomes more complex when considering a widely graded material.

For this reason, as well as the fact that they are well established criteria in the field, this study considers the Kezdi (1979) and Kenney and Lau (1985) criteria, described in Section 2.4.1. The final soil mix is designed to have a clear gap in the grading and no cohesive fines. Both the coarse and fine components are silica sands. The soil mix has a fines content of 20%, which can be considered "under-filled" (Section 2.2.9). Despite being internally susceptible to suffusion, the soil must be stable enough to be moist-tamped into the permeameter cell without segregation or excessive fines loss through the base filter.

3.2.2 *Final soil design*

For the coarse component of the final soil design, a uniformly graded Congleton HST95 fine silica sand is used. To create a clear gap between the fine and coarse particles and ensure internal instability, particles with $D < 90\mu\text{m}$ are removed from the sand. The sand is first dry sieved and then wet sieved through an $90\mu\text{m}$ (ASTM No.170) sieve. The sand is then oven dried and stored in airtight containers ready for testing. The fine component of the soil mix constituted

Table 3.1: Soil properties

Property	Coarse HST95 sand (modified)	Fine HIM2 silt	Tested gradation
$D_{10}(\mu m)$	115	3.3	17.4
$D_{15}(\mu m)$	126	4.5	30.1
$D_{50}(\mu m)$	162	16.6	149
$D_{60}(\mu m)$	172	21.0	162
$D_{85}(\mu m)$	200	37.8	195
C_u	1.5	6.3	9.3
G_s	2.68	2.65	-
$\rho_{d,min}(kg/m^3)$	1430	-	1470
$\rho_{d,max}(kg/m^3)$	1690	-	1990
e_{min}	0.590	-	0.350
e_{max}	0.876	-	0.822
$F_S(\%)$	-	-	20
$(H/F)_{min}$	-	-	0.609

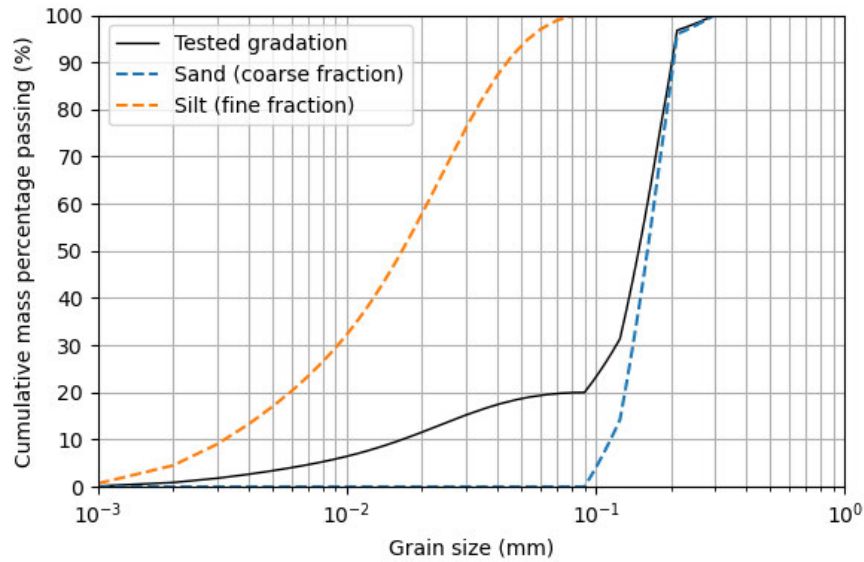


Figure 3.1: Particle size distribution of the tested material

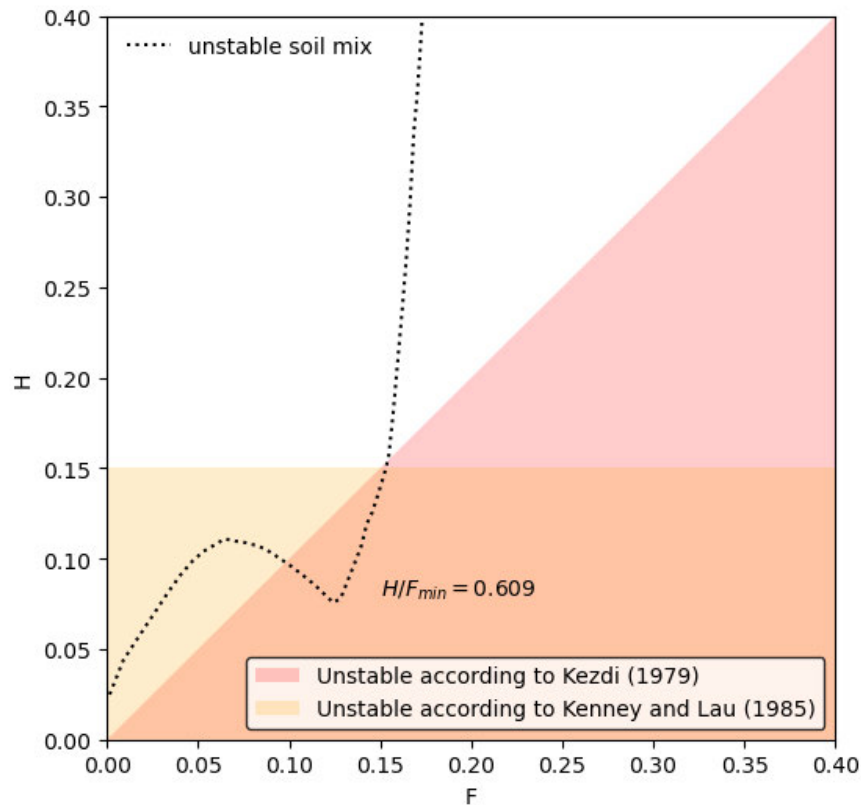


Figure 3.2: H/F diagram for tested material

HIM2 fine silica flour (silt) with an average grain diameter of $17\mu m$. The final tested gradation is shown in Figure 3.1, alongside its component parts. The final soil gradation has a fines percentage of 20%. Figure 3.2 shows the tested

gradation compared to the Kezdi (1979) and Kenney and Lau (1985) internal instability boundaries. The soil is unstable according to both criteria, with a minimum H/F value of 0.609. In Table 3.1, other soil parameters are given for the component soils as well as the tested gradation. The microscope images of the sand and silt are shown in Figure 3.3. The sand can be categorised as sub-rounded, which influences the shape parameter chosen for the Kozeny-Carman permeability calculation (Section 2.4.3).

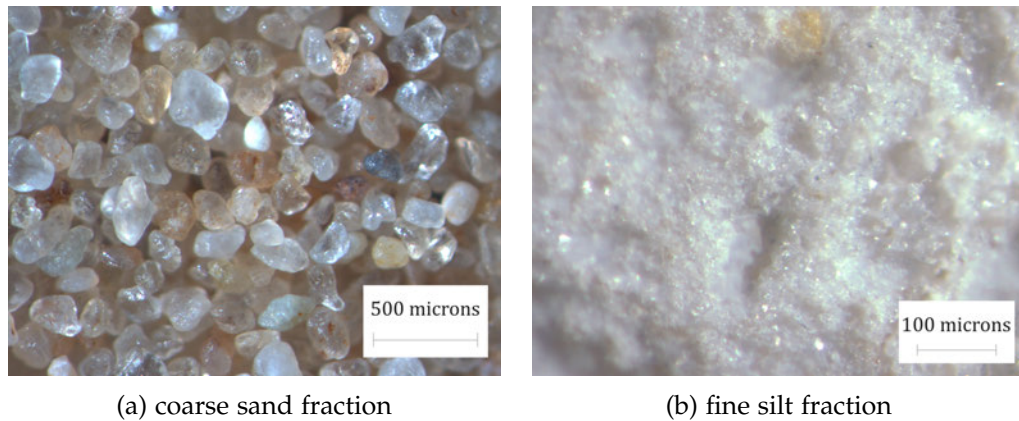


Figure 3.3: Microscope images of the coarse and fine soils tested

3.2.3 Determining the particle size distribution

Due to the relative size difference between the coarse and fine soil gradations used, two different methods were used to determine their particle size distributions, shown in Figure 3.1. For the coarse component, a stacked sieve approach in line with the standard procedure described in Head (1982) was used. Sieve sizes of 63, 90, 125, 180, 212 and 300 microns were used. The soil was placed in the top, coarsest sieve and then the sieve stack was placed on the vibrating platform for 15 minutes. The weight of sand remaining in each sieve and in the bottom catchment tray was recorded, and from this the PSD was obtained.

In contrast, the particle size distribution of the finer silt fraction was found using a laser diffusion particle size analyser (Mastersizer 3000) shown in Figure 3.4. A teaspoon of the silt was added to the beaker of distilled water, which is then sampled by the machine. To calculate the size of the particles present, the scatter of a laser beam through the dispersed soil is measured. The machine returns the particle size distribution by volume of the HIM2 silt,



Figure 3.4: Mastersizer 3000 used to ascertain the silt particle size distribution

which is converted to the particle size distribution by weight using the specific density of the soil, provided by Hoben International Ltd. This was repeated three times and the average distribution is used in Figure 3.1.

3.2.4 *Maximum and minimum density tests*

The maximum densities for both the pure sand and the soil mix used in permeameter testing were obtained using Method 1B in ASTM:D4253 (2016), using a wet soil and a vibrating table. The soil was mixed with a 15% water content and left for half an hour. On the vibrating table, the soil was spooned into a standard split mold. Once the mold was full, the surcharge was placed on top on the sample and the set-up was vibrated for 10 minutes at 50 Hz. After vibration, the guide sleeve is removed and the soil is levelled off in line with the split in the mold. Using the weight of the mold both empty and full of wet soil, the weight of the oven dried soil, and the mold's dimensions, the maximum density of the soil mixture can be obtained.

To find the minimum density, Method C from ASTM:D4254 (2016) was used. 1 kg of soil was placed in a graduated cylinder, which was then sealed. The cylinder was then inverted several times and the height of the soil was recorded. This was repeated several times until three values within 2% were recorded, according to the standard. The calculation presented in this standard were later used to find the mass of soil needed for each layer of the specimen to be prepared to a known relative density.

3.3 DEVELOPING A NEW CENTRIFUGE PERMEAMETER

One of the objectives of this study was to develop a device that can study the influence of parameters such as effective stress, hydraulic conditions and seepage path length on the suffusion process using the scaling capability of the geotechnical centrifuge. Although some suffusion work has previously been undertaken in the centrifuge environment by Marot et al. (2012), the aim for this study was to incorporate features from 1-g devices such as interstitial pore pressure sensors and multi-stage seepage flow, to capture the spatial and temporal development of fines migration. The rigid-walled downward flow device allows for direct comparison with experimental studies by Li (2008) and Li and Fannin (2012) to identify the critical hydraulic gradient and hydromechanical envelope controlling suffusion.

3.3.1 *Centrifuge permeater apparatus*

Figure 3.5 shows a schematic of the centrifuge payload as it is laid out for permeameter testing. An overview of the 50gT centrifuge at the University of Sheffield, for which the permeameter was designed, is given in Section 2.3.5. The key elements of the device are labelled in the diagram, following the path of the fluid through the apparatus. A photograph of the payload during testing is given in Figure 3.6. Each component is described in more detail in the following paragraphs, but in summary the apparatus works as follows:

Fluid flow through the permeameter cell containing the soil specimen is controlled by two constant head tanks (CHTs), *B* and *F*. At the start of a multi-stage seepage test these are held level, and then the downstream CHT (*F*) can be lowered incrementally to increase the head difference applied across

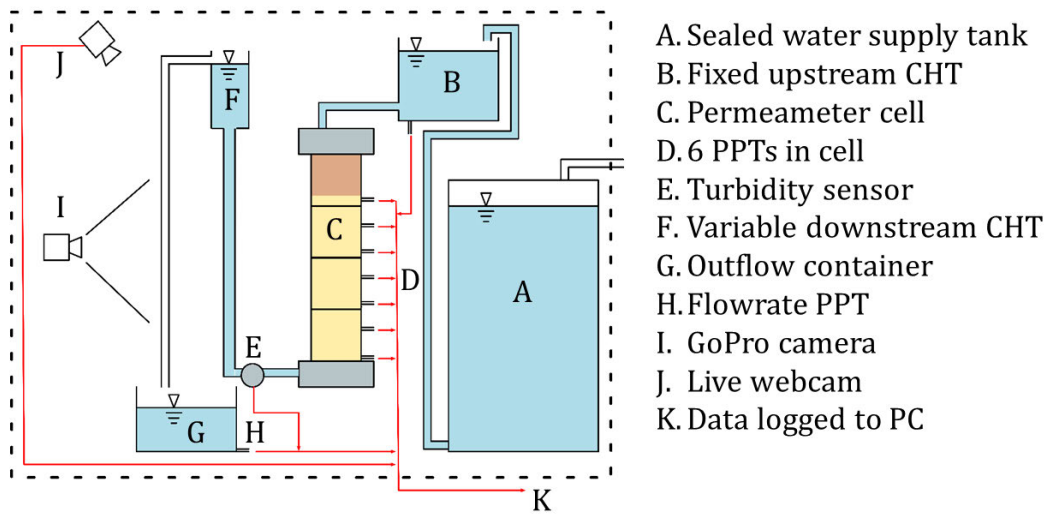


Figure 3.5: Schematic of centrifuge payload components

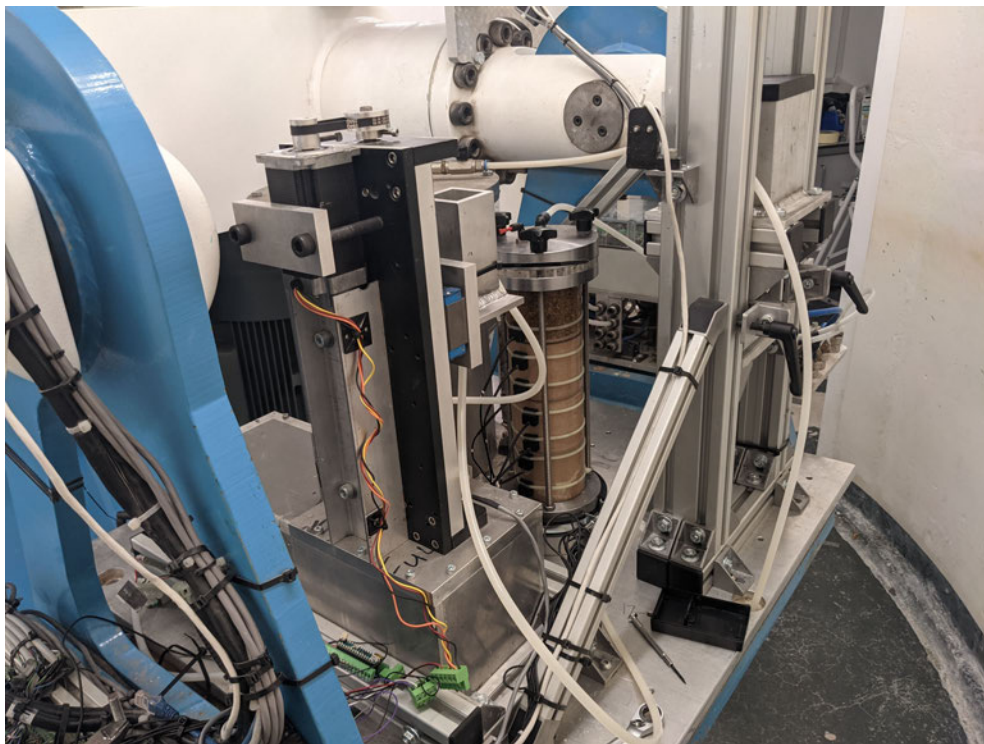


Figure 3.6: Centrifuge payload

the sample. The flow rate is captured by recording the increasing head of water in the outflow container *G* by means of a PPT (*H*) at the base of the tank. Pore pressures within the sample are measured at seven PPT ports spaced evenly along the soil specimen's height. The apparatus can be split into three main

systems; the water supply and flow control system, the permeameter cell itself, and the data acquisition system.

3.3.2 Water supply and flow control system

The water supply tank, *A*, in Figure 3.5 is used to carry all of the deaired water needed for the duration of the test as passing water across the centrifuge slip rings may introduce air bubbles to the fluid. This sealed and pressurised tank has a capacity of 18 L and is located towards the back of the payload in Figure 3.7. A supply of nitrogen gas is used to pressurise the tank and the pressure adjusted inflight from the control room to manage the flow into the upstream CHT (*B*).

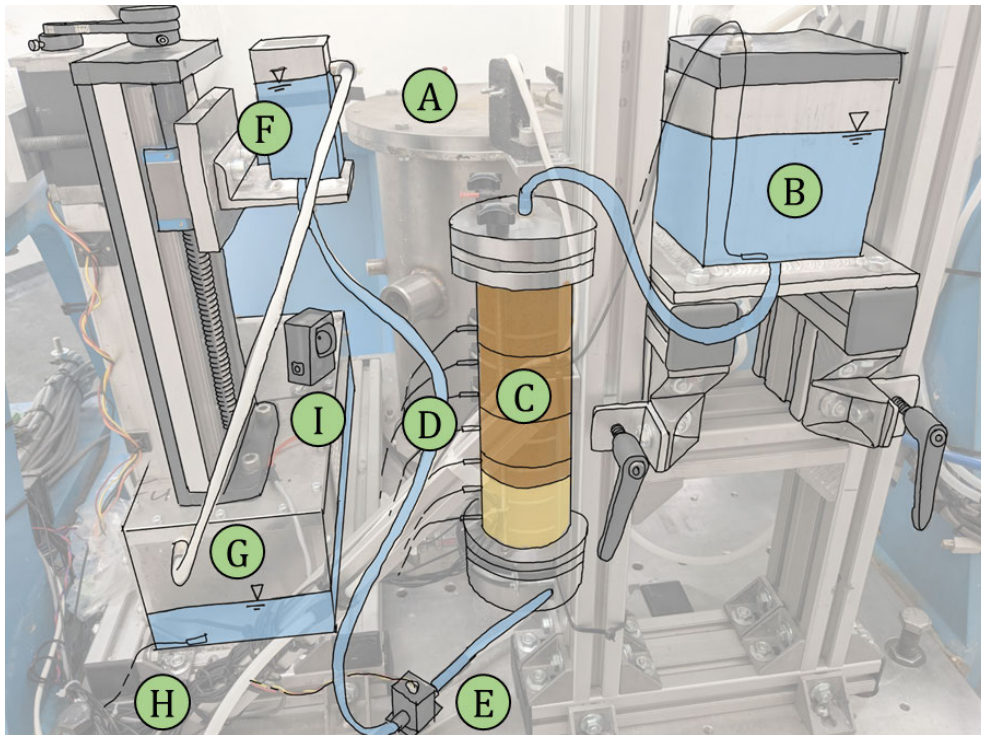


Figure 3.7: Centrifuge payload with water supply system highlighted, labelling consistent with the schematic in Figure 3.5

The water level in the upstream CHT (*B*) is monitored inflight by both a PPT submerged at its base and a webcam focussed on a piezometer in its side wall. The specification of the PPTs used in this study is given in Section 3.3.4. The CHT overflows through a pipe in the tank's sidewall that connects to the base of the payload and the water is evaporated in the high speed environment.

The upstream CHT is connected directly to the top of the permeameter cell via an 8 mm diameter flexible pipe.

Once the water has flowed through the permeameter cell it exits through the 8 mm pipe at the cells base. This pipe is connected to the base of the downstream, variable-height CHT (*F*), passing through a section of glass tube and a turbidity sensor (*E*). The sensor was trialled to measure the quantity of eroded fines in the effluent water based on the device from Marot et al. (2011) but the fluctuating light and high stress in the centrifuge lead to inconsistent results, which have consequently been omitted from this study.

A more detailed image of the variable-height CHT is given in Figure 3.8. The header tank is mounted on a linear actuator that can be lowered in 2.5 mm increments during testing. The full range of the actuator allows for a head difference between the two CHTs of 180 mm. This can be increased by raising the upstream CHT and securing it before testing, facilitating head differences across a sample of upwards of 500 mm. This is far beyond the requirements of this study but ensures the versatility of the apparatus for future applications.



Figure 3.8: Linear actuator with stepper motor to lower the outlet CHT whilst the centrifuge is in flight

The overflow from the downstream CHT (*F*) empties into a storage tank (*G*) with a PPT at its base. The flow rate through the sample is calculated from

the increasing head of water in the tank, measured by this PPT. This is then multiplied by the cross-sectional area of the outflow tank to give the volume of water in the tank at any given time. The flow velocity through the sample is calculated by dividing the change in fluid volume by the area of the specimen perpendicular to the seepage flow direction.

For the first stage of testing, or at lower centrifuge accelerations, a smaller outflow container is placed within the one pictured in Figure 3.7, to allow for more accurate capturing of the seepage flow rate. By decreasing the cross-sectional area of the container, the change in water height within the container is larger for the same volume of water. This means small changes in water volume can be distinguished more easily from the PPT data.

The capacity of the storage tank (G) dictates how long a test stage can run for before the centrifuge must be spun down to empty it. Between two and four stages are conducted on each specimen. A balance must be struck between using the smaller container to more accurately capture the flow rate and minimising the number of spin-downs required to complete the test, as they may impact the soil fabric of the specimen. The smaller and larger outflow containers have capacities of 1 litre and 8 litres respectively. The PPT in the outflow storage tank is identical to those placed in the cell and the upstream CHT, the details of which are given in Section 3.3.4.

3.3.3 *Permeameter cell*

The permeameter cell (C) is positioned in the centre of the payload and consists of a top and bottom cap and stacked acrylic cylinders, all held together with steel tie rods. The sample is prepared within the permeameter and pore pressures along the seepage path are measured by seven PPTs located at equal intervals along the sidewall. Using stacking cylinders rather than one solid acrylic section allows the sample to be dissected post-testing to find the final spatial distribution of fine particles within the sample and also allows for shorter samples to be tested without an increase in overburden stress. The benefit of this feature is discussed in Section 3.8. Figure 3.9 shows two photographs of the cell prepared with different sample lengths, and a schematic of the cell is given in Figure 3.10.

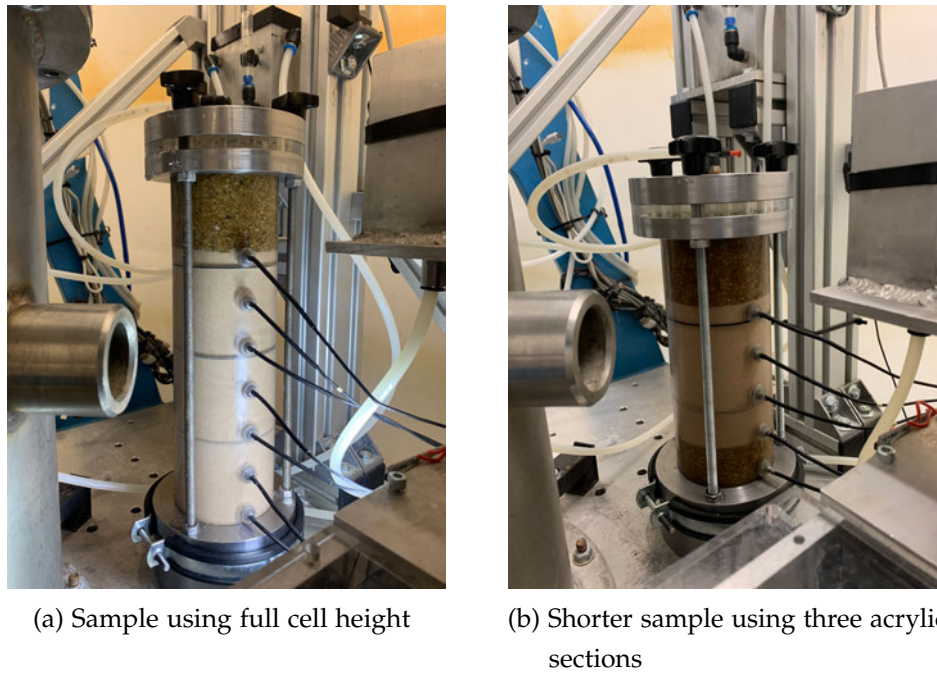


Figure 3.9: Configurations of the permeameter cell for different sample lengths

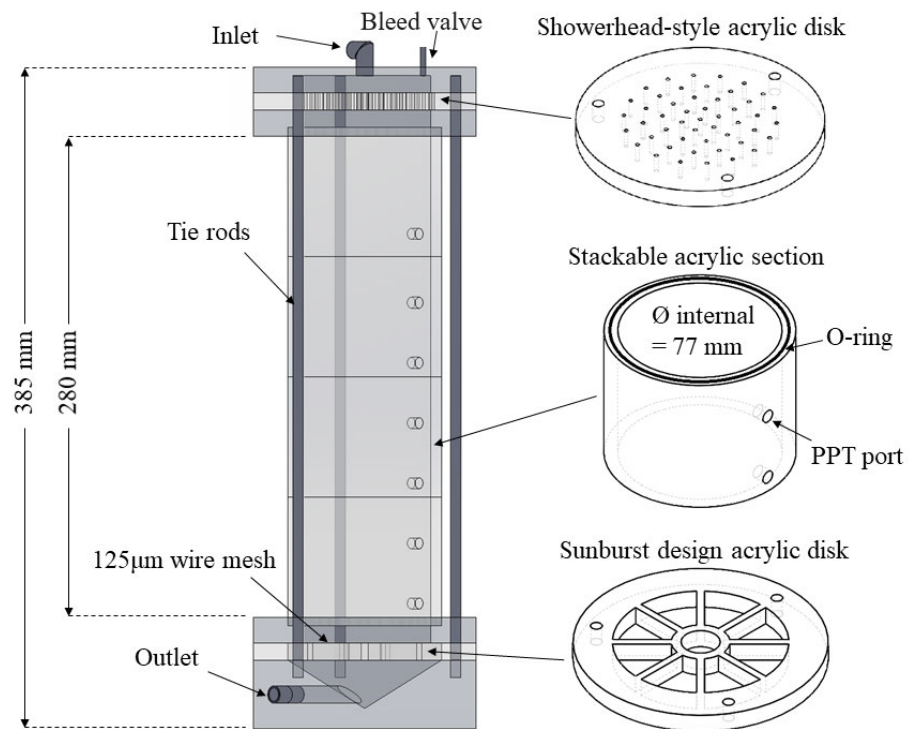


Figure 3.10: Schematic of the permeameter cell

The acrylic cylinders have an internal diameter of 77 mm and are connected with O-rings, shown in Figure 3.10. It is possible to test a specimen with only

two or three of the sections for a shorter sample with the same overburden pressure due to the same height of overlying coarse overburden soil (Figure 3.9b). Seven PPT ports are located along the sidewall of the cell at 35 mm centres, giving a testing specimen length of 210 mm and diameter of 77 mm. The specimen is typically prepared to 220 mm height for full height tests so that the top and bottom PPTs are located fully within the soil body.

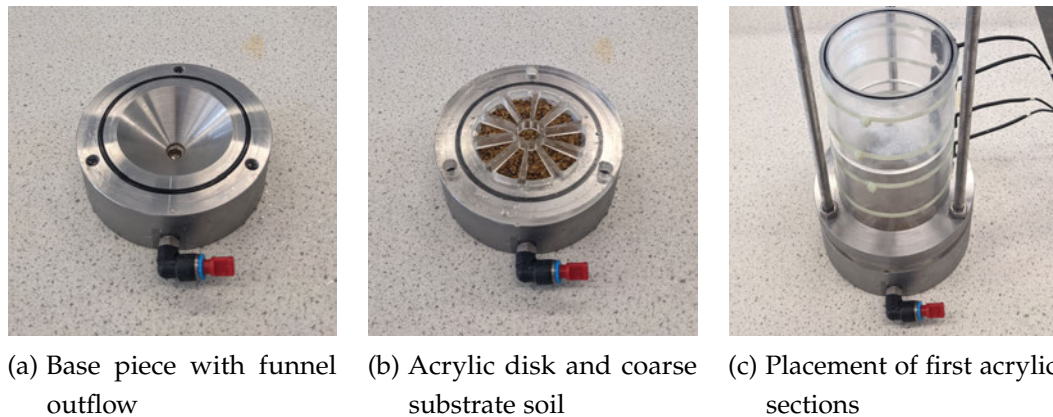


Figure 3.11: Base sections of the centrifuge permeameter

The base of the cell consists of three parts: the base with a conical funnel to the outlet (Figure 3.11a), an acrylic disc which supports the sample (Figure 3.11b), and an aluminium confining disc. In preliminary tests the sample were prepared directly on a fine mesh, which was placed on top of the sunburst design disc. Some of the eroded fine particles were collected within the funnel and others transported further downstream. Although this mesh was sized in line with the smallest coarse particle at $125 \mu\text{m}$, it appeared to still restrict the passage of fine particles out of the sample. Consequently, for the tests reported in this study the sample is constructed on top of a layer of coarse sand (Leighton Buzzard Fraction A - the same as used for the overburden soil and described in) to provide free passage for the migrating particles whilst still supporting the coarse granular matrix of the sample.

The top cap of the cell also consists of two aluminium sections sandwiching an acrylic disc. The acrylic disc is perforated with 1mm diameter holes to distribute the flow of water across the top of the specimen. The water is further dispersed as it flows through the coarse, free-draining sand layer overlying the specimen. The top section contains a reservoir for the inflowing water, which is supplied from the upstream CHT via the pipe connection on top of the cell. There is also a smaller bleed valve that ensures the system remains free from

air when connecting the cell to the water supply system on the centrifuge beam. The top cap and base are connected with steel tie rods, clamping the acrylic cylinders of the cell between them.

3.3.4 *Data acquisition and PPTs*

In the study, EPB-PW model pressure transducers with a 3.5 bar (50 psi) range supplied by StrainSense Ltd are used. The sensors are fitted with a 6 μm porous ceramic filter (air entry value 0.5 bar). The PPTs have a diameter of 6.4 mm and a length of 11.4 mm (Figure 3.12). In total there are seven PPTs located at 35 mm intervals along the sidewall of the permeameter. The sensors are fitted flush with the internal wall of the cell and sealed in place with an O-ring and silicon sealant. There are two further PPTs, one in the base of the upstream CHT and one in the base of the outflow tank for measuring flow rate during testing.

When not in use for testing, the acrylic wall sections with the fixed-in-place PPTs are submerged in a tank of deaired water to keep them saturated. During sample preparation there is inevitably some time where the PPTs are exposed to air and could desaturate, however care is taken to keep this time as short as possible. The saturation phase for the soil specimen, described in Section 3.4.1, also allows the PPTs to resaturate if needed. The PPTs were observed to respond near instantaneously to pressure changes in the sample, most noticeably when accelerating the centrifuge, and so can be assumed to be fully saturated during testing.

During centrifuge testing, the pore pressures were logged and written to a .csv file at a frequency of 1600 Hz. This extremely high logging rate was a result of a quirk in the experimental set-up. This rate is excessive for the problem at hand and the data was post-processed to achieve a more appropriate frequency of 320 Hz, as well as to reduce the data file size. This processing is detailed in more depth in Section 3.7. The signals were also monitored from the control room whilst in flight. Live webcam feeds of both the upstream CHT piezometer and the downstream CHT actuator were also viewed live to ensure the head was kept constant and the actuator was lowering as expected. There was additionally a GoPro camera trained on the specimen in the cell, which was set to take an image every 60 seconds for the duration of the test. These images

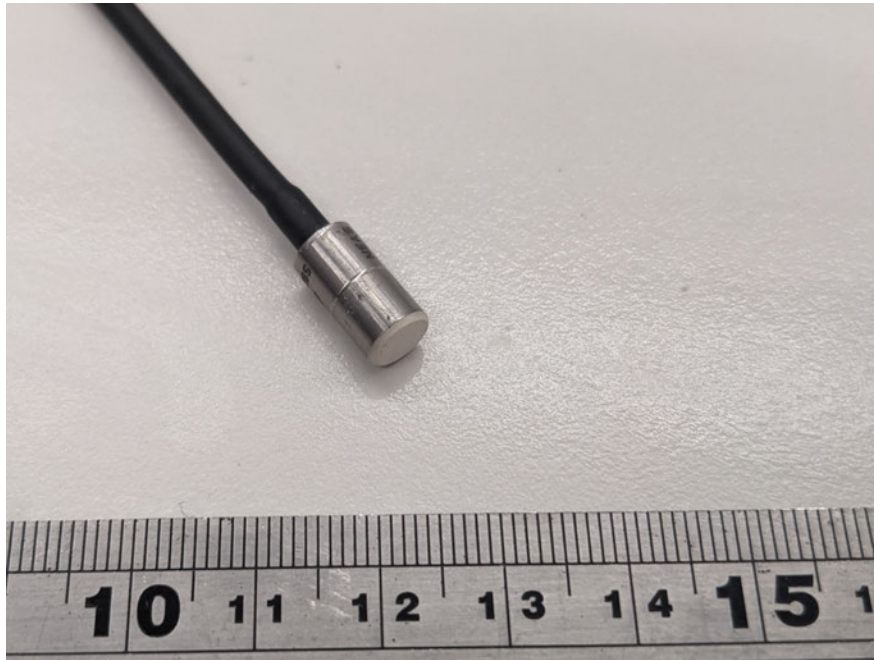


Figure 3.12: Pore pressure transducer used in centrifuge tests

were then recovered from the SD card and stored for later processing and analysis.

3.3.5 *Influence of variation in g across the model*

As discussed in Section 2.3.3, there are two ways that the relatively small radius of a centrifuge causes variations in gravitational acceleration across the model (in comparison to, say, the variation in g-level across the surface of the Earth, which has a very large radius). These variations occur across the model width and across the model height. Equation 2.10 can be used to calculate E_{width} across the whole base of the payload, which is equal to 3.0%, with the error across the relatively narrow soil column being less than 0.1%. This variation is very small and can be disregarded in this study, particularly as horizontal variations are not being measured.

The error that has more impact in this study is that the error across the relatively tall model height, with the difference in radius meaning that the design N is not the value experienced across the whole specimen. At 40-g ($\omega = 15.18$ rad/s), the scale factor experienced at the top of a full height sample is $N = 39.6$, whereas at the base of the sample $N = 44.8$. This is

variation is significant and must be accounted for when handling the data obtained during centrifuge testing, as discussed in Section 3.7.

3.4 PREPARATION OF SAMPLE FOR TESTING

3.4.1 Specimen preparation

The first step of specimen preparation was to create the soil mix. The sand and silt were weighed out in a 4:1 ratio, giving an initial fines content of 20%. Water was then added to reach a 5% water content and mixed thoroughly into the soil. The batch was sealed in an air-tight plastic bag and left for 16 hours to promote moisture homogeneity.

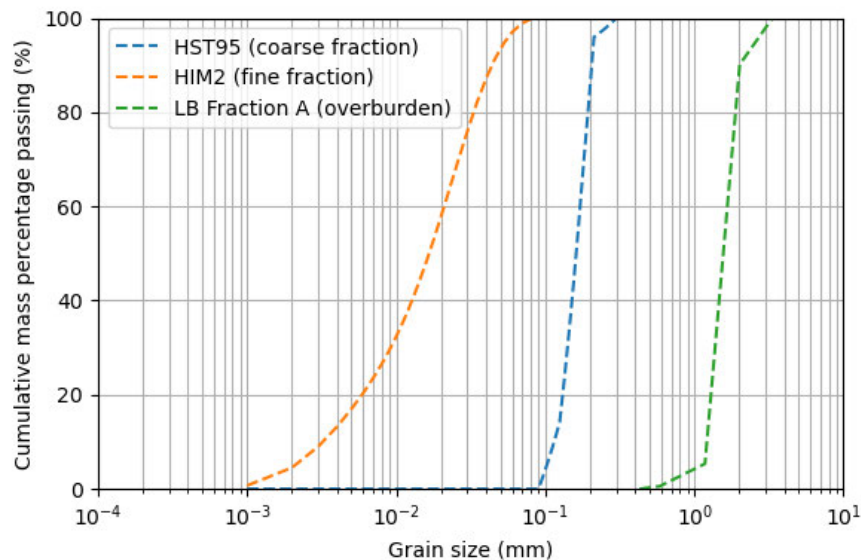


Figure 3.13: Particle size distribution of the component soils used in the unstable specimen alongside the Leighton Buzzard fraction A sand used in the overburden and free-draining base layer

The samples were prepared with the aim to create the most homogeneous specimen possible and avoid excessive fines migration (segregation) before seepage was applied. To achieve this the undercompaction moist-tamping procedure from Ladd (1978) was employed to reach a relative density of 70% ($e = 0.58$). Due to the fineness of the soil, no correction factor for undercompaction, U_{ni} , was needed.



Figure 3.14: Pre-portioned layers of silt-sand soil mix are moist-tamped to their desired height in the cell

A coarse free-draining sand (Leighton Buzzard fraction A) was dry pluviated to fill the base of the cell to 5 mm below the lowest PPT. This soil provided a sturdy base to compact on while its pore size is large enough to allow external suffusion of fine particles during testing. The particle size distribution of LB fraction A is shown alongside the coarse (HST95) and fine (HIM2) fraction in Figure 3.13, and its specific gravity, G_s , is equal to 2.67. Once the free draining coarse layer was compacted, the test soil was weighed into 130g portions and compacted directly into the permeameter cell (Figure 3.14). These 15 mm layers were tamped on top of each other until the desired specimen length was reached. The rest of the cell was then filled with more fraction A sand, providing the dual purpose of distributing the fluid flow over the specimen surface, and contributing overburden stress. On top of this a thin sheet of permeable plastic mesh was added to further distribute the fluid flow, shown in Figure 3.15.

Once the cell was sealed, a supply of CO_2 was connected to the bottom valve of the permeameter. A pipe was then connected to the top valve and the other end of the pipe was weighted and submerged in a beaker of water. The gas supply was adjusted so that a steady flow of small bubbles was seen in the beaker of water and the sample was then percolated with CO_2 for 20



Figure 3.15: Sample is overlain with a coarse free-draining sand and a layer of permeable mesh

minutes. During this time, a supply of water was deaired using the nitrogen purging method, which is discussed in more detail in Section 4.4. Once all of the air in the specimen was replaced by CO_2 , the cell was connected to a GDS advanced pressure control cell filled with the deaired water (Figure 3.16). The specimen was saturated with upwards flow at a rate of 100 ms/mm^3 for 24 hours, allowing several pore volumes of deaired water to flush through the sample and remove the CO_2 . This method works because the air within the sample is first replaced with CO_2 , which is both a more dense and more soluble gas, and the CO_2 is subsequently dissolved by the permeant water, leading to a fully saturated specimen (Fischer et al., 1999). The sample was then secured on the centrifuge beam ready for the test to begin.

Once the cell was sealed, the sample was purged with carbon dioxide (CO_2) and saturated with deaired water. CO_2 is more dense than air and, when applied at the base of the cell, replaces the existing air within the soil pore spaces. In addition, CO_2 is more soluble than air, and so dissolves in the permeant water during infiltration (Fischer et al., 1999). The CO_2 supply was

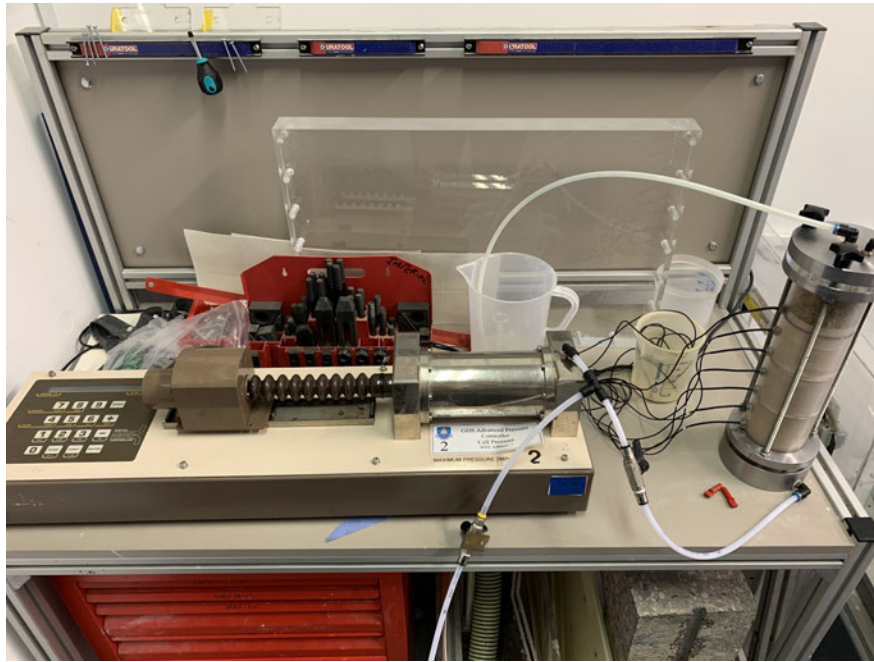


Figure 3.16: GDS advanced pressure controller used to saturate the sample

applied to the bottom valve of the cell and adjusted so that a steady flow of small bubbles was seen from the pipe that was connected to the top of the cell and submerged in a beaker of water. The sample was purged with CO_2 for 20 minutes. During this time, a supply of water was deaired using the nitrogen purging method, which is discussed in more detail in Section 4.4. Once all of the air in the specimen was replaced by CO_2 , the cell was connected to a GDS advanced pressure control cell filled with the deaired water (Figure 3.16). The specimen was saturated with upwards flow at a rate of 100 ms/mm^3 for 24 hours.

3.5 TEST PROCEDURE

3.5.1 Centrifuge tests

To prepare the payload for the start of a centrifuge test, several steps were taken. The water supply tank was filled with water, deaired using the nitrogen purging method, and then sealed. This water was then used to fill the upstream CHT. The downstream CHT actuator was returned to its top position so that the two water levels were in line. The permeameater cell was loaded into the

centre of the payload and secured with a bracket. The sensors were plugged in and the signals from the PPTs and cameras were checked from the control room. The cell was connected hydraulically to the two level CHTs and the GoPro trained on the specimen was set taking images just before closing the centrifuge door.

Once the preflight checks were complete, the centrifuge was accelerated to the desired g-level in increments of 10-g. Each increment was held for at least 30 seconds to ensure the sensor readings were level and there were no issues with any of the apparatus in the increased gravity. The specimen was left under hydrostatic conditions (no flow) for a few minutes once the desired g-level was reached to get a baseline hydrostatic pressure profile. To begin the test, the downstream CHT was lowered by one increment (size dependant on the g-level of the test) and flow through the sample commenced. Each increment was held for the desired length of time (between 120 and 600 seconds depending on the g-level) and then the downstream CHT was lowered again. To account for the increasing flow rate through the sample whilst maintaining a constant applied head, the pressure controlling flow from the supply tank to the upstream CHT was monitored and increased based on the webcam feed of the CHT piezometer.

The testing stage ended when the outlet tank filled with effluent water. The centrifuge was then spun down, whilst maintaining the height difference between the two CHTs. The outlet tank was emptied and potentially switched to the larger vessel. In some cases the supply tank also needed to be refilled, deaired and resealed. The same testing procedure was then repeated for the following stage. Tests had between two and four stages and ended when the desired head difference across the sample had been reached. Section 3.8 gives a full summary of the tests undertaken.

3.5.2 *Test conducted at 1-g*

Several changes had to be made to the permeameter cell to undertake test *T1LCH*, a 1-g test subjecting the specimen to a constant applied head. The PPTs in the topmost, middle and bottommost positions were removed and replaced with piezometer connections (Figure 3.17), meaning the sample can be considered as two stacked layers. In all other ways the sample was prepared

as for the centrifuge tests. The centrifuge tests lasted for between 60 and 175 minutes, whereas the 1-g tests were conducted continuously over a period of five days.



Figure 3.17: Permeameter cell measurement points modified for 1-g constant head test

The 1-g constant head apparatus is shown in Figure 3.18. The upstream CHT is connected to a winch system, allowing it to be raised to increase the head difference between it and the stationary downstream CHT on the left of the image, increasing the head difference applied to the specimen. This represents a change from the centrifuge tests, where the applied head was controlled by lowering the downstream CHT and keeping the upstream CHT fixed. In both cases, a downwards flow condition is achieved within the sample. Due to the constant water supply needed, tap water rather than deaired water was used. This is in line with the standard constant head permeability test outlined by Head (1982). The downstream CHT overflows into a beaker on a mass balance. A GoPro is set to photograph the scale reading every 60 seconds to capture the flow rate. A separate camera is trained on the three piezometer tubes and takes pictures of the levels at intervals of between 10 seconds and 5 minutes - the photography rate was reduced after the first few hours as PPT levels were not fluctuating significantly. These images were post-processed to find the temporally changing sample permeability.

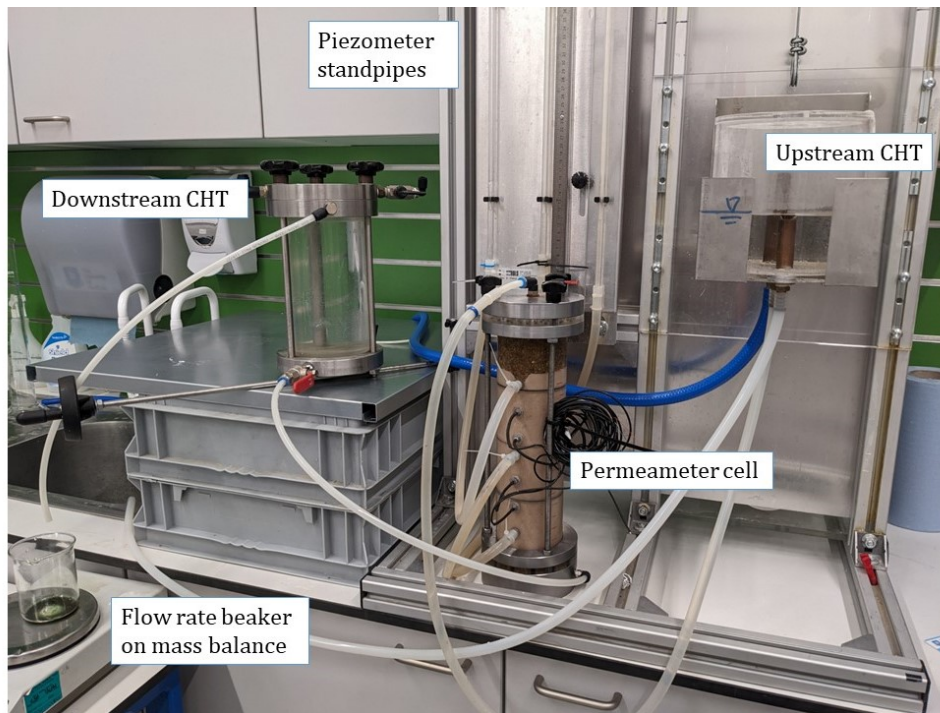


Figure 3.18: 1-g constant applied head test configuration

After leaving the sample for one hour under a hydrostatic head condition to allow the piezometers to equilibrate, the hydraulic gradient across the sample was increased to $i = 0.05$ and maintained for two hours. This low hydraulic gradient is well below the hydraulic conditions needed to initiate fines migration in the soil and allows the pre-erosion permeability of the specimen to be obtained. This is discussed further in Section 4.3. The constant head difference applied to the specimen was then increased to 100 mm and maintained for 120 hours (5 days). This corresponds to a hydraulic gradient of 0.41, or an energy gradient of 4.0 kPa/m. After testing, the sample was dissected to analyse the ultimate spatial distribution of the fine particles, in the same manner as the dissected centrifuge test specimens.

3.6 POST-TEST DISSECTION

In order to find the final spatial distribution of the fine particles after testing, the sample had to be dissected and the particle size distribution analysed. After testing, the test cell was dismantled and the specimen was dissected into two layers per acrylic stacking section of the cell. Because of the joints between the stacking sections, the dissected layers did not exactly line up with

the layers used in the experimental tests, which were dictated by the PPT port locations. Figure 3.19 shows the relative position of these layers to each other.

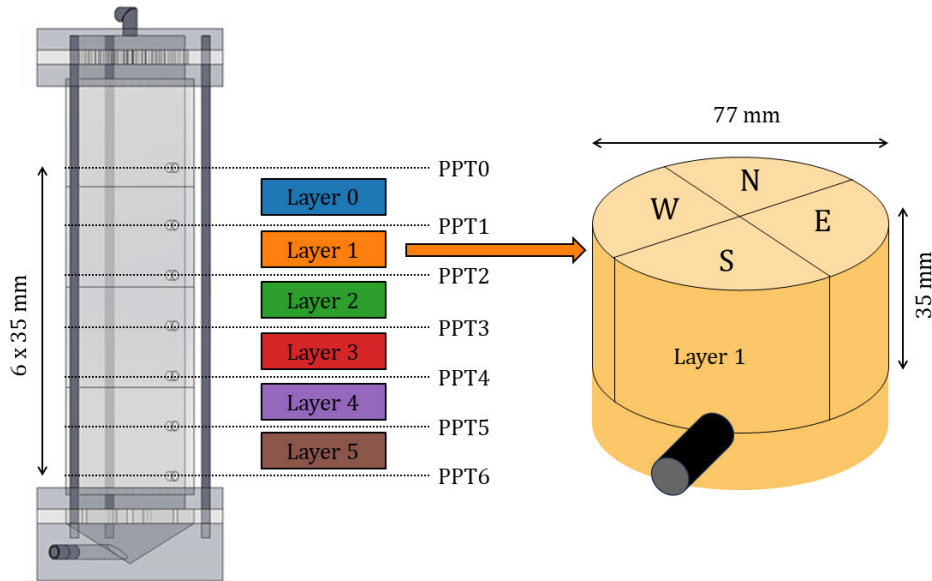
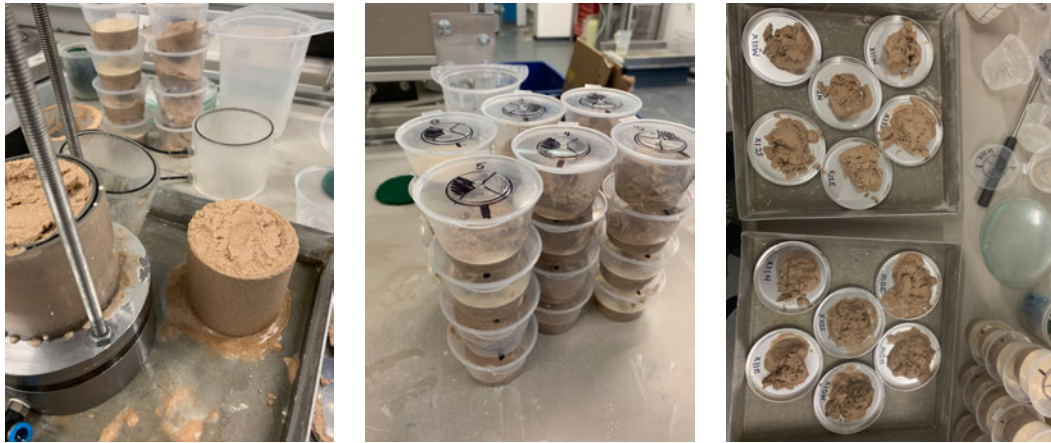


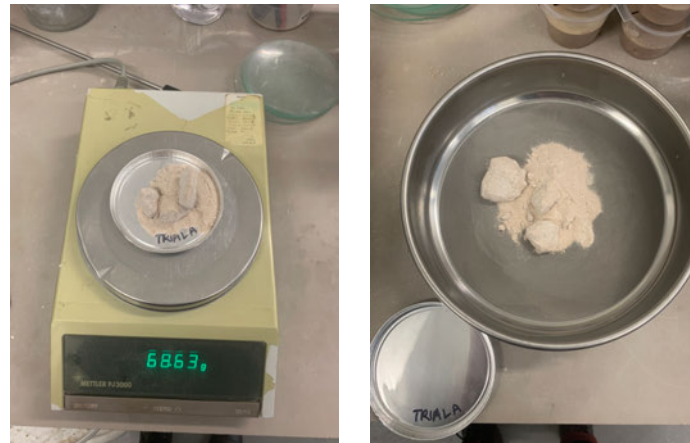
Figure 3.19: Layers of the sample for both specimen dissection and interstitial permeability measurements compared to PPT locations, with the cardinal directions used to define quadrants indicated

Once each layer was separated, it was divided into quadrants and stored in sealed containers for particle size analysis. This allowed an assessment of the cross-sectional variability in fine particle distribution. This is something that has been highlighted in studies such as Nguyen et al. (2019), and is in contrast to the typical assumption of homogeneity perpendicular to the seepage flow direction. Each quadrant was identified by a cardinal direction and the PPT port was always located in the South quadrant. This is also shown in Figure 3.19.

Several methods were considered for quantifying the particle size distribution, including the laser diffusion particle size analyser (Mastersizer 3000) used to initially characterise the soils tested. However, due to the small capacity of the Mastersizer this method gave a particle size distribution that was not representative of the whole dissected portion of the specimen. As only the final fine particle content, rather than the whole particle size distribution was needed to characterise the change in the soil, a sieving approach was used. The key steps of this are shown in the images in Figure 3.20.



(a) Section of tested sample removed from permeameter (b) Dissected into quadrants and stored for analysis (c) Layer quadrants are oven dried for 24 hours at 105°C



(d) Sample mass is recorded (e) Each sample is washed through 90µm sieve

Figure 3.20: Photographs of the sample dissection process

Each sample was oven dried for 12 hours and then weighed on a mass balance with a resolution of ± 0.01 g. The sample was then transferred to a 90 μm woven wire sieve and wet sieved to remove all of the fine particles. The sample was then oven dried again, and the final mass of just coarse particles taken. To ensure this method gave an accurate representation of the fines particles, test mixes of different fines content were prepared and then analysed, the results of which are given in Section 4.5.

3.7 DATA INTERPRETATION

To convert from the raw PPT signals logged during centrifuge testing to the permeability results presented in Chapters 5 and 6, several steps of data processing and interpretation needed to be made. The signals recorded during centrifuge testing came from the seven PPTs located in the cell, and the two PPTs in the inlet CHT and outlet effluent tank respectively. The first step of data processing was to pass the signals through a zero-phase second-order Butterworth filter with a critical frequency of 800 Hz to remove the high frequency electrical noise observed in the signals, suspected to be caused by the motor for the linear actuator.

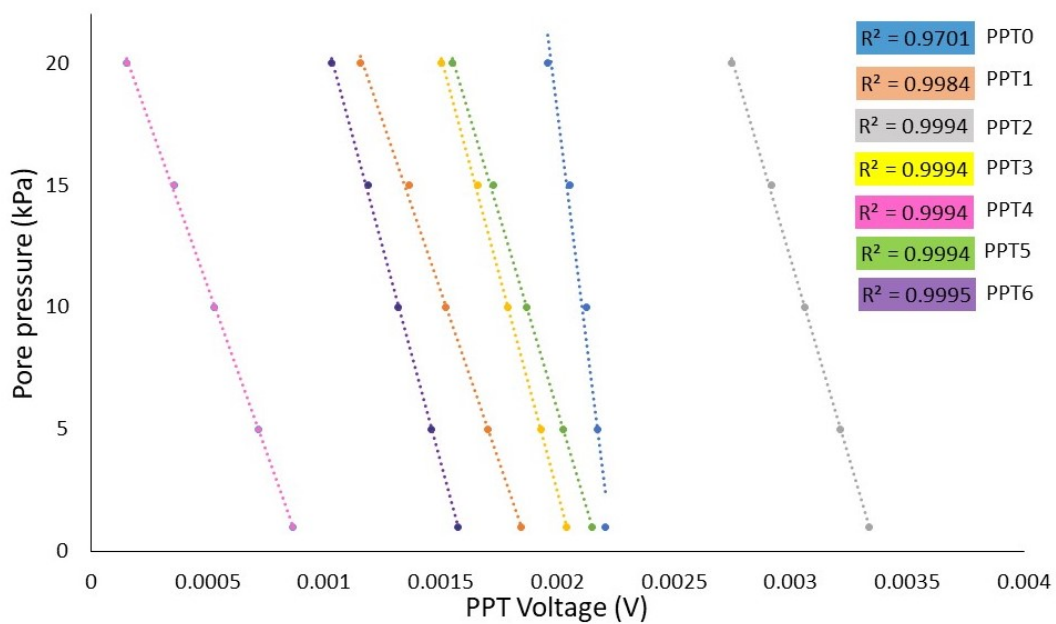


Figure 3.21: Calibration graph for PPTs located within the permeameter cell

The initial sampling rate was excessively high, at 1600 Hz, for the several hour-duration tests, which led to large file sizes that were unwieldy to work with. This sampling frequency was a result of a Labview idiosyncrasy that proved impractical to address within the time frame of the experimental programme, and the decision was made to reduce this rate post-testing. To do this, five data points were averaged into one for each signal, reducing the file size to one fifth of the original, whilst still keeping a high data frequency of 320 Hz. At this stage, the PPT calibration factors were applied to the raw voltage signals to convert them into pore pressures. These calibration factors are shown in Figure 3.21 and were obtained by submerging the PPTs under a

known water head and spinning them to g-levels between 5 and 40 to find the voltage outputs for a range of fluid pressures.

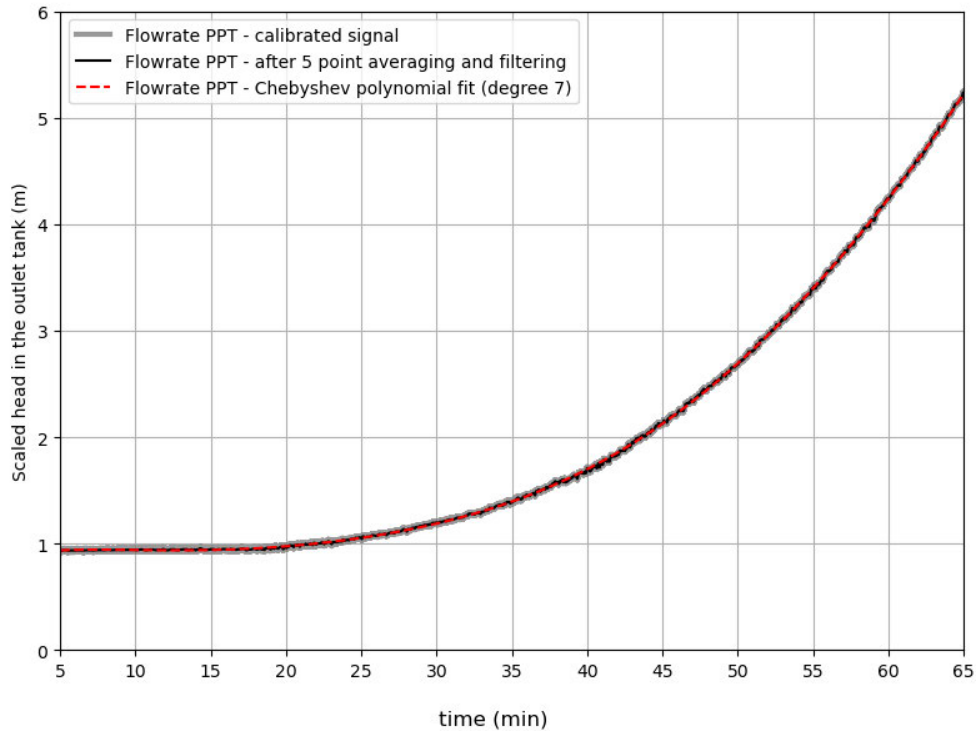


Figure 3.22: Example of post-processing of the outlet tank PPT data and Chebyshev polynomial fit for Stage 1 of *T40L2.5* used to calculate the flowrate through the specimen during testing

The flow velocity was calculated from the PPT located in the outflow tank. After the initial filtering and five point averaging of the signal, a Chebyshev polynomial was fitted to the PPT data, as shown in Figure 3.22. This smoothing polynomial was chosen because the filtered data was still somewhat noisy due to the waves on the surface of the outflow tank, caused by the wind in the centrifuge. A lid was added to the tank to mitigate the wave effect, but openings for the pipes and PPT meant its influence was not fully removed. The volumetric flow rate was calculated from this smooth curve by considering the change in head in the outlet tank over eight data points. This head change was multiplied by the outlet tank cross-section. The seepage velocity through the sample was found by dividing the flow rate by the specimen cross-section.

The applied head difference was known over the course of the test because the times at which the outlet CHT was lowered were recorded. Whilst effort was taken to maintain the constant head in the inlet CHT, it occasionally fluctuated due to the manual controls. These fluctuations were recorded by

the PPT in the base of the inlet CHT. These fluctuations were observed to influence the PPT at the top of the sample most significantly, whilst the PPT at the base was mostly unaffected, with the soil attenuating the variations. The decision was taken to mitigate the fluctuations in PPTs due to the varying head in the inlet CHT because it gave variations in permeability that were not due to internal erosion. This was done by calculating the residual sum of squares of the inlet CHT PPT signal from the target value at each point in time. This residual signal was subtracted from each of the PPT signals in proportion to their distance from the top of the sample.

The pore pressure signals from the PPTs in the permeameter cell were added to their elevation pressure calculated using Equation 2.8 to find the total pressure head. This equation accounts for the error due variation in g -level across the height of the model, as discussed in Section 2.3.3. At the start of the test, the sample was under hydrostatic conditions, and so the total head at each PPT port should be equal. To eliminate the drift in PPT readings, the average total head for each PPT over the hydrostatic interval was calculated, and the PPT signals were adjusted slightly to meet this value.

The pore pressure at each PPT port and flow velocity in time was then used to calculate the energy gradient across each layer of the specimen, by considering the pressure difference between adjacent PPTs using Equation 2.8. This was used to calculate the $1-g$ permeability using Equation 2.6 from Thusyanthan and Madabhushi (2003). The hydraulic gradient across each layer, which is used to compare the results of this study to previous studies reported in the literature in Chapter 7, was calculated by dividing the measured pressure difference across the layer by the scaled layer height. The same methods were used to find the energy gradient and permeability of the whole specimen, this time considering the pressure loss between the topmost and bottommost PPTs within the sample.

The total stress profile within the specimen can be calculated from the known depth from the overburden surface, taking into account the variation in g -level across the specimen's height (Section 2.3.3). The effective stress profile can then be found by subtracting the pore pressure measured at each PPT port. The effective stress at the midpoint of a layer is calculated by taking the average of the values at the PPT ports above and below. There is only a small variation in g -level over this 35 mm radial model distance, and so this effect is ignored for this calculation.

For this experimental programme, no correction was made for the horizontal variation in g in the model (Equation 2.10) when undertaking calculations. The error from the centreline to the most extreme measurement point - the flow rate PPT, was 1.1%, which was not considered to significantly impact the results. In addition, the cell was placed almost directly on the centre line, with the upstream and downstream CHTs located almost equidistant either side, removing this horizontal error from head difference calculations.

The final data interpretation was the energy expended by the seepage flow over the course of each test. The instantaneous power of the seepage flow can be calculated using Equation 2.22 with the previously calculated flow rate and pressure difference applied to the sample. The expended energy, E_{exp} , is the cumulative sum of the instantaneous seepage flow power over the test duration (Equation 2.23).

In a typical centrifuge modelling-of-models approach, the soil height is a continuum parameter and is scaled by a factor of N (Table 2.1). Previous studies at 1-g have considered the seepage path length of a permeameter specimen to be equal to the specimen height. In the results chapters of this thesis, both the model-scale and prototype-scale specimen height (corrected for the varying g -field) have been reported. The prototype height is used as the seepage path length in the hydromechanical analysis in Section 7.1). The implications of the seepage path length parameter at the particle-scale are discussed in Section 7.2.2 and a standardisation of the parameter is proposed to allow direct comparison of the spatial development of suffusion between different testing apparatuses.

3.8 EXPERIMENTAL PROGRAMME

In total, eight downwards flow permeameter tests were undertaken for this study, four at 40-g and four at lower g -levels. Out of these, seven tests used the centrifuge configuration detailed in Section 3.3 and one was conducted using the permeameter cell modified for 1-g testing, shown in Section 3.5.2. Table 3.2 gives a comprehensive overview of the tests in this study and their respective test conditions. Five of the tests, including the one conducted at 1-g, were dissected and had their final spatial fines distribution analysed.

Table 3.2: Summary of the key parameters of each test in the permeameter testing programme

Test	N	$\Delta z_{M/P}$ (m)	Duration (mins)	δh (mm)	$i_{app,max}$	$EG_{app,max}$ (kPa/m)	E_{exp} (J)	Dissected
T40L2.5	40	0.21/7.85	105	2.5	0.47	195.6	206.5	✓
T40L2.5(R)40		0.21/7.85	119	2.5	0.57	236.5	285.8	
T40S2.5	40	0.105/4.01	116	2.5	1.07	446.2	480.7	✓
T40LCH	40	0.21/7.85	172	-	0.39	161.5	414.3	✓
T30L2.5/5	30	0.21/5.93	67	2.5/5	0.49	151.1	55.2	✓
T20L5	20	0.175/3.37	58	5	0.66	138.8	34.6	
T10L10	10	0.21/1.96	146	10	0.60	61.6	15.1	
T1LCH	1	0.21/-	7200	-	0.41	4.0	0.015	✓

3.8.1 Naming convention

To ensure easy identification of key testing parameters, a consistent naming convention has been implemented for the permeameter tests. Each test name consists of three segments, for example test $T_{40}S_{2.5}$ or test T_1LCH . The first block, T_{40} , refers to the experimental g-level, varying between 1 and 40. The second segment refers to the specimen length at model scale, being either L for a full-length sample (≈ 210 mm), or S for a half-height specimen (105 mm). The final segment indicates the hydraulic loading regime for the sample. This can either be a number, 2.5 in $T_{40}S_{2.5}$, or CH , as in T_1LCH . When a number is used, it refers to the distance in millimetres that the outlet constant head tank is lowered for each interval of the multi-stage seepage flow test, δh . Alternatively, CH indicates that a constant head difference was applied to the specimen for the duration of the test.

3.8.2 Modelling-of-models

The modelling-of-models concept in centrifuge testing is introduced in this thesis in Section 2.3.1, and is a technique implemented to explore the influence

of potentially conflicting factors on a geotechnical phenomenon by utilising the scaling laws of the centrifuge. In this study, three modelling-of-models approaches are used to explore the influence of different parameters on the suffusion process.

T_{40L2.5}, T_{30L2.5/5}, T_{20L5} and T_{10L10}

In this study, a set of four tests, *T_{40L2.5}*, *T_{30L2.5/5}*, *T_{20L5}*, and *T_{10L10}*, were conducted at *g*-levels ranging between 10- and 40-*g* on identically prepared specimens. The primary aim of this suite of tests is to explore the hydromechanical framework first introduced by Moffat (2005) and most recently updated by Li and Fannin (2022) as detailed in Section 2.5.2. This set of model tests does not follow the standard modelling-of-models approach in which the model parameters are controlled to create the same prototype at scale, instead employing a testing approach similar to Ovalle-Villamil and Sasanakul (2020) or Marot et al. (2012), where specimens with the same model configurations are tested at different *g*-levels to recreate a range of effective stress conditions and hydraulic loading patterns.

The increments in applied head difference between the CHTs controlling flow for these four tests were designed to apply approximately the same increments of flow velocity in the early stages of testing, with the increment being 2.5 mm at 40-*g*, increasing to 10 mm at 10-*g*. This results in the increment energy gradient applied to the specimen increasing with *g*-level. The energy expended by the seepage flow also increases with the centrifuge acceleration. The scaled seepage path length increases with *g*-level, despite the specimens having the same model length, allowing prototype seepage path lengths between 1.96 and 7.85 m to be tested in the same permeameter, whilst in other studies, multiple apparatuses must be used (Li, 2008; Zhong et al., 2018).

The comparison of these four tests facilitates an understanding of the progression of suffusion within the specimens after initial fines migration was observed. The work of Moffat (2005) and Li (2008) terminated the tests once the onset of suffusion occurred. In the centrifuge study of Marot et al. (2012), the external suffusion of the specimen was identified by fine particles collected in the effluent, and significant reductions in specimen permeability were observed, but it was not possible to observe the variation across the specimen length. This spatial variation can be examined by considering the interstitial

soil layers within the centrifuge apparatus developed as part of the current study.

T_{40S2.5} and T_{20L5}

This pair of tests, *T_{40S2.5}* and *T_{20L5}*, follow the traditional modelling-of-models approach, where two models are prepared to represent the sample prototype conditions. Both tests were subjected to the same incremental increase in hydraulic gradient, as this is the approach typically taken in 1-g multi-stage permeameter tests. Due to the different g-levels, this resulted in different applied energy gradients (Section 2.3.2). The effective stress gradients across the specimens are almost identical. From a macroscale perspective, these two specimens should be bounded by the same hydromechanical envelope (Li and Fannin, 2022) and therefore exhibit the same suffusion behaviour. By comparing the spatial and temporal variation in permeability between these two tests, this approach for modelling suffusion can be interrogated in this study.

T_{40LCH} and T_{1LCH}

By conducting two constant head tests, one at 40-g and one at 1-g outside of the centrifuge environment, on identically prepared specimens, the influence of expended energy on the outcome of suffusion can be explored. The enhanced-g of the centrifuge means that orders of magnitude more energy can be imparted on the specimen, whilst maintaining the ratio between seepage flow velocity and particle settlement velocity, which both scale with gravity. The influence of effective stress can also be examined at extreme limits, as the effective stress at the midpoint of the specimen in the centrifuge is 40 times that at the midpoint of the 1-g test. Using a constant head, rather than a multi-stage, hydraulic loading regime means that the assumption that suffusion is occurring can be made, allowing the spatial and temporal progression of suffusion to be considered in isolation.

3.8.3 Other comparative tests

T_{40L2.5} and T_{20L5}

Tests *T_{40L2.5}* and *T_{40L2.5(R)}* are designed in this study to be a repeat of each other, with the specimens prepared identically and subjected to the same hydraulic loading and effective stress gradient in the centrifuge environment. Comparing these tests gives an understanding of the repeatability of testing in the commissioned centrifuge permeameter. Examination of the local permeability development within the two specimens over the duration of the test is used to explore how minor local variations in soil structure introduced during the specimen preparation stage can influence the progression of suffusion within the soil. By making this comparison, a link between the macroscale and microscale behaviour of the soil can be made, as discussed in Section 2.7.3.

T_{40L2.5} and T_{40LCH}

As identified in Section 2.6.1 of the literature review, the type of loading regime chosen for permeameter testing can influence the progression of suffusion within a sample, with Rochim et al. (2017) observing greater fines lost in a multi-stage seepage test in comparison to a test with constant applied head difference. In contrast, Lee et al. (2021) saw more fines lost under a constant head compared to a multi-stage regime. Luo et al. (2013) cites the difference in observed responses to multi-stage versus constant head as due to the build up of regions of clogged particles, based on visual observation after testing.

In this study, the influence of the hydraulic loading regime on the local permeability response of the soil and post-test fine particle distribution is examined in the comparison of two tests, *T_{40L2.5}* and *T_{40LCH}*. These specimens were prepared identically and tested at 40-g under a multi-stage and constant applied head regime respectively. Due to the centrifuge acceleration, a significant amount of energy can be expended by the seepage flow in only a couple of hours with constant permeability monitoring, a limitation of the previous studies, which had durations up to 8 days.

Previous studies only considered the changing permeability of the whole specimen over the course of the test, whereas the interstitial PPTs in this apparatus facilitate an understanding of the temporal internal fines migration.

The particle size distributions from the dissected specimens of these two tests will be analysed to assess the final distribution of fine particles, and understand the connection between the PPT readings during testing and the final structure of the specimens.

T_{40L2.5} and T_{40S2.5}

These two tests were designed so that the stress profile in the half height sample *T_{40S2.5}* is the same as the top layers of test *T_{40L2.5}*, but the shorter sample does not have all the layers of specimen underneath. This allows the influence of the exit boundary conditions to be examined. In addition, the influence of the seepath length can be examined, not by using the macroscale assumptions of modelling-of-models, but instead considering it relative to the size of the granular particles. The results of this study can be compared directly to those of Marot et al. (2012), which found that the hydraulic gradient needed to externally erode fine particles decreased with decreasing model seepage path length. The current study also has the benefit of pore pressure readings along the seepage path, that allow the earlier internal migration of fine particles to be observed at the mesoscale.

3.9 SUMMARY

This chapter details the materials and methods used in the experimental testing programme of this study. The development of a bespoke rigid-walled permeameter for centrifuge testing is detailed, alongside the procedure for sample preparation within the apparatus. The test procedure for the centrifuge tests is presented, and details are given on the modifications made to undertake a 1-g suffusion test in the same permeameter. The method for post-test dissection of specimens, used in this study to obtain the ultimate fines distribution, is also given.

The material chosen is a gap-graded, under-filled silt/sand mixture that is classified as unstable by the most common geometric instability criteria. Hydraulic conditions during testing were chosen to capture the early onset of suffusion and assess the progression of suffusion within a specimen subjected to hydraulic conditions that are similar to those occurring in existing water-retaining structures, such as dams and levees.

The testing programme of this study involves a total of eight suffusion tests, seven in the centrifuge, and one conducted at 1-g. The testing programme presented in this chapter gives a description of the three modelling-of-models comparisons that can be made between these tests, as well as three comparisons that evaluate the impact of hydraulic loading history, specimen length and initial heterogeneity on the suffusion process.

VALIDATION OF EXPERIMENTAL METHODS

4.1 INTRODUCTION

Before starting the suite of centrifuge permeameter tests, the methods used for experimental design and analysis had to be validated to ensure their suitability for use in the context of this project. This chapter is dedicated to presenting the outcomes of these initial tests.

Whilst the majority of the results in this section are included to verify the experimental methods used when these are non-standard for permeameter testing, this chapter begins with examining whether the assumption of laminar flow needed for Darcy's law (Equation 2.2 in Section 2.5.1) was valid within the enhanced-g environment of the centrifuge. In addition, the theoretical Kozeny-Carman permeability of the soil based on its particle size distribution is presented and compared to the permeability of the soil measured at 1-g before any internal erosion had begun.

Section 4.4 examines the nitrogen purging method used to prepare the deaired water prior to sample saturation and centrifuge testing. This method is commonly used in hydrogeology studies (Butler et al., 1994), but is not typically used in geotechnical testing. The final two sections on this chapter focus on the method for post-test dissection and particle size analysis of the specimens. Section 4.5 demonstrates that the wet-sieving methodology described in Section 3.6 accurately captures the fine particle content of a sample and Section 4.6 establishes that the assumption of homogeneity in particle size distribution of the pre-test specimen is a reasonable one to make.

4.2 DARCY'S LAW ASSUMPTION

The flow within the pore structure of a granular material is complex and cannot easily be visualised within a real soil specimen. To account for this,

macroscopic assumptions are made about the fluid flow regime within the pores. As internal erosion is often discussed in terms of hydraulic gradients, Darcy's law (presented in Equation 2.2) is used to find the permeability from a head loss between two points along the seepage path. One of the key assumptions made is that the fluid flow is laminar at the macroscale.

Typically in internal erosion testing it is safe to say that the flow is laminar, as flow rates are controlled and easily measured throughout testing. Within the centrifuge environment however, the fluid velocity scales with the acceleration (Garnier et al., 2007) and so it is important to check if it is still within the "creeping flow" regime with a Reynolds number, R_e , below 1 (Khalifa et al., 2000).

The Reynold's number for flow within a soil can be calculated using Equation 4.1 and is a function of the soil's pore constriction size, represented by the median grain diameter, D_{50} .

$$R_e = \frac{\rho_w D_{50} v}{\mu} \quad (4.1)$$

where ρ_w is the density of water, v is the velocity of the water, and μ is the water viscosity.

For the soil described in Section 3.2.2, the highest flow scenario, and therefore the most likely not to constitute laminar flow, would theoretically occur when all of the fine silt particles had been eroded. In this case the soil would consist purely of the coarse sand matrix, which has a $D_{50} = 162\mu m$. For a limiting $R_e \leq 1$, this would give a maximum fluid velocity, v_{max} , at which the laminar flow assumption is valid of $v_{max} = 7.1 \times 10^{-3} m/s$.

Throughout the centrifuge testing programme presented in this thesis, the maximum flow velocity through the permeameter occurred at the end of test $T40S2.5$. The flow velocity in this case was $8 \times 10^{-4} m/s$. As this value is almost nine times smaller than the limit v_{max} and has a corresponding $R_e = 0.13$, it is valid to assume that Darcy's law can be applied throughout this study.

4.3 PRE-EROSION PERMEABILITY OF THE SOIL

Soil permeability is a geotechnical property that depends not only on the soil material, but also its internal structure. To determine permeability, standard constant head permeameter tests are typically conducted on coarser grained soils whilst falling head tests are prescribed for finer materials such as silts (Head, 1982). Another approach to finding a soil's permeability is to take a theoretical approach based on the geometric properties, for example using the Kozeny-Carman equation, introduced in Section 2.4.3. In the following sections, the Kozeny-Carman permeability of the initial soil used in this study is calculated and then compared to the pre-erosion permeability found from the 1-g constant head permeameter test.

4.3.1 Kozeny-Carman permeability

The Carrier (2003) formulation of the Kozeny-Carman equation was previously given in Equation 2.14 in Section 2.4.3 of the literature review and is based on the curvature of the particle size distribution, along with several other parameters. These are namely; the shape of factor of the grains, SF , and the void ratio of the soil, e .

The latter of these, the void ratio, can easily be obtained from the relative density of the soil - in this case 70% - and the minimum and maximum void ratios measured in the density tests detailed in Section 3.2.4.

$$\begin{aligned} e_{rd=70\%} &= e_{max} - 0.7(e_{max} - e_{min}) \\ &= 0.887 - 0.7(0.887 - 0.352) \\ &= 0.513 \end{aligned} \tag{4.2}$$

The shape factor, SF , is a more subjective parameter. From the material description in Section 3.2.2, and in particular the microscope images of the soil in Figure 3.3, the soil used in this study can be characterised as having a sub-rounded grain shape. As discussed in Carrier (2003), Fair and Hatch suggested a shape factor between 6.1 for a "rounded" and 6.4 for a "worn" grain shape, whilst Loudon suggested using $SF = 6.6$ for "rounded" and $SF = 7.5$ for a "medium angularity" soil.

Taking a shape factor of 6.6, in the midst of these suggested factors, gives a Kozeny-Carman permeability of the un-eroded soil of $k_{K-C} = 4.70 \times 10^{-6} \text{ m/s}$. Using the minimum and maximum suggested shape factors of 6.1 and 7.5 varies this permeability between $3.64 \leq k_{kc} \leq 5.50 \times 10^{-6} \text{ m/s}$, a maximum variation from the chosen k_{kc} of 22.6%.

4.3.2 Pre-erosion experimental permeability

In order to explore the centrifuge test results presented in the following two chapters, it was important to obtain a typical value for experimental permeability before any fines migration could occur. In order to do this the first stage of the 1-g constant head permeameter test described in Section 3.5.2 was used. In this stage a very low hydraulic gradient of $i = 0.05$ was applied to the sample for two hours, well below the predicted critical hydraulic gradient of $i_{cr} = 2.57$ at the midpoint of the sample where $\sigma' = 1.48 \text{ kN/m}^2$ (using the method in Equation 2.20, from Li and Fannin, 2022). The average flow rate for the stage was calculated by recording the mass of water in the outflow beaker.

The soil specimen was prepared in an identical manner to the full length samples used in the centrifuge test. Rearranging Darcy's law (Equation 2.2), the permeability of the specimen was found from the flow rate Q , cross-sectional area of the specimen A , and the hydraulic gradient i (Equation 4.3).

$$k = \frac{Q/A}{i} \quad (4.3)$$

During the initial stage of the 1-g permeameter test, 45.54 ml of water flowed through the sample over the 7440 seconds of testing. This gave a pre-erosion permeability of the specimen of $2.63 \times 10^{-5} \text{ m/s}$. This value is approximately five larger than the theoretical Kozeny-Carman permeability of $4.70 \times 10^{-6} \text{ m/s}$ calculated in the previous section.

Although this variation seems quite large, it is in the same magnitude as the variation between the measured permeability and that which was predicted by the Kozeny-Carman equation for the sandy clayey silts in Pap and Mahler (2019). The study attributes this under-prediction of permeability to the presence of clay in the soil mix, but this constitutes less than 20% of the total soil mix, and the rest of the particle sizes are in the same range as those

used in this study. This suggests that the discrepancy between the measured and predicted values could be a function of the small particle size rather than clay cohesion, due to the heavier weighting on the fine particles in a long-tailed PSD using this method.

4.4 DEAIRING WATER USING NITROGEN PURGING

To ensure that entrained air does not affect the soil behaviour or sensor measurements during element testing, deaired water was used for both the specimen saturation and the seepage flow stages of permeameter testing. The standard method of removing entrained air for geotechnical testing is to use a combination of agitating the water and applying a vacuum to the container. For example, ASTM:D4253 (2015) suggests the use of tap water deaired by “forceful agitation ... attached to a vacuum source” for soils with a permeability $k \leq 1 \times 10^{-5} \text{ m/s}$. However, the volumes of water needed in this test and the practicality of transporting the treated water between the element testing and centrifuge laboratories made this method unfeasible. This led to investigation into alternative methods to remove entrained air from water.

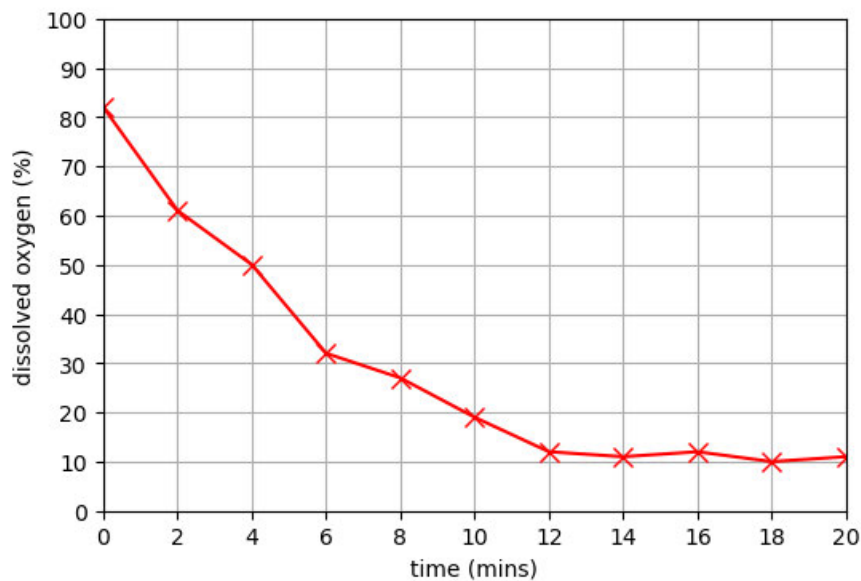


Figure 4.1: Dissolved oxygen content of 15 L of water over time during nitrogen purging

A comparative study by Butler et al. (1994) found that nitrogen purging was the quickest and most efficient of four popular deairing methods tested.

This method involves bubbling inert nitrogen gas through the water by means of a porous sintered stone placed at the base of a water vessel. Figure 4.1 shows the results of the nitrogen purging test undertaken for this study. The porous stone was placed at the base of a 15 L vessel and nitrogen was bubbled through the water for 20 minutes. After 12 minutes, the level of dissolved oxygen concentration reached 11% and did not reduce any further. For the centrifuge tests conducted in this study, nitrogen purging was undertaken for 20 minutes for both the water used for sample saturation and the water that was loaded into the payload reservoir and used for permeameter testing.

4.5 VALIDATING SPATIAL FINE PARTICLE CONTENT MEASUREMENT

As discussed in the previous chapter, a dissection and sieving approach was adopted to find the spatial distribution of fine particles in the specimens at the end of a selection of the permeameter tests. This approach has been used in several studies (Horikoshi and Takahashi, 2015; Ke and Takahashi, 2014b), although typically with larger grain sizes (0.008-5 mm for both studies). Consequently the sieving method had to be verified for the particle size distribution used in this study where the largest particle size is only 300 μm .

Five soil mixtures with between 18 and 22% fine particle content were prepared with 5% water content in the same manner as for an actual centrifuge test specimen. The dry mass of each sample was 100 g for ease of preparation and the masses were recorded to two decimal places. This is similar to the mass of each quadrant dissected from a sample, which varies between 30 and 120 g, but has an average value of 65 g. The samples were left in sealed bags for 12 hours to promote moisture homogeneity and replicate the specimen preparation stage as closely as possible.

After drying, wet sieving, and drying using the method described in Section 3.6, the measured fine particle content of each sample was recorded and is shown in Figure 4.2. There is a very good agreement between the prepared and measured fine particle content, with an $R^2 = 0.9965$, meaning that the method accurately captures the fine particle content of each dissected segment of a test specimen.

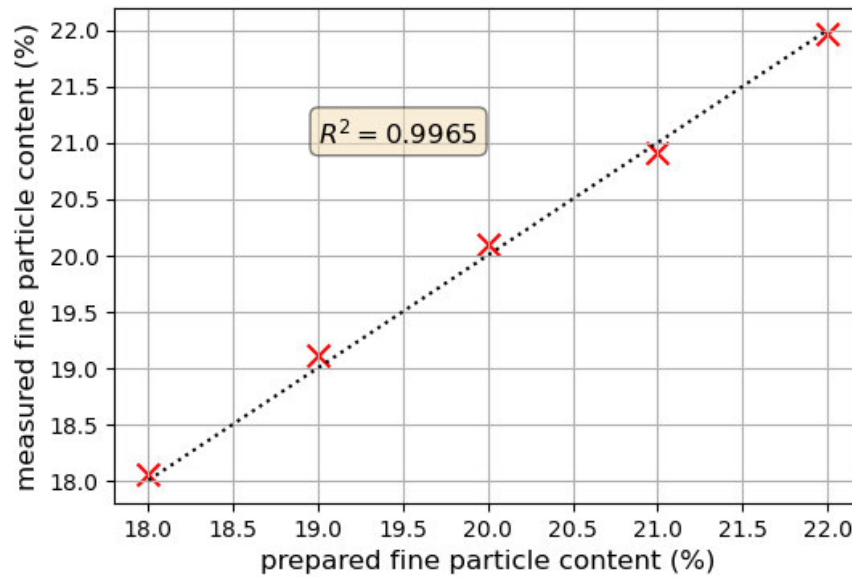


Figure 4.2: Wet sieving method applied to prepared test samples accurately captures the fine particle content of a 100g sample

4.6 INFLUENCE OF SATURATION STAGE OF HOMOGENEITY

Many suffusion studies assume that because the saturation of the sample is done at a much lower seepage flow rate than the erosion stage, there is no migration of fine particles at this time and the specimen begins testing with a homogeneous fine particle distribution. This is not verified by either destructive particle size analysis or non-invasive imaging methods.

One notable exception to this is the work of Nguyen et al. (2019). By analysing the X-ray CT scans of the specimen before and after saturation they showed that there was significant variation in fines content from the designed value along the length of the seepage path. The soil used was a gap-graded mixture with 25% fines content, but the horizontal profile shows that after saturation via upwards flow the top and bottom layers have lower fines contents, 17 and 18% respectively. Due to the timing of the X-ray scans, it cannot be said whether this heterogeneity occurred during specimen preparation stage or due to the influx of CO₂ and water into the sample, but at the start of erosion testing the sample is not fully uniform. It can be expected that a similar effect would have been observed in other studies, had the initial fines content been analysed.

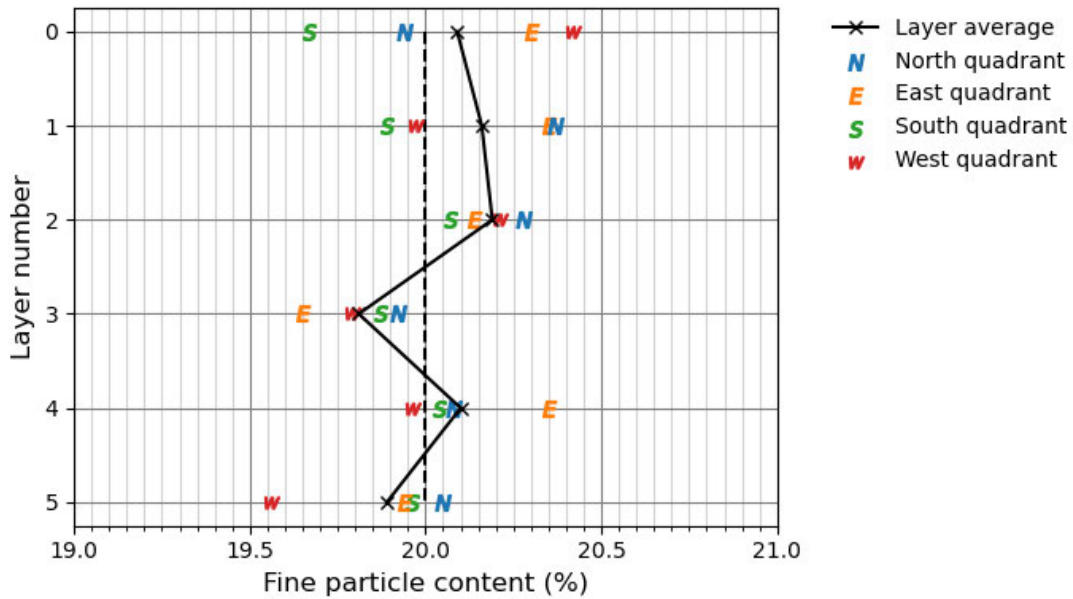


Figure 4.3: Post test spatial fine particle content for a saturated, untested sample

To ascertain the impact of the upward flow saturation stage on the spatial variability of fine particle content for this study, a permeameter specimen was prepared and saturated in an identical manner to the other tests. This specimen was then immediately dissected without performing any permeameter testing. The final fine particle content of each quadrant and the average for each layer is presented in Figure 4.3. As a reminder, the target fine particle content for the sample was 20%, indicated by the vertical dashed line.

For both this study, and the study by Nguyen et al. (2019) there was no analysis of the spatial variation of fine particles before saturation, so it cannot be said whether any heterogeneity is a product of the moist-tamping method or fine particle migration is instigated even by the slow encroaching upwards flow of the saturation stage. The work of Frost and Park (2003) shows, also through X-ray imaging, that the moist tamping method introducing variation of density across the prepared layers, even when under-compaction allowances are made.

The results presented in Figure 4.3 show that the greatest cross-sectional variation in fine particle content occurred in the uppermost layer (Layer 0), at the end of the saturation seepage flow path. Unlike the results in Nguyen et al. (2019), the top layer had an average fine particle content higher than the target value, although both the South and North quadrant fell below the target 20% value.

Both the central layers (Layers 2 and 3) show the lowest amount of variability between the quadrants, with all values being within 0.6% fines content of each other. However Layer 2 has an average fine particle content of 20.19%, higher than the target value, whilst Layer 3 has an average fine particle content of 19.81%.

From these results it can be seen that some short distance migration of fine particles between layers may be occurring during saturation, or alternatively these variations are introduced by the moist-tamping method. In either case, the effluent water from the saturating sample was clear and the average fine particle content for the whole specimen was 20.04%, showing that there was no global loss of fine particles before erosion testing began. It is reasonable to consider the specimens as homogeneous at the start of testing as experimental samples prepared in other studies.

4.7 SUMMARY

The first assumption verified in this chapter concerns the assumption of laminar fluid flow at the macroscale during testing. This is important for the permeability calculations, which are based on Darcy's law. By considering the highest flow and worst case erosion scenario, it is proven that the seepage flow can still be considered laminar, even in the enhanced-g environment.

1-g permeameter results under a very low hydraulic gradient presented in this chapter give an initial, un-eroded permeability of the soil as 2.63×10^{-5} m/s. This is found to be almost five times larger than the theoretical Kozeny-Carman permeability, calculated from the particle size distribution and void ratio of the sample.

Alongside these results, this chapter also validates several experimental methods used in this study, demonstrating their suitability. The approach of nitrogen purging to remove entrained oxygen from the water used for sample preparation and permeameter testing was shown to be effective, reducing the dissolved oxygen by 88% in 20 minutes. The method for dissecting and wet sieving small soil samples to find their fine particle content was assessed, finding very high agreement between the prepared and measured values.

The validity of the assumption of specimen homogeneity after the saturation stage was also challenged. Although the dissected, saturated sample showed

some spatial variation in fine particle content, this variation was smaller than that reported by other rigid-walled permeameter studies. It is likely in line with most experimental studies, where initial heterogeneity typically goes unmeasured, and consequently unreported.

TESTS CONDUCTED AT 40-G

5.1 INTRODUCTION

In this study, a total of four tests were performed at 40-g, providing the baseline for comparison with the tests undertaken at lower g-levels, discussed in Chapter 6. All tests were undertaken under downwards seepage flow and lasted between 105 and 172 minutes. Three of these tests were conducted under multi-stage seepage flow conditions, with the applied head difference increasing incrementally throughout the test. The final test, T_{40LCH} , had a constant applied head difference throughout the test. Table 5.1 summarises this suite of tests, whilst the centrifuge scaling links between these and the lower-g tests presented in Chapter 6 are discussed in Section 3.8 of the methodology.

Of the three multi-stage tests at 40-g, the first two tests presented, $T_{40L2.5}$ and $T_{40L2.5(R)}$, were prepared identically to each other using the full testing length of the permeameter (specimen height 210 mm). For both tests, each applied head difference interval was maintained for two minutes and the increase in applied head difference, δh , was 2.5 mm. $T_{40L2.5}$ comprised of three stages, with a maximum applied head difference of 120 mm and final energy gradient, $E_{app,max}$, of 195.6 kPa/m. $T_{40L2.5(R)}$ was undertaken in

Table 5.1: Summary of parameters for centrifuge permeameter tests at 40-g

Test	$\Delta z_{M/P}$ (m)	δh (mm)	h_{max} (mm)	$i_{app,max}$	$EG_{app,max}$ (kPa/m)	E_{exp} (J)	dissected
$T_{40L2.5}$	0.21/7.85	2.5	120	0.47	195.6	206.5	✓
$T_{40L2.5(R)}$	0.21/7.85	2.5	142.5	0.57	236.5	285.8	
$T_{40S2.5}$	0.105/4.01	2.5	142.5	1.07	446.2	480.7	✓
T_{40LCH}	0.21/7.85	-	100	0.39	161.5	414.3	✓

two longer stages, giving an $E_{app,max}$ of 236.5 kPa/m. Table 5.1 also gives the equivalent conventional hydraulic gradient, $i_{app,max}$, reached in each test (Section 2.3.2). $T_{40L2.5}(R)$ serves as a repeat of the $T_{40L2.5}$ test, but taken to a higher hydraulic loading to investigate whether there was further change in specimen permeability after the plateau in permeability observed in the first test.

The third test detailed in this section, $T_{40S2.5}$, followed the same hydraulic loading pattern as the previous two tests, but the sample was prepared with a shorter seepage path length, 105 mm compared to 210 mm. Although each increment of head difference is the same for all three tests at 2.5 mm, this corresponds to a larger change in applied energy gradient in $T_{40S2.5}$ due to the shorter seepage path length. The maximum applied energy gradient for this test was 446.2 kPa/m and it comprised of four stages, as higher flow rates through the shorter sample meant that the centrifuge had to be spun down to empty the outflow container more frequently.

Test $T_{40S2.5}$ was designed to have the same prototype conditions as $T_{20L2.5}$ described in the next chapter, utilising the centrifuge scaling principle of modelling-of-models. The benefit of this in investigating the initiation and progression of suffusion is explored in more depth in Section 3.8. This test also allows influence of seepage path length on the spatial development of suffusion erosion to be investigated via comparison with $T_{40L2.5}$ and $T_{40L2.5}(R)$. Li (2008) found that, when the seepage path increased, the critical hydraulic gradient for the specimen decreased (Section 2.5.2).

The fourth and final test described in this section, T_{40LCH} , differs from the others in terms of its hydraulic loading regime. In contrast to the multi-stage seepage flow of the previous tests, this test was conducted under a constant applied head difference of 100 mm, giving an applied energy gradient of 161.5 kPa/m. The test was conducted in two equal length stages, with a total test duration of 172 minutes, slightly longer than the multi-stage seepage flow tests. In other respects, the preparation and dimensions of the specimen are the same as $T_{40L2.5}$ and $T_{40L2.5}(R)$. The total energy expended by the seepage flow for this test was 414.3 J.

The centrifuge permeameter results of the four tests summarised above are presented in the following sections. Of these tests, three were dissected and had their ultimate spatial distribution of fine particles measured. The final

spatial fine particle content of tests $T_{40L2.5}$, $T_{40S2.5}$ and T_{40LCH} are presented alongside their centrifuge testing results.

5.1.1 *Defining a suffusion event*

In this study, a suffusion event is classified as a period of time in which a specimen layer increases in permeability, assumed to be due to the loss of fines, calculated by the pore pressure difference between adjacent PPT ports. Whilst, in theory, this is simple to define, the practicalities of isolating suffusion events from background noise in the constantly fluctuating permeability readings necessitated the creation of a set of criteria to identify these events. This also allows for easy comparison between the tests. The criteria to identify a suffusion event are as follows:

- The suffusion event must have a duration of longer than 120 seconds.
- Over the course of the event, the permeability must increase by a minimum of 1×10^{-6} m/s.
- Whilst slight decreases in permeability may occur during the event, these must not last more than 30 seconds and the permeability must not drop below the value at the start of the event.
- The suffusion event ends at the point before the permeability begins to decrease or plateau at a constant value for longer than 30 seconds.

These criteria do not quantify the rate of erosion and, as the results show, some suffusion events see the permeability increase by significantly more than the lower limit of 1×10^{-6} m/s. In other cases, the increase in permeability may have occurred gradually over tens of minutes. Both this Chapter and Chapter 6 deal only with identifying these events and their magnitude is discussed when comparing the test results in Chapters 7, 8 and 9.

5.1.2 *Interpreting results*

The results of the tests undertaken in this study, which are introduced in both this and the following chapter, will be presented in a series of graphs and tables accompanying the text. The order of the figures is consistent between

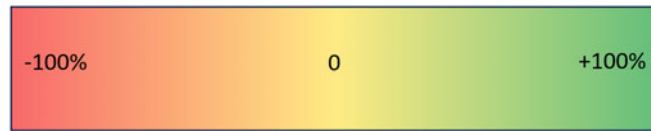
tests and a brief introduction in how to interpret these graphs is given here, in particular to allow the reader to appreciate where and when suffusion events have been identified during the centrifuge tests. The only test that deviates from this presentation is the test conducted at 1-g, for the reasons discussed in Section 6.5.

The first figure presented for each test shows the energy gradient applied to the specimen with time, as well as the cumulative expended energy of the seepage flow. Using the energy gradient rather than the hydraulic gradient is not typical for permeameter tests, but the reasoning of this choice is fully explained in Section 2.3.2. The loading increments of the tests and the final cumulative energy is also presented in the table of data accompanying each test.

The second figure presents the effective stress profile within the specimen at the start and end of the test. This was calculated from the known total stress distribution and the measured pore pressures at each PPT port (Section 3.7). This method takes into account the variation in g across the height of the specimen.

In the third figure, the global permeability of the sample with time is given. This has been calculated using the pressure difference between the topmost and bottommost PPT located within the specimen itself using the formulation of Thusyanthan and Madabhushi (2003) (Equation 2.6). In the full length samples this is typically PPT₀ and PPT₆, but where this differs for a test, this is made clear in the section introduction. The graph is divided into the separate testing stages, between two and four depending on the test. During the breaks between stages, the centrifuge was spun down, the outflow tank was emptied, and then the beam was accelerated back up to test g -level.

The final graph shows the permeability of each of the specimen layers with time and is accompanied by a timeline of suffusion events, as defined by the criteria in Section 5.1.1. The highlighted sections denote the duration of a suffusion event that occurred within a layer. These events are presented alongside the experimental results to show where they have come from, but are analysed in greater detail in later chapters. The magnitude of the suffusion event can be inferred from the event duration and associated permeability increase.



(a) Tables presenting the variation in permeability across the test



(b) Tables presenting the ultimate fines content in each quadrant

Figure 5.1: Colour scales used to aide interpretation and comparison of tables of results in Chapters 5 and 6

Alongside the figures, some of the test results are presented in colour-graded tables. All centrifuge tests are accompanied by a table that reports the net change in permeability of each layer, as well as the whole specimen, over each centrifuge testing stage. The net change in permeability is also reported in the final column. The colour in each cell has been included to emphasize the magnitude of the permeability changes and aide comparison between the results of related tests. The colour scale for this is shown in Figure 5.1a.

In tests which were dissected post-testing to obtain the final fines particle distribution, the results of this are presented in a second colour-graded table. In this case the final fines content values within the table is emphasized with a different colour scale, shown in Figure 5.1b, showing the variation from the initial 20% fine particle content.

5.2 T40L2.5

5.2.1 *Test description*

This test was conducted at 40-g and comprised of three stages. The specimen occupied the full six layers of the permeameter cell, giving a tested specimen height of 210 mm. This test was designed to be the comparison test, against which the influence of seepage path length and centrifuge scaling of seepage

velocity can be compared. Section 3.8 gives a full outline of how all of the permeameter tests can be compared.

Over the course of the test, the head difference across the sample was increased in 2.5 mm intervals until a final head difference of 120 mm was applied. This corresponds to a final energy gradient of 195.6 kPa/m. Figure 5.2 shows the incremental increase in applied energy gradient of the sample alongside the energy expended by the seepage flow. The applied head difference was kept the same between stages, when the centrifuge was temporarily spun down, to ascertain whether the relaxation of stresses caused a significant change in the permeability of the layers. The total cumulative energy expended by the seepage flow was 206.5 J. The test was dissected post testing and the ultimate distribution of fine particles is presented in Section 5.2.3.

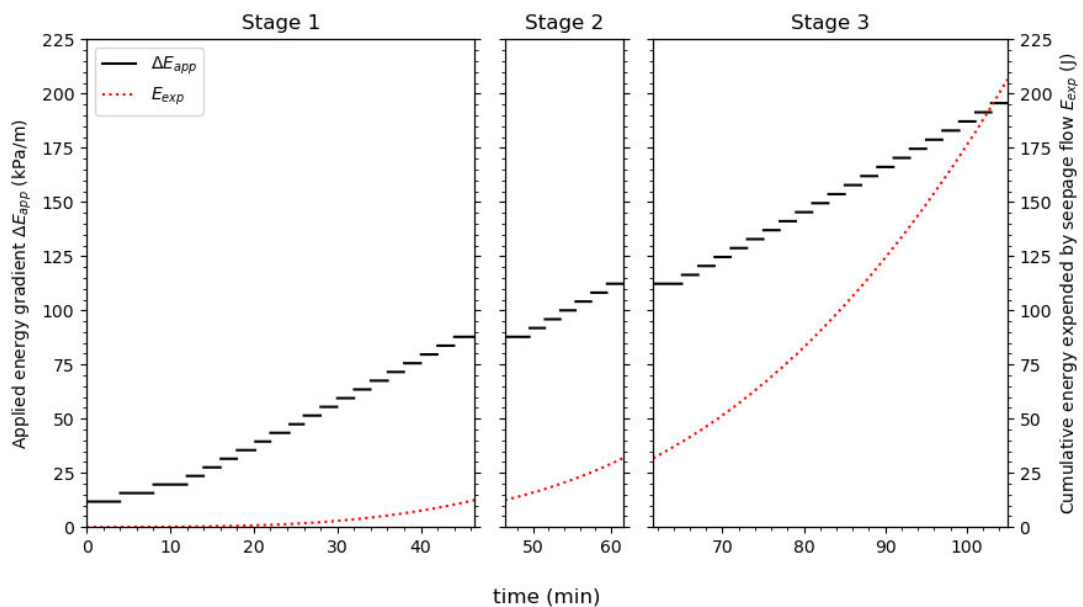


Figure 5.2: Energy gradient applied to *T40L2.5* and cumulative energy expended by the seepage flow over the 3 stages of testing

The effective stress profile within the permeameter cell both under the hydrostatic conditions at the start of the test, and at the end of testing, is shown in Figure 5.3, as calculated using the method in Section 3.7. The effective stress at the base of the cell (PPT6) increased from 199 kN/m to 242 kN/m over the duration of the test due to decreased pore pressure from the downwards seepage flow and due to internal fines migration.

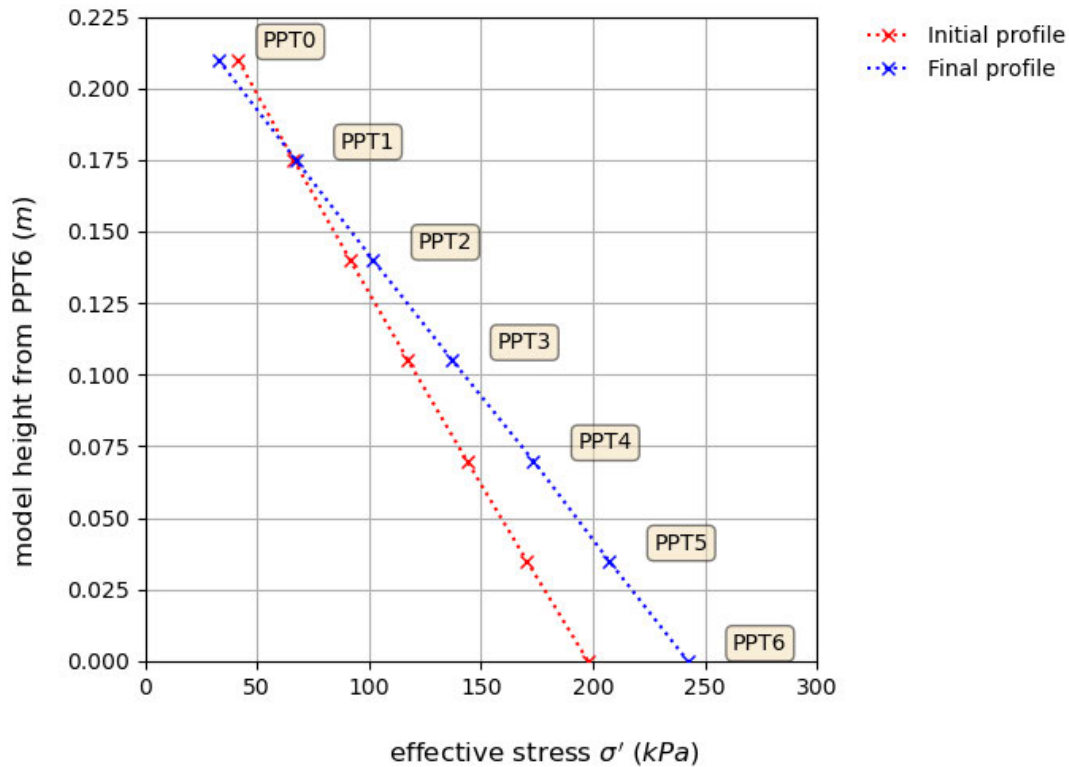


Figure 5.3: Effective stress profile in *T40L2.5* at the beginning and end of the centrifuge seepage flow test

5.2.2 Permeability response during centrifuge testing

Figure 5.4 shows the global permeability of the specimen, measured between the topmost and bottommost PPTs. During the first stage the specimen increased in permeability rapidly from 1.43×10^{-5} to 1.98×10^{-5} m/s in the first eight minutes of seepage flow. The global permeability then began to decrease, suggesting global clogging was occurring. From 23 minutes in until the end of the first stage, the permeability increased from 1.57×10^{-5} to 1.89×10^{-5} m/s, with only a short period of decreasing permeability between 32 and 36 minutes. The maximum whole sample permeability of 2.14×10^{-5} m/s occurred 77 minutes into testing at an applied energy gradient of 141 kPa/m.

After spinning up for the second stage, the specimen was not affected by the stress change, shown by the very similar permeability before and after the break, 1.89 and 1.92×10^{-5} m/s respectively (Table 5.2). This was not the case between Stages 2 and 3, where there was a marked increase in permeability from 1.81 to 2.10×10^{-5} m/s, suggesting the change in stress regime from

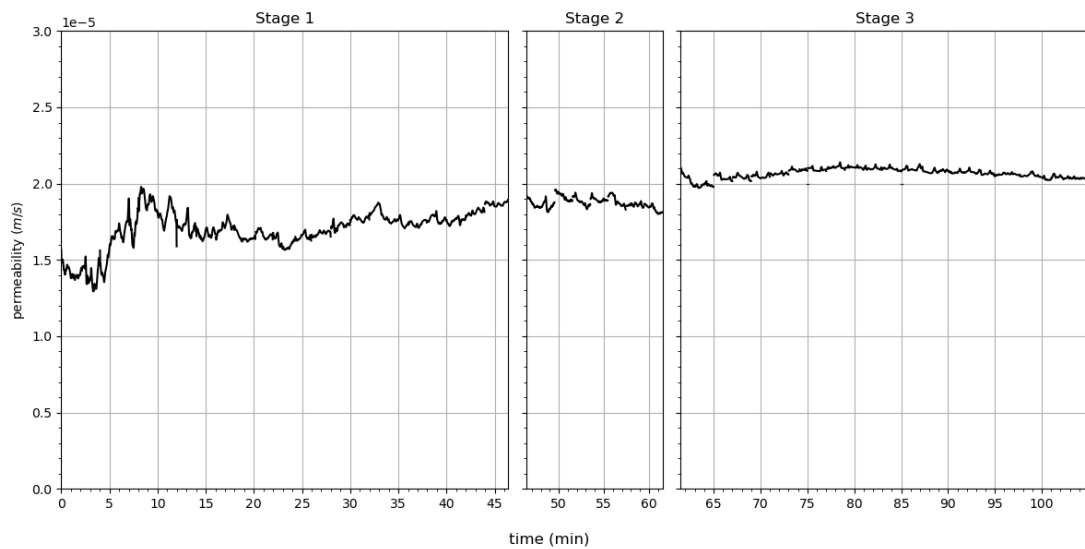


Figure 5.4: Global permeability of $T_{40L2.5}$

restarting the centrifuge released a significant number of trapped fine particles, and caused the permeability to increase.

Table 5.2: Variation in permeability for each layer of test $T_{40L2.5}$

Layer	Change in permeability (%)					
	During S1	S1 to S2	During S2	S2 to S3	During S3	Whole test
0	180.3	48.6	-49.3	31.8	-26.1	105.5
1	117.5	-16.6	22.1	8.5	-1.6	136.4
2	14.0	4.7	-16.6	27.7	-11.7	12.3
3	-35.3	14.1	5.0	12.2	9.6	-4.8
4	-37.9	6.9	-7.7	21.0	-1.7	-27.0
5	6.9	-22.5	11.2	1.2	15.6	7.9
Whole	32.3	1.4	-5.6	16.1	-3.4	42.1

During the second stage of the test, the whole sample permeability steadily decreased by 5.6% (Table 5.2). Over the third and final stage of testing the whole sample permeability behaviour altered again, initially increasing by 11.5% between minutes 63 and 77, and then decreasing to a final permeability of 2.03×10^{-5} m/s by the end of the test. The overall permeability of the sample increased by 42.1% across the course of the test.

Looking closer at the individual layers of the sample in Figure 5.5, it is clear that the internal behaviour of the specimen was more complex than the permeability reading across the whole sample suggests. Over the first stage, there was a significant amount of local permeability variation within all of the layers. The two layers at the beginning of the seepage path, Layers 0 and 1, showed an increase in permeability across the first stage of 180% and 117% respectively, whilst the lower layers showed a general decrease in permeability (Table 5.2). Over Stage 1, all layers alternated between increasing and decreasing permeability, with each suffusion event lasting anywhere between 2 and 20 minutes.

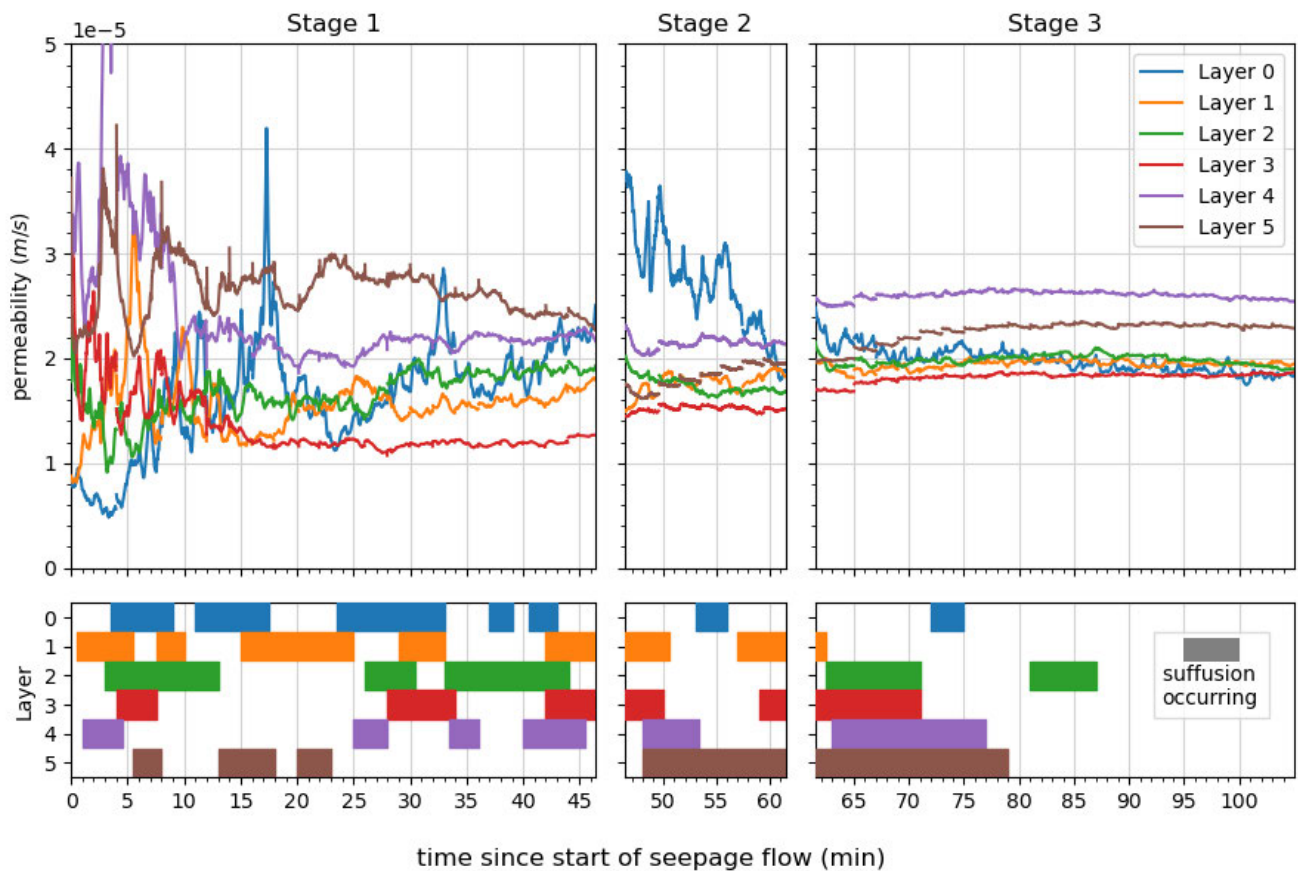


Figure 5.5: Permeability and timeline of suffusion events for each layer of *T40L2.5*

Although the global permeability of the sample decreased across Stage 2, Table 5.2 shows that only Layers 0, 2 and 4 experienced a decrease in permeability throughout the stage. The reduction in permeability by 49.3% in the top layer was much larger than any variation in the lower layers. The bottom layer, Layer 5, increased in permeability throughout both this stage and the first half of Stage 3, from 1.76×10^{-5} to 2.67×10^{-5} m/s. All but Layer

2 experiences some suffusion behaviour during Stage 2, as indicated by the timeline in Figure 5.5.

Whilst the whole sample permeability was almost the same before and after the first spin-down break, there was a clear redistribution of fine particles along the seepage path, shown by the change in layer permeabilities. The permeability of the lightly stressed Layer 0 increasing by 48.6% during the break, whilst the higher stressed layer at the end of the seepage path, Layer 5, dropped from 2.27×10^{-5} to 1.76×10^{-5} m/s. Although the change in permeability of the whole sample across the second spin-down break was larger than the first, the response of the individual layers was more consistent with each other, with all layers increasing in permeability, by magnitudes between 1 and 32%.

By the third stage, the layers reached a relatively stable configuration in comparison to the previous stages. With the exception of Layer 0, all layers exhibited the same trend of increasing permeability until midway through the stage and then beginning to decrease. These suffusion events were characterised by much smaller changes in permeability of longer durations compared to previous stages. Across the third stage the largest total variation of permeability for any layer was a 7.39×10^{-6} m/s decrease in Layer 0, and the other layers had a maximum variation of 2.77×10^{-6} m/s in Layer 2. In general, the layers towards the start of the seepage path were less permeable than the lower layers throughout the test T40L2.5.

5.2.3 Post-test dissection

The results of the dissection of T40L2.5 are given in Table 5.3. Due to an error in preparing the dissected samples for sieve analysis, the final fine particle content for Layer 3 and the majority of Layer 2 could not be calculated, however the data from the other layers provides reasonable insight into the ultimate fine particle distribution within the sample. The sample was dissected into 6 layers roughly aligning with the layers defined by the PPT ports using the method detailed in Section 5.2.2. Each layer was subdivided into four quadrants named after the cardinal directions, with the PPT ports being located in the South quadrant.

Table 5.3: Ultimate spatial distribution of fine particles from specimen dissection for test T40L2.5 (some data lost)

Layer	Final fine particle content (%)				
	North	East	South	West	Total
0	19.49	19.49	19.77	19.23	19.49
1	19.64	19.59	19.73	19.41	19.60
2	19.89	-	-	-	19.89
3	-	-	-	-	-
4	19.80	19.67	19.91	19.38	19.70
5	19.53	19.59	19.31	19.72	19.55
Total	19.70	19.55	19.72	19.42	19.61

Globally across the sample, the final fine particle content was 19.61%, representing a net loss of fine particles compared to the prepared content of 20%. For the layers which were analysed, this was a total loss of 5.82 g of silt, 2.43% of the total fine silt fraction. When examining the layers individually, it can be seen that there were more fine particles lost from the top and bottom layer, Layers 0 and 5, which have final fine particle contents of 19.49 and 19.55% respectively. Layer 2, located near the midpoint of the seepage path had the highest content, at 19.89%, although this is based on only the North quadrant.

The South quadrant of Layer 4, in which PPT₅ was located, lost the least amount of fine particles of all the measured samples, with a final fines content of 19.91%. Layer 4 was also the most varied in fines content across its cross section, with fine particle content varying from 19.38% to 19.91%. Although clogging may well have occurred in layers due to particles being deposited in that layer after migrating from overlying layers, none of the quadrants in this test had an ultimate fine particle content higher than the initial 20%.

5.3 T40L2.5(R)

5.3.1 Test description

Test $T_{40L2.5(R)}$ serves as a repeat of the previous test, but pushed to a higher final applied energy gradient of 236.5 kPa/m, compared to 196.4 kPa/m. This was done in order to investigate whether the stable state that was reached at the end of $T_{40L2.5}$ would continue when subjected to a higher hydraulic loading. As with $T_{40L2.5}$, the test used the full height of the centrifuge permeameter, giving a seepage path length of 210 mm, subdivided into 6 layers between PPT port locations. A total of 285.8 J of energy was expended by the seepage flow in this test, 79.3 J more than during $T_{40L2.5}$. The hydraulic loading regime is shown in Figure 5.7.

In all other respects test $T_{40L2.5(R)}$ was prepared and conducted in the same manner as $T_{40L2.5}$, except for there being only one spin-down break. This occurred at an applied head difference of 107.5 mm in order to empty the outflow tank, ensuring there was sufficient capacity to capture the flow velocity at the end of the test. This test was not dissected on completion of centrifuge testing. The effective stress distribution in the specimen is shown in Figure 5.6. The maximum effective stress at the base of the sample (PPT6) at the beginning of the test was 198.8 kPa, which increases to 248.9 kPa by the end of the test.

5.3.2 Permeability response during centrifuge testing

It can be seen from Figure 5.8 that the profile of the whole sample permeability for this test was very similar to the previous test, with an initial period of permeability increase, reaching a maximum permeability, and then decreasing steadily towards the latter half of the test. The specimen started with a permeability of 1.60×10^{-5} m/s, which increased to 2.07×10^{-5} m/s by 95 minutes into the first stage, when the applied energy gradient was 142.6 kPa/m.

Figure 5.9 shows the permeability of each layer for the duration of the test. The timeline at the base of Figure 5.9 identifies suffusion events that occurred. As before, the layers at the top of the seepage path had a consistently lower permeability than those at the bottom. In the first 15 minutes of testing, all

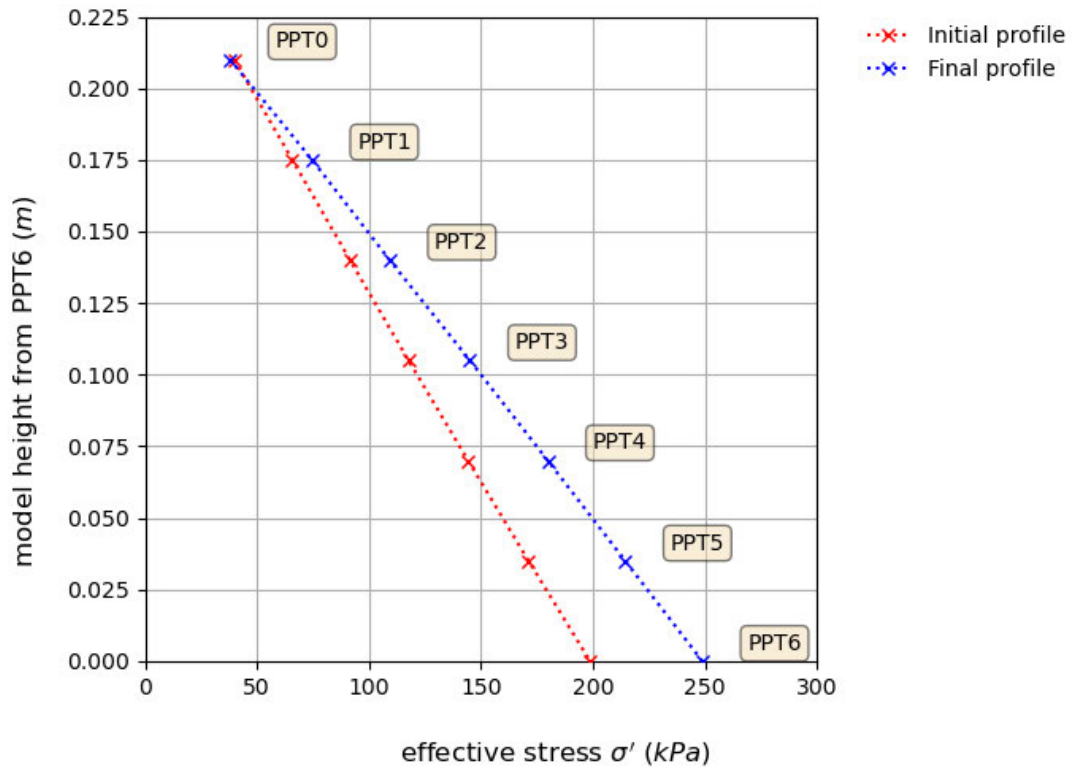


Figure 5.6: Effective stress profile in $T_{40}L_{2.5}(R)$ at the beginning and end of the centrifuge seepage flow test

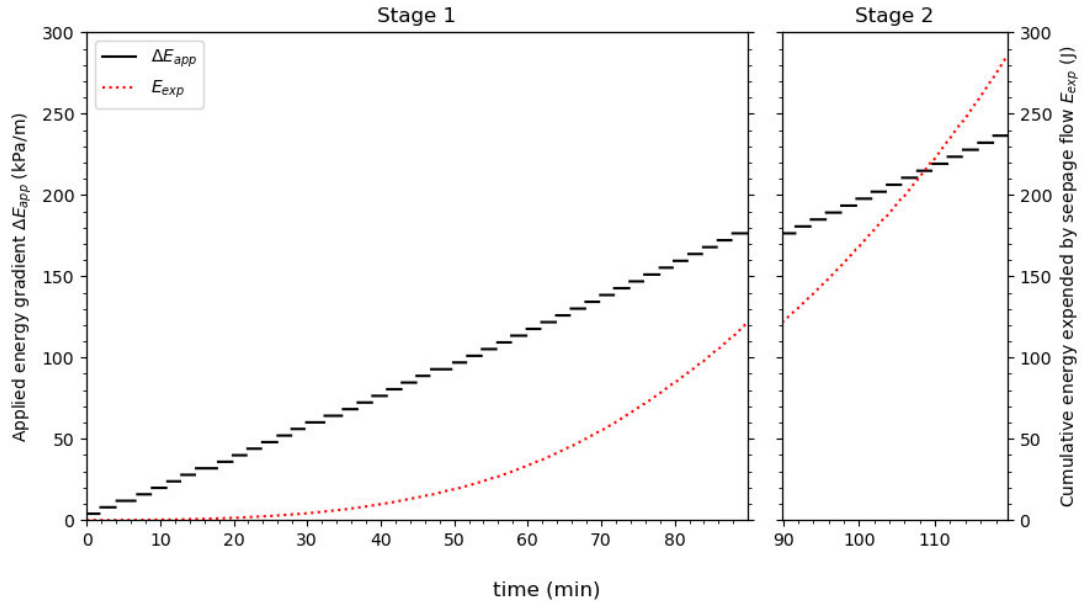
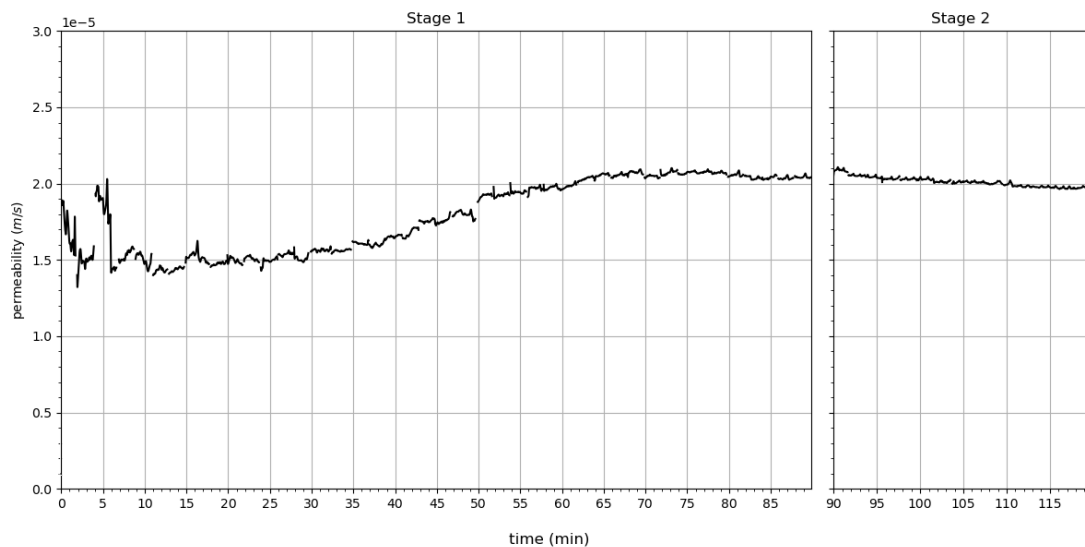


Figure 5.7: Energy gradient applied to $T_{40}L_{2.5}R$ and cumulative energy expended by the seepage flow over the 2 stages of testing

Table 5.4: Variation in permeability for each layer of test $T_{40L2.5}(R)$

Layer	Change in permeability (%)			
	During S1	S1 to S2	During S2	Whole test
0	147.7	3.6	-4.4	145.4
1	0.5	-3.7	4.3	0.9
2	6.2	1.9	-12.1	-4.8
3	60.7	1.8	-8.2	50.2
4	-19.2	6.0	-6.6	-20.0
5	-32.8	1.5	-2.5	-33.5
total	28.0	1.7	-5.0	23.7

but Layer 5 experienced short bursts of suffusion of between 2 and 5 minutes in duration, whereas suffusion events that occurred later in the test tended to have longer durations. The exception to this was Layer 0, which showed a continual increase in permeability throughout the first 50 minutes of the test.

Figure 5.8: Global permeability of $T_{40L2.5}(R)$

Between the stages, there was very little variation in permeability of the layers, with the largest change being an increase of 6.0% in Layer 4. As with the previous test, at applied energy gradients of around 170-200 kPa/m, corresponding to the start of the second stage, the layers reached a stable state with very little fluctuation in permeability. However, when the applied energy gradi-

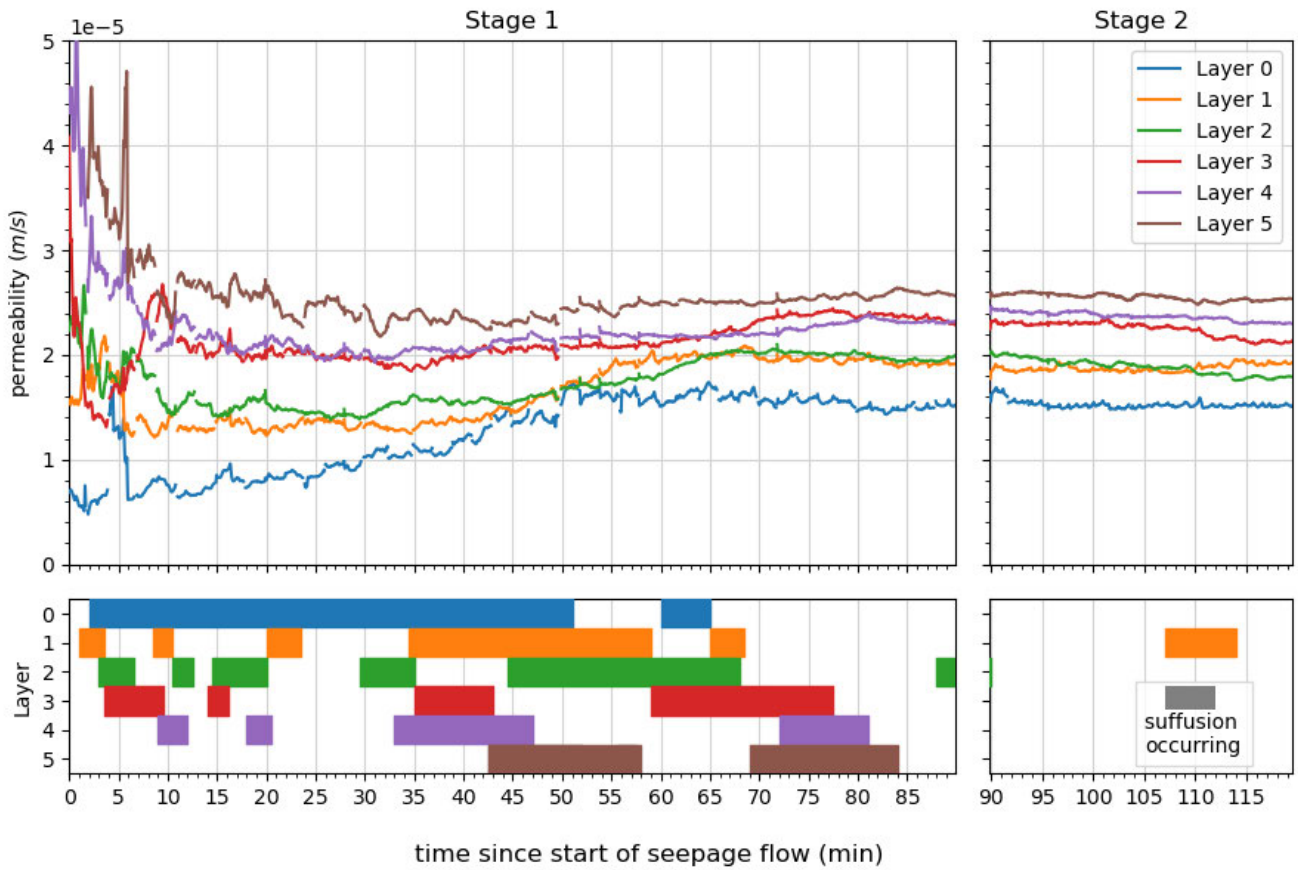


Figure 5.9: Permeability and timeline of suffusion events for each layer of *T40L2.5(R)*

ent reach 220 kPa/m 107 minutes into testing, a steady increase in permeability initiated in Layer 1 combined with some clogging in the two layers below. The rate of this permeability change was on a significantly smaller scale than the variations observed earlier in the test, with Layers 1, 2 and 3 decreasing by only 7.71×10^{-7} , 8.60×10^{-7} and 1.22×10^{-6} m/s respectively between minute 107 and the end of the test. There was no significant permeability variation in Layer 0 over the second stage, with a decrease of just 4.4% (Table 5.4), although it is notable that this layer had a lower permeability than the other layers, as well as layers in other specimens, throughout this test.

5.4 T40S2.5

5.4.1 Test conditions

Test *T40S2.5* was conducted using only three acrylic segments of the permeameter cell, which allows a shorter seepage path to be tested whilst using the same amount of overburden material. This gave a sample comprised of three layers and a reduced specimen height of 105 mm, shown in the photograph in Figure 5.10. The specimen was subjected to a multi-stage seepage flow regime with the same 2.5 mm increments of applied head difference as for tests *T40L2.5* and *T40L2.5(R)*. However, due to the half height seepage path length compared to those tests, the increment of applied energy gradient was approximately doubled, from an average of 3.95 kPa/m in the full height tests to 7.83 kPa/m in *T40S2.5*. The slight variation in energy per increment across the course of the test is due to the increase in g-level experienced by the downstream CHT as the its distance from the centre of the centrifuge increases (Section 2.3.1).



Figure 5.10: *T40S2.5* used only three of the permeameter segments to allow testing of a shorter seepage path

Figure 5.11 shows both the hydraulic loading regime and the energy expended by the seepage flow across the four stages of centrifuge testing. The test was conducted in four stages as the high flow rates meant that the outflow container had to be emptied frequently. As before, the same head difference was applied to the sample before and after spin-down for each stage. The cumulative energy expended by the seepage flow for this test was 480.7 J across the 115 minute test duration. After centrifuge testing, this sample was dissected into three layers, the results of which are presented in Section 5.4.3.

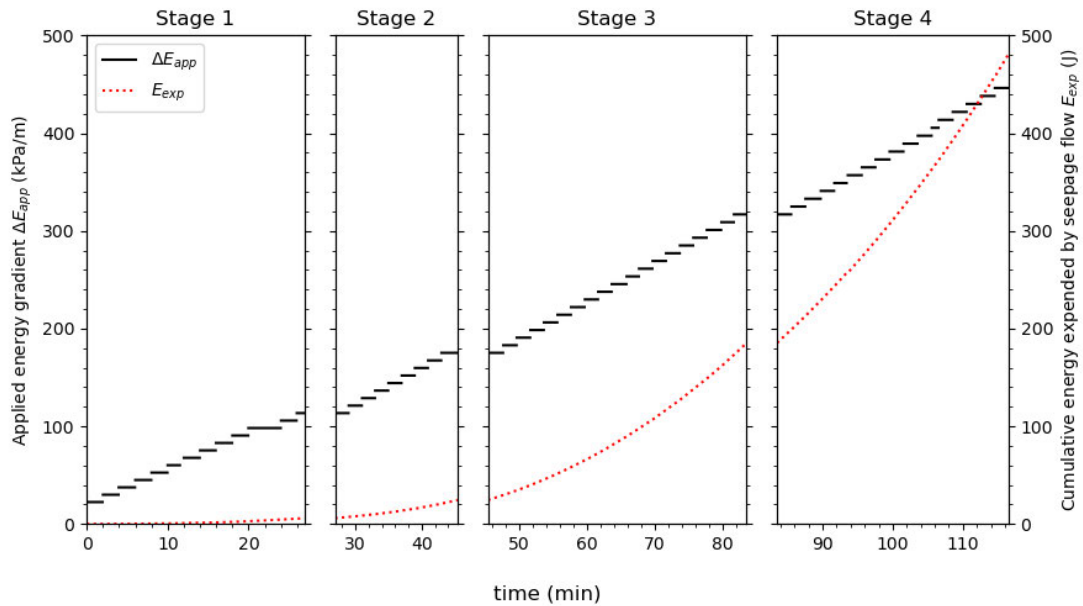


Figure 5.11: Energy gradient applied to $T_{40S2.5}$ and cumulative energy expended by the seepage flow over the 4 stages of testing

Figure 5.12 shows the effective stress profile in this shorter sample. PPT5 was located at the base of the specimen, with PPT6 in the coarse granular base material. The effective stress profile across the whole sample of $T_{40S2.5}$ was equivalent to the profile in the top three layers of $T_{40L2.5}$ and $T_{40S2.5}$, increasing from 42.8 to 122.3 kPa across the length of the seepage path at the start of the test.

5.4.2 Permeability response during centrifuge testing

Figure 5.13 shows the global permeability of this test over the four testing stages, measured between the topmost and bottommost PPTs, which in this shorter sample were PPTs 0 and 5, as the shorter permeameter configuration

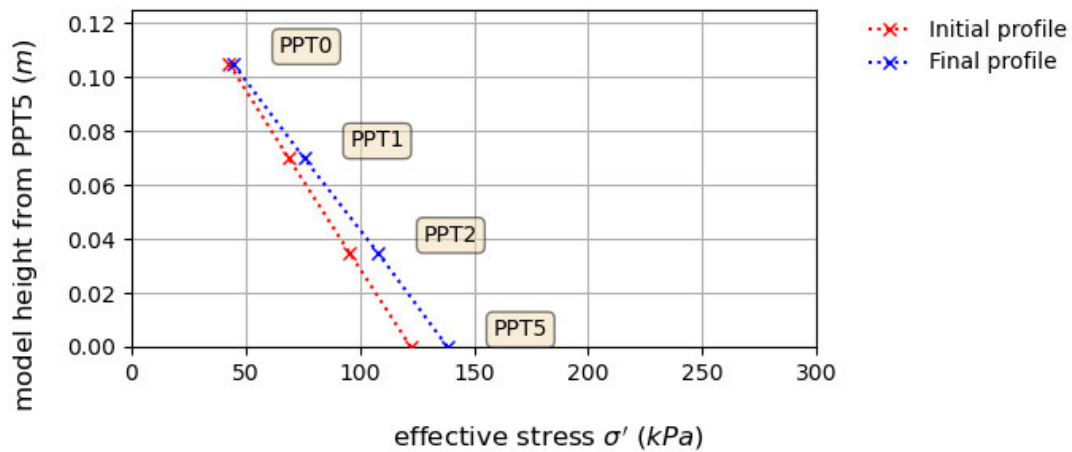


Figure 5.12: Effective stress profile in $T_{40S2.5}$ at the beginning and end of the centrifuge seepage flow test

omitted the section housing PPTs 3 and 4. During the first stage, the permeability initially fluctuated between 1.29×10^{-5} and 1.51×10^{-5} m/s between minutes 2 and 5, but the first significant increase in permeability occurred at 15 minutes in, when the applied energy gradient was 27.6 kPa/m. over the next 12 minutes, until the end of the stage, the permeability increased from 1.40×10^{-5} to 1.64×10^{-5} m/s.

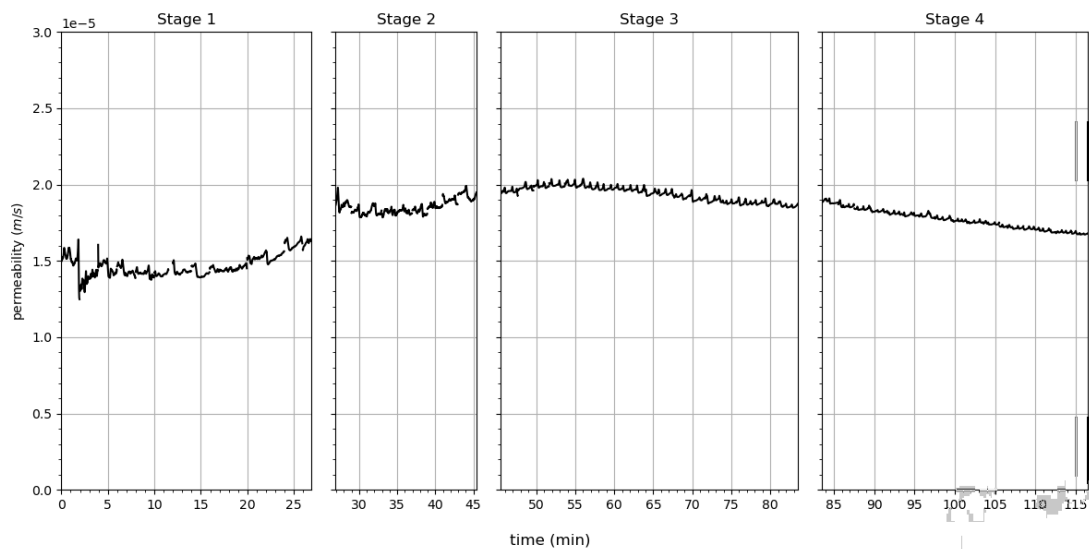


Figure 5.13: Global permeability of $T_{40S2.5}$

In the spin-down between the first and second stage the permeability of the whole sample increased by 14.1% (Table 5.5). During Stage 2, the trend of increasing permeability did not continue immediately, with the sample

showing very little variation in permeability until 38 minutes into seepage flow, where once again the permeability began to increase from 1.84×10^{-5} to 1.99×10^{-5} m/s by the end of the stage.

Table 5.5: Variation in permeability for each layer of test $T_{40S2.5}$

Layer	Change in permeability (%)							
	During S ₁	S ₁ -S ₂	During S ₂	S ₂ -S ₃	During S ₃	S ₃ -S ₄	During S ₄	Whole test
0	31.1	16.2	4.5	-8.8	2.4	-5.2	-10.9	25.6
1	4.1	5.6	10.1	5.3	-0.7	2.5	-7.3	20.4
2	-13.6	26.1	-4.5	5.1	-15.9	5.6	-14.8	-17.2
Whole	9.2	14.1	4.4	-0.1	-3.8	0.4	-10.7	12.1

In contrast to the first spin down, there was a only a small 0.1% decrease in permeability across the second spin down, and in Stage 3 the sample continued increasing in permeability for the first five minutes. At 12 minutes in to the third stage, the sample began to steadily decrease in permeability, from 1.97×10^{-5} to 1.86×10^{-5} m/s by the end of the stage. Although there is a very small (0.4%) increase between Stages 3 and 4, the trend of decreasing permeability continued over the final stage, reaching a final global permeability of 1.68×10^{-5} m/s.

When examining the permeability of the three individual layers across the test, shown in Figure 5.14, it can be seen that, unlike for the two longer tests previously discussed, all three layers of the sample behaved in a similar way to each other throughout the test, and the shape of their permeability profile is similar to the global permeability profile shown in Figure 5.13. At the start of testing the bottom layer, Layer 2, had a significantly higher permeability of 2.46×10^{-5} m/s compared to the two layers above it, Layers 0 and 1, which had initial permeabilities of 1.17×10^{-5} and 1.35×10^{-5} m/s respectively.

Layer 0 was the first to increase in permeability, 15 minutes into the seepage flow testing, at the same timestamp at which the whole sample permeability was noted to increase. The permeability of Layer 0 increased by 3.64×10^{-6} m/s across Stage 1 and then jumped up by 16.2% across the first spin down break (Table 5.5). Again in the second stage, the profile of Layer 0 mirrored the global permeability, beginning to increase at minute 38, although in this case

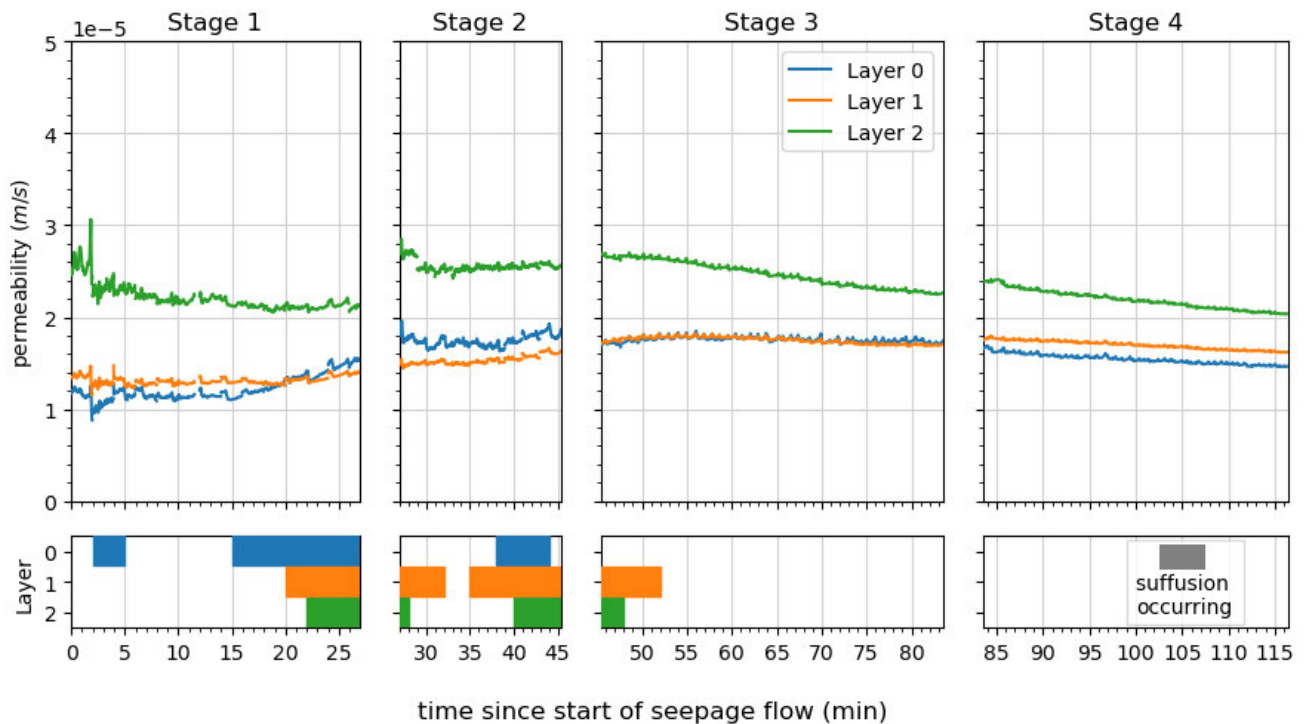


Figure 5.14: Permeability and timeline of the suffusion events for each layer of *T40S2.5*

from a lower permeability compared to the whole sample, increasing from 1.05×10^{-5} to 1.86×10^{-5} m/s.

Layer 1 also exhibited a significant increase in permeability across the first two stages, from 1.35 to 1.63×10^{-5} m/s. The layer maintained its initial permeability until minute 20, when it began to increase steadily. During the second stage, the permeability of Layer 1 increased by 4.1%. According to the criteria for a suffusion event, there was a 3 minute period during stage 2 where the permeability was deemed to have plateaued, shown by the two suffusion events in Layer 1 in the timeline at the base of Figure 5.14.

Layer 2 did not show any signs of suffusion across the first stage, with its permeability actually decreasing by 3.34×10^{-6} m/s, suggesting that particles were being deposited in this layer at the end of the seepage path. However, there was an increase in permeability of 26.1% between Stages 1 and 2, evidencing a significant change in internal structure. For the majority of Stage 2, Layer 2 maintained a permeability of around 2.6×10^{-5} m/s. In the later spin down breaks, the increases in permeability were much smaller in comparison, with jumps of 5.1% and 5.6%.

All three sample layers exhibited clogging, or a decrease permeability, to different degrees over the final two stages, with the most variation occurring in Layer 2, a decrease of 6.54×10^{-6} m/s compared to the decrease of 2.29×10^{-6} and 9.62×10^{-7} m/s that occurred in Layers 0 and 1 respectively. Layer 2 ended the test with a permeability lower than its initial value at the start of seepage flow, whilst the other two layers increased in permeability during testing. The whole sample increased in permeability by 12.1% across the course of test, as shown in Table 5.5.

5.4.3 Post-test dissection

After centrifuge testing, this shorter sample was dissected into 3 layers aligning to the layers referred to in the centrifuge testing section. The final fine particle content of the whole sample was 19.7% in comparison to the initial 20% fine particle content. From the dissected mass, 2.56 g of the fine silt fraction were externally eroded from the sample across the course of the test, representing a loss of 2.05% of the initial silt content by weight.

Table 5.6: Ultimate spatial distribution of fine particles from specimen dissection for test T40S2.5

Layer	Final fine particle content (%)				
	North	East	South	West	Total
0	19.84	19.89	19.57	19.60	19.74
1	19.37	19.98	19.44	19.94	19.68
2	19.12	19.59	20.06	19.02	19.53
Total	19.59	19.84	19.67	19.57	19.67

Layer 0, the top layer of the sample, had the highest ultimate fine particle content at 19.74%, with the amount of fine particles lost increasing along the seepage path. Layers 1 and 2 had lower final fine particle contents of 19.68 and 19.53% respectively. The cross-sectional variability also increased along the seepage path, with a maximum variation between quadrant's fine particle content of 0.32% for Layer 0, 0.61% for Layer 1 and 1.04% for Layer 2.

Interestingly, the south quadrant of Layer 2, in which PPT₅ was located, ultimately had a fine particle content of 20.06%, higher than the original 20%. This side of the sample was clogging during the test, whilst the North and West quadrants showed some of the highest particle losses of the whole testing programme, with final fine particle contents of 19.12 and 19.02% (Table 5.6). The question of how well PPTs located in the sidewall can represent the permeability of the whole layer cross section, particularly in cases such as this with high heterogeneity, is explored in Chapter 8.

5.5 T40LCH

5.5.1 *Test conditions*

In contrast to the multi-stage seepage tests undertaken at 40-g, *T40LCH* had the same applied head difference of 100 mm for the duration of the test. This corresponds to an applied energy gradient of 161.5 kPa/m. The test was conducted in two equal length stages and the total energy expended by the seepage flow was 414.3 J. On completion of testing, the specimen was dissected and the results of this are presented in Section 5.5.3. Figure 5.15 depicts this constant hydraulic loading and associated linear cumulative energy expended by the seepage flow.

With the multi-stage seepage flow tests conducted as part of this study, there was an initial interval where the applied head difference across the sample was zero. These hydrostatic readings allowed for any drift in the PPTs between tests to be adjusted for in post-processing, by aligning the PPTs to the known elevation and pressure heads at this point (Section 3.7). Whilst these adjustments were small, they were different for each test. For this constant head test, there was no initial hydrostatic case from which the adjustment values could be obtained. For this test it was decided to omit this stage in analysing the PPT readings, presenting only the change in permeability of each layer from its initial value. This approach is valid in the interpretation of suffusion and clogging events, as these are identified from changes in permeability rather than absolute values. Applying adjustments to initial PPT values obtained under seepage flow conditions requires assumptions on the

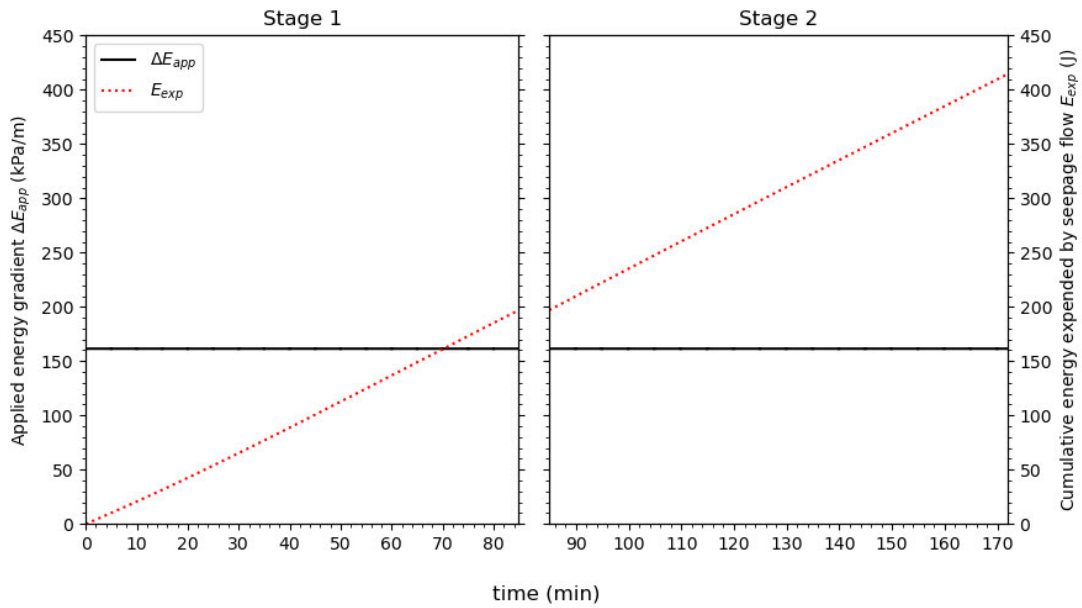


Figure 5.15: Energy gradient applied to *T40LCH* and cumulative energy expended by the seepage flow over the 2 stages of testing

initial homogeneity of the sample that are not necessary to understanding the suffusion behaviour of the specimen.

5.5.2 Permeability response during centrifuge testing

From the beginning of the first stage, the specimen exhibited global suffusion, shown by the increasing permeability in Figure 5.16. The global permeability increased by 3.08×10^{-6} m/s between minutes 0 and 45, before the behaviour changed and the permeability steadily decreased from 1.83×10^{-5} to 1.77×10^{-5} m/s for the rest of stage, despite no change in external hydromechanical influences. The global permeability increased by 9.33×10^{-7} m/s between the two stages, suggesting some movement of fine particles due to the stress relaxation. During Stage 2, the global permeability decreased at a near constant rate, dropping 1.07×10^{-6} m/s over the 87 minutes duration. The final permeability of the specimen was 2.24×10^{-6} m/s higher than the initial value.

Layer 0, at the start of the seepage path, experienced the most variation in permeability across the first 11 minutes of the test, with its permeability increasing rapidly by 6.73×10^{-6} m/s. For the remainder of the test the layer steadily decreased in permeability by 1.21×10^{-6} m/s, apart from a three small

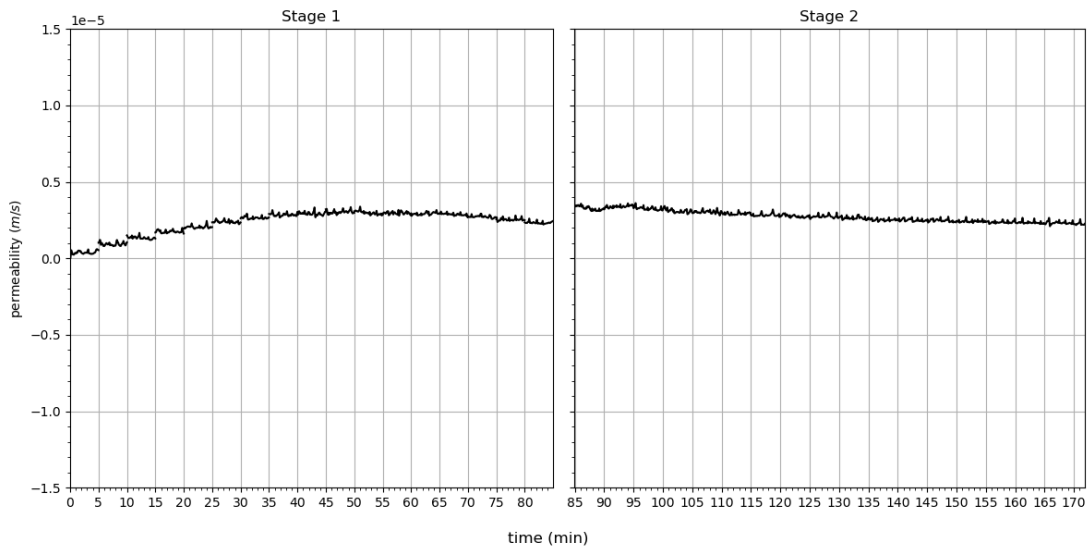


Figure 5.16: Global permeability variation of *T40LCH* during centrifuge testing

suffusion events lasting no longer than four minutes each, identified in the timeline at the base of Figure 5.17.

Not only did Layer 0 exhibit suffusion at the beginning of the test, the timeline in Figure 5.17 shows that all of the layers demonstrated an increase in permeability during the first stage. Layer 2 eroded for a significant portion of Stage 1, with its permeability increasing by 2.37×10^{-6} m/s. After an initial suffusion event which began at the start of the second interval of applied head difference, Layer 3 reached a steady permeability 2.37×10^{-6} m/s higher than its initial value 30 minutes into testing. Apart from an increase in permeability of 1.34×10^{-6} m/s between minutes 80 and 92, Layer 3 maintained a permeability of 2.45×10^{-6} m/s higher than its initial value for the rest of the test.

After initial suffusion events, Layers 4 and 5 began to decrease in permeability during Stage 1 at minutes 59 and 40 respectively. Both layers increased in permeability during the spin-down break, with Layer 4 experiencing an increase of 2.07×10^{-6} m/s compared to the smaller 7.50×10^{-7} m/s increase in Layer 5 (Table 5.7). For the second stage, both layers steadily decreased in permeability. The ultimate permeability of Layer 5 was 4.30×10^{-7} m/s lower than its initial value, whilst Layer 4 had a net increase in permeability of 3.21×10^{-6} m/s.

The permeability results of Layer 2 stand out in this test, as the permeability jumped by a significant 8.67×10^{-6} m/s between the two stages. Although the

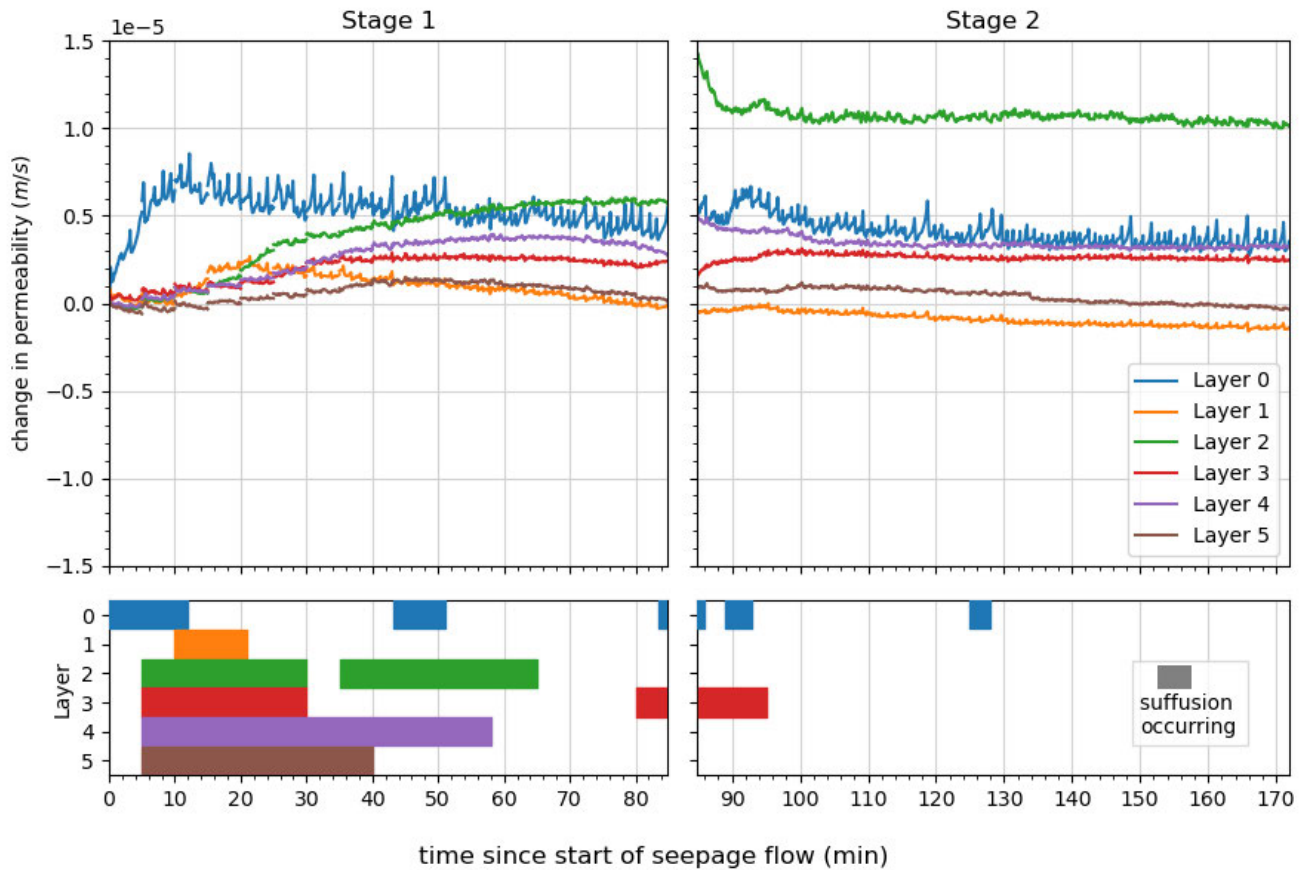


Figure 5.17: Permeability variation and timeline of suffusion events for each layer of *T40LCH*

permeability dropped to approximately 1.05×10^{-5} m/s greater than the layer's initial permeability after the 90th minute, the layer remained significantly more permeable than its surrounding neighbours. This suggests the development of a preferential seepage flow pipe with a higher permeability near the PPT ports on the permeameter sidewall in this area. As shown in Figure 5.16, the permeability of the whole sample increased a small amount between stages, capturing the global impact of one layer's significant increase in permeability.

5.5.3 Post-test dissection

As with the previous full height test dissected, *T40L2.5*, this test was subdivided into six layers, with each layer split into four quadrants, the results of which are shown in Table 5.8. In total, the specimen lost 5.58 g of the fine silt fraction, leaving an ultimate fine particle content of 19.71%. This represents a loss of

Table 5.7: Variation in permeability for each layer of test *T40LCH*

Layer	Change in permeability (%)			
	During S1	S1 to S2	During S2	Whole test
0	33.1	1.3	-8.9	22.9
1	-0.2	-3.0	-5.8	-8.9
2	37.6	40.6	-13.4	67.6
3	15.9	-5.0	5.7	16.4
4	17.7	11.4	-7.9	20.8
5	0.2	4.8	-7.3	-2.7
total	16.0	5.4	-5.9	15.0

1.84% of the initial silt fraction. The three layers towards the end of the seepage ended up with similar fine particle contents, around 19.8%, whereas the top layers had a higher global loss in fine particles, in particular Layer 1, which had a final fine particle content of 19.36%.

Table 5.8: Ultimate spatial distribution of fine particles from specimen dissection for test *T40LCH*

Layer	Final fine particle content (%)				
	North	East	South	West	Total
0	19.55	19.69	19.76	19.78	19.69
1	19.88	18.62	19.59	19.47	19.36
2	19.67	19.67	19.75	19.78	19.72
3	20.15	19.69	19.71	19.70	19.81
4	19.79	20.14	19.73	19.56	19.79
5	20.11	19.65	19.83	19.56	19.81
total	19.90	19.56	19.72	19.63	19.71

Layer 1 also showed the most variation in fine particle content across its cross section, with a total variation of 1.26%, higher than the average of 0.38% seen in the other layers. The East quadrant of Layer 1 has the lowest ultimate fines content of across all tests, finishing at 18.62%. The other quadrants in

this layer also had less than the initial 20% fine particle content, but not to the same extent.

Unlike $T_{40L2.5}$ and $T_{40S2.5}$, the two other dissected tests conducted at 40-g, this test had some quadrants with an ultimate fines content higher than the initial design value of 20%. These occurred in the lower half of the seepage path, with three quadrants in the North and East of the sample having fine particle contents between 20.11 and 20.15% (Table 5.8). These areas of high particle content were localised, with the horizontally adjacent West quadrants of Layers 4 and 5 having much lower ultimate fine particle contents of 19.56%. The high fines content was also localised to the layer in the seepage flow direction, with the quadrants above and below these layers all showing a typical amount of fine particle loss.

5.6 SUMMARY

In this chapter, the results of the four tests conducted at 40-g have been presented. Of these tests, three were also dissected post-centrifuge testing and had their ultimate spatial variation in fine particles analysed. The key findings of this chapter are summarised as follows:

- In all of the 40-g tests, both suffusion and clogging behaviour was identified in all layers of the specimens, despite their different seepage path lengths and hydraulic loading regimes.
- For all of the tests, regardless of configuration, the suffusion events ceased by the end of testing. All tests reached a final seemingly stable stage, with layer permeabilities either completely plateauing or slightly and gradually decreasing in permeability.
- Global permeability readings taken across the whole specimen failed to capture significant local variation in permeability, shown by PPT readings mid-seepage path and verified by the heterogeneous ultimate distribution of fine particles within the specimens.
- Although the two repeat tests, $T_{40L2.5}$ and $T_{40L2.5}(R)$, showed similar global permeability behaviour, small heterogeneities naturally introduced during specimen preparation of otherwise identical samples lead to

variations in permeability of individual soil layers not replicated between tests. This is discussed further in Section 8.1.

- Post test fine particle content analysis showed a net decrease in fine particles in all quadrants of test *T40L2.5*, whilst both *T40S2.5* and *T40LCH* exhibited fine particle contents higher than their initial 20% in quadrants towards the end of their seepage paths.
- In the tests where the ultimate spatial distribution of the fine particles was measured, there was very little change in the fines content, with only one quadrant (*T40LCH* Layer 1 east) exhibiting a final fines content below 19%. These variations amount to fines detriments of less than a gram in each quadrant and so it cannot be confidently stated that the difference observed is not due to procedural error. In the validation test reported in Section 4.5, where a known fines percentage was prepared and then measured using the procedure, the largest difference in fines content prepared and observed was 0.1 g, representing 20.1% fines content, compared to the 20% prepared. This provides a baseline value for significant change in fines content due to suffusion rather than the sieving method.
- There was no obvious link between trends observed in the temporal permeability readings and the ultimate spatial distribution of fine particles. Layers which doubled in permeability, for example Layers 0 and 1 in *T40L2.5*, only dropped in fines content to 19.49 and 19.60% respectively, whilst some layers showed a decrease in permeability (typically interpreted as clogging), but upon dissection showed a net loss of fine particles (e.g. Layer 2 of *T40S2.5*). From the results of these tests, the final distribution of fine particles cannot be used to predict the local permeability changes, and so net change in fine particles is not a suitable method to quantify local suffusion.

TESTS AT LOWER G-LEVELS

6.1 INTRODUCTION

In addition to the permeameter tests undertaken at 40-g presented in Chapter 5, four permeameter tests at lower g-levels were also performed. The results of these tests are presented in this chapter. The first three tests presented were conducted in the centrifuge environment, at 30-, 20- and 10-g respectively. The fourth test presented, test *T1LCH*, was a constant head test conducted at 1-g, following the slightly modified procedure laid out in Section 3.5.2 of the methodology. An overview of the testing conditions of the four tests are given in Table 6.1.

All three of the centrifuge permeameter tests were subjected to multi-stage seepage flow, with the applied head increment of each test, Δh_{app} , designed to apply the approximately the same fluid velocity increment to the specimens, but different hydraulic gradients and total expended energy. Using this approach manipulates centrifuge scaling laws in order to interrogate the concept of critical hydraulic gradient, commonly used to classify suffusion onset (Section 2.5.1). This centrifuge scaling approach was introduced in depth in the

Table 6.1: Summary of parameters for centrifuge and 1-g permeameter tests at lower g-levels

Test	$\Delta z_{M/P}$ (m)	δh (mm)	h_{max} (mm)	$i_{app,max}$	$EG_{app,max}$ (kPa/m)	E_{exp} (J)	dissected
<i>T30L2.5/5</i>	0.21/7.85	2.5/5	125	0.49	154.1	55.2	✓
<i>T20L5</i>	0.175/5.93	5	145	0.66	138.8	34.6	
<i>T10L10</i>	0.21/1.96	10	150	0.60	61.6	15.1	
<i>T1LCH</i>	0.21/-	-	86	0.41	4.0	0.015	✓

centrifuge testing programme portion of the methodology in Section 3.8. The applied head difference and fluid velocity increments during the early stages of testing, before significant fine particle migration could occur, are presented in Table 6.2 to demonstrate the similarity in seepage flow regime between the specimens. These centrifuge tests lasted between 58 and 145 minutes.

Table 6.2: Increments of applied head difference and fluid velocity for multi-stage centrifuge tests at different g-levels

	$T_{40L2.5}$	$T_{30L2.5/5}$	T_{20L5}	T_{10L10}
Increment of applied head difference (mm)	2.5	3.75	5	10
Length of applied head interval (s)	120	120	120	600
Average fluid velocity increment for first 5 intervals ($\times 10^{-6}$ m/s)	5.08	5.86	5.98	4.74

The second centrifuge test presented in this chapter, test T_{20L5} , can also be compared to test $T_{40S2.5}$ presented in the previous chapter. These two specimens have different model lengths, 175 and 105 mm respectively, but were tested with applied head increments at g-levels that meant that the same vertical effective stress conditions were achieved using the modelling-of-models approach outlined in Section 2.3.1. The results of this comparison in terms of the initiation and progression of suffusion are discussed in Section 7.2, as well as the influence of the different prototype boundary conditions present due testing in the same equipment at different g-level

The final test presented in this chapter, test T_{1LCH} , was undertaken at 1-g using the constant head apparatus shown in Figure 3.17. The permeameter was modified slightly to allow pore pressure readings to be taken for the duration of the 120 hour (5 day) test, but the specimen was otherwise prepared identically to the centrifuge tests. This is discussed in more depth in Section 6.5 of this chapter. Direct comparison between this test and the 40-g constant head test, T_{40LCH} , is made in Section 7.3 and this comparison explores how applying the same hydraulic gradient, but expending different magnitudes of energy by the action of the seepage flow affects the progression of suffusion within the sample. Both tests $T_{30L2.5/5}$ and T_{1LCH} were dissected post-testing and

these results are presented in conjunction with their permeability results in their respective sections.

6.2 T30L2.5/5

6.2.1 Test description

In this test, a full length specimen with a seepage path length of 210 mm was prepared in the centrifuge permeameter and then tested under multi-stage seepage flow at a centrifuge acceleration of 30-g. The head difference applied to the sample, dh_{app} , was alternatively increased by 2.5 and 5 mm, to a final applied head difference of 125 mm. This corresponds to a final applied energy gradient of 154.1 kPa/m at the end of the three centrifuge testing stages, with a total test duration of 69 minutes. The increments of applied head difference were alternated in order to apply and average increment that gave a velocity increment similar to test $T40L2.5$ presented in the previous chapter, as well as the centrifuge tests at lower g-levels in this chapter, as seen in Table 6.2.

The final cumulative energy expended by the seepage flow during testing was 55.2 J. Each increment of energy gradient applied to the specimen was held for 2 minutes before the applied head difference was increased again. The hydraulic loading regime and associated energy expended by the seepage flow is shown in Figure 6.1. After centrifuge testing was completed, the sample was dissected and the ultimate spatial distribution of fine particles was recording in order to draw comparisons with the 40-g tests presented in Chapter 5 and the 1-g test results in Section 6.5. This test forms part of a suite of modelling-of-models tests with $T40L2.5$, $T20L5$ and $T10L10$, discussed in detail in Section 7.1.

Figure 6.2 shows the effective stress profile within the sample at the beginning and end of testing, calculated from the pore pressures measured at each of the PPT ports. The stress at the base of the sample (PPT6) increased from 149.3 to 178.9 kPa over the duration of the test due to the downwards seepage flow. Because of the lower g-level, the effective stress at the base of the sample in this tests was lower than in the full height 40-g tests, despite the specimens having the same model dimensions.

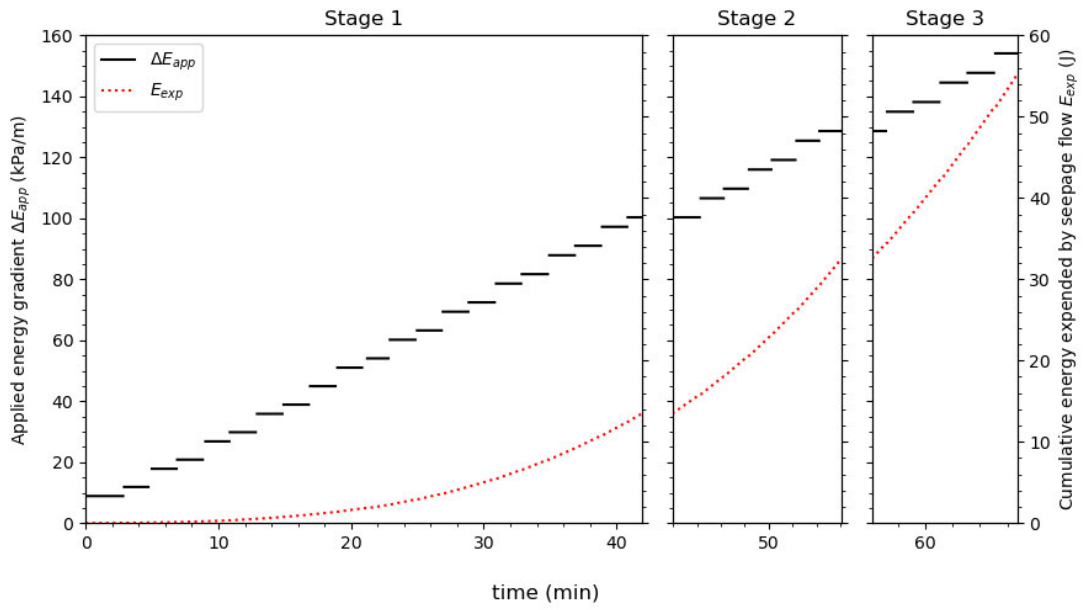


Figure 6.1: Energy gradient applied to *T30L2.5/5* and cumulative energy expended by the seepage flow over the 3 stages of testing

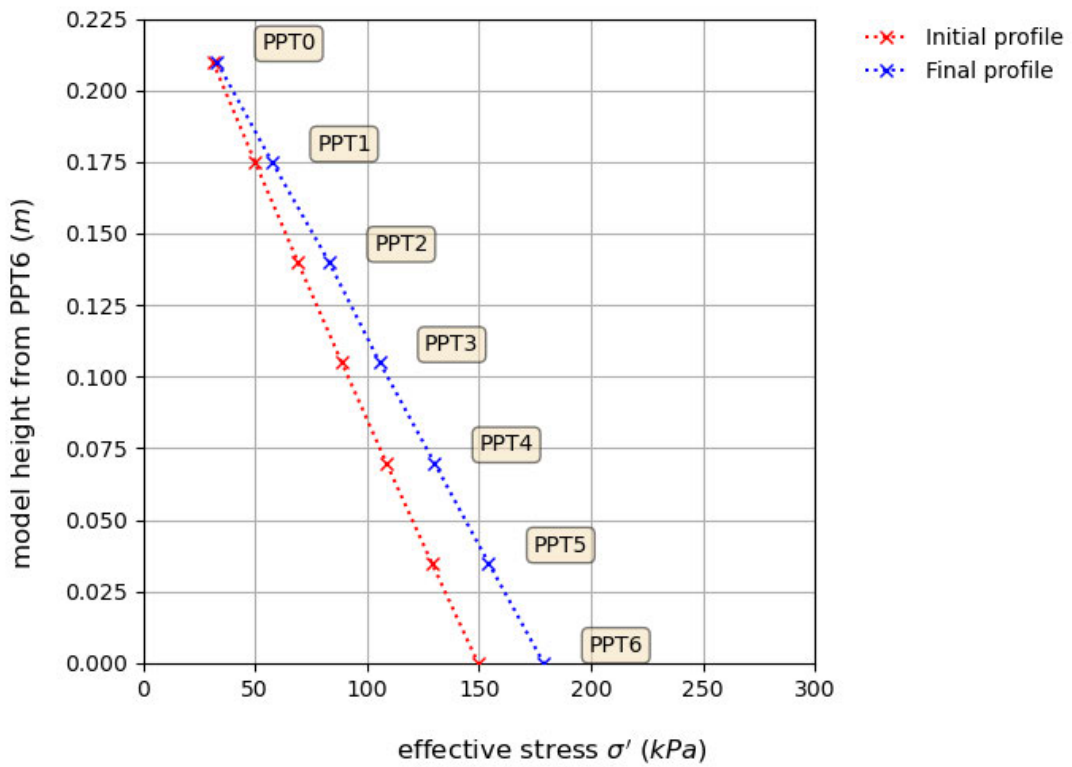


Figure 6.2: Effective stress profile in *T30L2.5/5* at the beginning and end of the centrifuge seepage flow test

6.2.2 Permeability response during testing

Figure 6.3 shows the global permeability of the sample across the three stages of centrifuge testing, measured between the topmost and bottommost PPTs, PPT 0 and 6. The specimen began the test with a permeability slightly higher than the other tests in this chapter, averaging 2.45×10^{-5} m/s over the first 5 minutes. The permeability decreased throughout Stage 1, dropping by 28.2% in the 44 minutes, initially more rapidly and then levelling out to around 1.77×10^{-5} m/s by the end of the stage.

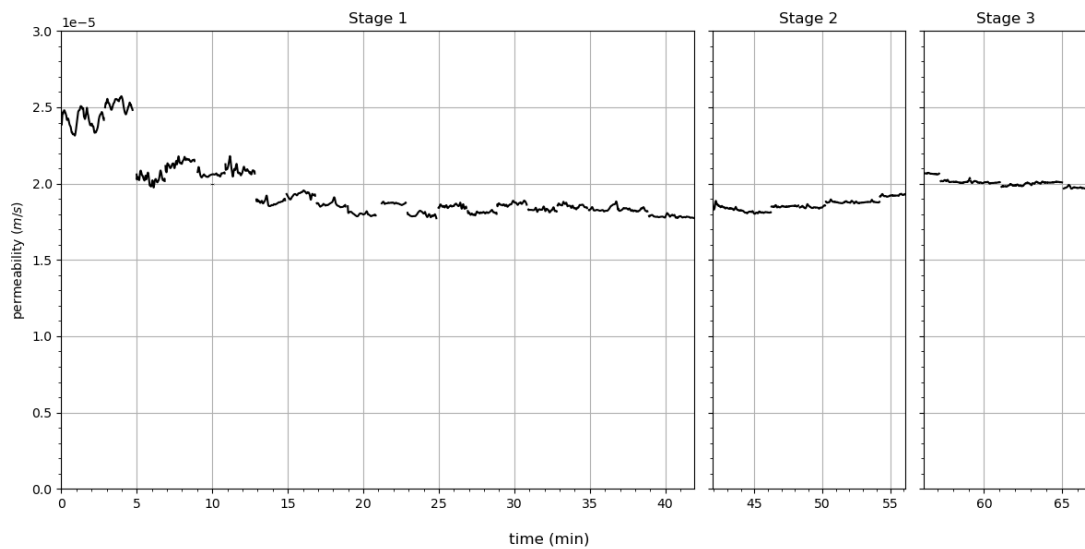


Figure 6.3: Global permeability of *T30L2.5/5*

In the centrifuge spin-down periods between both Stage 1 and Stage 2, and Stage 2 and 3, the permeability of the whole sample increased, by 6.1 and 7.1% respectively. Across the 14 minutes of Stage 2 the permeability increased by 4.90×10^{-6} m/s, suggesting the occurrence of suffusion. In contrast, the permeability of the whole sample then decreased across Stage 3, dropping from 2.07×10^{-5} m/s to a final value of 1.97×10^{-5} m/s, a percentage decrease of 4.6%, indicating some deposition of fine particles within the sample.

When looking at the permeability of the individual layers in Figure 6.4, it is clear that the top two layers, Layer 0 and 1, were quite a lot less permeable throughout the test than those layers further down the seepage path. In the spin-down breaks before Stages 2 and 3 the permeability of Layer 2 increased by 73.4 and 24.0% respectively, and this layer remained consistently more permeable than the rest of the sample during these later stages. This suggests

Table 6.3: Variation in permeability for each layer of test T30L2.5/5

Layer	Change in permeability (%)					
	During S ₁	S ₁ to S ₂	During S ₂	S ₂ to S ₃	During S ₃	Whole test
0	-15.3	5.5	-10.8	1.9	-6.0	-23.6
1	-39.4	-13.7	25.4	4.0	-1.0	-32.5
2	-21.0	73.4	-12.5	24.0	-15.4	25.7
3	-37.4	-10.1	8.6	0.2	2.0	-37.6
4	-22.7	8.9	-3.7	9.2	-4.4	-15.3
5	-30.2	16.4	-3.3	14.3	-7.6	-17.1
Total	-28.2	6.1	2.6	7.1	-4.6	-20.2

the formation of a preferential flow path in the vicinity of PPTs 2 and 3, similar to the response of *T40LCH*. In both tests, it was Layer 2 that exhibits this exaggerated response. This is likely a coincidence, rather than a PPT sensor failure, as each PPT reading is used in the calculations of permeability for both the layers above and below, which in both cases had permeability values in line with the rest of the specimen.

Within the first 13 minutes of Stage 1, all of the layers experienced at least one suffusion event, as defined in Section 5.1.1. The longest of these events occurred in Layer 0, where the permeability increased by 5.69×10^{-6} m/s over 6 minutes. The top four layers of the sample continued to experience bouts of suffusion throughout the test, with Layer 3 increasing in permeability over the course of both Stage 2 and 3, by 8.6 and 2.0% respectively. Although the lower layers experienced short suffusion events in the first half hour of Stage 1, they showed the general trend of decreasing in permeability across this first stage, show by the variation in permeability presented in Table 6.3. During both of the spin-down breaks, both Layer 4 and 5 increased in permeability. For Layers 0, 1 and 3, the first spin down stage brought about a reduction in permeability, whilst the second break caused minimal permeability change.

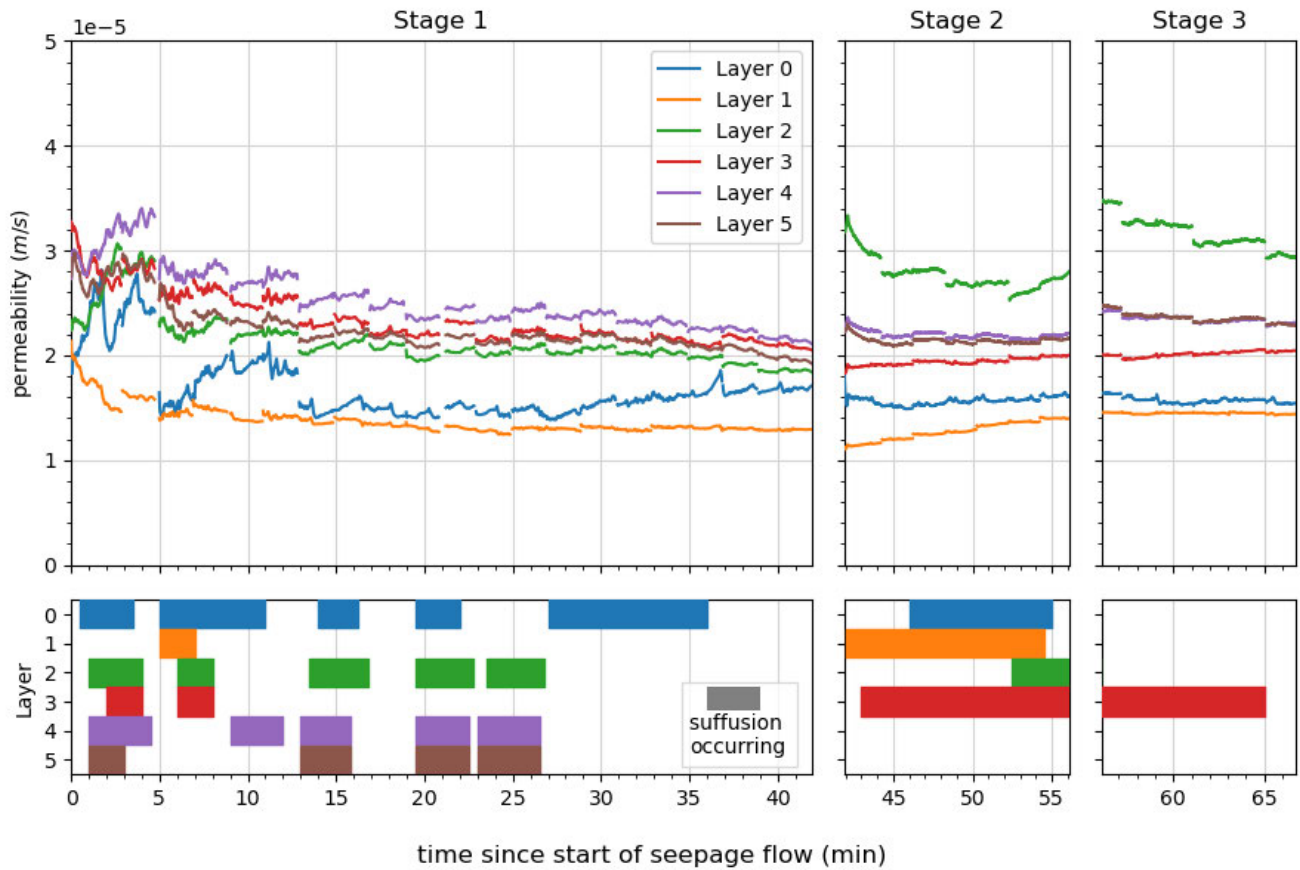


Figure 6.4: Permeability and timeline of suffusion events for each layer of $T_{30}L_{2.5/5}$

6.2.3 Post-test dissection

Looking at each layer of $T_{30}L_{2.5/5}$ in Table 6.4, the sample appears to have had a fairly homogeneous ultimate fine particle distribution, with very little difference between the lowest final fine particle contents of 19.60% in Layers 1 and 3, and the highest, 19.81% occurring in the bottom layer, Layer 5. There was a slight trend of a higher fine particle content towards the base of the sample, but with the ultimate content for the whole sample of 19.71%, there was little heterogeneity along the length of the seepage path.

When the cross-section of each layer is considered by examining its four quadrants, it is clear that there was significant variation perpendicular to the flow direction. For example, the North and East quadrants of Layer 3 exhibited a decrease in fine particle content from 20 to 19.16%, whilst the West quadrant has an ultimate percentage of 20.11%, meaning that this quadrant had a net gain in fine particles over the course of the centrifuge test. Layers 3, 4 and 5,

Table 6.4: Ultimate spatial distribution of fine particles from specimen dissection for test T30L2.5/5

Layer	Final fine particle content (%)				
	North	East	South	West	Total
0	19.84	20.04	19.12	19.78	19.68
1	19.56	19.30	19.77	19.78	19.60
2	19.71	19.90	19.64	19.92	19.79
3	19.16	19.16	19.81	20.11	19.60
4	19.55	19.55	19.97	20.03	19.80
5	19.81	19.65	20.09	19.67	19.81
Total	19.62	19.60	19.72	19.89	19.71

representing the bottom half of the sample, all recorded one quadrant with a fine particle content of over 20%, as did Layer 0 at the top of the seepage path.

In the South quadrant, in which the PPT ports were located, there was a clear trend of increasing fine particle content from the top to the bottom of the sample, varying from 19.12% in Layer 0 to 20.09% in Layer 5. This was much more pronounced than the increase observed in the whole layer average. The total ultimate fine particle content of the South quadrant was very similar to the whole sample, 19.72 compared to 19.71%, despite the variation across the layers being much greater.

Table 6.5: Total mass of the silt fraction lost over the duration of permeameter testing calculated from the dissected specimens

	<i>T40L2.5</i>	<i>T40S2.5</i>	<i>T40LCH</i>	<i>T30L2.5/5</i>	<i>T1LCH</i>
Mass of fine particles unaccounted for (g)	5.82	2.56	5.58	5.68	7.73
Percentage of initial fine particles lost (%)	2.43	2.05	1.84	1.79	2.29

In total, 5.68 g of the silt fraction were lost from the sample across the duration of the test, calculated from the dissected quadrants. This represents 1.79% of the total silt fraction, a smaller proportion than was lost from the 40-g

multi-stage seepage flow tests, discussed in Chapter 5. The mass of silt lost from each sample for all the dissected tests is compared in Table 6.5.

6.3 T20L5

6.3.1 Test description

Test *T20L5* was undertaken in two stages at a centrifuge acceleration of 20-g. The specimen in this test did not use the complete length of the permeameter, with the layer between PPT₀ and PPT₁, called Layer 0 in other full length tests, being filled with the overburden coarse sand. The first PPT on the seepage path located within the sample was consequently PPT₁ and the specimen height was 175 mm. In other respects the test was prepared in the same manner as the other full height samples. To aid comparison, the layer numbering in this test begins at 1 at the top of the sample, increasing to Layer 5 at the base of the sample, as with other tests. Figure 6.5 shows a photograph of the specimen configuration.



Figure 6.5: For *T20L5*, the top layer of the permeameter contained coarse sand, the specimen layers are numbered 1-5.

Over the course of the test the applied head difference was increased in increments of 5 mm to a maximum applied head difference of 145 mm, corresponding to an applied energy gradient of 138.8 kPa/m. Each interval of the multi-stage seepage flow was held for 2 minutes. The total energy expended by the seepage flow during the test was 34.6 J and the test lasted a total of 58 minutes. The hydraulic loading regime and cumulative energy expended by the seepage flow is presented in Figure 6.6. This test was designed to have a similar effective stress distribution and prototype seepage path length as the half-height sample *T40S2.5*, the results of which are presented in Section 5.4 and explored in relation to this test and the modelling-of-models concept in Chapter 7.

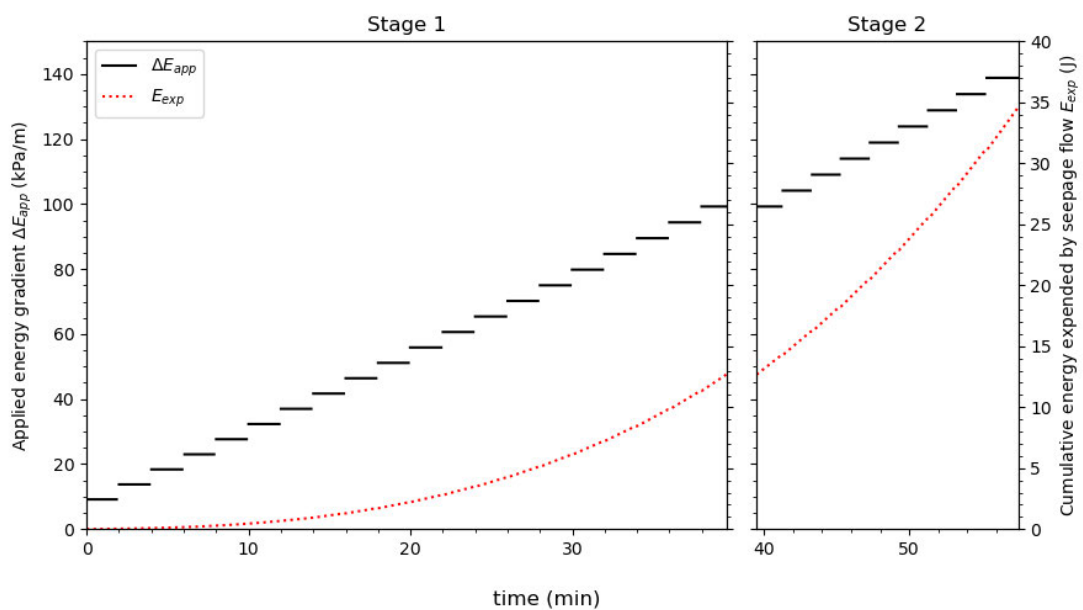


Figure 6.6: Energy gradient applied to *T20L5* and cumulative energy expended by the seepage flow over the 2 stages of testing

Figure 6.7 shows the effective stress profile within the sample at the beginning and end of centrifuge testing. Initially the effective stress increased from 33.5 to 100.0 kPa along the seepage path. At the end of the test, the effective stress at PPT₁ remained the same, whilst the stress at the base had increased to 124.4 kPa.

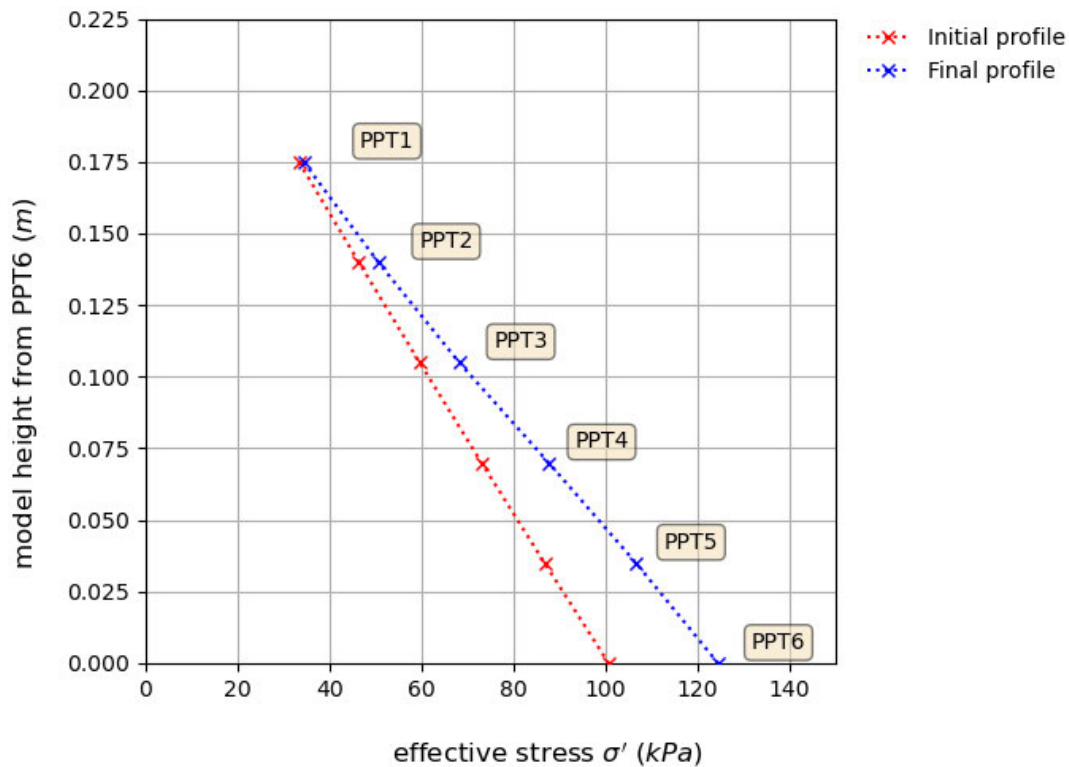


Figure 6.7: Effective stress profile in *T20L5* at the beginning and end of the centrifuge seepage flow test

6.3.2 Permeability response during testing

The global permeability of test *T20L5*, presented in Figure 6.8, shows that the specimen decreased in permeability for the entirety of testing, falling from 2.85×10^{-5} m/s at the start of Stage 1, to 1.61×10^{-5} m/s at the end of Stage 2, a decrease of 43.4%. The initial permeability of the sample was somewhat higher than the other centrifuge tests at the beginning of seepage flow, at 2.89×10^{-5} m/s. This was also higher than the initial permeability of the un-eroded soil from 1-g permeameter testing, which was 2.63×10^{-5} m/s (Section 4.3), but the final permeability in test *T20L5* was very similar to those reported in the other centrifuge tests, shown in Table 6.6.

The rate of global permeability decrease was faster at the beginning of the first stage, with the permeability starting to plateau at around 1.85×10^{-5} m/s towards the end of Stage 1. There was an increase in permeability of 7.6% over the spin-down break (Table 6.7). The permeability then steadily decreased by 2.38×10^{-6} m/s over the 18 minutes of Stage 2. During each applied head

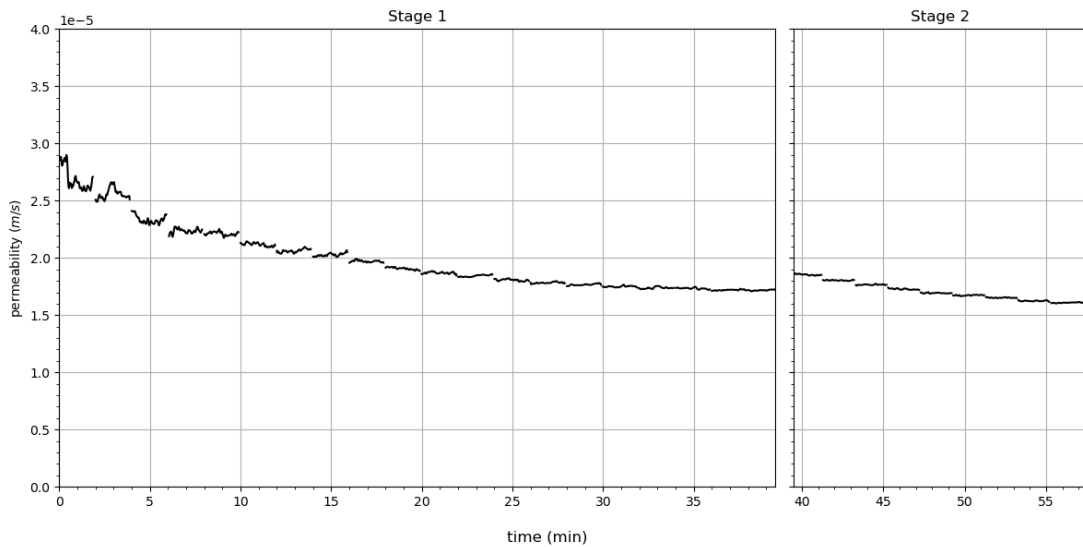
Figure 6.8: Global permeability of *T20L5*

Table 6.6: Final global permeability of centrifuge permeameter tests

Test	Final global permeability (m/s)
<i>T40L2.5</i>	2.03×10^{-5}
<i>T40L2.5(R)</i>	1.98×10^{-5}
<i>T40S2.5</i>	1.68×10^{-5}
<i>T40LCH</i>	1.71×10^{-5}
<i>T30L2.5/5</i>	1.97×10^{-5}
<i>T20L5</i>	1.61×10^{-5}
<i>T10L10</i>	1.18×10^{-5}

interval there was very little change in permeability, with any decrease in permeability occurring upon an increase in applied energy gradient.

The permeability of individual layers of the specimen during the test is shown in Figure 6.9, in this case Layer 1 is the first layer at the start of the seepage path. At the beginning of the test there was a general trend of layers further down the seepage path having a higher permeability than those at the top. Over Stage 1 all of the layers decrease significantly in permeability, with the exception of the top layer, Layer 1. The most pronounced of these clogging events was observed in the bottom layer, Layer 5, although this layer did start a

Table 6.7: Variation in permeability for each layer of test T20L5

Layer	Change in permeability (%)			
	During S1	S1 to S2	During S2	Whole test
1	-21.8	25.5	-5.7	-7.5
2	-29.1	11.0	-10.4	-29.5
3	-54.6	-0.9	-8.5	-58.8
4	-40.5	6.4	-18.5	-48.4
5	-49.6	2.4	-20.7	-59.1
Total	-39.7	7.8	-12.8	-43.4

comparatively high permeability of 4.63×10^{-5} m/s. By the end of the second stage, the permeability of Layer 5 was lower than that of Layer 1.

During Stage 1, the bottom two layers experienced short suffusion events lasting between 2 and 4 minutes, despite their general clogging behaviour. These events were markedly larger in Layer 5, where the permeability increased by 3.12×10^{-6} m/s between minutes 5 and 9, and 2.71×10^{-6} m/s between minutes 13 and 16. Layer 1 also experienced two shorter bouts of suffusion 10 minutes of testing, but much more pronounced was the increase its permeability of 2.75×10^{-6} m/s from 19 minutes until the end of the first stage. This increase in permeability did not continue into Stage 2, with no suffusion events recorded during this stage, although Layer 2 potentially showed some signs of beginning to increase in permeability towards the end of the test. This was not to a large enough degree to meet the criteria for a suffusion event.

The permeability of Layer 1 increased by 25.5% during the break between the testing stages, to a maximum value of 2.35×10^{-5} m/s. Layers 2, 4 and 5 also increased in permeability across the spin down break, despite their clogging behaviour during the centrifuge testing stages, although to a smaller degree than Layer 1 (Table 6.7). In comparison with the tests undertaken at higher g-levels presented in earlier sections, there was much less permeability fluctuation over the duration of this 20-g test.

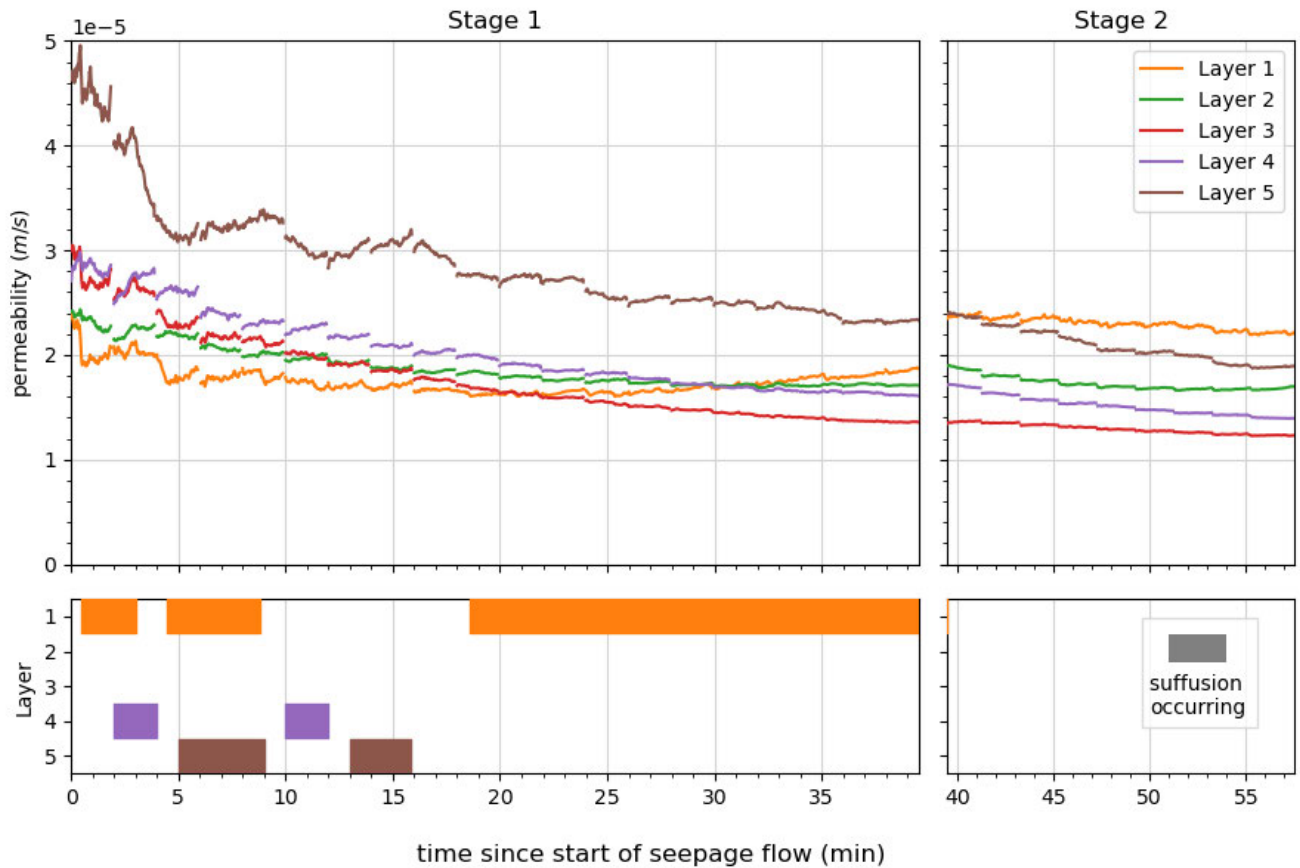


Figure 6.9: Permeability and timeline of suffusion events for each layer of $T20L5$

6.4 T10L10

6.4.1 Test description

Conducted at a centrifuge acceleration of $10-g$, test $T10L10$ was a multi-stage seepage flow test comprising of two stages and a total of 152 minutes. The head difference applied to the sample was increased in increments of 10 mm until a final head difference of 150 mm was applied. The final applied energy gradient was 61.6 kPa/m , with increments of approximately 4 kPa/m . Each interval was held for 10 minutes. This loading regime is presented in Figure 6.10.

Unlike other tests in this study, the head difference before and after the centrifuge spin-down were not the same, with a 10 mm increment having been added at the end of the first stage. This was due to the CHT being lowered just before the outlet tank reached capacity at the end of the first stage, and there was not enough flow rate data to analyse this interval. The head difference

was applied for under 30 seconds in Stage 1 before the outlet tank condition was noted, and the centrifuge spun down. The total energy expended by the seepage flow was 15.1 J, the lowest amount for any of the centrifuge tests due to the low g -level (Table 6.1). The specimen occupies the full six layers of the permeameter, giving a seepage path length of 210 mm. This test forms part of a suite of full length samples at different g -levels, including $T40L2.5$, $T30L2.5/5$ and $T20L5$, where each increment of applied head was designed to produce the same increase in flow velocity but a different applied energy gradient (Section 3.8).

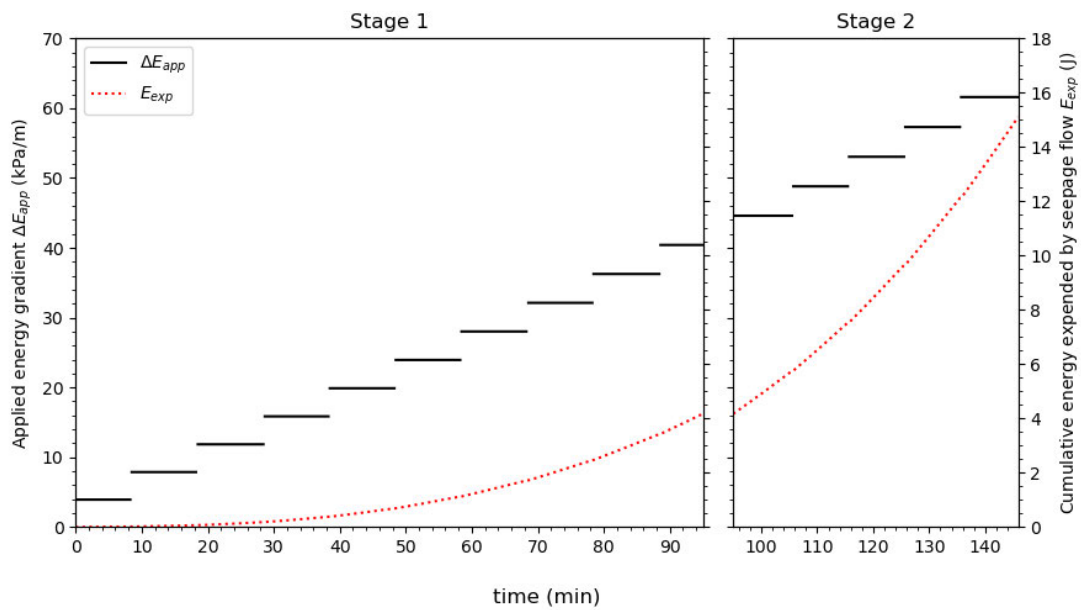


Figure 6.10: Energy gradient applied to $T10L10$ and cumulative energy expended by the seepage flow over the 2 stages of testing

Figure 6.11 shows the effective stress profile of the full height specimen at the beginning and end of centrifuge testing. Due to the low g -level, this was the smallest variation across the sample height and also the lowest effective stress at the base of the specimen. Initially, the effective stress level ranged from 10.3 kPa at the top to 49.5 kPa at the base. By the end of the test, the stress at the base increased to 63.0 kPa, whilst the stress at PPT 1 maintained almost the same value throughout the test.

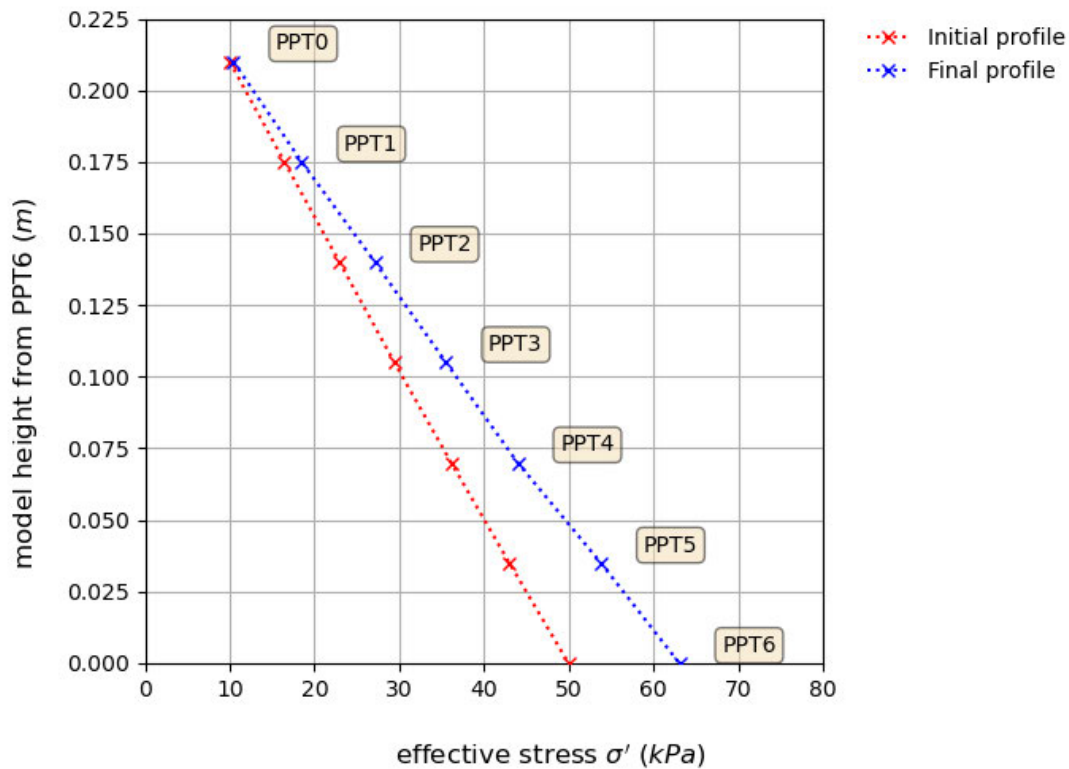


Figure 6.11: Effective stress profile in *T10L10* at the beginning and end of the centrifuge seepage flow test

6.4.2 Permeability response during centrifuge testing

Figure 6.12 shows the global permeability of the specimen over the two stages of testing. At the start of Stage 1, the global permeability was 1.51×10^{-5} m/s, which reduced to 1.18×10^{-5} by the end of Stage 2. During the centrifuge spin-down break, the permeability dropped by 5.0%. This decrease was countered by a slight gradual increase in permeability across Stage 2, with the final permeability being only 5.52×10^{-7} m/s higher than the permeability at the end of the first stage. In the first stage of testing, there was some variation in permeability across the 10 minute intervals, with the permeability generally increasing slightly. In contrast, there was very little permeability variation across the intervals in the second stage. The final permeability of 1.18×10^{-5} m/s was quite a lot lower than the the final permeabilities of other tests conducted in the centrifuge, shown in Table 6.6.

As shown in Figure 6.13, the permeability of Layer 2 fluctuated significantly during the first stage, having started from a permeability much higher than

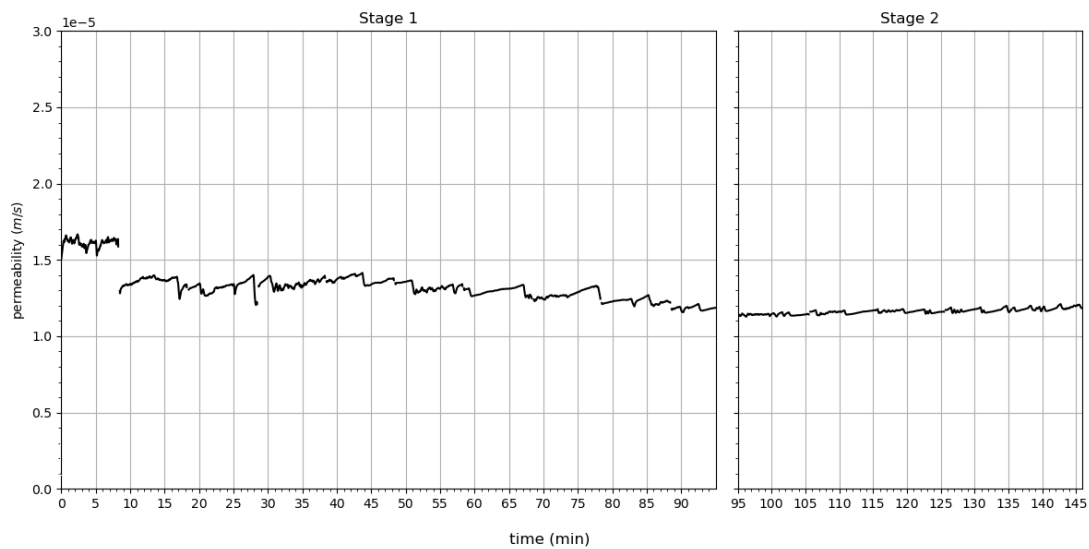


Figure 6.12: Global permeability of *T10L10*

the rest of the sample. This represents very little fluid head loss between PPTs 2 and 3, likely caused by the soil not being fully compacted against the wall of the cell in this area. As the hydraulic loading increased, local rearrangement of the granular matrix may have been the reason that the layer settled down to a permeability more in line with the rest of the specimen, aided by the stress relief of the spin-down break. This break saw Layer 2 reduce drastically in permeability, to a starting value of 1.37×10^{-5} m/s at the beginning of Stage 2. The permeability changes in this layer did not seem to follow the typical pattern of suffusion events and were likely caused by a local defect and so this layer has not been included in the timeline at the base of Figure 6.13 and is not considered in later analyses.

Layer 0, at the top of the seepage path, had a low starting permeability of 7.58×10^{-6} m/s and began to erode from the start of Stage 1, increasing by 6.13×10^{-6} m/s between minutes 0 and 44. After this point, the layer maintained a fairly constant permeability of around 1.4×10^{-5} m/s, although there were some suffusion events lasting between 4 and 8 minutes during some applied head intervals. All of the layers further down the seepage path decreased in permeability across the course of the first stage, with a minimum decrease of 33.7% occurring in Layer 5. There was much less fluctuation in permeability across all layers during the second stage of testing, which began with an applied head difference of 44.6 kPa/m. During Stage 2, both Layers 1 and 5 experienced gradual suffusion, increasing by 2.11 and 1.22×10^{-6} m/s respectively over the last 40 minutes. The other layers either maintained a

Table 6.8: Variation in permeability for each layer of test T10L10

Layer	Change in permeability (%)			
	During S1	S1 to S2	During S2	Whole test
0	89.1	-7.8	10.3	92.4
1	-37.5	-7.9	28.2	-26.2
2	-51.1	-24.8	0.9	-62.9
3	-38.3	13.3	-1.7	-31.3
4	-38.8	9.8	-6.5	-37.2
5	-33.7	-14.5	1.6	-42.4
Total	-21.3	-5.0	4.9	-21.6

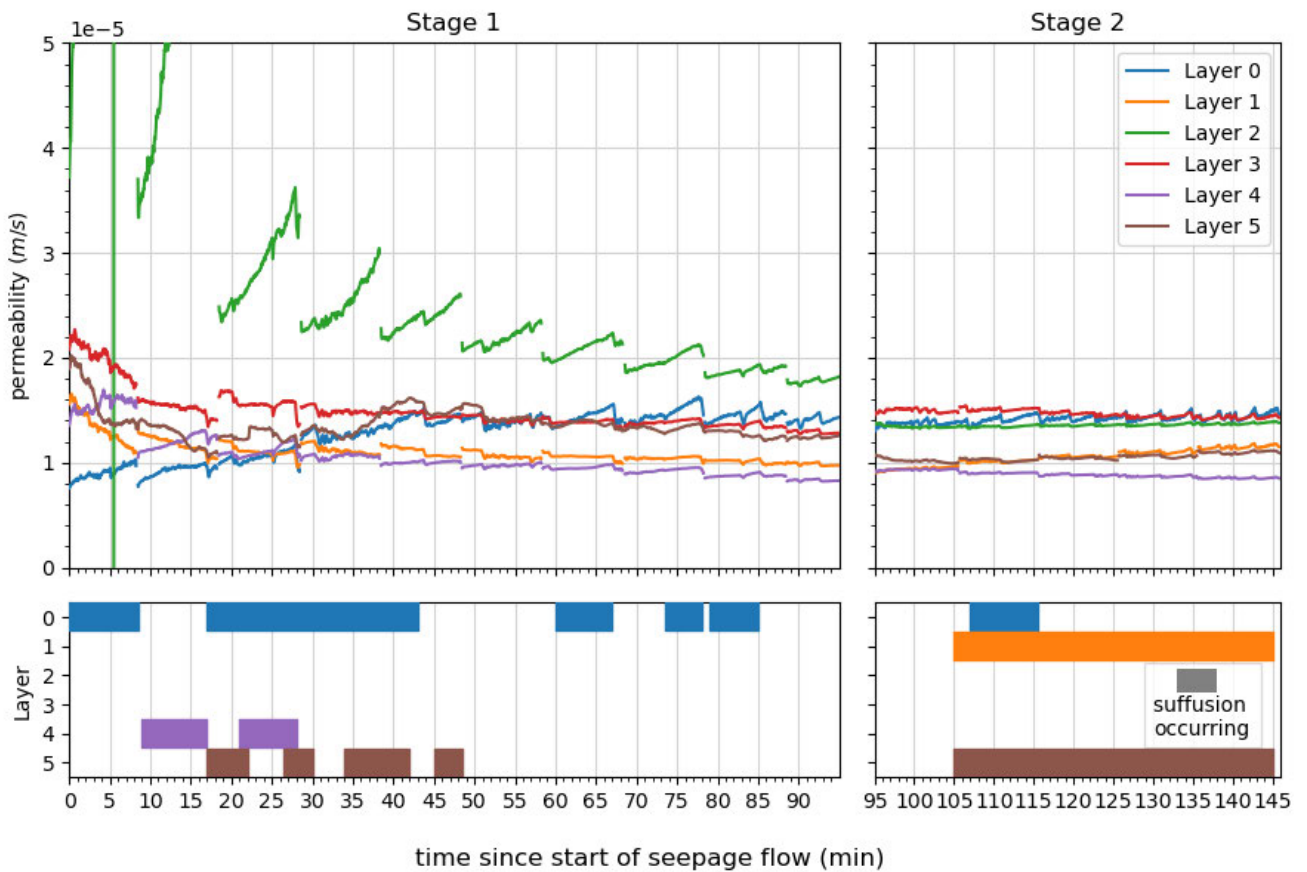


Figure 6.13: Permeability and timeline of suffusion events for each layer of T10L10

constant permeability or decreased slightly across this stage. Like with test

T20L5, there was significantly less temporal fluctuation in permeability of the specimen layers than observed in the tests conducted at higher g-levels.

6.5 T1LCH

6.5.1 Test description

Apart from the obvious difference that test *T1LCH* was conducted at 1-g, rather than in the centrifuge environment, there were several key differences in the way that this test was conducted compared to the centrifuge tests. These are outlined in Section 3.5.2 but repeated here for clarity.

- Piezometers were attached to PPT ports 0, 3 and 6 to take the pore pressure readings throughout the test. The water levels in the tubes were photographed throughout the test and analysed post testing.
- The other PPT ports were filled in, meaning that the specimen is only considered as two stacked layers of 105 mm each in height.
- As with test *T40LCH*, this test was conducted under a constant applied head difference, in this case 86 mm, leading to an applied hydraulic gradient of 0.41, rather than the multi-stage regimes of the other tests.
- The constant head seepage flow stage of the test lasted 120 hours, significantly longer than the maximum of around 2.5 hours for a centrifuge test. However, due to the 1-g conditions, the cumulative expended energy of the seepage flow was only 0.015 J.
- The flowrate though the sample was obtained by regular images of the mass balance of an outflow beaker filling with water.

Other than these variations, the test was prepared and dissected in much the same manner as the full length centrifuge tests. The total seepage path length of the sample was 210 mm. The effective stress under hydrostatic conditions was 1.48 kPa at the midpoint of the sample (PPT port 3). The results of dissecting the specimen are presented in Section 6.5.3.

6.5.2 1-g permeameter testing

Figure 6.14 shows the permeability of the specimen layers throughout the $i = 0.41$ stage of constant head testing. Prior to the constant head stage presented in this section, there was a stage conducted at a much lower hydraulic gradient ($i = 0.05$) lasting 2 hours, which was used in order to obtain the pre-erosion permeability of the soil. The results of this are presented in full in Section 4.3. The initial permeability of the specimen was found to be 2.63×10^{-5} m/s.

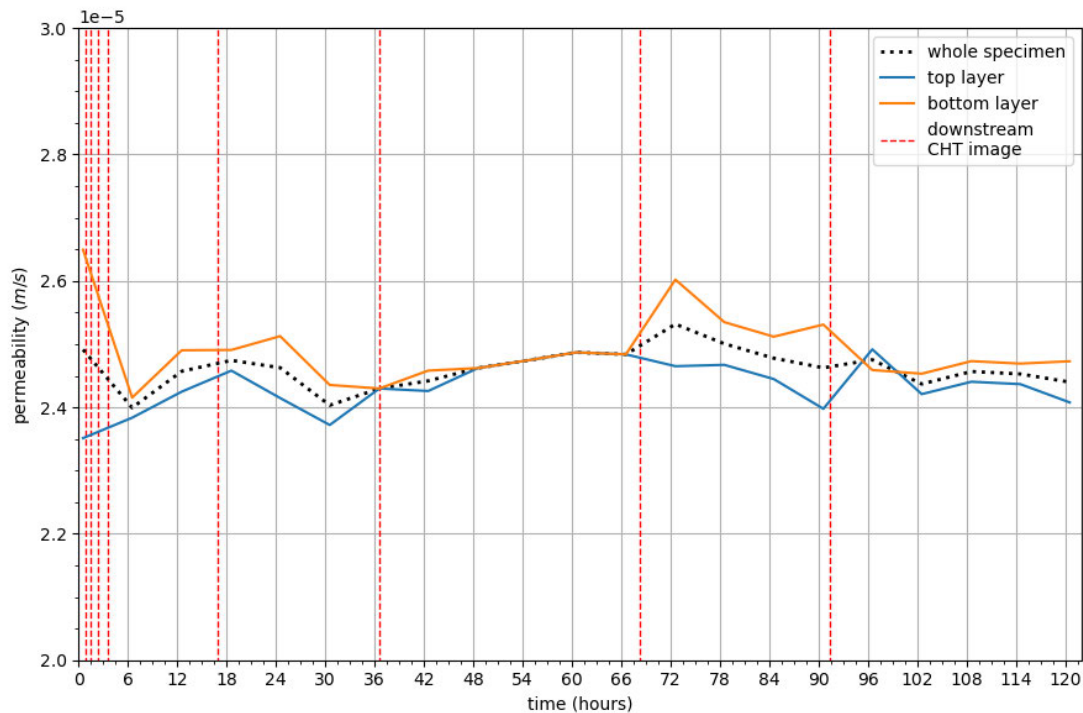


Figure 6.14: Permeability of each layer and whole specimen during 1-g constant head permeameter testing of $T1LCH$, with the time of the images in Figure 6.15 and Figure 6.16 indicated

For the main stage of testing, an applied head difference of 86 mm and hydraulic gradient of 0.41 was chosen, as this was the same hydraulic gradient applied in the 40-g constant head test, $T40LCH$. In that 40-g test, the applied head difference was 100 mm at model scale, but the variation in g across the radius of the sample reduces the pressure exerted from the raised CHT tank (Section 2.3.1).

Figure 6.14 shows the permeability of the layers of the specimen across the duration of the test. At the start of testing, when the head difference of 86 mm was first applied, there was the greatest permeability difference between

the top and bottom layers, with permeabilities of 2.35 and 2.65×10^{-5} m/s respectively. Over the first 6 hours of testing the specimen became more homogeneous in permeability, with both layers reaching a permeability of 2.4×10^{-5} m/s. As observed in the centrifuge tests, the permeability of the sample fluctuated throughout testing, although in this 1-g case, over much longer time periods.

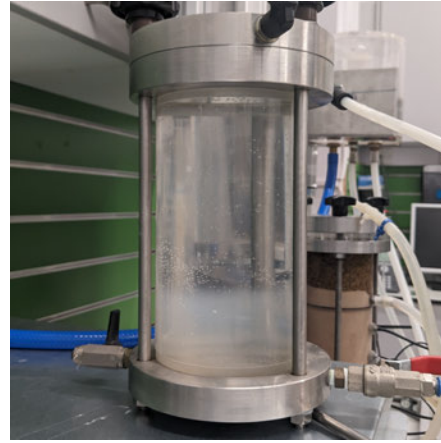
On several occasions over the course of the test, the top layer began to either increase or decrease in permeability, and then the bottom layer would begin to exhibit the same behaviour around six hours later, suggesting an interconnected behaviour between the two layers. For example, after 12 hour period of steadily decreasing permeability, the top layer began to increase in permeability at hour 30, with the bottom layer following suit at hour 36. The top layer then began to decrease in permeability at hour 66, and, after an increase in permeability of 1.67×10^{-6} m/s, the bottom layer also started to clog at hour 72.

When considering the whole sample permeability, there were two suffusion events identifiable from the permeability profile, although the first of these did not meet the minimum increase set out in the criteria presented in Section 5.1.1. The first occurred from hour 6 to hour 18, increasing by 7.49×10^{-7} m/s, and the second, longer, suffusion event began at hour 30. This suffusion event ceased at hour 72, and the global permeability of the specimen increased by 1.28×10^{-6} m/s. For most of this suffusion event's duration, the two layers demonstrated very similar behaviour. Although there were short variations in permeability for the individual layers after this event, on the whole the specimen decreased in permeability, to a final value of 2.44×10^{-5} m/s.

In Figure 6.14, vertical red dashed lines indicate the timestamps at which the images of the downstream CHT in both Figure 6.15 and Figure 6.16 were taken. Due to the configuration of apparatus, the clear-sided downstream CHT allowed observation of clouds of fine particles that were externally eroded from the specimen. In Figure 6.15, the four images taken within the first six hours of testing show an initial global suffusion event occurring. The front of cloudy water was first observed after 48 minutes, when fine particles removed by the seepage flow had migrated from the bottom of the sample into the effluent water. This erosion continued for at least one hour, and by 2 hours and 24 minutes into testing, there was clear water below the clouded portion, indicating that the suffusion event had ceased. This band of cloudy water



(a) Fine particles first observed at the inlet to the constant head tank (time: 48m)



(b) Fine particles were still being eroded (time: 1 h 30 m)



(c) Clear water under the cloudy portion show that the global suffusion event had ceased (time: 2 h 24 m)



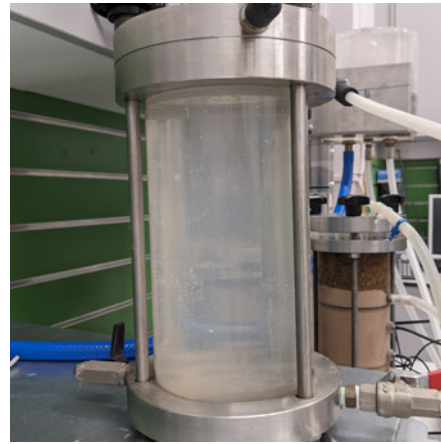
(d) The erosion front continued to move up the tank with the clear water below (time: 3 h 35 m)

Figure 6.15: A front of externally eroded fine particles moving through the downstream constant head tank at the start of 1-g permeameter testing, T_{1LCH}

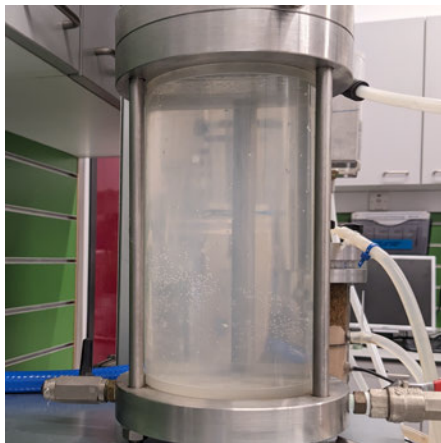
continued to move with the seepage flow, as shown in the fourth photograph, suggesting that the suspended particles were carried along with the upwards fluid flow.



(a) Effluent water very cloudy (time: 16h 56m)



(b) Effluent water still cloudy (time: 36 h 30 m)



(c) Opacity of effluent water began to reduce (time: 68 h 15 m)



(d) Effluent water clearer than previous observations (time: 91 h 24 m)

Figure 6.16: Cloudiness in downstream constant head tank indicates fine particles eroded from sample throughout 1-g permeameter testing, *T1LCH*

Figure 6.16 shows images of the downstream CHT further into the test. In all of the photographs, there is some evidence of fine particles suspended in the effluent water, but this level varied, indicated by the relative opacities of the water. It would be useful to know whether the cloudiness observed in the images, which were taken between 19 and 32 hours apart, was the result of fine particles from the same or different suffusion events. This can be examined

through Stoke's Law for particles settling in a stagnant medium. The settling velocity, v_s , can be expressed as follows:

$$v_s = \frac{(\rho_p - \rho_w) g d_p^2}{18\mu} \quad (6.1)$$

where:

ρ_p and ρ_w are the densities of the particle and fluid, 2650 and 997 kg/m³ respectively,

g is gravitation acceleration, 9.81 m/s²,

d is the diameter of the particle in m (assumed to be spherical),

and μ is the fluid viscosity, equal to 10⁻³ Pa.s.

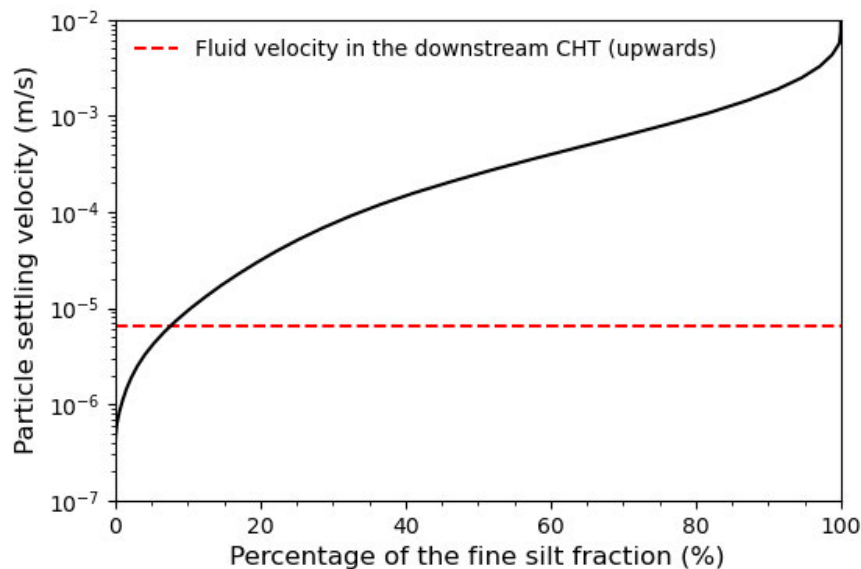


Figure 6.17: Settling velocities of the fine silt particles based on Stoke's Law compared to the upwards flow velocity in the downstream CHT tank for test *T1LCH*

The flow velocity in the downstream CHT was fairly steady for the duration of the test, at around 6.45×10^{-6} m/s. If the settling velocity of the fine particles was greater than the fluid velocity, then the particles would have remained in the CHT for longer than the suffusion event, whereas smaller particles with lower settling velocities would have been carried along with the flow. Figure 6.17 shows the calculated settling velocity for the fine grains by their cumulative percentage. From this graph it is clear that particles larger than d_8 , which had a grain size of 2.5 microns, would have settled in the outflow tank, as their settling velocities are higher than the upward fluid velocity.

Whether or not the fine particles in the CHT are the same for each image in Figure 6.16 depends on how the fine particles were being removed from the sample. If the smallest fine particles were migrating first, then the images likely show either four separate or one continuous external suffusion event, whereas if fine particles of any diameter were equally likely to be picked up from the pores of the specimen by the seepage flow, then the cloudiness in the fourth image could be remnants of a suffusion event that occurred significantly earlier in the test.

Interestingly, the temporal permeability profile in Figure 6.14 shows that the first three photographs in Figure 6.16 were taken after periods of increasing permeability, and therefore suffusion. In contrast, the fourth and final image was taken after around 18 hours of clogging. The effluent water is noticeably less opaque in the final image, although there is still evidence of some silt in the water.

6.5.3 *Post-test dissection*

As with the centrifuge tests dissected, test *T1LCH* was subdivided into six layers which were then split into four quadrants each. Due to the coarser spacing of the piezometer ports compared to the PPTs, Layer 0, 1 and 2 correspond to the top layer analysed for permeability in Section 6.5.2, and Layers 3, 4 and 5 comprised the bottom layer. The piezometer ports were located in the south quadrant of the sample.

The ultimate silt content of the sample post-testing was found to be 19.63%, with a measured loss of fine particles of 7.73 g from the original 20% fine particle content. This represents a loss of 2.29% of the initial silt fraction. As mentioned in the previous section, a band of cloudy water was observed in the downstream CHT during testing, showing that external suffusion, i. e. global loss of fine particles, did occur during the test.

In general, there was a similar amount of cross-sectional variability in each of the layers of this test, with the highest variability occurring in Layer 1 (0.71%). In contrast to most of the tests conducted in the centrifuge, with the exception of the incompletely dissected *T40L2.5*, none of the quadrants in *T1LCH* had an ultimate fine particle content higher than the initial 20%. Whilst some localised

Table 6.9: Ultimate spatial distribution of fine particles from specimen dissection for test *T1LCH*

Layer	Final fine particle content (%)				
	North	East	South	West	Total
0	19.56	19.69	19.75	19.30	19.58
1	19.37	19.13	19.84	19.33	19.42
2	19.95	19.67	19.68	19.59	19.73
3	19.60	19.58	19.75	19.43	19.60
4	19.78	19.74	19.67	19.79	19.73
5	19.88	19.80	19.68	19.57	19.73
Total	19.69	19.60	19.72	19.49	19.63

clogging may have occurred, each quadrant exhibited a net loss of its fine particles.

Layer 0, at the top of the seepage path had on average the highest loss of fine particle at a final content of 19.58%, with a general trend of increasing fine particle content along the seepage path. Both the bottom layers, Layers 4 and 5, had ultimate fine particle contents of 19.73% and, along with the overlying Layer 3, showed variability perpendicular to the seepage flow direction of less than 0.32%.

6.6 SUMMARY

In this chapter the results of four experimental tests were presented. Three of these were conducted in the centrifuge using a multi-stage seepage flow approach at g-levels lower than 40-g. The final test presented was a constant head test conducted at 1-g in the modified centrifuge permeameter. Of these four tests, two were dissected after permeameter testing, and their ultimate spatial variation in fine particle contents were presented alongside the temporal permeability results. A summary of the key findings of this chapter is given here.

- The lower-g tests presented in this chapter exhibited significantly fewer fluctuations between suffusion and clogging behaviours over the duration of applied seepage flow compared to the tests conducted at 40-g.
- As with the tests in Chapter 5, the global permeability taken across the sample was not representative of the local variations in permeability, whilst the interstitial pore pressure readings revealed a more complex spatial development of fine particle migration.
- Although they exhibited local increases in permeability, globally the specimens at 10- and 20-g appeared to clog throughout the tests, whilst the 30-g test initially decreased in permeability, but did show signs of global erosion by the end of the test. This is in contrast to the tests conducted at 40-g, which demonstrated a general trend of initial erosion, followed by a gradual decrease in permeability.
- The 1-g test, *T1LCH*, showed signs of erosion during the test and upon dissection of the specimen, despite being subjected to significantly less energy from the seepage flow than the centrifuge tests. This erosion could be visually observed through fine particles in the effluent water.
- In both the dissected centrifuge test presented in this chapter, *T30L2.5/5*, and those presented in Chapter 5, typically areas of net increase in fine particles were observed towards the bottom half of the seepage path. This was not the case for the dissected 1-g test, *T1LCH*.
- As with the dissected samples at 40-g, shown in Chapter 5, the net change of fine particles across the course of the test was very small, with the lowest reported local fines percentage being 19.12% in Layer 0 South for *T30L2.5/5* and 19.13% in Layer 1 East for *T1LCH*. In the latter test, external suffusion is known to have occurred, by observation of fine particles in the effluent water, but in both tests there is no obvious connection between the change in local permeability and the spatial final fines content. There was a net decrease in all but one layer permeability over the duration of *T30L2.5/5*, but the dissection shows a fine content reduction in all layers, suggesting that the absolute quantity of fine particles does not control the permeability variation seen during suffusion, but instead their position within the coarse particle matrix. This idea is explored further in Section 8.4.

ANALYSIS AND DISCUSSION: CENTRIFUGE PERSPECTIVES

In this chapter, the results obtained in this study are interpreted using a modelling-of-models approach, based on conventional centrifuge scaling laws and assumptions. Three different combinations of tests are analysed, considering both the onset, progression and final outcome of suffusion observed in the permeameter tests. The first suite of tests compares identically prepared models with different stress gradients and loading regimes applied to them, whilst the second comparison explores whether modelling the same centrifuge prototype leads to the same suffusion response within the specimen. These two comparisons allow the concept of the hydromechanical envelope for suffusion onset from Li and Fannin (2022) to be examined from a centrifuge perspective. The final comparison considers the two constant head tests from this study, one conducted in the centrifuge and the other at 1-g. The post-test dissection of these tests are analysed using the expended energy approach originally proposed by Marot et al. (2011).

7.1 MODELLING-OF-MODELS 1: $T_{40L2.5}$, $T_{30L2.5/5}$, T_{20L5} AND T_{10L10}

The first of the three modelling-of-models comparisons made in this study concerns tests $T_{40L2.5}$, $T_{30L2.5/5}$, T_{20L5} , and T_{10L10} . This suite of multi-stage seepage flow tests was designed to explore the influence of vertical effective stress and scaled seepage path length on the onset and progression of suffusion by testing identically prepared models at g-levels between 10- and 40-g (Section 3.8). The hydraulic loading regimes were designed so that the increments of applied energy gradient and seepage velocity through the specimen were equivalent between tests, whilst the applied hydraulic gradient and effective stress profile scaled with g-level. This was done with the aim of achieving the same seepage flow regime within the specimens at the early stages of testing, before significant erosion could occur. The full results for the

tests in this comparison can be found in Sections 5.2.2, 6.2.2, 6.3.2 and 6.4.2 respectively.

7.1.1 Initial observations: whole specimen behaviour

Table 7.1 compares the test results between the four tests to highlight how the centrifuge acceleration influenced the final hydromechanical regime within the specimens. At the higher g-levels, the specimens were subjected to a higher maximum applied energy gradient, $E_{G_{app,max}}$, and consequently had a higher cumulative energy expended, E_{exp} . The tests at 10- and 20-g were subjected to a slightly higher maximum applied hydraulic gradient than the two at 30- and 40-g, as they had a larger final displacement of the downstream CHT. Test $T_{40L2.5}$ was the only one to show a net increase in global permeability, Δk_{var} , over the course of the test, increasing by 42.1%. The tests at lower g-levels showed net reductions in global permeability, although a global suffusion event was identified during the second stage of testing for $T_{30L2.5/5}$.

Table 7.1: Comparison of the key testing parameters in the four centrifuge tests conducted as part of modelling of models comparison 1.

Test	$i_{app,max}$	$\Delta E_{app,max}$ (kPa/m)	v_{max} (m/s)	E_{exp} (J)	Δk_{var} (%)	Global suffusion
T40L2.5	0.474	195.6	5.3×10^{-4}	206.5	+42.1	✓
T30L2.5/5	0.495	151.1	2.7×10^{-4}	55.2	-20.2	✓
T20L5	0.661	138.8	2.2×10^{-4}	34.6	-43.4	-
T10L10	0.598	61.6	8.0×10^{-5}	15.1	-21.6	-

Comparing the global permeability profiles for the four tests, shown in Figure 7.1, gives a clearer understanding of how the net changes in permeability in Table 7.1 developed over time. There is a clear difference between the behaviour of the tests between the higher and lower centrifuge accelerations. Test $T_{40L2.5}$ experienced suffusion from almost the very start of the test, and test $T_{30L2.5/5}$ also showed an increase in global permeability at around 40 minutes into testing. In contrast, tests T_{20L5} and T_{10L10} show continual global clogging for the duration of testing. These seems to suggest that the longer

the seepage path, the more susceptible a sample is to global suffusion. This is consistent with the results of Zhong et al. (2018), who found that the onset of suffusion occurred at lower hydraulic loading with an increasing seepage path length. Experimental studies tend to observe that higher effective stresses either increases (Li, 2008; Moffat, 2005) or does not affect (Crawford-Flett, 2014; Slangen, 2015) the critical hydraulic conditions for the onset of suffusion (Section 2.5.3), but that does not appear to be the case when comparing these tests, as global suffusion initiates at lower hydraulic gradients in the more highly stressed samples.

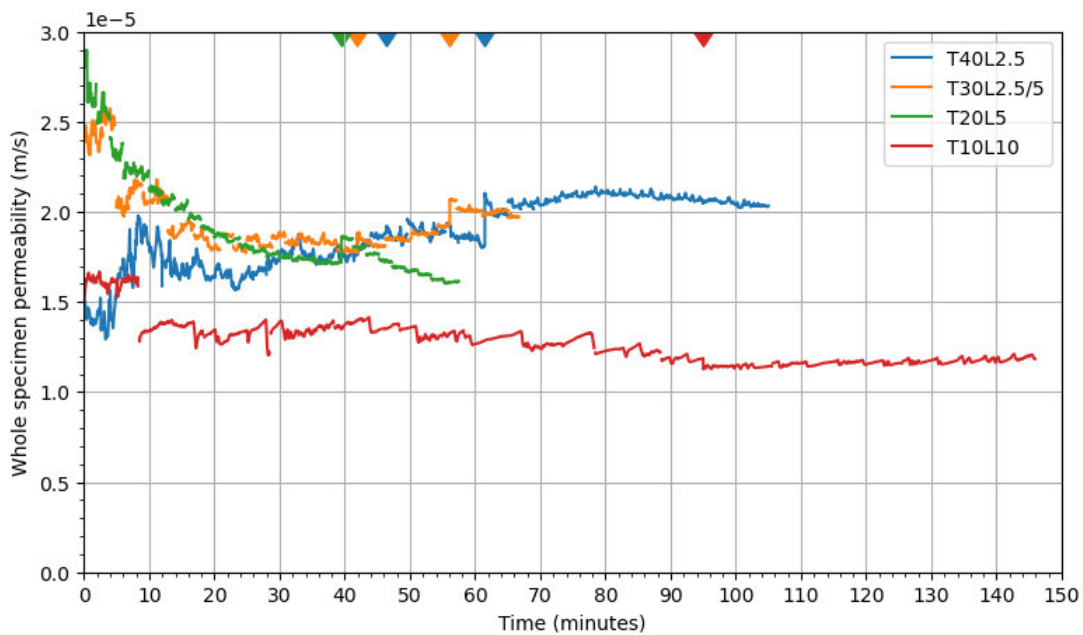


Figure 7.1: Global permeabilities of each of the tests $T_{40L2.5}$, $T_{30L2.5/5}$, T_{20L5} and T_{10L10} in time (centrifuge spin-down breaks marked with coloured triangles)

By the end of all four tests, suffusion events in all the layers had ceased. The suffusion events during the early intervals had shorter durations than those towards the end of the tests. This supports the findings of Rochim et al. (2017), who observed that specimens appeared to have a finite amount of fine particles available to be externally eroded from the sample, and termed this the fully eroded state. The tests in this current study were designed to capture the early stages of erosion at hydraulic gradients likely to be observed in real water-retaining structures. To fully explore whether the fully-eroded state was reached in these tests, an extension to this work would be to subject a test

specimen to the high hydraulic gradients used in studies such as Moffat (2005) and Li (2008), and see if further suffusion would occur.

Figure 7.1 shows that tests *T20L5* and *T10L10* did not experience global suffusion during testing, although local suffusion was observed in individual layers for both tests. This is shown in the permeability profiles of the individual layers in Figure 6.9 and Figure 6.13. In both of these tests, suffusion events occurred only in the layers at the start and end of the seepage path, with no discernible suffusion occurring in the middle layers of the specimens. This preferential suffusion at the extremities of the specimen was also observed in the X-ray tomography of Nguyen et al. (2019), where the specimen was only subjected to its own self-weight. Short, sporadic suffusion events occurred in both *T20L5* and *T10L10* during the first few hydraulic loading increments, whilst longer, more gradual increases in permeability were observed towards the end of the tests. This general trend was the same between all four tests in this comparison, and suggests that the incremental onset of very low seepage flow causes an initial rearrangement of fine particles, but a higher hydraulic loading is needed to cause continuing suffusion to occur.

The hydromechanical conditions at the onset of each global suffusion event for the 40-g and 30-g tests are given in Table 7.2. The first onset of suffusion in both tests corresponded to the first increment in hydraulic loading, which initiated at an energy gradient EG of 7.2 kPa/m across *T40L2.5* and 7.1 kPa/m across *T30L2.5/5*. This is equivalent to hydraulic gradients of 0.021 and 0.026 respectively. At 40-g, the change in permeability for the first suffusion event was 2.5 times larger than the first event for the specimen at 30-g. The mean vertical effective stress in *T40L2.5* was 1.3 times higher than in *T30L2.5/5*. The table demonstrates that global suffusion occurred throughout the two tests. The duration of the suffusion events increased as the tests progressed, whilst the magnitude of each permeability change decreased. The critical hydraulic gradients for the gap-graded, under-filled soils of Zhong et al. (2018) were between 0.07 and 0.13 (Section 2.6.3), a similar range to those at the start of the suffusion events in Table 7.2.

Comparing the maximum conditions reached in each of the tests in Table 7.1 with the conditions at onset of suffusion in Table 7.2, it can be seen that both tests *T20L5* and *T10L10* ultimately reached seepage flow velocities and applied energy and hydraulic gradients higher than those needed to initiate suffusion in the higher-g tests, and yet no suffusion events were observed. This could

Table 7.2: Testing conditions at the onset of the four global suffusion events for test $T_{40L2.5}$ and three events for $T_{30L2.5/5}$

Test	Duration (s)	Δk ($\times 10^{-6}$ m/s)	v ($\times 10^{-5}$ m/s)	i	EG (kPa/m)	σ_{vm} (kPa)
$T_{40L2.5}$						
	260	4.06	1.27	0.021	7.2	118.8
	540	2.55	6.65	0.110	40.4	122.0
	330	1.21	13.5	0.209	76.2	125.8
	900	1.21	31.1	0.422	154.2	126.4
$T_{30L2.5/5}$						
	210	1.63	1.48	0.026	7.1	89.5
	120	1.30	3.12	0.055	15.1	90.8
	600	1.19	17.7	0.350	96.5	100.6

be caused by a fundamental change in fines distribution in the early clogging stages shown in Figure 7.1, meaning that by the time the conditions in Table 7.2 were reached, the material being tested was functionally very different. The CFD-DEM work of Liu et al. (2023) supports this idea, as it found that local variability in fines content caused a zone where particles are more likely to be deposited, causing a larger area of clogging, which influences the flow regime in the surrounding area.

When comparing the behaviour of the interstitial layers of these four specimens (Figure 5.5, Figure 6.4, Figure 6.9 and Figure 6.13), there was greater fluctuation in permeability in the higher g -tests, suggesting a more dynamic formation of zones of suffusion and clogging locally under higher hydromechanical loading. The more rapid loading case of Rochim et al. (2017) resulted in a more sudden increase in permeability, whilst the more gentle loading caused a slower more gradual response. This trend was also reported in the under-filled permeameter tests of Annapareddy et al. (2023) (Section 2.6.1). This is also observed when comparing the amount of permeability fluctuation under the comparatively large increases of EG_{app} of $T_{40L2.5}$ compared to T_{10L10} .

7.1.2 Initial observations: top layer behaviour

Clearly, the behavioural response of the specimens varies with the varying vertical effective stress and particle migration history along the length of the specimens. The relatively long length of samples in this study allows for a variation behaviour across the seepage path, with some layers exhibiting suffusion events that are not picked up at the global scale. Another way to consider the results from these tests is to consider the top 35 mm layer of the specimen between the first two PPT ports in isolation. These layers in the centrifuge permeameter represent a seepage path length of around $215 d_{50}$ particles, similar to the whole specimen length in Li (2008). The top layers of the sample can be considered as smaller individual elements, as there are no overlying layers, so no new particles can enter the layer during the test. At prototype scale these layers have different seepage path lengths and different mean vertical stresses, as shown in Table 7.3.

Table 7.3: Scaled seepage path length and initial effective stress in the top layers of the four tests conducted as part of modelling of models comparison 1, along with their net permeability change across the test duration.

Test	Δz_P (m)	σ'_{vm0}	Δk (%)	Suffusion event
T40L2.5	1.16	53.7	+105	✓
T30L2.5/5	0.88	40.5	-23.6	✓
T20L5	0.62	40.0	-7.4	✓
T10L10	0.29	13.5	+92.4	✓

Interestingly, the two top layers with the lowest permeability shown in Figure 7.2, *T40L2.5* and *T10L10*, eroded from the start of the test, whereas the top layers with higher permeabilities initially exhibited a decrease in permeability, only starting to erode after some time. By the end of testing, the layers all appear to have reached a somewhat stable state, with no further suffusion occurring. The top layers with the higher effective stresses were steadily decreasing in permeability at the end of the test, whilst the top layer of *T10L10* maintained a constant permeability. The decrease in permeability in these top layers must be attributed to a rearrangement of the fine particles

within the layer, as there can be no particles deposited from overlying layers. There was no discernable settlement in any of the tests, which were prepared to a high relative density (70%). Upon dissection, the two tests of this set with a known ultimate fine particle distribution, $T_{40L2.5}$ and $T_{30L2.5/5}$, showed a reduction in fine particle content in the top layer, from 20% to 19.49% and 19.68% respectively.

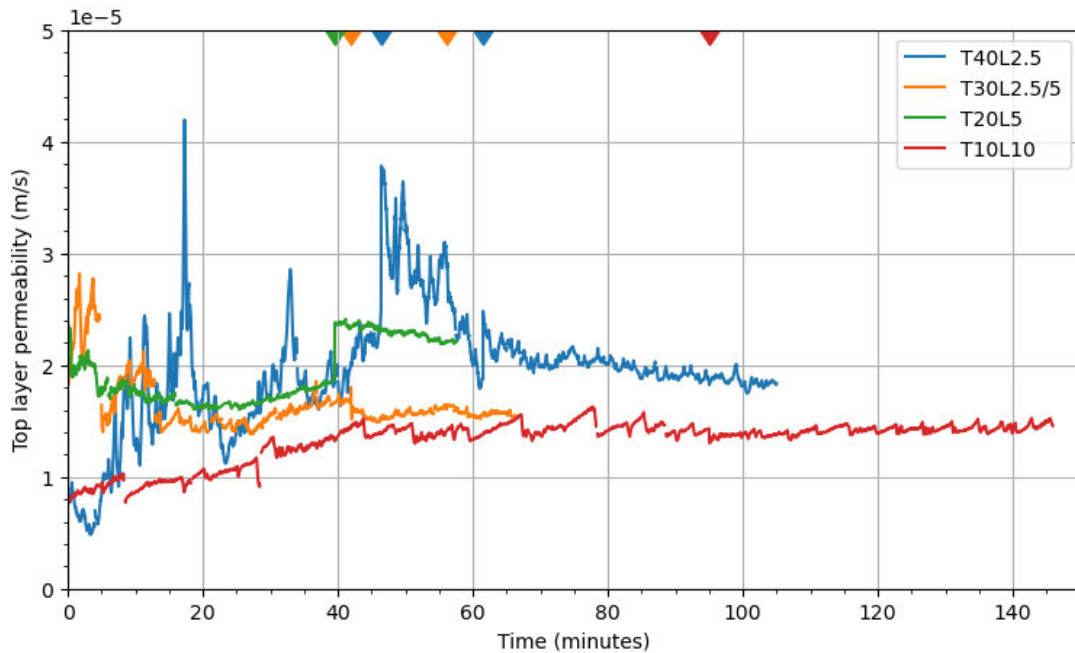


Figure 7.2: Local permeabilities of the top layer of each of the tests $T_{40L2.5}$, $T_{30L2.5/5}$, T_{20L5} and T_{10L10} in time (centrifuge spin-down breaks marked with coloured triangles)

7.1.3 Onset of suffusion: hydromechanical envelopes

As discussed in Section 2.5.1, Li (2008) suggested that the α factor can be calculated from an empirical relationship between the 85th percentile of the finer fraction grain size, d'_{85} , and the effective diameter of the coarser fraction's pore constrictions, O_{50} , given in Equation 2.17 and reiterated here as Equation 7.1. Using this equation, α is an intrinsic property of a soil and defines the hydromechanical envelope of Li and Fannin (2022), as discussed in Section 2.5.2.

$$\alpha = 3.85 \left(\frac{d'_{85}}{O_{50}} \right) - 0.616 \quad (7.1)$$

By using Equation 7.1, the geometric α factor can be calculated for the soil used in this study, an approach that has been used in other suffusion studies, including the centrifuge work by Marot et al. (2012). Previously in this study, the coarse and fine fraction have been split at the 20% fines content, as presented in Section 3.2.2. However, to apply the Kovacs (1981) method, the location of the split between the coarser and finer fraction that gives the minimum value of d'_{85}/O_{50} must be found, which is computationally inconvenient to calculate. Consequently, Li and Fannin (2013) proposed a simplified approach where the soil is split at the point of minimum H/F value (Section 2.4.1) which returned very similar threshold values. For this soil, this threshold point, F_n , occurs at 12.8% passing on the PSD. The d'_{85} of the modified finer fraction can be easily determined as 18 microns. A more complicated value is O_{50} , which can be calculated following the simplified Kovacs (1981) method as follows:

$$O_{50} = 4 \times \frac{n_c}{1 - n_c} \times \frac{D_h^c}{SF} \quad (7.2)$$

n_c is the porosity of the coarser fraction,

D_h^c is the Kozeny effective diameter of the coarse fraction and

SF is the Kozeny Carman shape factor (taken as 6.6 for sub-angular particles, as discussed in Section 2.4.1).

The porosity of the coarse fraction, n_c , can be calculated using Equation 7.3 based on the porosity of the soil mixture, n , and the mass percentage of the finer fraction, F_n . The porosity of the soil was calculated in Section 3.2.2 and at 70% relative density was equal to 0.339.

$$n_c = n + F_n(1 - n) = 0.423 \quad (7.3)$$

The Kozeny effective diameter for the coarse fraction can be calculated using the summation portion of Equation 2.14, shown in Equation 7.4. For just the coarse soil fraction, the effective diameter, D_h^c , can be calculated as 0.119 for the soil gradation used in this study.

$$D_h^c = \frac{100\%}{\sum \frac{f_i}{D_{li}^{0.404} \times D_{si}^{0.595}}} \quad (7.4)$$

Inputting these values into Equation 7.2 returns an O_{50} value of 52.8 microns. Substituting this and $d'_{85} = 18$ microns into Equation 7.1 gives a d'_{85}/O_{50} value of 0.341 and a theoretical α value of 0.696. This indicates a marginally unstable soil, and suggests a significant portion of the effective stress is transferred by the finer particles (Section 2.5.1). This is at odds to the Skempton and Brogan (1994) interpretation of a bimodal soil (Figure 2.4), where under-filled soils with less than 24% finer fraction are predominantly supported by the coarse matrix.

The theoretical critical hydraulic gradient under downwards seepage flow will be calculated using Equation 2.20 from Li and Fannin (2022), for test T40L2.5 as an example case. This approach will then be applied to the results from the top layers of the samples to assess the feasibility of a hydromechanical envelope in the context of this study.

The initial effective stress, σ'_{vm0} , at the midpoint of the specimen in test T40L2.5 was 117 kPa. The model distance between the topmost and bottommost PPTs was 210 mm, and when scaled to prototype distance at 40-g (accounting for the radial variation in N – Section 2.3.1), this gives $\Delta z_P = 7.85$ m. Substituting these values into Equation 2.18 to find the value of the normalised initial effective stress gives $\bar{\sigma}'_{vm0} = 1.52$. As this test, along with all others in this study, was conducted under downwards seepage flow, Equation 2.20 from Li and Fannin (2022) is used here to calculate the theoretical critical hydraulic gradient, $i_{cr,d}$, as follows:

$$i_{cr,d} = \frac{\alpha}{1 - \alpha} \left(\bar{\sigma}'_{vm0} + 0.5 \frac{\gamma'}{\gamma_w} \right) = \frac{0.696}{1 - 0.696} \left(1.52 + 0.5 \frac{17.6 - 9.8}{9.8} \right) = 4.39 \quad (7.5)$$

By including the Δz_P term in normalising the vertical mean effective stress, the distance between the measurement points becomes very important, recalculating Equation 7.5 for the same midpoint of the specimen but considering the seepage path between PPT2 and PPT4 rather than across the whole sample gives $i_{cr,d} = 11.34$, a significantly higher value. Compared to the critical hydraulic gradients reported in literature, Zhong et al. (2018) reported i_{cr} values

below 0.13 for their under-filled soils and Rochim et al. (2017) found critical values between 0.5 and 2 for the same soil depending on the hydraulic loading regime. A significant amount of variation can be attributed to the different definitions of suffusion onset.

Zhong et al. (2018) defined suffusion onset at a 10% permeability change measured across an interval, whilst Li (2008) looked for a seepage velocity change and rapid increase in hydraulic conductivity. These could be said to correspond to the lower and higher hydraulic gradients for onset and latter failure used by Liang et al. (2019). The definition of suffusion onset used in this study (Section 5.1.1), is more similar to that of Zhong et al. (2018), corresponding to a permeability increase of approximately 5% over the course of two minutes. This is likely why suffusion is observed at significantly lower hydraulic gradients in this study compared to Li (2008).

Table 7.4: Observed critical hydraulic conditions for the onset of the first suffusion even in the top layer of each test in modelling-of-models comparison 1 alongside the critical hydraulic gradient calculated from Li and Fannin (2022). The top layer of T20L5 was located between PPT1 and 2, rather than PPT0 and 1 as in the other tests, explaining the higher effective stress and layer number.

Test	Layer	$i_{cr,d}$	$i_{cr,observed}$	$EG_{cr,observed}$ (kPa/m)	$v_{cr,observed}$ ($\times 10^{-5}$ m/s)
T40L2.5	0	11.69	0.049	19.4	1.27
T30L2.5/5	0	11.62	0.028	8.2	1.48
T20L5	1	15.95	0.063	12.7	2.29
T10L10	0	11.74	0.085	8.3	0.44

Table 7.4 shows the critical hydraulic gradients for the top layers of each of the specimens in this modelling-of-models comparison, calculated using Equation 7.5. The hydraulic gradients at the first onset of a suffusion event within the layer are reported, alongside the critical observed energy gradient and seepage velocity at that point. The observed critical hydraulic gradient shows a possible trend of increasing with decreasing g-level, although the study was designed so that the ratio of effective stress and seepage path length gave the same theoretical critical hydraulic gradient in each test. There was

no common energy gradient or seepage velocity between the first onset of suffusion in the top layers of the specimens. The critical hydraulic gradients are somewhat similar to the values between 0.13 and 0.2 observed by Crawford-Flett (2014), despite those tests being conducted under upwards flow on soils that are predicted to be significantly more unstable than those tested in this study ($\alpha \approx 0$ compared to $\alpha = 0.696$).

It is clear to see that the critical hydraulic gradient model does not capture the onset of suffusion in these centrifuge tests. The tests in the UBC permeameters were conducted at comparatively high hydraulic gradients and stress levels. Although the testing regime of Li (2008) and Moffat (2005), also followed an incremental hydraulic loading approach, each increment was of at least $i = 1$, which is already greater than the maximum applied hydraulic gradient in this study. Nevertheless, suffusion did occur during the tests presented in this study. Fundamentally, the concept of critical hydraulic gradient is based on one zone of the specimen reaching a hydraulic condition which is enough to instigate the migration of under-stressed fine particles. However, the only way to 'build up' hydraulic gradient in a particular area is to change the inter-particle network of the soil. In dense under-filled soils in particular, where settlement of the granular matrix is unlikely, this local increase in hydraulic gradient can only occur due to the deposition of particles from further upstream by the seepage flow. In which case, internal fines particle migration must be occurring before the critical value implied by this hydromechanical framework.

7.1.4 *Summary of modelling-of-models 1*

- The four tests in this suite of modelling-of-models tests did not show the same suffusion behaviour, and so some combination of the effective stress, loading regime, and seepage path length have an influence on the initiation of suffusion not captured by the hydromechanical envelope model. Other comparisons between the permeameter tests of this study in both this and the following chapter explore these factors individually (Section 3.8).
- The fact that the lower-g tests did not begin to erode when the same conditions that caused erosion in the higher-g tests occurred shows that multi-stage hydraulic loading history has a significant impact of

the suffusion response of the soil, as observed in the recent studies of Rochim et al. (2017) and Annapareddy et al. (2023).

- Comparing the results of this study, where hydraulic regimes were chosen to capture the early stages of suffusion, with the hydromechanical envelope concept of Li and Fannin (2022) highlights that, while ostensibly capturing the 'onset' of suffusion, the model is in fact capturing the point at which sufficient fines migration has occurred so that one zone reaches the point of sudden 'blow-out', and the flow rate through the soil increases rapidly.

7.2 MODELLING-OF-MODELS 2: T40S2.5 AND T20L5

7.2.1 *Comparison of two tests under the same effective stress conditions*

In this study, two tests, *T40S2.5* and *T20L5*, were conducted to achieve the same effective stress conditions, following a conventional modelling-of-models approach. Due to the enhanced-g environment of the centrifuge, these two specimens had similar effective stress profiles across their height, despite the 40-g test being approximately half the model height of the 20-g test. In terms of hydraulic loading, the increments of hydraulic gradient applied to the specimens were the same for both tests, because the outlet CHT was lowered twice the distance for each increment in *T20L5* in comparison to *T40S2.5*. Although at 1-g this would constitute identical loading scenarios, in the centrifuge the applied energy gradient and seepage flow are scaled and consequently not the same between the tests. The parameters for the tests are shown together in Table 7.5.

For these two tests, which have the same stress gradient across their height, the hydromechanical envelopes for suffusion onset will be the same, according to the model of Li and Fannin (2022), assuming that the permeameter has a sufficiently large diameter to particle size ratio to avoid arching effects. This assumption is valid because the ratio of D_{100} to internal cell diameter is 257 particles. This is many times the minimum ratio of 10 suggested in ASTM:D5101 (2017), and is also larger than the ratio of 160 particle diameters in the centrifuge study of Marot et al. (2012) and the ratio of 51 in the small permeameter of Li (2008) (Section 2.3.4).

Table 7.5: Comparison of the testing parameters for the two tests conducted to achieve the same prototype, $T_{40S2.5}$ and T_{20L5} . The same effective stress at the mid-point is achieved by adjusting the height of coarse sand used as overburden

Parameter	$T_{40S2.5}$	T_{20L5}
Δz Model/Prototype (m)	0.105 / 4.01	0.175 / 3.37
σ'_{vm0} (kPa)	69.5	66.8
δi_{app}	0.018	0.023
$i_{app,max}$	1.07	0.661
δEG_{app} (kPa/m)	7.6	4.7
$EG_{app,max}$ (kPa/m)	446.2	138.8
v_{max} (m/s)	8.3×10^{-4}	2.2×10^{-4}
E_{exp} (J)	480.7	34.6

The critical hydraulic gradients for the whole specimens according to the hydromechanical envelope of Li and Fannin (2022) are $i_{cr} = 4.95$ for $T_{40S2.5}$ and $i_{cr} = 5.53$ in T_{20L5} respectively (Equation 2.20). Although these critical values are significantly higher than those reached in the test, as discussed in Section 7.1, their similarity exhibits that the two tests may be expected to behave comparably. In addition, the use of the same soil and hydraulic testing conditions suggests that, according to the energy methods from Marot et al. (2012), at equivalent amounts of cumulative applied energy, the specimens should experience an equivalent amount of fines migration.

Even by just visually comparing the global permeability profiles of the two tests in Figure 7.3, it is clear that the tests exhibited very different behaviour under the same hydraulic-gradient based loading regime. Test T_{20L5} , as mentioned in Section 7.1, decreased in permeability throughout the test, with the permeability dropping by 43.4% over the 64 minutes of testing. In contrast, three global suffusion events were observed in $T_{40S2.5}$, a shorter, sudden event near the start of testing, and then two steadier increases in permeability within the first hour of testing, shown in Table 7.6. After this point, the specimen exhibited a gradual, near-linear decrease in permeability until the end of the test.

As shown in Table 7.5, The final test conditions for T_{20L5} reached a higher energy gradient, seepage velocity and expended energy than those values

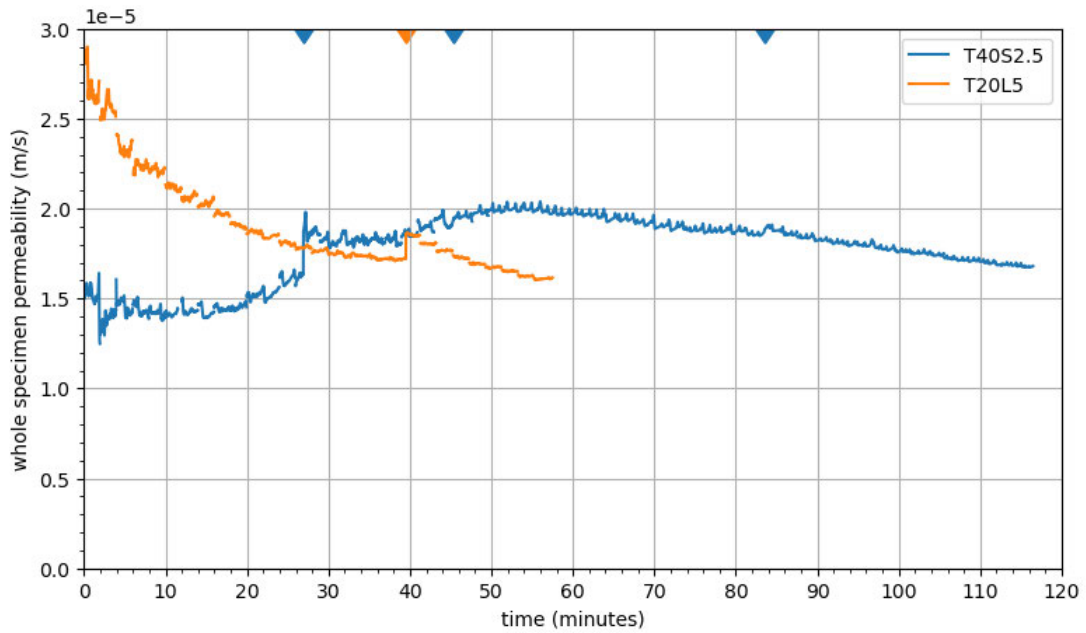


Figure 7.3: Global permeabilities of two tests conducted to model the same prototype, $T_{40S2.5}$ and T_{20L5} (centrifuge spin-down breaks marked with coloured triangles)

noted at the onset of the three suffusion events in $T_{40S2.5}$, and yet the 20-g test did not show global suffusion behaviour. This shows that there is not one simple hydraulic threshold that needs to be met in order for global suffusion to occur within similarly stressed samples, and there is likely some local behaviour within the specimens that affects their overall permeability response. Looking at the permeability of the individual sample layers in time (Figure 5.14 and Figure 6.9), gives an understanding of the spatially varying suffusion behaviour.

Table 7.6: Testing conditions at the onset of global suffusion events in test $T_{40S2.5}$

Event time (min)	start	Duration (s)	Δk ($\times 10^{-6}$ m/s)	i_{onset} / EG_{onset}	v_{onset} ($\times 10^{-5}$ m/s)	$E_{exp,onset}$ (J)
2		180	1.41	0.078 / 24.8	2.88	0.05
15		720	2.17	0.216 / 67.5	9.65	1.38
38		840	1.80	0.379 / 118.8	22.3	14.7

The spatial development of fines migration within the two tests also progresses very differently. When looking at the individual layers of test *T20L5* in Figure 6.9, the majority of suffusion occurs in the top layer of the specimen, apart from two suffusion events at the base of the test in the early intervals of testing. The other layers decreased in permeability for the duration of the test. In comparison, there is a much clearer progression of suffusion through the sample in test *T40S2.5*, shown in Figure 5.14. At first the top layer erodes, followed by the middle, and then bottom layer. Clogging only occurs within the specimen at higher applied energy gradients.

In existing experimental studies on suffusion in a variety of permeameter configurations, higher levels of erosion in layers towards the start of the seepage path have been consistently observed, either through post-test dissection, or by in-situ imaging of the specimen (Section 2.6.2). By considering the change in permeability of each of the layers over the test duration in this study, it is possible to compare the level of suffusion and clogging along the seepage path. In *T40S2.5*, the highest increase in permeability was observed in Layer 0 at the start of the seepage path (Table 5.5), and whilst there was a net decrease in permeability for Layer 1 of *T20L5* (Table 6.7), this was the smallest decrease of all the layers. These observations agree with the existing literature discussed in Section 2.6.2.

The two tests discussed in this section can be compared with tests 7 and 20 from the centrifuge paper by Marot et al. (2012), which follow a similar modelling principle of modelling the same prototype, although they are not directly compared within that paper. The results of those two studies are given in Table 7.7. The 20-g test, Test 20, experienced an erosion rate three times higher than Test 7 at 40-g, and had almost twice the mass of externally eroded fine particles, despite having the same energy expended by the seepage flow. This contrasts with what was observed in this study, where the higher g test experienced more suffusion. This could be because there was significantly more expended energy by the seepage flow in test *T40S2.5*. The final expended energy of *T20L5* is reached by 50 minutes into test *T40S2.5*. By this point, all three suffusion events detailed in Table 7.6 had already occurred, and the sample then clogged for the rest of the test. This suggests that the higher level of suffusion observed in *T40S2.5* was not due to the higher expended energy, and therefore must be due to either the hydraulic loading history, or the fact that, whilst at a continuum level, the specimens have the same

prototype seepage path length, they are not the same in relation to the size of the individual particles.

Table 7.7: Results of two tests conducted to the same prototype conditions from the centrifuge study of Marot et al. (2012)

Parameter	Test 7	Test 20
N	40	20
Δz Model/Prototype (m) †	0.06 / 2.4	0.12 / 2.4
σ'_{vm0} (kPa)	28.3	28.3
i_{app} ‡	2.25	2.25
Average erosion rate (g/sm ²)	0.003	0.009
Eroded mass (g)	0.09	0.19
Eroded mass / original mass of fines (%)	0.23	0.24
E_{exp} (J)	108.6	108.7

† without knowing the exact payload configuration, it is not possible to include the error from centrifuge elevation (Section 2.3.1), but the specimens are relatively short and so N has been assumed to be constant.

‡ the original i_{app} value reported was scaled by N, giving 90 for test 7 and 45 for test 20, but this has been recalculated for this study (Section 2.3.2).

Even when looking at just the top layer of the two tests, which can be justified as described in Section 7.1, the average rate of increase in permeability during suffusion events in the top layer of *T40S2.5* was 8.5×10^{-9} m/s/s, whilst in the top layer of *T20L5* it was less than half that, at 3.8×10^{-9} m/s/s. This is the opposite of what was observed in Marot et al. (2012). One key difference between that study and the current one is the hydraulic loading regime. Where this study uses a multi-stage approach, theirs applied a constant head difference to the specimens. The influence of hydraulic loading regime is discussed in Section 8.2. The current study also has a larger model height to diameter ratio, 1.36 and 2.27 for the short and long tests, whilst the ratio in Marot et al. (2012) was between 0.82 and 1.64, meaning that there was a more significant stress gradient along the seepage path in the current study. Bianchi et al. (2018) observed that clogging tended to propagate upstream through

the soil after initiating locally towards the bottom portion of the sample. It appears that, in the test in the shorter specimen, $T_{40S2.5}$, suffusion was able to progress more easily along the seepage path length, whereas in the longer model T_{20L5} , clogging in the lower layers prevents the suffusion in the top layer from progressing into the layers below.

7.2.2 *The difference between seepage path length and specimen height*

Previously in this thesis, the interchangeability of the terms seepage path length and specimen height has been taken at face value, and the scaled prototype distance between measurement points has been used in Equation 2.20 to calculate the theoretical critical hydraulic gradient. This is because the distance is specifically referred to as the "specimen or layer thickness" in Li and Fannin (2022), a parameter that is well-accepted to scale in the enhanced-g environment of the centrifuge. Similarly, in the studies discussed in Section 2.6.3, different lengths of apparatuses have been used as a shorthand to explore the influence of seepage path length. However, the difference in the results from tests $T_{40S2.5}$ and T_{20L5} clearly demonstrate that the length influence observed by Li (2008) and Zhong et al. (2018) is a product of the granular matrix length, rather than the continuum specimen height.

Internal fines migration, encompassing both suffusion and clogging, is inherently a granular phenomenon, the movement of individual fine grains within the pore void spaces of a stable granular matrix. The seepage path length parameter in this case is not purely a function of the model height, but is embodying the number of pores that a migrating fine particle can be picked up from, transported through, and redeposited in. Therefore the seepage path length should be given in relation to the particle size, and consequently does not scale with centrifuge acceleration. Both tests in this modelling-of-models comparison have the same prototype-scale specimen height, but from a micro-scale perspective, T_{20L5} has a greater number of pore constrictions. This is due to the relative height of the model compared to the grain size of the soil. Using D_{50} of the coarse fraction as representative of the coarse stable matrix, T_{20L5} has a length of 1075 grains, whilst $T_{40S2.5}$ has a length of only 645 grains. The more particles, the more constrictions between them, and therefore locations for particle erosion or deposition to occur.

In this study, the scaling laws of the centrifuge emphasize a separation between the seepage path length and specimen height that is not as obvious in typical permeameter set-ups, but the lessons learnt from this highlight the subtle difference in seepage path length and specimen height when conducting 1-g studies on a variety of soils. Re-framing the seepage path relative to the particle size distribution of the soil being tested would allow more direct comparison between studies. The smaller model specimen heights of Zhong et al. (2018) and Marot et al. (2012) are quite similar, 50 and 60 mm respectively, but the latter represents 300 of their D_{50} particles end to end, whereas the former is only around 25 particles. The larger apparatus of Li (2008) facilitates seepage path lengths of 300 of their FR7 D_{50} particles, and so a migrating fine particle travelling from one end to another would encounter a similar number of pore constrictions as in the 60 mm model of Marot et al. (2012), despite being five times the size, not taking into account other soil properties like packing density and particle shape.

7.2.3 Summary of modelling-of-models 2

- Two specimens tested to achieve the vertical effective stress gradient did not exhibit the same suffusion behaviour, neither in terms of onset nor spatial progression.
- As suggested in Section 2.3.2, the applied hydraulic gradient is a useful measure to quantify the flow regime within a soil sample at 1-g, but it is not the controlling factor when it comes to suffusion onset or progression within a sample. In practice, design guidance based on critical hydraulic gradient values should be used cautiously, understanding the limitations introduced by simplifying the hydraulic loading down to just the macroscale hydraulic gradient.
- Alternative macroscale criteria for suffusion onset and progression proposed in literature, for example critical seepage velocity or expended energy, also did not capture the behaviour of these two similar prototypes, as test *T20L5* reached the seepage velocity and expended energy needed to cause suffusion in *T40S2.5*, but no global suffusion was observed.
- The relationship between macroscale seepage path length and effective stress proposed by Li and Fannin (2022) to determine the critical

hydraulic gradient did not apply to the tests undertaken in this study. Instead the seepage path length effects observed by Li (2008) and Zhong et al. (2018) may be related to a microscale rather than continuum perspective of the seepage path length.

- When previous studies have discussed the seepage path length they have considered it to be analogous to the continuum-scale specimen length. The centrifuge tests of this study accentuate that this parameter is quantifying the granular matrix of the soil, and so should be given in relation to the size of the test soil gradation, for example using a representative particle diameter. Although the scaled centrifuge specimen height and the microscale seepage path length represent an extreme case, using a term relative to the particle size is also relevant when different gradations are tested in the same device, where previous studies have considered the seepage path as constant between tests, simply the specimen height.

7.3 MODELLING-OF-MODELS 3: T40LCH AND T1LCH

7.3.1 *Initial observations*

From the previous two comparisons in this chapter, it has been observed that effective stress affects the progression of suffusion, and that the multi-stage hydraulic loading regime renders it complex to interpret controlling physical factors for suffusion in the centrifuge environment. Internal fines migration was also observed at very low hydraulic loading conditions that were not consistent with the concept of an initial stabilising force that must be overcome for a particle to start to migrate, implied by the hydromechanical envelope concept of Li and Fannin (2022).

An alternative framework to conceptualise the process of internal fines migration is by linking the work done by the seepage flow to the amount of fine particles removed from the specimen using the I_α erosion resistance index (Equation 2.24). The application of this concept, in particular in the centrifuge permeameter work of Marot et al. (2012), was discussed in detail in Section 2.6.3 of the literature review. Instead of considering a geometric susceptibility to erosion and then a hydraulic gradient sufficient to initiate suffusion, as in the

hydromechanical envelope approach of Li and Fannin (2022), this framework implies that for each soil gradation, a certain amount of energy will yield a consistent quantity of fine particles to be removed from the soil. As with i_{cr} , this method is based on using the macroscale pressure difference across the specimen to capture the suffusion behaviour. This pressure is used to calculate the cumulative expended energy of the seepage flow across the specimen. In the formulation of this approach, the effective stress level does not play a role in the suffusion process.

In this set of comparable tests, T_{40LCH} and T_{1LCH} , the impact of the hydraulic loading regime was eliminated entirely by conducting the tests at an applied hydraulic gradient above a threshold value that definitely causes continuing erosion. The choice of this hydraulic gradient was based on the observed critical values from the first modelling-of-models comparison in this chapter. Both tests T_{40LCH} and T_{1LCH} were observed to lose fine particles during testing, so suffusion was categorically occurring. By applying a large head difference across the sample from the start of testing, it is not possible to find a threshold value for the onset of suffusion, but the spatial and temporal progression of fines migration within the sample can be analysed. Due to the choice to scale to achieve equivalent applied hydraulic gradients, the ratio between the seepage velocity and the settlement velocity of the particles (Stoke's law - Section 6.5.2) was preserved between the two tests, despite being conducted in and out of the centrifuge, respectively.

For test T_{40LCH} , presented in Section 5.5.2, the entire sample was eroding from the start of the test, with a particularly high suffusion rate in Layer 0, at the start of the seepage path. This layer was then the first to begin clogging, and soon after, the rest of the layers followed suit, with the exception of the top and central layer, which showed a small increase in permeability across the spin down break. (Figure 5.17). By the end of the test, all suffusion events had ceased, suggesting that all of the available fine particles had been eroded and the specimen had reached the 'fully-eroded' stable state proposed by Gelet and Marot (2022). Test T_{1LCH} was also observed to have a global loss of fine particles over the duration of the test, which was conducted over a matter of days, rather than hours. For the first 60 hours, the sample tended to increase in permeability, followed by a general clogging trend, as with the 40-g test.

Comparisons can also be made between the final spatial distribution of the fine particles within the specimens. Unlike the test conducted at 1-g,

the dissection of *T40LCH* showed areas that had a net gain in fine particles, with final percentages above the initial 20%. Although clogging may have occurred in *T1LCH*, none of the recovered quadrants exhibited this net gain in particles. Test *T1LCH* also had a higher total loss in fine particles, with a final percentage of 19.63% compared to 19.71% in *T40LCH*. This is in direct contrast to the results of Luo et al. (2013), who observed that the long-term constant head test caused local regions of clogging fine particles, this however was in comparison to a short term multi-stage test. These quadrants with a net gain in fine particles were also observed in other tests conducted in the centrifuge, *T30L2.5/5* and *T40S2.5*, although not in the recovered quadrants of test *T40L2.5*. A micromechanical perspective on this observation is presented in Section 8.2.

Comparing the two constant head tests of Rochim et al. (2017), the constant head testing regime *k* experienced significantly more mass loss than the regime *c*, despite having a much lower applied energy gradient across the sample (Section 2.6.1). In this study, *T40LCH*, which was subjected to a much higher seepage flow, lost a total of 5.58 g of fine particles calculated from the post-test dissection, whilst *T1LCH* lost 7.73 g, following the same trend. Lee et al. (2021) also recorded a higher amount of externally eroded fine particles in the long term case, although in that case the comparison was made against a multi-stage short term test.

7.3.2 Outcome of suffusion: mass of fines lost

For tests *T40LCH* and *T1LCH*, the ultimate mass of fines lost can be used to apply the erosion resistance approach introduced in Section 2.6.4. The results of several studies that have used the expended energy and eroded mass approach in various forms are collected in Figure 7.4 and presented alongside the dissected tests of this study. Section 2.6.4 presents the findings of these previous studies in more detail. For this discussion, it is important to note that all of the studies, with the exception of Marot et al. (2012), were conducted on an array of soil gradation, which, according to their respective studies, explains the scatter on the graph. Based on their location on the graph, the specimens are classified on a scale from highly resistant (HR) to highly erodible (HE). The tests of Marot et al. (2012), as with this study, were conducted on a consistent soil gradation at centrifuge accelerations between 10 and 40-g.

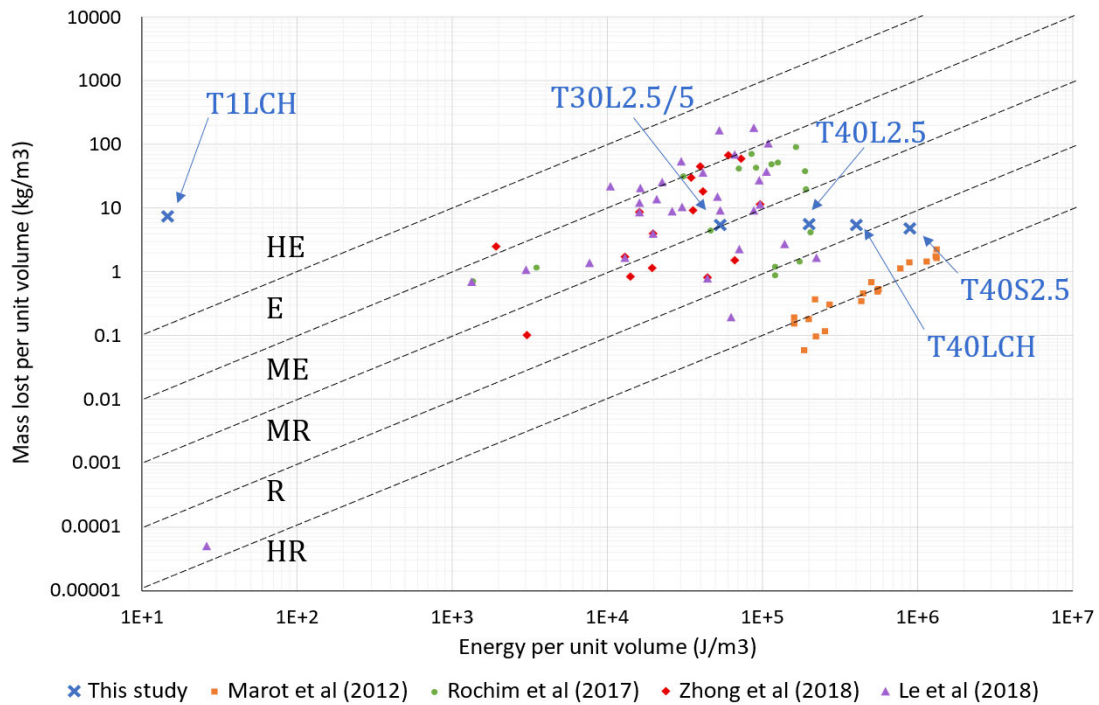


Figure 7.4: The total mass of fines lost per unit volume against the cumulative energy expended energy from the seepage flow for the dissected tests of this study (shown with blue crosses) alongside data reported in previous studies by Le et al. (2018), Marot et al. (2012), Rochim et al. (2017) and Zhong et al. (2018)

If just the centrifuge tests of this study are compared in Figure 7.4, the tests fall within the same boundary and the soil would be considered moderately resistant (MR) to internal erosion. However, when the results for test *T1LCH* is included, it is clear that for this study, the mass eroded is independent of the energy per unit volume expended in the sample by the seepage flow. For each dissected test (*T40L2.5*, *T40S2.5*, *T40LCH*, *T30L2.5/5* and *T1LCH*), there was similar quantity of fine particles externally eroded, with masses between 5.4 and 8.6 g (Table 6.5). The smallest mass lost per unit volume was for test *T40S2.5*, which had the highest expended energy, but the shortest model height.

In previous studies exploring this expended energy concept, the variation of energy per unit volume was only varied by a less than two orders of magnitude. When comparing the centrifuge tests to the 1-g test in this study, nearly 5 orders of magnitude are considered, and it becomes clear that the suggested erosion boundaries do not capture the erosion behaviour in the soil. The erosion resistance index, I_{α} , is not an intrinsic soil property and the soil

tested in this study can be classified anywhere from highly erodible (HE) to moderately resistant (MR), depending on the testing conditions.

The fact that similar quantities of fine particles were eroded in all tests can be interpreted in different ways. Either this is consistent with the concept proposed by Gelet and Marot (2022), where there are a finite number of erodible fine particles, and a fully eroded state can and has been reached in these tests. This is unlikely, due to the very low quantities of eroded fines observed in post test dissection, combined with no observations of "blow out" erosion, where the permeability suddenly dramatically increases. In many of results reported in the studies that apply this expended energy approach, permeability increases by an order of magnitude (e. g. Rochim et al. (2017) - Figure 2.21), whereas in this study, the maximum change in permeability of a layer over the course of a test was 145% in Layer 0 of *T40L2.5(R)*.

Another interpretation of the observed independence between expended energy and mass lost is that the significantly higher effective stress in the centrifuge tests has a stabilising effect against fines migration. This agrees with the studies discussed in Section 2.5.3, that found an increase in effective stress was stabilising. However, this is at odds with the model of an under-filled, gap-graded material with the fines under no stress in the void spaces, which has been corroborated in DEM studies (Section 2.7.1). That understanding implies that vertical effective stress does not influence the migration of the fine rattlers.

Comparing the results of this study with the centrifuge tests of Marot et al. (2012) brings some interesting differences that highlight the need for interstitial pore pressure measurements. Unlike this study, the tests of Marot et al. (2012) plot at approximately the same location in Figure 7.4. They did not, however report a 1-g permeameter test on the same soil. As presented in Section 2.6.3, although their tests experienced a global loss in fine particles, the permeability of the whole sample decreases across the course of the test, suggesting significant fines redeposition within the sample. The specimens in their study had a maximum height to width ratio of under two, whilst in this study, the full length samples were almost three times as tall as they were wide.

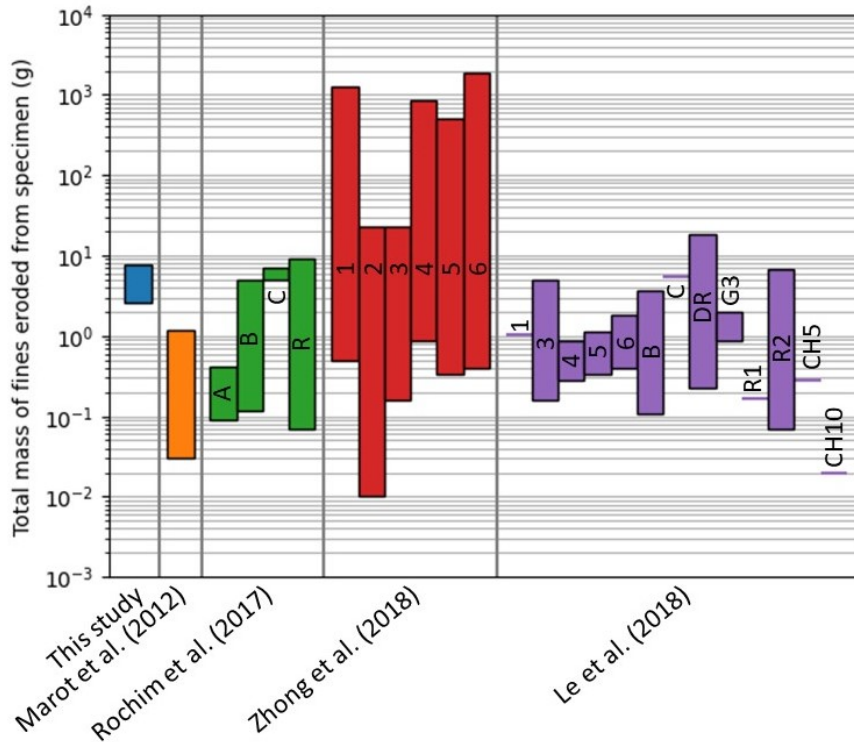
As previously discussed, the masses of fine particles lost from each of the specimens in this study was very small, with the measured mass lost from each quadrant often under 1 g. This brings into question whether the

observed change in fine particles is distinguishable from errors introduced in the experimental process. The range in fine particle loss for this and the other studies discussed in this section is given in Figure 7.5, both as a total mass in grams, and relative to the initial quantity of fines. Although the range of observed mass loss in this study was small, it was in a similar order to a number of previously published work, which used this value to calculate the erosion resistance index. In Figure 7.5, some studies tested multiple soils, and the naming convention has been kept consistent with the published study. Where soil names are the same across studies, the same soil was used under different experimental conditions

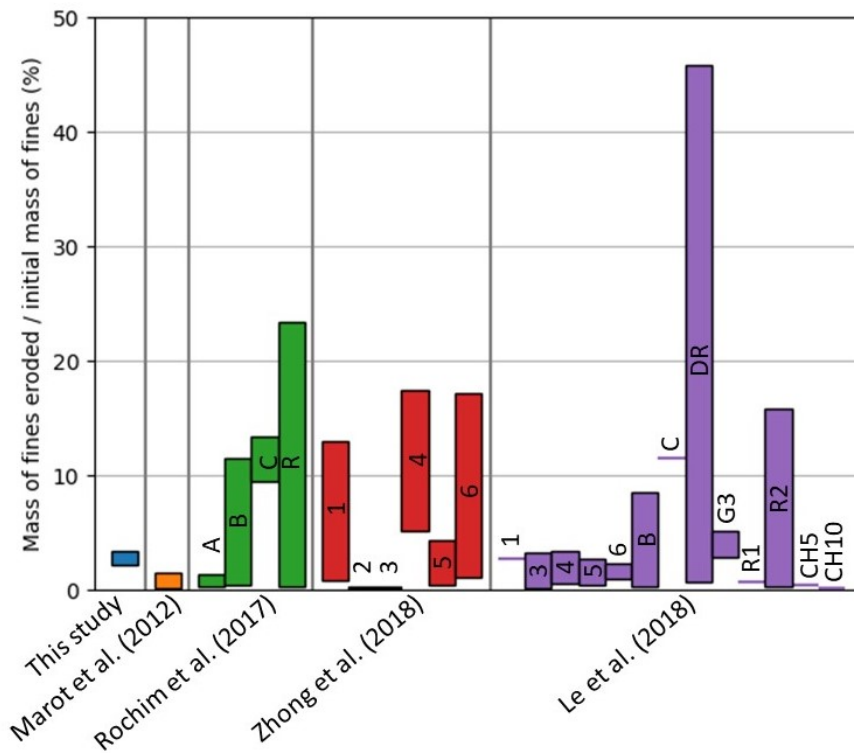
The studies of Le et al. (2018), Marot et al. (2012), Rochim et al. (2017) and Zhong et al. (2018) all take total eroded fine particles, alongside a temporal global permeability reading, to classify the suffusion process. From inspecting the experimental layouts, only the larger apparatus of Zhong et al. (2018) is equipped with interstitial pore pressure measurement points, but the individual layer permeabilities were not reported in the published paper. These larger-device tests (Section 2.6.3) represent the upper boundaries of the ranges shown in Figure 7.5, with some tests losing over a kilogram of fine particles. Post test dissection of their specimens showed some samples exhibiting clogging at the end of the seepage path, but as only the larger or the apparatuses enabled dissection, it is not possible to quantify the influence of specimen size and boundary conditions on this effect.

For material 2, Zhong et al. (2018) give the temporal variation in hydraulic conductivity for the test in their smaller triaxial device. After initially decreasing steadily, the hydraulic conductivity of the specimen increased nearly 100-fold, but the sample lost only a fraction of a gram of fines, as shown in Figure 7.5. Despite this significant change in hydraulic conductivity, using the erosion resistance index method, this soil was classed as moderately resistant (Figure 2.27) to internal erosion.

From this it is clear that the total mass lost from the sample does not give an indication of the suffusion behaviour within the soil. The current study also supports this observation through the reported disconnect between the spatial distribution of the fine particles upon dissection and the local permeability behaviour (Section 5.6, Section 6.6). The change in permeability observed during a suffusion or clogging event is due to the local rearrangement of fine particles, rather than a net loss or gain which would be observable at an



(a) Range of total mass of eroded fine particles from each specimen



(b) Range of percentage of the total initial mass of fine particles that were eroded over the course of the test for each specimen

Figure 7.5: Comparison of the range in masses of fine particles eroded in this study and previous studies using the erosion resistance index approach.

experimental level. A better understanding of the phenomena can be reached by striving for a higher resolution of measurement points when experimentally modelling suffusion, as it is clear that a global value of either eroded mass or permeability change does not represent the conditions at the laboratory scale, let alone in a field-scale structure.

7.3.3 Summary of modelling-of-models 3

- All of the specimens conducted in this study that were dissected post-testing exhibited a similar mass of fine particles lost per unit volume of the soil, regardless of their testing conditions, showing that the mass lost from samples was independent of the energy expended by the seepage flow.
- The results of this study conducted on the same material show that the erosion resistance index, I_{α} is not an intrinsic soil property and the hydromechanical conditions and history within the soil during testing have some influence on the test outcome.
- There was significantly more spatial variation in ultimate fines distribution in the 40-g constant head tests compared to the 1-g head test, suggesting that the high effective stress, high seepage flow conditions in the centrifuge promoted the development of more local zones of particle deposition and migration. It must be noted that the quantities of eroded fine particles, as with previous experimental studies, were very small and did not correspond to the locally observed change in permeability measured during testing.

7.4 SUMMARY

In this chapter, a centrifuge-based modelling-of-models approach was undertaken to explore the initiation and progression of suffusion in the same soil, under different testing conditions. Summaries of each of the comparisons are given at the end of their respective sections. The results of this study highlight the limitations of existing methods to calculate the onset and outcome of suffusion, including the concepts of critical hydraulic gradient i_{cr} , and the

erosion resistance index I_{α} . At the scale of laboratory element tests, whether in the centrifuge, as is the case with this study, or at 1-g, the complete suffusion process can only be considered at the resolution of the measurement locations. To understand the suffusion phenomenon, it is the author's opinion that future studies need to consider local spatial and temporal variations at an even finer scale, rather than finding a single value to classify the soil, which is significantly influenced by the boundary and test conditions, as well as the measurement type and locations chosen.

By using the centrifuge scaling laws, the macroscale assumptions of these methods are challenged, and it becomes clear that the hydraulic loading history and microscale conditions within the soil are arguably more impactful on the suffusion process than parameters such as effective stress and applied energy gradient, although these did have some influence on the test outcomes. The limitations of a macroscale perspective highlighted in this chapter, inspires the more particle scale approach taken in the following chapter.

ANALYSIS AND DISCUSSION: FACTORS INFLUENCING SUFFUSION

In this chapter, three pairs of tests are analysed and discussed to explore factors that have been identified in the literature to affect both the initiation and progression of suffusion. The first comparison considers the concept of repeatability in permeameter tests, addressing both the repeatability of the final state of the soil, as well as the spatial and temporal progression of suffusion. In general, this chapter takes a more microscale approach to interpreting the observed permeameter results, with the second comparison in the chapter presenting a conceptual framework for microscale particle migration based on the difference in results for the multi-stage and constant head centrifuge tests.

The third comparison of the chapter concerns the influence of the seepage path length from a microscale perspective, following on from the modelling-of-models observations in Chapter 7, as well as the influence of the outlet boundary conditions. The final section of this chapter attempts to resolve the seeming discrepancy between permeability change observed from PPTs and the final fines content of the specimen by exploring the influence of spatial variation in fine particle content on the macroscale assumptions of Darcy's law and Kozeny-Carman permeability.

8.1 COMPARISON 1: REPEATABILITY AND MICROSCALE VARIATION

For this study, two specimens, $T_{40L2.5}$ and $T_{40L2.5}(R)$ were prepared in an identical manner and subjected to the same multi-stage hydraulic loading regime. The repeat test, $T_{40L2.5}(R)$, was taken to a higher applied energy gradient, 236.5 compared to 195.6 kPa/m. It also comprised of two centrifuge spin stages, compared to the three shorter stages of test $T_{40L2.5}$. As discussed in Section 2.7.3, the initiation of suffusion is an intrinsically microscale phenomenon, which at its core is the perturbation of one fine particle in the granular structure under the action of the seepage flow. In light of this, there

will always be intrinsic differences in the behaviour of experimental models prepared identically and tested under the same experimental conditions. However, it is still valuable to assess the repeatability of the permeameter tests from a macroscale perspective, to assess both the reliability of the testing apparatus and understand the macroscale development of fine particle migration within the tested soil.

The centrifuge permeability results from test $T_{40L2.5}$ and $T_{40L2.5}(R)$ are presented in Section 5.2.2 and Section 5.3.2 respectively. Figure 8.1 shows the global permeability of the two specimens in time. From this figure, it is clear that there was a very similar global suffusion behaviour in the two tests. The two tests started with very similar permeabilities, 1.43×10^{-5} m/s and 1.60×10^{-5} m/s, averaged over their first seepage flow increment, with the repeat test being slightly more permeable. Both tests show an initial increase in permeability to around 2.1×10^{-5} m/s, reaching their most permeable after between 70 and 80 minutes of seepage flow testing. For $T_{40L2.5}$, this was when the applied energy gradient was 145.3 kPa/m, and for $T_{40L2.5}(R)$, $EG_{app} = 138.5$ kPa/m. Within the first seven increments of testing, comprising approximately the first 14 minutes, the global permeability response was rather different, with a sudden suffusion event and subsequent clogging in $T_{40L2.5}$ that was not observed in the repeat test.

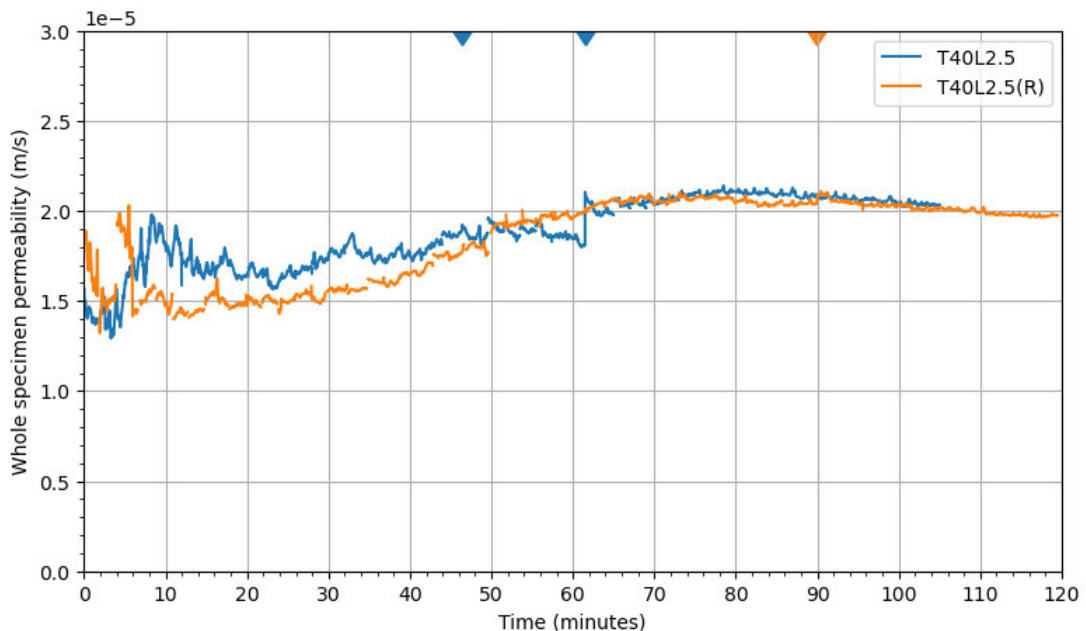


Figure 8.1: Global permeabilities of two repeat tests $T_{40L2.5}$ and $T_{40L2.5}(R)$ plotted against time (centrifuge spin-down breaks marked with coloured triangles)

The similarity between the two tests can also be examined by considering the global permeability of the samples with the cumulative energy expended by the seepage flow, as shown in Figure 8.2. The final permeability of $T_{40L2.5}$ was 2.03×10^{-5} m/s after an expended energy of 206.5 J, an increase of 42.1%. Test $T_{40L2.5}(R)$ reached 206.5 J of energy 107 minutes into the 119 minutes of testing, at which point the permeability had increased to 2.01×10^{-5} m/s. For the remaining 12 minutes of the tests, the specimen continued to clog, giving a final net change in permeability of 23.7%. Zhong et al. (2018) observed that their two repeat tests, 6-O-1 and 6-O-2, plotted in the same location on the mass eroded against ultimate expended energy graph (Figure 2.27) and concluded that there was "fairly good" repeatability on specimen preparation and testing procedure. During the seepage tests, the two repeat samples in that study behaved rather differently. Only one of two tests had an identifiable critical hydraulic gradient, defined by the authors as a 10% relative increase in permeability between measurement intervals, however both samples clearly experienced suffusion as they lost around 17% percent of their fine particles over the test. For the present study it was unfortunately not possible to obtain an ultimate mass of fine particles lost during seepage for the repeat test, but the similarity in permeability profiles between the two tests suggests a similar quantity of fine particle migration, assuming that the pore pressure readings are representative of the whole layer cross section. This assumption is explored in more depth in Section 8.4.

The local variation in permeability of each of the specimen layers can be seen in Figure 5.5 for $T_{40L2.5}$ and Figure 5.9 for $T_{40L2.5}(R)$, with the suffusion events highlighted in the timelines below the profiles. Whilst individual layers experienced intermittent suffusion events throughout the early loading increments in both tests, the layers at the start of the seepage path in both cases, Layers 0 and 1, experienced significant suffusion from early in the test, whereas the bottom layers tended to clog until later intervals. Layer 5 in both tests did not show a prolonged suffusion event until around 45 minutes into seepage flow, when the energy gradient in the layer reached 65.7 kPa/m for $T_{40L2.5}$ and 82.1 kPa/m for $T_{40L2.5}(R)$.

To understand the influence of the spatial variation on repeatability between tests in this study, it is important to place them in the context of existing studies undertaken in similar (although not centrifuge-based) suffusion permeameter studies. In the doctoral work of Li (2008), discussed in Section 2.5.2,

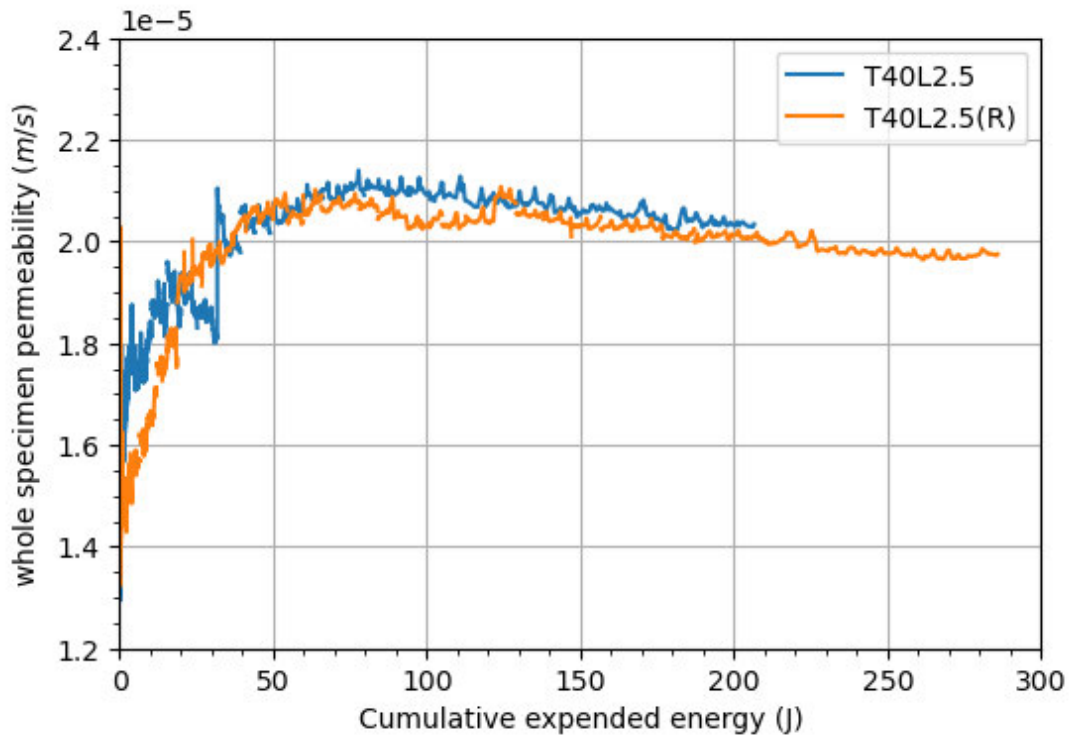


Figure 8.2: Global permeabilities of two repeat tests plotted against the cumulative energy expended by the seepage flow

repeatability was assessed by repeating one of the stress cases, $\sigma'_{t0} = 25$ kPa, for one gradation, *FR8*. As with the current study, the tests showed similar global permeability behaviour, with comparable critical hydraulic gradients for each repeat. However, the variation in behaviour of the interstitial layers was significant, hinting at the specimens' internal heterogeneity. For example, in one of the repeats, test *FR8-25-D1*, there was high clogging shown in layer 5-6, towards the end of the seepage path, demonstrated by the relatively high hydraulic gradient across the layer. In contrast, the second repeat, *FR8-25-D2*, showed no significant signs of clogging in any of the layers after suffusion onset near the midpoint of the sample. In comparison to this, the tests in the present study showed very similar spatial progression of both suffusion and clogging between the repeat tests.

Li (2008), suggested that suffusion can initiate at any location within the sample, and it likely begins at a local defect or variation in microstructure. In this study, which, unlike Li (2008), had a significant stress gradient across the seepage path, suffusion occurred at lower hydraulic loading in the more lightly stressed layers at the start of the seepage path. It seems that the particles

migrating out of these layers were deposited further downstream, shown by the clogging in lower layers, where either the presence of existing fine particles, or the higher stress level inhibited their further transportation until a higher energy gradient was applied to the specimen.

When examining repeatability in experimental testing of suffusion, there is a conversation to be had about whether the modeller desires the repeatability of the final outcome of suffusion, or the repeatability of the spatial and temporal development of suffusion, knowing that the migration behaviour is inherently at least partially stochastic at the microscale. Even the interstitial layers of this study only consider the mesoscale (Section 2.2.9), with a 35 mm model height of each layer being the equivalent of 215 D_{50} particle diameters, a far cry from the DEM studies with a total of few thousand particles presented in Section 2.7.3. At the scale of the measurements taken in this study, the comparison of tests $T_{40L2.5}$ and $T_{40L2.5}(R)$ shows that the mesoscale suffusion and clogging behaviour is replicated between centrifuge permeameter experiments.

8.1.1 Summary

- The preparation procedures undertaken in this study lead to consistent specimens, shown by the similarity in permeability of both the repeat tests, and the tests discussed in other sections of this chapter.
- Two identically prepared tests tested under the same loading conditions exhibited very similar permeability responses, both across the whole sample and within the interstitial layers, suggesting that the onset of suffusion is not entirely dependant on random microstructural defects, and the hydromechanical loading regime has some influence.
- The progression of suffusion is also very similar between tests, something that was not consistently observed in repeat tests in previous experimental studies, even when the reported outcome of suffusion in terms of total fines lost was consistent.

8.2 COMPARISON 2: HYDRAULIC LOADING REGIME

One of the aims for this study is to explore how the choice of hydraulic loading regime influences the spatial progression of internal fines migration, something that has been examined directly in the works of Luo et al. (2013), Rochim et al. (2017) and Lee et al. (2021), with somewhat contradictory results, likely due to the range in testing conditions (Section 2.6.1). In this study, two identically prepared specimens were tested at 40-g in the centrifuge permeameter, one under a multi-stage seepage regime, and the other subjected to a constant applied head difference. The energy gradient applied to the multi-stage test, $T_{40L2.5}$, was increased in steps of ≈ 4 kPa/m to a maximum 195.6 kPa/m over a duration of 120 minutes (increments of $i_{app} \approx 0.01$ to a maximum of 0.47), whereas test T_{40LCH} had a constant applied energy gradient of 161.5 kPa/m for a total of 172 minutes ($i_{app} = 0.41$). After permeameter testing, both samples were dissected. The temporal permeability results for these two tests, $T_{40L2.5}$ and T_{40LCH} , are presented in Section 5.2.2 and Section 5.5.2 respectively, alongside the final fines distributions obtained from post-test dissection.

On comparison of these two tests, it is evident that the hydraulic loading regime has an impact on the progression of suffusion within the specimen. Figure 8.3 shows the global permeability profiles of both tests. The general shape of the profiles is similar, with initial suffusion occurring until the specimen reached a peak permeability, followed by a decrease in permeability toward the end of the test. However, the time scales are very different, with $T_{40L2.5}$ reaching its peak permeability after 80 minutes and 32 increments of loading, whilst T_{40LCH} peaked in permeability after just 45 minutes of constant applied head. Interestingly, this point of peak permeability occurred at similar amounts of cumulative expended energy, 83.1 J and 100.7 J for the multi-stage and constant head tests respectively. This was also observed when comparing the repeat test in Section 8.1. This agrees with the I_α concept based on experimental observations (Section 2.6.4), that a soil has a finite amount of particles ‘available’ to be externally eroded, and a certain amount of expended energy is needed to remove them and reach the ‘fully eroded’ state, as coined by Gelet and Marot (2022).

The experimental studies of Gelet and Marot (2022), Rochim et al. (2017) and Zhong et al. (2018), however, suggest that I_α is an intrinsic property of

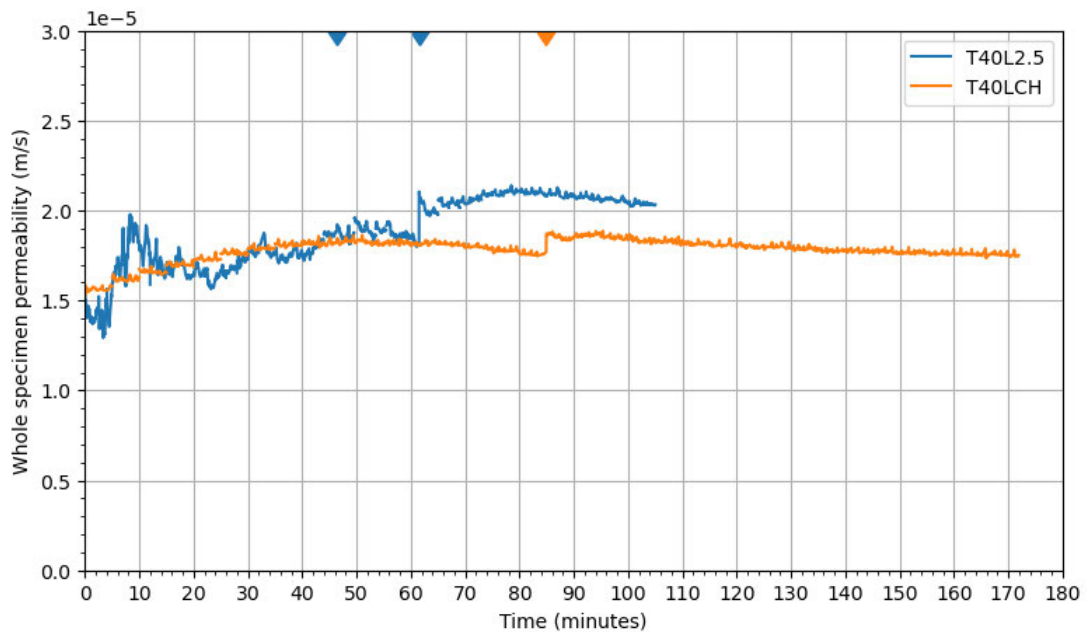


Figure 8.3: Global permeabilities of two 40-g tests conducted under different loading regimes, $T_{40L2.5}$ and T_{40LCH} (centrifuge spin-down breaks marked with coloured triangles)

the soil not affected by the hydraulic loading regime, which does not explain the differences in magnitude of suffusion occurring in $T_{40L2.5}$ compared to T_{40LCH} . The multi-stage test experienced a net increase in permeability of 42.1% over the test duration, whilst the constant head test only had a net increase of 15.0%. This is also shown in the final average fine particle content of the specimens. The final fines content of $T_{40L2.5}$ upon dissection was 19.61%, a reduction from the prepared 20%. There was less fine particle loss from T_{40LCH} , where the final percentage of fines was 19.71%. This is despite the longer duration and higher expended energy in the constant head test. This observation is addressed in the proposed conceptual model in Section 8.2.1.

In previous experimental studies, researchers chose to apply a constant head value either above or below the value they observed to cause suffusion onset in multi-stage tests, depending on the focus of the study. In tests above the multi-stage onset threshold (Rochim et al., 2017 regime *c*, Luo et al., 2013) there was a higher total mass lost in the multi-stage test. In contrast, if the applied head was designed to be below the threshold for suffusion onset, there was a comparable or higher amount of mass eroded from the specimen subjected to constant applied head (Section 2.6.1). This is observed in the tests undertaken in this study, with more mass lost in $T_{40L2.5}$ compared to T_{40LCH} ,

where the hydraulic load was higher than that which was observed to cause global suffusion in multi-stage tests. When comparing the centrifuge constant head test, T_{40LCH} , with the long-duration, low expended energy test T_{1LCH} (Section 7.3), the 1-g test lost more fine particles. T_{1LCH} exhibited a similar amount of fine particles as $T_{40L2.5}$, having a final fines content of 19.63%.

Luo et al. (2013) suggested that difference in response between the two hydraulic loading regimes, was due to the preferential development of regions of fine particles building up under the constant head, a behaviour which they did not visually observe in their multi-stage tests. The ultimate spatial distributions of the fine particles within test $T_{40L2.5}$ and T_{40LCH} are presented in Tables 5.3 and 5.8. Notably, some of the middle quadrants are missing for $T_{40L2.5}$. Despite this, there seems to be a clear difference in the spatial variation in fine particles between the two tests. In test T_{40LCH} , there were three quadrants in the lower half of the seepage path that showed a net increase in fine particles from the prepared 20%. This net increase was not observed in any of the measured quadrants of $T_{40L2.5}$. It is important to reiterate that this does not mean particle deposition did not occur during the multi-stage test, rather that the supply of fine particles migrating in from the overlying layer did not replenish that which migrated out of the layer itself.

The mesoscale progression of suffusion in the two tests can be compared by considering the layer permeability profiles in Figure 5.5 and Figure 5.17. The multi-stage test was characterised by short suffusion events in all of the layers from the very early applied intervals. The most pronounced suffusion occurred in Layer 0. As the test went on, these suffusion events became longer and had a more gradual increase in permeability. In contrast, all layers in test T_{40LCH} experienced large suffusion events within the first 8 minutes of applied seepage flow. In most of the layers, this first event represented their only major suffusion event, and they gradually decreased in permeability for the remainder of the test. This is considered from a micro-mechanical perspective in the following section.

8.2.1 *Particle scale conceptual framework of the evolution of suffusion under the two loading conditions*

In this section, a microscale perspective on the macroscale observations of the difference in responses between the hydraulic loading regimes is proposed. This aims to bring together the mesoscale CFD-DEM observations of Ma et al. (2021) and Wautier (2018) and Liu et al. (2023), with the macroscale experimental observations of this study, as well as the existing experimental permeameter studies under varying hydraulic loading of Luo et al. (2013), Marot et al. (2012) and Rochim et al. (2017). Whilst the proposed model is purely conceptual, and not validated with soil-mechanics based calculations, it could in future be developed alongside the probability-based model proposed by To et al. (2016) for the transportation potential of a migrating fine particle (Section 2.4.2).

The coarse granular matrix of the soil can be considered to be comprised of a series of interconnecting pore voids joined by pore constrictions (Nguyen et al., 2021). Each pore void is likely to have multiple constrictions of different sizes adjoining it. Under gravity, the fine particles within the saturated sample will be quasi-stable, resting in a local divot or ledge. These ‘rattlers’ (Wautier, 2018) will likely only have 1 or 2 inter-particle contacts and will not take part in the force-carrying matrix of this under-filled soil (Section 2.7.1).

When a downwards Darcy’s seepage flow regime is applied to the soil, the seepage flow within the pore voids will be tortuous and acting perpendicular to the surfaces of the coarse grains on which the fine particles are resting. This horizontal perturbation is sufficient to cause an unstressed rattler to be dislodged by the flow (Ma et al., 2021). The settling velocity, v_s , of a median fine particle, $d_{50} = 17$ microns, in a 40-g test can be calculated using Stoke’s Law (Section 6.5). In the centrifuge, this is scaled by N (Section 2.3.1) and is calculated using Equation 8.1.

$$v_s = \frac{(\rho_p - \rho_w) N g d_{50}^2}{18\mu} = 1.0 \times 10^{-2} m/s \quad (8.1)$$

This settling velocity of 1.0×10^{-2} m/s is significantly higher than the average flow velocity in the constant head test T_{40LCH} , which was equal to

2.4×10^{-4} m/s. This means that a dislodged particle will not be carried along in the seepage flow, and rather drop to a lower point within the pore void.

If the particle drops into a constriction that it can pass through (i. e. larger than its diameter), it continues into the next pore void. Conversely, if it cannot fit through the constriction, it is held there by the seepage flow. The particle is only able to leave that constriction if there is enough horizontal force or lift to ‘kick’ it into an adjacent divot. This is similar to the concept of saltation in sediment transport (Pye, 1994), where the pore void is analogous to a microscale river bed. If this iterative process continues, the particle will eventually be knocked into a constriction that it is able to pass through. This is represented by the left-hand branch of the diagram in Figure 8.4.

In cases of high seepage flow and constant applied head, as is the case with *T40LCH*, the iterative jumps are less likely to occur, because the high seepage flow pins the particle into the divot. The particle then blocks the constriction, stopping other migrating particles from passing through it, even if they may have been able to fit through the unclogged constriction. This leads to zones of clogging, as observed in the CFD-DEM work of Liu et al. (2023), and eventually may clog enough to affect an area large enough to be picked up experimentally, for example in the significant decrease in permeability reported in the centrifuge tests of Marot et al. (2012) and shown in Figure 2.25. This process would also explain the local areas of net increase in fine particles seen upon dissection of *T40LCH* and is represented by the right-hand branch in Figure 8.4.

In a multi-stage regime, the seepage force starts very low. The loose particles are dislodged by even this small force and transported to a low point as before. However, the lower flow does not pin the particles into the divot as strongly, and local variation in the tortuous seepage flow promotes the iterative saltation-style process. This would suggest the migration of fine particles from pore to pore is more likely in these early stages of testing, and would explain why so much fluctuation was seen in interstitial layer permeability at the start of test *T40L2.5* in comparison to *T40LCH*. It could also give a microscale perspective on the observation of Gelet and Marot (2022), that the ‘fully-eroded’ state is preferentially reached under multi-stage loading.

This conceptual framework can also give an explanation for why clogging is seen at the higher increments of loading in the multi-stage tests in this study, even in the top layers, which have no particles transported into them

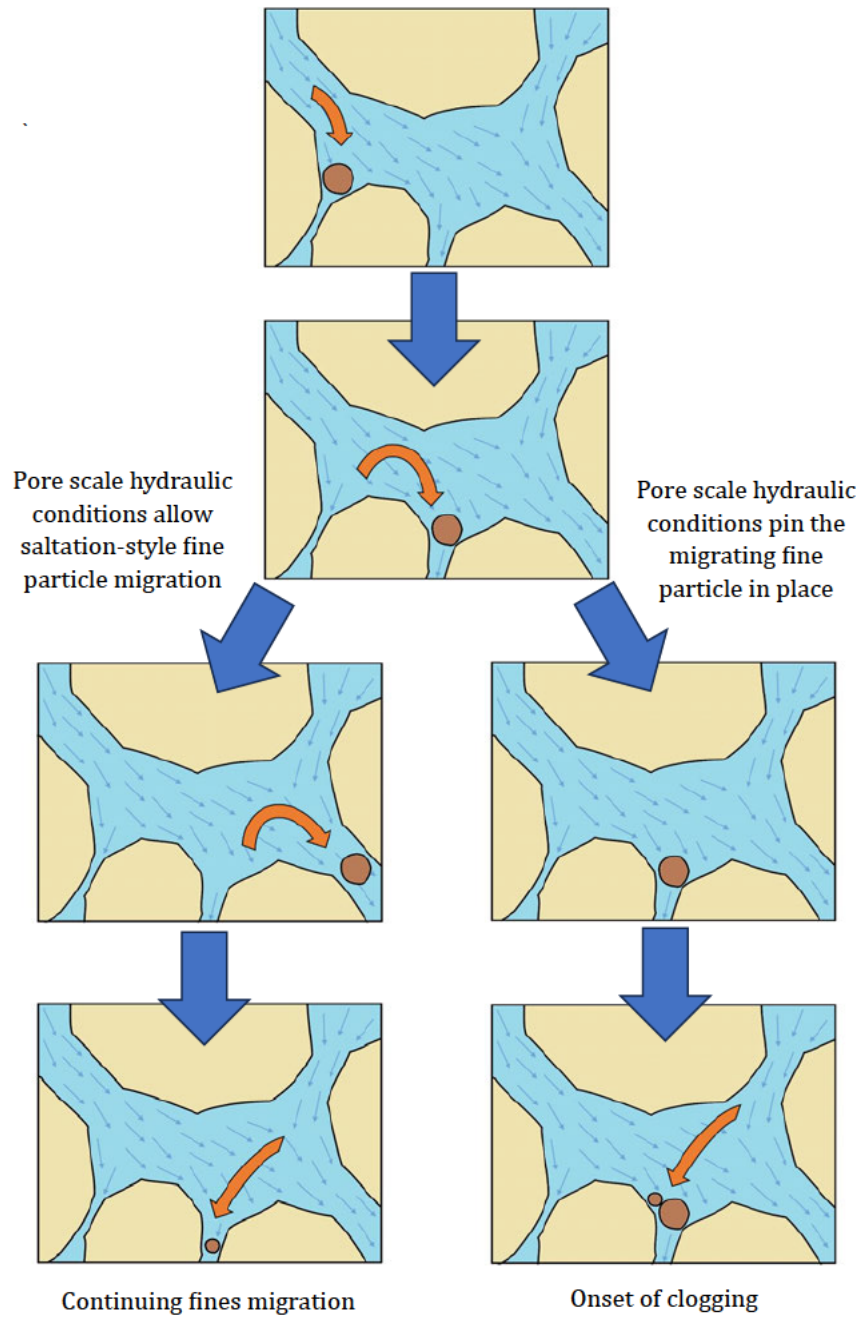


Figure 8.4: Step-wise diagram of the particle scale conceptual framework, with the left branch leading to continual fines migration and suffusion, and the right branch leading to particle deposition and clogging

from the layer above. The harsher flow conditions increase the likelihood that particles get trapped in constrictions and cause local deposition zones backing upstream, as observed by Bianchi et al. (2018).

8.2.2 Summary

- The choice of hydraulic loading regime between multi-stage and constant head has a significant impact on the progression of suffusion within the specimens.
- Multi-stage testing caused a greater loss in fine particles than an identically prepared specimen tested in the centrifuge under a constant applied head. There was greater spatial variability in final fine particle locations in the constant head test, with areas of net clogging, not observed in the dissection of the multi-stage test, consistent with observations in previous experimental studies.
- A particle-scale conceptual model is proposed to understand why these two testing regimes have different outcomes, bringing together the observations of the current study, previous experimental works, and the results of CFD-DEM simulations undertaken in recent years.

8.3 COMPARISON 3: SEEPAGE PATH LENGTH AND BOUNDARIES

From the modelling of models comparison in Section 7.1, it was found that the relationship between macroscale seepage path length and effective stress proposed by Li and Fannin (2022) to determine the critical hydraulic gradient did not apply to the tests undertaken in this study. From the observations of that modelling of models comparison it was proposed that the seepage path length influence observed by Li (2008), as well as Marot et al. (2012) and Zhong et al. (2018), was based on the microscale rather than the macroscale specimen height, representing the number of constrictions that a migrating seepage particle must pass through to cause a change in permeability observable using experimental measurement (PPTs, manometers, for example). The relationship between prototype and model scale seepage path length was investigated further in this study with the comparison of the two tests designed to replicate

the same prototype conditions ($T_{40S2.5}$ and T_{20L5} - Section 8.2). There was a clear difference between the test behaviours but, by comparing only two tests, this could be attributed to either the seepage path length, or the difference in hydraulic loading regime, or a combination of the two. To explore this from a different angle, the results of $T_{40S2.5}$ can also be compared with $T_{40L2.5}$.

Both tests were conducted at 40-g and subjected to the same incremental increase of head difference across the specimen. For the half-height test, $T_{40S2.5}$, this resulted in increments of energy gradient twice the size of the full-height test. The stress gradient across $T_{40S2.5}$ was the same as across the top three layers of $T_{40L2.5}$, which allows for the influence of outlet boundary conditions to be explored. The half-height test was prepared directly on top of the coarse, free-draining sand (Section 3.4.1), whilst the top three layers of $T_{40L2.5}$ had an exit boundary consisting of the underlying layers of internally unstable silt-sand mix. The full results of the tests are presented in Chapter 5, with a summary of key parameters shown here in Table 8.1.

Table 8.1: Comparison of the testing parameters for the two tests conducted at 40-g with different model heights, $T_{40L2.5}$ and $T_{40S2.5}$

Parameter	$T_{40L2.5}$	$T_{40S2.5}$
Δz Model/Prototype (m)	0.21/7.85	0.105 / 4.01
$i_{app,max}$	0.47	1.07
$EG_{app,max}$ (kPa/m)	195.6	446.2
v_{max} (m/s)	5.4×10^{-4}	8.3×10^{-4}
E_{exp} (J)	206.5	480.7

Comparing the whole specimen response in Figure 8.5, the global permeability profiles of the two tests show the same general trend of an initial increase in permeability, followed by clogging towards the end of the test. This clogging was much more pronounced in $T_{40S2.5}$, which was subjected to a significantly higher maximum applied energy gradient and expended energy. The full-height specimen experienced much more fluctuation in permeability during the early stages of testing, whilst the half-height sample showed a much more gradual response. The two samples had a similar final fines distribution upon dissection, with $T_{40L2.5}$ losing a slightly higher proportion of its fine particles, despite experiencing less energy expended by the seepage flow. This was not

what was observed by Marot et al. (2012), where an approximately linear relationship was seen between the expended energy and mass lost per unit volume. However, as reported in their work, of the tests with lower cumulative expended energies, the longest specimens (120 mm) lost proportionally fewer of their fine particles than the comparable 60 and 90 mm specimens.

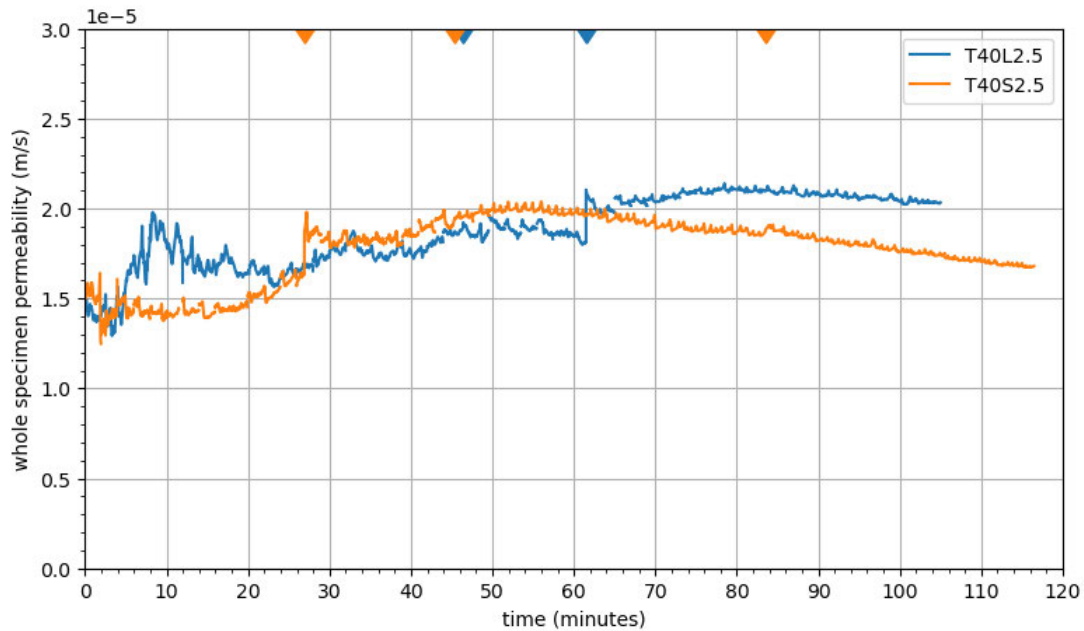


Figure 8.5: Global permeabilities of the tests $T_{40L2.5}$ and $T_{40S2.5}$ in time (centrifuge spin-down breaks marked with coloured triangles)

Analysing just the top portion of $T_{40L2.5}$, Layers 0 to 2, in comparison to the whole of $T_{40S2.5}$ gives an understanding of the difference in response of two similarly stressed specimens with different outlet conditions. After 51.6 minutes, $T_{40S2.5}$ was under the same applied energy gradient, 195.6 kPa/m, as $T_{40L2.5}$ at the end of testing. By this point, the permeability of $T_{40S2.5}$ had increased by a net 34%, from 1.5×10^{-5} to 2.0×10^{-5} m/s. There was comparatively more suffusion from the top layers of $T_{40L2.5}$, which increased by 84.5%, from 1.0×10^{-5} to 1.9×10^{-5} m/s. Although there was a difference in permeability change, the two tests did reach a similar permeability by $E_{app} = 195.6$ kPa/m. Similarly to the whole sample, the top three layers of $T_{40L2.5}$ had a higher loss of fine particles than the equivalent $T_{40S2.5}$ specimen, with a final fines percentage of 19.59% compared to 19.67%. There was greater cross-sectional variability in the final fines distribution in the half-height test though, with the bottom layer showing a quadrant with a net gain in fine particles (Table 5.6). This localised clogging could be due to the higher seepage

loading by the end of the test, as discussed in the conceptual framework in Section 8.2.1. An adjacent quadrant in the bottom layer of $T_{40S2.5}$ had the highest amount of fines lost in the specimen at a final fines content of 19.02%.

An interpretation of these results is that the outlet condition, either coarse soil or more silt-sand mix, caused the difference in observed suffusion progression. $T_{40S2.5}$, which had a more open exit boundary of coarse soil, saw more gradual suffusion behaviour, perhaps because fewer particles were trapped in these lower layers during the early stages of testing. In $T_{40L2.5}$, the more fluctuating permeability response of the top layers could have been caused by particle migration occurring in the underlying soil. Local developments of suffusion and clogging in the lower levels may have caused behaviour propagation upstream, as observed by Bianchi et al. (2018). This dynamic environment, however, may be the reason that the top layers of $T_{40L2.5}$ experienced a higher change in permeability and mass lost, with the constantly changing hydraulic regime providing the horizontal perturbations needed to migrate deposited particles, as proposed in the conceptual framework in Section 8.2.1.

8.3.1 Summary

- The results of this comparison supports the observations in Section 7.2 that the microscale seepage path length affects the development of suffusion within a specimen.
- The behaviour in lower layers of a specimen appear to affect the fines migration in the overlying layers, with more fluctuations in permeability observed in a identical layers overlying unstable soil mix compared to a coarse support soil that allows easy migration of fine particles.
- The observations in this comparison are qualitatively consistent with the proposed conceptual model of fines migration in Section 8.2.1.

8.4 LINKING PERMEABILITY READINGS TO FINAL FINES DISTRIBUTION

In conventional experimental suffusion studies, the permeability response is measured across a seepage path length much larger than the grain scale. In this study, the seepage path length across one interstitial layer is in the order

of 200 D_{50} particles. Internal erosion is identified by a variation in Darcy's permeability coefficient, k , between two measurement points, based on macro-scale assumptions. If the permeability increases, suffusion is assumed to have occurred. Conversely, a reduction in permeability is attributed to particle deposition in that layer.

Comparison of the dissected fines content and permeability response of the tests in this study does not support this interpretation. For example, the top layer of test $T_{30}L_{2.5/5}$ exhibited a reduction in permeability of around 24% over the test duration, which would suggest that clogging occurred. However, this observation cannot be attributed to a deposition of fine particles, as there was no overlying unstable soil mix. In addition, post-test dissection of the top layer showed a net reduction in fine particles from 20% to 19.68%. In suffusion studies undertaken in over-filled soils (Chang and Zhang, 2013a; Ke and Takahashi, 2014a), this reduction in permeability can be attributed to a rearrangement and densification of the soil matrix (Section 2.2.9). However, the under-filled (20% fines) and dense (70% relative density) specimens of this study would typically be assumed to be fully suffusive, with the fine particles located in the voids and playing no part in the force transfer matrix (Section 2.7.1). Their removal by the seepage flow in this case would not cause volumetric rearrangement. This is consistent with the images taken at 60 second intervals throughout the centrifuge tests, which showed no discernible settlement of the soil surface, even in the enhanced-g environment. An alternative explanation for these seemingly conflicting observations is needed.

The permeability of a soil is known to be a function of its granular structure, and many methods have been developed to calculate the permeability from a soil's properties. In the following thought experiment, the Kozeny-Carman approach (Equation 2.14) is used to calculate the permeability of the soil block, as justified in Section 2.4.3. This thought experiment aims to demonstrate by use of the soil phase diagram how the spatial variation in fine particles within a representative volume can influence the measured permeability across the volume, and show that a decrease in permeability does not necessarily mean a net increase in fine particles.

Consider a representative volume of the unstable soil mix with a unit height. The soil has a fines content, F_n , of 20%. For simplicity, the initial void ratio of this soil, e_0 , is equal to 0.5 (the material properties of the actual soil used in

this study had a void ratio of 0.512 at 70% relative density - Section 3.2.2). We can assume that this representative volume has a homogeneous distribution of fine and coarse particles, as well as void spaces, and that it can be represented by the phase diagram in Figure 8.6.

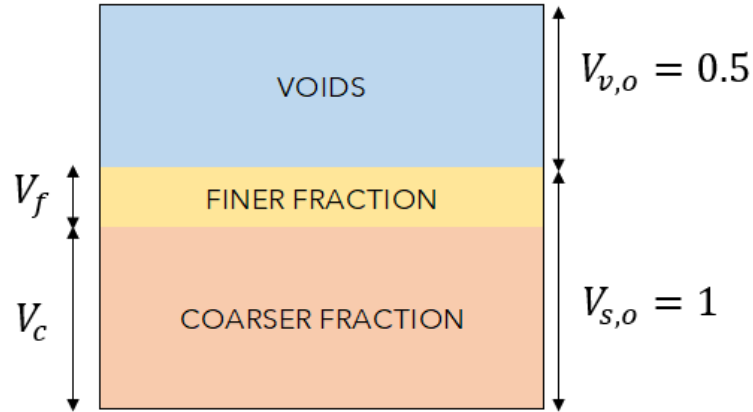


Figure 8.6: Phase diagram for the uneroded soil representative volume

As the material has a fines content of 20%, the initial volume of the fine fraction, V_f , and coarse fraction, V_c are calculated as follows:

$$V_f = F_n \times V_{s,0} = 0.2 \times 1 = 0.2 \quad (8.2)$$

$$V_c = (1 - F_n) \times V_{s,0} = (1 - 0.2) \times 1 = 0.8 \quad (8.3)$$

The Kozeny-Carman permeability of this homogeneous block is calculated as 4.67×10^{-6} m/s using Equation 2.14 and a shape factor of 6.6.

Now consider a downwards seepage flow being applied to the soil, sufficient to cause initial fines migration. The particles are blocked from leaving the volume. The fine particles would move into the bottom portion of the block. This case represents when the fine particle transportation distance is less than the distance between the measurement points in a permeameter experiment. For simplicity's sake, it can be assumed that all the fine particles are removed from the top of the volume, and deposited in the bottom, as shown in Figure 8.7, and both of these layers can now be considered homogeneous.

We can now calculate the permeability of this block as a layered system, $k_{combined}$, using the approach to find the combined permeability of layers

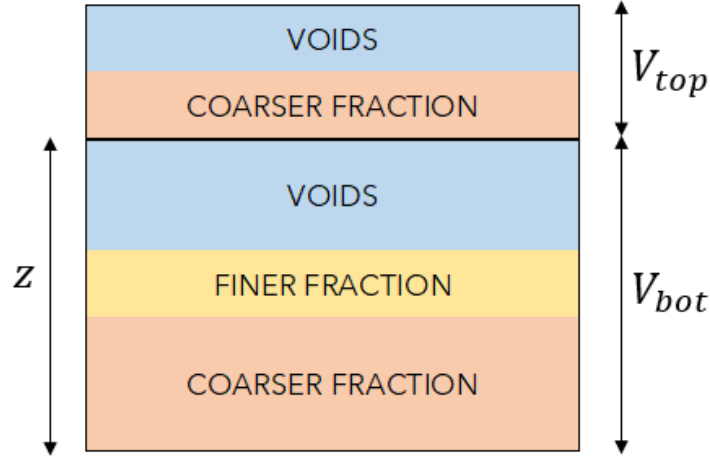


Figure 8.7: Phase diagram for the eroded soil representative volume, where the fine fraction is located in the bottom portion of the soil

perpendicular to the flow direction (Powrie, 1997) shown in Equation 8.4, where k_{top} and k_{bot} are the Kozeny-Carman permeabilities of the top and bottom layer respectively.

$$k_{combined} = \frac{d_1 + d_2}{\frac{d_1}{k_1} + \frac{d_2}{k_2}} = \frac{1}{\frac{(1-z)}{k_{top}} + \frac{z}{k_{bot}}} \quad (8.4)$$

The following example assumes that all of the fine particles are in the bottom 70% of the soil block, $z = 0.7$. The top layer is composed of only the stable coarse fraction, and has a total volume, V_{top} , of 30% of the total volume V_{tot} .

$$V_{top} = (1 - z)V_{tot} = (1 - 0.7) \times 1.5 = 0.45 \quad (8.5)$$

The volume of solids in the top layer, $V_{s,top}$, is equal to the volume of the proportion of coarse particles.

$$V_{s,top} = (1 - z)V_f = (1 - 0.7) \times 0.8 = 0.24 \quad (8.6)$$

The volume of the voids in the top layer, $V_{v,top}$ is equal to sum of the original volume of voids and the voids left by the departed fine particles.

$$V_{v,top} = (1 - z)V_{v,0} + (1 - z)V_f = (1 - 0.7) \times 0.5 + (1 - 0.7) \times 0.2 = 0.21 \quad (8.7)$$

The void ratio of the top layer, e_{top} , can then be calculated using Equation 8.8, and used to find the Kozeny-Carman permeability of the layer comprising of just coarse particles, $k_{top} = 3.89 \times 10^{-4}$ m/s.

$$e_{top} = \frac{V_{v,top}}{V_{s,top}} = \frac{0.21}{0.24} = 0.875 \quad (8.8)$$

By following the same logic, the void ratio in the fines-filled lower layer, e_{bot} can also be calculated. The volume of solids, $V_{s,bot}$, is equal to the existing proportion of the original solids, plus the fines from the layer above, and the volume of voids, $V_{v,bot}$, is equal to the existing voids minus the volume of the fine particles from the layer above.

$$V_{s,bot} = zV_{s,0} + (1 - z)V_f = 0.7 \times 1 + 0.3 \times 0.2 = 0.76 \quad (8.9)$$

$$V_{v,bot} = zV_{v,0} - (1 - z)V_f = 0.7 \times 0.5 - 0.3 \times 0.2 = 0.29 \quad (8.10)$$

$$e_{bot} = \frac{V_{v,bot}}{V_{s,bot}} = \frac{0.29}{0.76} = 0.382 \quad (8.11)$$

The final fines content of the bottom layer, $F_{n,bot} = V_f/V_{s,bot} = 26.3\%$. This gives a Kozeny-Carman permeability, k_{bot} , of 1.46×10^{-6} m/s for the fines-filled bottom layer.

Substituting these permeabilities in Equation 8.4 gives a combined permeability in the vertical direction of 2.08×10^{-6} m/s. If pore pressure measurements were taken at the top and bottom of this representative volume, they would register a 55.4% decrease in permeability and the researcher would surmise that significant clogging had occurred, but upon dissection the layer would show no fines change at all.

Obviously this a very idealised example, but this thought experiment shows that the experimental methods used are heavily based on macro-scale homogeneous assumptions for Darcy's permeability and the direct link between a permeability measured and a mass of fine particles lost. This spatial variation of fine particles within the distance between two measurement locations

explains the discrepancy between the dissected mass and the permeability change observed in this study, for example in the case of the top layer of *T30L2.5/5*.

The process of obtaining a post-test spatial distribution of fine particles within a specimen is laborious and time consuming, which is why only a few studies base their spatial suffusion analysis purely on specimen dissection, for example the work of Horikoshi and Takahashi (2015). Measuring the permeability change, sometimes in combination with the mass of externally eroded fines, is preferred in permeameter studies (Li (2008), Marot et al. (2012) and Rochim et al. (2017) to name but a few). Even in studies where the final specimens are dissected, these ultimate spatial fines distributions are reported in isolation from the permeability results. For example, in Zhong et al. (2018) the PSDs of the layers were recorded (Figure 2.24) but, despite having interstitial pore pressure ports, only the whole specimen permeability was reported in the paper.

This also brings into question the accepted practice of taking interstitial pore pressure readings at the sidewall of a permeameter. The X-ray work of Nguyen et al. (2019) showed significant preferential loss of fine particles at the wall of the permeameter (Figure 2.23). In the current study, as well, the dissection of the tests showed cross-sectional variation in fines content perpendicular to the global seepage direction, but the pore pressure readings were taken from points along the same vertical axis. It is interesting to consider whether the permeability responses reported in Chapters 5 and 6 would have been the same if measured on the opposite side of the specimen.

In element tests, like permeameters, the flow at the macro-scale is uni-directional, and for a particle to migrate out of the specimen, it must find a traversable path through a relatively small cross-section. If this becomes clogged, then the external suffusion of fine particles may be arrested. However, the flow field within the body of a dam or levee is 3D, and a zone of clogging may not exist from boundary to boundary as in an element test, letting suffusion progress. Caution should be taken when using concepts like the I_{α} factor for suffusion resistance determined from small element tests. The centrifuge tests of Marot et al. (2012) classified the soil as resistant to suffusion by the I_{α} method (Figure 7.4), but the decrease in permeability by up to a half across the tests shows that internal fines migration must have been occurring. If those specimens had been dissected post-testing, the top layers of the specimen

would likely have been classified as highly erodible, with most of the fines being found in towards the bottom of the sample.

8.5 SUMMARY

The analysis of three pairs of centrifuge tests were presented in this chapter, concerning repeatability, the influence of hydraulic loading regime, and micro-scale seepage path length. These results were discussed from both a macro- and microscale perspective, leading to a conceptual model for the migration history of individual fine particles being proposed. A summary of each comparison is presented at the end of the relevant sections. Very good repeatability was found between the repeat tests in the centrifuge, both in terms of specimen preparation and permeability response under the same hydraulic loading regime, providing confidence that the difference observed between tests were due to the various hydraulic loading regimes, specimen configurations and stress conditions, rather than innate variation between samples.

In the final section of this chapter, the link between final fines content and permeability response during a permeameter test was considered. This highlighted that the experimental measurements commonly taken in permeameter tests do not capture the full behaviour of the soil. Care needs to be taken when interpreting results of element tests, as the conditions in real structures are much more complex. Further work is needed to resolve the spatial variability of suffusion observed in numerical and tomographic modelling, with the macroscale assumptions typically taken in experimental studies.

CONCLUSIONS AND RECOMMENDATIONS

9.1 CONCLUSIONS

In this chapter, the conclusions drawn from this study will be presented, broadly following the objectives of the study, presented in Section 1.1. In addition, recommendations for future work are given, focussing both on the experimental study of suffusion and the lessons learnt during the development of the centrifuge permeameter. These are given in the hope of inspiring further studies in the centrifuge device, as well as to offer advice for researchers developing their own internal erosion equipment.

9.1.1 *The development of a centrifuge permeameter*

For this study, a bespoke centrifuge permeameter was commissioned and built, providing several improvements on the only other centrifuge permeameter for suffusion known to the author, from Marot et al. (2012). These improvements include the addition of interstitial pore pressure measurement ports, the ability to apply multi-stage as well as constant seepage flow regimes, and the facility to remove and dissect specimens post-testing to obtain the ultimate spatial fine particle distribution.

The apparatus was used to perform a suite of seven centrifuge tests, and then temporarily modified to allow for a further 1-g suffusion test to be conducted within the same cell. The unstable soil, a gap-graded, under-filled silt/sand mixture, was kept constant between the tests to isolate the influence of parameters such as seepage path length, effective stress, and hydraulic loading history on both suffusion initiation and progression. The suite of tests was designed to follow a modelling-of-models approach to centrifuge testing. The tests also explored the difference in specimen response under multi-stage versus constant applied head hydraulic loading regimes. In the multi-stage

tests, the in-flight lowering of the downstream constant head tank allowed the onset and early stages of suffusion to be captured.

Seven pore pressure transducers along the length of the permeameter cell allow the temporal variation in permeability to be tracked across up to six layers of the specimen. Results from all tests showed that the global permeability across the whole specimen height did not provide a comprehensive understanding of suffusion behaviour, as local suffusion and clogging events could be identified using the interstitial pore pressure readings. At lower g-levels, there was no observed increase in overall permeability, indicating a lack of suffusion on a global scale. However, individual layers within the specimen did show significant increases in permeability, suggesting that suffusion was occurring locally within those layers.

Post-test dissection and particle size analysis of the specimens was inconclusive, due to the small mass differences in fine particles before and after testing. All dissected tests did show a decrease in fines content from the prepared value, but external suffusion (the removal of fine particles from the specimen) could not be verified by alternative means within the centrifuge environment. Observations of the clouded effluent water in the 1-g test did show that fine particles were externally eroded from the sample in that test. The ultimate spatial distribution of fine particles within the specimen had seemingly no connection with the observed permeability change within the soil, suggesting that it is not the absolute value of fine particles that affect the permeability change observed during suffusion, and instead the relocation of those particles at a scale smaller than the measurement distance.

9.1.2 *The relationship between tested parameters and the onset and progression of suffusion and clogging*

This study set out to undertake a parametric modelling-of-models approach to explore the influence of seepage path length, effective stress gradient, and hydraulic loading conditions on the onset and progression of suffusion. A major finding of this study is that there appeared to be no threshold value at which suffusion begins, with increases in local permeability from the first stages of testing in some specimen layers. Figures 9.1 to 9.3 present the test conditions at the onset of suffusion and clogging events, as defined in Section 5.1.1. Each

marker represents the conditions in the affected layer at the initiation of the event, and all of the centrifuge tests are considered.

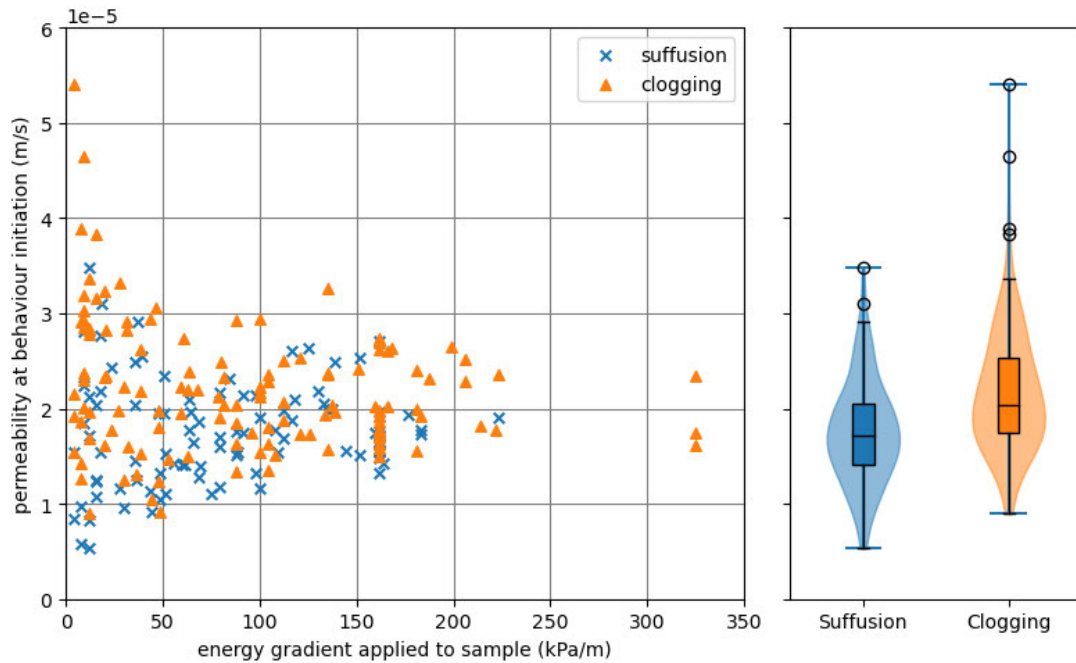


Figure 9.1: Permeability of soil layer at the initiation of either suffusion or clogging behaviour compared to the energy gradient applied to the whole specimen at that time

In Figure 9.1, the local permeability of the layer at the onset of suffusion and clogging is plotted against the energy gradient applied to the whole sample. On the right hand side of the figure, a violin plot showing the spread of the data is also presented. In general, suffusion tended to initiate in layers with lower permeability, whilst clogging initiated in layers with higher permeability. An interpretation of this at the granular scale is that lower permeability layers have more fine 'rattlers' available to erode at early stage of testing, whilst higher permeability layers have more available void spaces for particles to be deposited. Further experimental or numerical studies are required to verify this interpretation. At higher applied energy gradients, typically indicating towards the end of a test, there is smaller spread in the layer permeabilities where suffusion and clogging occur.

Figure 9.2 shows the effective stress at the midpoint of the affected layer against the energy gradient applied to the specimen for the same suffusion and clogging initiation points. All of the tests at 40-g have the same starting effective stress at the midpoint of each layer, which explains why the data is

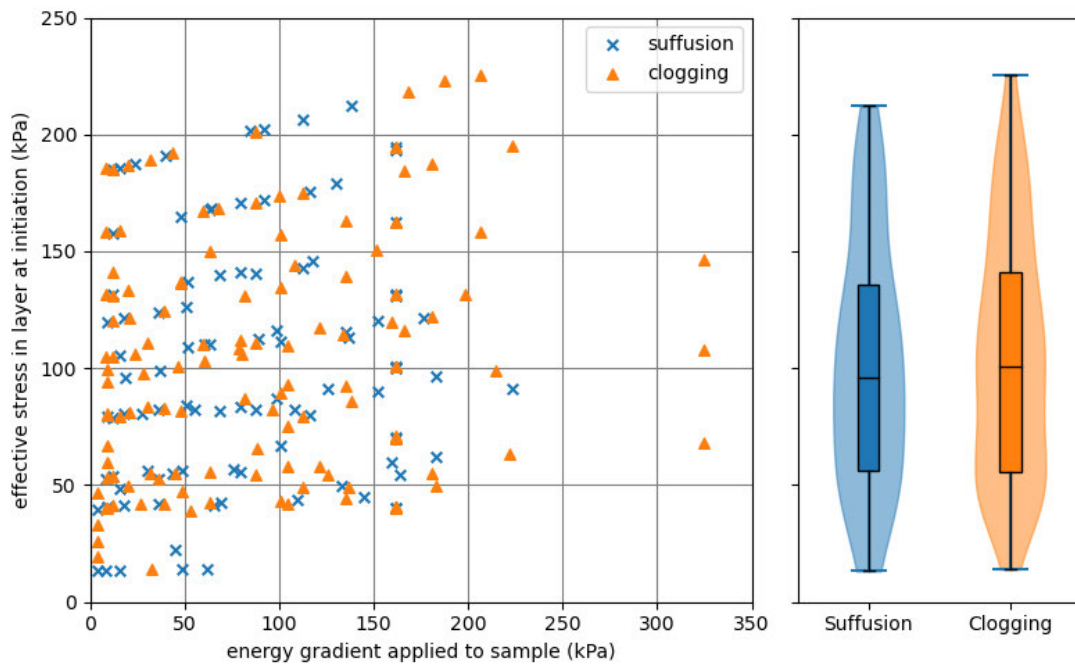


Figure 9.2: Effective stress at the midpoint of the soil layer at the initiation of either suffusion or clogging behaviour compared to the energy gradient applied to the whole specimen at that time

arranged in near horizontal lines. The upwards trend is due to the fact that as the applied energy gradient increases, the effective stress increases due to the decreased pore pressure, an effect that is more prominent at the base of the specimen. This graph shows that there is no preference towards the initiation of suffusion or clogging depending on the effective stress level in the layer. Both suffusion and clogging initiate at very low applied energy gradients, regardless of the effective stress level.

The third figure in this series, Figure 9.3, shows the energy gradient across the layer in which the suffusion or clogging event occurred relative to the applied energy gradient, which is the average energy gradient across the whole sample. The violin plots on the right show that clogging begins to initiate in layers that have a lower than average energy gradient across them. As with Figure 9.1, this demonstrates that clogging tends to occur in layers that are more permeable, not only compared to the other tests, but also relative to the other layers of the same specimen. This could suggest that heterogeneity within a specimen promotes particle deposition. Local suffusion events tend to occur on average in layers that have a similar energy gradient across them as across the whole specimen.

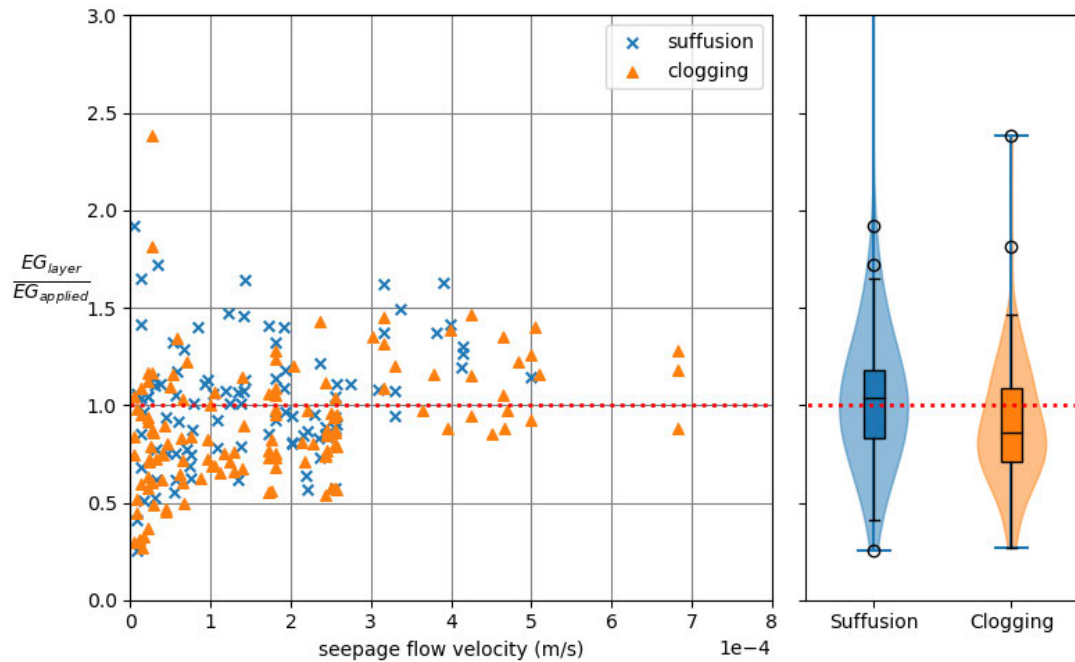


Figure 9.3: Relative energy gradient (EG) in the soil layer which exhibited suffusion or clogging behaviour, compared to the energy gradient applied to the specimen, in relation to the seepage flow velocity through the whole specimen

From the results of this study, it is clear that the onset of fine particle migration within the specimen is significantly affected by the local initial granular soil structure and development of heterogeneities due to the hydraulic loading history, rather than the global scale effective stress conditions. The hydraulic loading history also affects the progression of suffusion. When comparing four identical models tested at g -levels between 10- and 40- g (Section 7.1), tests at lower- g levels did not begin to erode once the test conditions that caused erosion in higher- g tests were reached. Local fine particle migration at early stages of the multi-stage seepage flow test altered the suffusion response of the soil.

The suite of tests also allowed comparison between the outcomes of multi-stage compared to constant head testing regimes, with two identically prepared samples subjected to these hydraulic loading conditions and then dissected post-testing. A multi-stage regime lead to a greater loss in fine particles than the constant head test, which also showed greater spatial variability in ultimate fine particle distribution. A constant head regime favoured larger suffusion events towards the start of testing, whereas over the duration of the multi-

stage test the initially short, sharp suffusion events transitioned to longer more gradual increases in permeability.

9.1.3 *Threshold conditions for suffusion onset and erosion resistance as an inherent soil property*

The onset of suffusion observed in this study was not captured by the hydromechanical envelope concept of Li and Fannin (2022), with local fines migration picked up by interstitial pore pressure readings from almost the onset of seepage flow. This highlights that the concept of a threshold hydromechanical condition for suffusion does not in fact capture the point at which suffusion begins, rather the point at which suffusion becomes noticeable at the measurement scale chosen. The idea of a small zone of the soil reaching the critical value for suffusion is predicated on the fact that spatial heterogeneity has developed within the soil structure. Consequently it is not appropriate to consider suffusion tests in permeameter to be 'element tests', and local measurements of pore pressures are advised when conducting experimental studies.

Dissection of the permeameter tests in this study demonstrate that the mass of fine particles lost from samples is independent from the energy expended by the seepage flow, emphasized particularly when comparing the 1-g and 40-g constant head test results. This suggests that the erosion resistance index, I_{α} , is not an intrinsic soil property independent of effective stress and seepage path length, and that other factors such as hydraulic loading history and boundary conditions also influence the quantity of fine particles lost during suffusion. Previous experimental results relating to I_{α} have been treated as element tests, considering only fine particles removed from the sample, even when analysis of the ultimate spatial distribution of fine particles within those studies has shown that local clogging was occurring (Figure 2.24).

Both of the approaches in this section are based on continuum assumptions of soil behaviour, and yet this study adds to the growing body of work demonstrating that suffusion is intrinsically a spatially varying and granular scale phenomenon. There is a need for these simple-to-apply methods that can be published and used by practising engineers, but their current limitations must be acknowledged so they are not applied irresponsibly. Further research

is needed to resolve microscale experimental results with a particle scale understanding of the suffusion process, which is discussed in the following section.

9.1.4 *Suffusion as a microscale phenomenon and the disconnect between permeability and fines distribution*

Although this study shows that progression of suffusion is a particle scale mechanism which depends on the local granular structure and hydraulic loading conditions, there was good agreement between the repeat tests conducted in the centrifuge, both in terms of the global and local permeability. This suggests that suffusion behaviour does not entirely depend on random microstructural defects in the granular matrix, and there is some systematic influence of the hydromechanical loading regime. Both local suffusion and clogging behaviours were observed to influence surrounding layers, with similarly stressed layers behaving differently depending on their outlet boundary conditions.

In Section 8.2.1, a conceptual model is proposed to interpret the difference in responses observed in the multi-stage and constant head tests from a particle scale perspective. This combines the observations from this study with previous experimental work, as well as recently published CFD-DEM simulation results. Another key finding of this study is that, whilst in literature the concepts of seepage path length and specimen height are used somewhat interchangeably, a simple measurement of the specimen height does not capture the influence of seepage path length on suffusion behaviour. Although this is particularly obvious when considering the scaling laws of the centrifuge, it should also be considered when testing different soils in the same apparatus, where the seepage path length should be given in terms of a representative size of the soil particles. This captures the reality that a migrating soil particle must travel through a certain number of pore voids to be externally eroded from the soil, and each void represents a potential location for the particle to be redeposited, or a location for another loose particle to be picked up by the seepage flow.

In this study, both the temporal local permeability of the specimen during testing, and the ultimate distribution of fine particles are used to explore the progression of suffusion within the specimen. There was a disconnect

between the two measurements, with apparently no connection between the small changes in fine particle content and relatively large variations in local permeability. In fact in some layers, the permeability decreased, suggesting clogging, but upon dissection the fines content was lower than the initial 20%. From this it can be concluded that the permeability changes observed during suffusion tests are due to a local rearrangement of fine particles within the pore spaces at a scale smaller than the measurement points, rather than a net change in fine particle content in the soil. This is demonstrated by the phase-diagram based model presented in Section 8.4, where a change in permeability between two points can be observed with no overall change in fine particle content.

9.2 RECOMMENDATIONS

9.2.1 *Recommendations for further exploration of the suffusion phenomenon*

- Future experimental studies in this area should consider using a minimum of two methods to quantify suffusion, for example interstitial pore pressure readings in combination with post-test dissection, or more advanced techniques such as X-ray tomography. Studies should prioritise recording the spatial development of suffusion within the apparatus. Element testing, in particular when determining soil parameters such as the α factor and erosion resistance index, should not be assumed to produce a homogeneous sample, and care should be taken when extrapolating this data to a larger scale.
- This study highlights the difference between seepage path length in terms of particle size, and specimen height, something that is not typically acknowledged in suffusion studies. Further studies to explore a more appropriate way to quantify the seepage path length, perhaps in terms of a represent particle or void size, should be undertaken. In general, this type of focus on the granular scale rather than continuum scale is recommended going forward, as the results of this study highlight that suffusion is inherently a particle-scale phenomenon.
- This study focussed on one under-filled, gap-graded soil gradation in order to examine other parameters affecting suffusion in isolation. However, suffusion is known to be soil-dependent and there is scope for

a similar centrifuge testing programme to be undertaken on a variety of soils. This could be extended to over-filled soils in order to address the transition from suffusive to suffosive soil behaviours, which has the added complexity specimen volume change.

- Whilst the tests in this study were specifically designed to apply very small increments of hydraulic loading in order to capture the early stages of fines migration, many existing studies applied much larger hydraulic loading increments to their specimens. It would be interesting to replicate some of these loading regimes within the centrifuge permeameter, to see if the soil mix tested would experience the 'blow-out' suffusion observed in those studies, or whether the seemingly stable state reached by the end of the tests in this study would continue indefinitely.
- To advance research in suffusion within real structures, it is recommended to adopt a more integrated methodology that bridges the modelling of particle-scale and element-scale processes. This integration should involve introducing more realistic conditions in numerical models, such as complex hydraulic loading and representative particle size distributions. Additionally, in experimental investigations, a shift toward a particle-scale perspective, can enhance our understanding of suffusion progression, by moving towards more localised measurements and observations. The jump in scale between numerical and experimental modelling, and then again to real structures limits our ability to directly model the full suffusion process in one type of test. Unifying these three scales to achieve a fundamental understanding of the suffusion process would offer a more versatile and comprehensive approach to this complex phenomenon.

9.2.2 *Lessons learnt during the development of a centrifuge permeameter*

During the development of the final centrifuge permeameter used for this study, several iterations of the apparatus were trialled. The following paragraphs outline some limitations of the current device, with some suggestions for improvements, that, for various reasons, could not be made during the period of this study.

One of the major limitations of the device is that the centrifuge must be spun down to empty the outflow container used for flowrate measurements. In the current configuration, the cross-sectional area of the outflow tank must be limited to allow the change in water height to be picked up by the submerged PPT, but this restricts the testing duration. To improve this, the flowrate could be measured in a small container which empties periodically into a wider and shallower outflow container mounted underneath the payload. This could be achieved by either a solenoid that opens when the small container fills or using a siphoning effect like a Pythagorean cup.

Another factor that limits the length of centrifuge stages is the need to carry all the deaired water on the centrifuge payload. It was assumed in this study that passing deaired water over the centrifuge split rings would potentially reintroduce gas bubbles, but this was not verified experimentally. If an external store of deaired water was possible, higher flow rates and longer test durations would become more feasible. From a more general perspective, the standard practice of using deaired water in suffusion experiments was followed in this study, as it is widely assumed that gas bubbles may interfere with the fine particle migration and permeability readings. However, to the author's knowledge no study has been done to verify whether the use of deaired water affects the suffusion process at all. The results of such a study would inform methods in all experimental apparatus for internal erosion, not just this centrifuge permeameter.

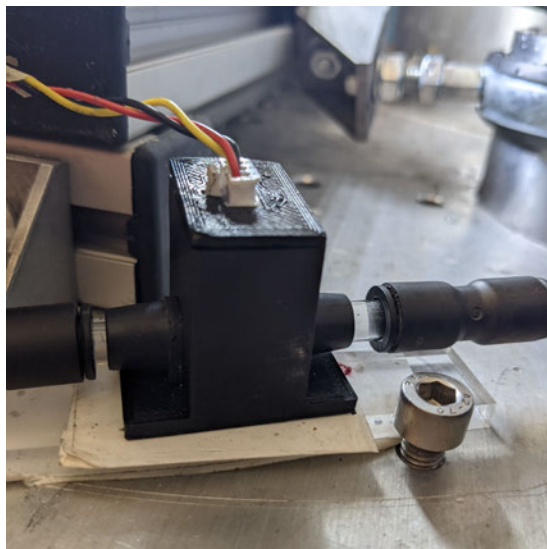


Figure 9.4: Gravity analogue turbidity sensor (SKU SENo189) from DFRobot, with a modified casing on the centrifuge payload

Brief mention was given in Section 3.3.2 to the trialling of a turbidity sensor at the outlet of the permeameter cell. This concept has been used successfully in previous suffusion studies, to the point of being able to determine the particle size distribution of the eroding fine particles (Marot et al., 2011). The sensor used in this study was a gravity analogue turbidity sensor from DFRobot (SKU SENo189). The sensor was placed across a clear glass section in the outflow pipe, as shown in Figure 9.4. At 1-g it worked well and could be calibrated against known quantities of fine particles in water flowing through the pipe. However, in the centrifuge the readings no longer lined up to the turbidity of the effluent water. It was unclear whether this was due to the fluctuating light conditions within the centrifuge, although a custom black-out housing was 3-D printed for the component, or due to flexing of components in the enhanced-g environment. The development of a small turbidity sensor for the centrifuge, either from scratch or by fine-tuning an off-the-shelf component, would be very beneficial for future studies.

The linear actuator which allowed for the adjustment of the downstream CHT was a late addition to the payload configuration, as the initial layout had a constant head applied to the top of the sample and the bottom of the cell draining to atmosphere. The upstream CHT could only be adjusted in between testing stages, with a minimum applied hydraulic gradient of 1 with the CHT in its lowest position. This layout was originally conceived because of the high predicted critical hydraulic gradients for suffusion, but preliminary tests showed very high levels of suffusion almost immediately. To capture suffusion onset, the downstream CHT was added, which allowed applied hydraulic gradients much less than 1, and also the application of multi-stage seepage flow regimes in-flight.

Were the centrifuge payload to be redesigned, it would be arguably better to mount the upstream CHT on a winch system (as in the 1-g permeameter set up - Section 3.5.2) and keep the downstream tank fixed. This would mean a larger range of head differences could be applied, not limited by the length of the linear actuator, and would also potentially be a much lighter-weight solution. Having two-directional control on the variable CHT would give capability to study cyclical or more complex hydraulic loading scenarios within this centrifuge permeameter.

The results of this study have clearly highlighted the spatially varying nature of suffusion and have brought into question whether sidewall pore pressure

readings alone are sufficient to capture the behaviour of a specimen, even with multiple readings along the specimen length. It would be interesting to see the results of a rigid-walled permeameter study with multiple lines of PPTs at opposite sides of the cylindrical cell. Would the permeability results from each side provide a consistent interpretation of the suffusion behaviour?

REFERENCE LIST

- ASTM:D4253 (June 2015). *Standard Test Method for Measurement of Hydraulic Conductivity of Porous Material Using a Rigid-Wall, Compaction-Mold Permeameter*. Standard. Pennsylvania, United States: ASTM International.
- ASTM:D4253 (Mar. 2016). *Standard test methods for maximum index density and unit weight of soils using a vibratory table*. Standard. Pennsylvania, United States: ASTM International.
- ASTM:D4254 (Mar. 2016). *Standard test methods for minimum index density and unit weight of soils and calculation of relative density*. Standard. Pennsylvania, United States: ASTM International.
- ASTM:D5101 (Feb. 2017). *Standard Test Method for Measuring the Filtration Compatibility of Soil-Geotextile Systems*. Standard. Pennsylvania, United States: ASTM International.
- Anderson, C., Sivakumar, V. and Black, J. A. (2015). 'Measurement of permeability using a bench-top centrifuge'. In: *Géotechnique* 65.1, pp. 12–22.
- Annapareddy, V. S. R., Sufian, A., Bore, T. and Scheuermann, A. (2023). 'Spatial and temporal evolution of particle migration in gap-graded granular soils: insights from experimental observations'. In: *Transport in Porous Media* 122 (1), pp. 169–184.
- Balmforth, D. (2020). *Toddbrook Reservoir independent review report*. DEFRA.
- Bendahmane, F., Marot, D. and Alexis, A. (2008). 'Experimental Parametric Study of Suffusion and Backward Erosion'. In: *Journal of Geotechnical and Geoenvironmental Engineering* 134.1, pp. 57–67.
- Bi, J., Luo, X. and Shen, H. (2021). 'Modeling of suffusion considering the influence of soil gradation'. In: *Transport in Porous Media* 136 (3), pp. 765–790.
- Bianchi, F., Wittel, F. K., Thielmann, M., Trtik, P. and Herrmann, H. J. (2018). 'Tomographic Study of Internal Erosion of Particle Flows in Porous Media'. In: *Transport in Porous Media* 122 (1), pp. 169–184.
- Black, J.A., Baker, N. and Ainsworth, A. (2014). 'Establishing a 50g-ton geotechnical centrifuge at the University of Sheffield'. In: *Proceedings of the 8th International Conference on Physical Modelling in Geotechnics (ICPMG2014)*. Perth, Australia: London: Taylor and Francis.

- Blight, G. E. (1997). 'Interactions between the atmosphere and the Earth'. In: *Géotechnique* 47.4, pp. 713–767.
- Bonelli, S. and Marot, D. (2011). 'Micromechanical modeling of internal erosion'. In: *European Journal of Environmental and Civil Engineering* 15 (8), pp. 1207–1224.
- Bridle, R. (2008). 'Assessing the vulnerability of a typical British embankment dam to internal erosion'. In: *Ensuring reservoir safety into the future: proceedings of the 15th conference of the British Dam Society*. Warwick, UK: London: Thomas Telford, pp. 13–28.
- Brown, A.J. and Gosden, J.D. (2004). *Interim guide to quantitative risk assessment for UK reservoirs*. Thomas Telford London.
- Burenkova, V. (1993). 'Assessment of suffosion in non-cohesive and graded soils'. In: *1st International Conference on Geo-filters: Filters in Geotechnical and Hydraulic Engineering*. Ed. by Brauns, J. and Schuler, U. and Heibaum, M. Karlsruhe, Germany, October 20–22, 1992, pp. 357–360. ISBN: 90-5410-342-6.
- Butler, I. B., Schoonen, M. A. A. and Rickard, D. T. (1994). 'Removal of dissolved oxygen from water: a comparison of four common techniques'. In: *Talanta* 41.2, pp. 211–215.
- Carrier, W. D. (2003). 'Goodbye, Hazen; Hello Kozeny-Carman'. In: *Journal of Geotechnical and Geoenvironmental Engineering* 129.11, pp. 1054–1056.
- Chang, D. S. and Zhang, L. M. (2011). 'A stress-controlled erosion apparatus for studying internal erosion in soils'. In: *Geotechnical Testing Journal* 34.6, pp. 579–589.
- Chang, D. S. and Zhang, L. M. (2013a). 'Critical hydraulic gradients of internal erosion under complex stress states'. In: *Journal of Geotechnical and Geoenvironmental Engineering* 139.9, pp. 1454–1467.
- Chang, D. S. and Zhang, L. M. (2013b). 'Extended internal stability criteria for soils under seepage'. In: *Soils and Foundations* 53.4, pp. 569–583.
- Chitravel, S., Otsubo, M., Kuno, M. and Kuwano, R. (2022). 'Post-erosion mechanical responses of internally unstable gap-graded soil under drained torsional simple shear and triaxial compression'. In: *Soils and Foundations* 62.6, p. 101224.
- Crawford-Flett, K. (2014). 'An improved hydromechanical understanding of seepage-induced instability phenomena in soil'. PhD thesis. University of British Columbia.

- Dassanayake, S. M., Mousa, A. A., Ilankoon, S. and Fowmes, G. J. (2022). 'Internal instability in soils: a critical review of the fundamentals and ramifications'. In: *Transport and Research Record* 2676.4, pp. 1–26.
- Fannin, R. J. and Slangen, P. (2014). 'On the distinct phenomena of suffusion and suffosion'. In: *Géotechnique Letters* 4, pp. 289–294.
- Feng, S., Vardenega, P. J., Ibraim, E., Widyatmoko, I. and Ojum, C. (2019). 'Permeability assessment of some granular mixtures'. In: *Géotechnique* 69.7, pp. 646–654.
- Fischer, G. R., Maré, A. D. and Holtz, R. D. (1999). 'Influence of Procedural Variables on the Gradient Ratio Test'. In: *Geotechnical Testing Journal* 22 (1), pp. 22–31.
- Fonseca, J., Sim, W. W., Shire, T. and O'Sullivan, C. (2014). 'Microstructural analysis of sands with varying degrees of internal stability'. In: *Géotechnique* 64.5, pp. 405–411.
- Foster, M., Fell, R. and Spannagle, M. (2000). 'The statistics of embankment dam failures and accidents'. In: *Canadian Geotechnical Journal* 37, pp. 1000–1024.
- Frost, J. D. and Park, J. Y. (2003). 'A critical assessment of the moist tamping technique'. In: *Journal of Geotechnical Testing* 26.1, pp. 57–70.
- Garner, S. J. and Fannin, R. J. (2010). 'Understanding internal erosion: a decade of research following a sinkhole event'. In: *Hydropower and Dams* 17.3, pp. 93–98.
- Garnier, J. et al. (2007). 'Catalogue of scaling laws and similitude questions in geotechnical centrifuge modelling'. In: *IJPMG International Journal of Physical Modelling in Geotechnics* 3, pp. 1–23.
- Gelet, R. and Marot, D. (2022). 'Internal erosion by suffusion on cohesionless gap-graded soils: model and sensibility analysis'. In: *Geomechanics for Energy and the Environment* 31, p. 100313.
- Goodings, D. J. (Sept. 1994). 'Implications of changes in seepage flow regimes for centrifuge models'. In: *Proceedings of the International Conference Centrifuge 94*. Singapore, pp. 393–398.
- Head, K. H. (1982). *Manual of Soil Laboratory Testing Volume 2: Permeability, shear strength and compressibility tests*. 2nd ed. New York: Halsted Press.
- Horikoshi, K. and Takahashi, A. (2015). 'Suffusion-induced change in spatial distribution of fine fractions in embankment subjected to seepage flow'. In: *Soil and Foundations* 55 (5), pp. 1293–1304.

- Hu, Z., Zhang, Y. and Yang, Z. (2019). 'Suffusion-induced deformation and microstructural change of granular soils: a coupled CFD–DEM study'. In: *Acta Geotechnica* 14.3, pp. 795–814.
- Hughes, A. (2020). *Report on the nature and root cause of the Toddbrook Reservoir auxiliary spillway failure on 1st August 2019*. Canals and River Trust.
- Hunter, R. P. and Bowman, E. T. (2018). 'Visualisation of seepage-induced suffusion and suffosion within internally erodible granular media'. In: *Géotechnique* 68.10, pp. 918–930.
- ICOLD (2013). 'Internal Erosion of Existing Dams, Levees and Dykes, and Their Foundations'. In: *Bulletin 164, Volume 1: Internal Erosion Processes and Engineering Assessment*. Ed. by R. Bridle and R. Fell. Paris: International Commission on Large Dams.
- ICOLD (2017). 'Internal Erosion of Existing Dams, Levees and Dykes, and Their Foundations'. In: *Bulletin 164, Volume 1: Internal Erosion Processes and Engineering Assessment*. Ed. by J. J. Bridle R. Fry and R. Fell. Paris: International Commission on Large Dams.
- Indraratna, B., Israr, J. and Rujikiatkamjorn, C. (2015). 'Geometric method for evaluating the internal instability of granular filters based on constriction size distribution'. In: *Journal of Geotechnical and Geoenvironmental Engineering* 141.10, pp. 1–14.
- Israr, J. (2016). 'Internal instability of granular filters under cyclic loading'. PhD thesis. University of Wollongong.
- Israr, J., Indraratna, B. and Rujikiatkamjorn, C. (2016). 'Laboratory investigation of the seepage induced response of granular soils under static and cyclic loading'. In: *Geotechnical Testing Journal* 39.5, pp. 795–812.
- Kawano, K., Shire, T. and O'Sullivan, C. (2018). 'Coupled particle-fluid simulations of the initiation of suffusion'. In: *Soils and Foundations* 58.4, pp. 972–985.
- Ke, L. and Takahashi, A. (2014a). 'Experimental investigation on suffusion characteristics and its mechanical consequences on saturated cohesionless soil'. In: *Soils and Foundations* 54, pp. 713–730.
- Ke, L. and Takahashi, A. (2014b). 'Triaxial erosion test for evaluation of mechanical consequences of internal erosion'. In: *Geotechnical Testing Journal* 37 (2), pp. 347–363.
- Kenney, T. C., Chahhal, R., Chiu, E., Ofoegbu, G.I., Omange, G.N. and Ume, C.A. (1985). 'Controlling constriction sizes of granular filters'. In: *Canadian Geotechnical Journal* 22.1, pp. 32–43.

- Kenney, T. C. and Lau, D. (1985). 'Internal stabilities of granular filters'. In: *Canadian Geotechnical Journal* 22.2, pp. 215–225.
- Kezdi, A. (1979). *Soil physics: selected topics (developments in geotechnical engineering)*. 1st. Elsevier Science Ltd.
- Khalifa, A., Garnier, J., Thomas, P. and Rault, G. (May 2000). 'Scaling laws of water flow in centrifuge models'. In: *International Symposium on Physical Modelling and Testing in Environmental Geotechnics*. La Baule, France, pp. 207–216.
- Kovacs, G. (1981). *Seepage Hydraulics*. Amsterdam: Elsevier.
- Ladd, R.S. (1978). 'Preparing test specimens using undercompaction'. In: *Geotechnical Testing Journal* 1.1, pp. 16–23.
- Le, V. T., Marot, D., Rochim, A., Bendahmane, F. and Nguyen, H. H. (2018). 'Suffusion susceptibility investigation by energy-based method and statistical analysis'. In: *Canadian Geotechnical Journal* 55.1, pp. 57–68.
- Lee, H. J., Kim, I. H. and Chung, C. K. (2021). 'Evaluation of the internal stability of well-graded silty sand through long-term seepage test'. In: *International Journal of Geo-Engineering* 12 (21), pp. 1–12.
- Li, M. (2008). 'Seepage induced instability in widely graded soils'. PhD thesis. University of British Columbia.
- Li, M. and Fannin, R. J. (2008). 'Comparison of two criteria for internal stability of granular soil'. In: *Canadian Geotechnical Journal* 45, pp. 1303–1309.
- Li, M. and Fannin, R. J. (2012). 'A theoretical envelope for internal instability of cohesionless soil'. In: *Géotechnique* 62.1, pp. 77–80.
- Li, M. and Fannin, R. J. (2013). 'Capillary tube model for internal stability of cohesionless soil'. In: *Journal of Geotechnical and Geoenvironmental Engineering* 139.5, pp. 831–834.
- Li, M. and Fannin, R. J. (2022). 'Internal erosion: critical hydraulic gradient in one-dimensional vertical seepage and its relation to soil gradation'. In: *Canadian Geotechnical Journal* 59.5, pp. 769–772.
- Liang, Y., Yeh, T-C. J., Zha, Y. Y., Wang, J. J., Liu, M. W. and Hao, Y. H. (2019). 'Onset of suffusion in upward seepage under isotropic and anisotropic stress conditions'. In: *European Journal of Environmental and Civil Engineering* 23.12, pp. 1520–1534.
- Liu, Y. F. and Jeng, D. S. (2019). 'Pore scale study of the influence of particle geometry on soil permeability'. In: *Advances in water resources* 129, pp. 232–249.

- Liu, Y., Yin, Z.-Y. and Yang, J. (2023). 'Micromechanical analysis of suffusion in gap-graded granular soils considering soil heterogeneity and non-uniform seepage flow'. In: *Computer and Geotechnics* 159, p. 105467.
- Luo, Y., Qiao, L., Liu, X., Zhan, M. and Sheng, J. (2013). 'Hydro-mechanical experiments on suffusion under long-term large hydraulic heads'. In: *Natural Hazards* 65 (3), pp. 1361–1377.
- Ma, Q., Wautier, A. and Zhou, W. (2021). 'Microscopic mechanism of particle detachment in granular materials subjected to suffusion in anisotropic stress states'. In: *Acta Geotechnica* 16.8, pp. 2575–2591.
- Machan, P. (1999). *The dramatic story of the Sheffield Flood*. 1st. ALD Design and Print.
- Madabhushi, G. (2013). *Centrifuge Modelling for Civil Engineers*. Cambridge: CRC Press.
- Marot, D., Bendahmane, F. and Konrad, J. M. (2011). 'Multichannel optical sensor to quantify particle stability under seepage flow'. In: *Canadian Geotechnical Journal* 48.12, pp. 1772–1787.
- Marot, D., Le, V. D., Garnier, J., Thorel, L. and Audrain, P. (2012). 'Study of scale effect in an internal erosion mechanism: centrifuge model and energy analysis'. In: *European Journal of Environmental and Civil Engineering* 16.1, pp. 1–19.
- Marot, D., Rochim, A., Nguyen, H. H., Bendahmane, F. and Sibille, L. (2016). 'Assessing the susceptibility of gap-graded soils to internal erosion: proposition of a new experimental methodology'. In: *Natural Hazards* 83.1, pp. 365–388.
- Mehdizadeh, A., Disfani, M. M. and Shire, T. (2021). 'Post-erosion mechanical response of internally unstable soil of varying size and flow regime'. In: *Canadian Geotechnical Journal* 58.4, pp. 531–539.
- Moffat, R. (2005). 'Experiments on the internal stability of widely graded cohesionless soils'. PhD thesis. University of British Columbia.
- Moffat, R. and Fannin, R. J. (2011). 'A hydromechanical relation governing internal stability of cohesionless soil'. In: *Canadian Geotechnical Journal* 48, pp. 413–424.
- Moffat, R., Fannin, R. J. and Garner, S. J. (2011). 'Spatial and temporal progression of internal erosion in cohesionless soil'. In: *Canadian Geotechnical Journal* 48.3, pp. 399–412.
- Muir Wood, D., Maeda, K. and Nukudani, E. (2010). 'Modelling mechanical consequences of erosion'. In: *Géotechnique* 60 (6), pp. 447–457.

- Nguyen, C. D., Benahmed, N., Andò, E., Sibille, L. and Philippe, P. (2019). 'Experimental investigation of microstructural changes in soils eroded by suffusion using X-ray tomography'. In: *Acta Geotechnica* 14.3, pp. 749–765.
- Nguyen, N. S., Taha, H. and Marot, D. (2021). 'A new Delaunay triangulation-based approach to characterize the pore network in granular materials'. In: *Acta Geotechnica* 16, pp. 2111–2129.
- Ovalle-Villamil, W. and Sasanakul, I. (2020). 'Assessment of Centrifuge Modelling of Internal Erosion Induced by Upward Flow Conditions'. In: *International Journal of Physical Modelling in Geotechnics* 21.5, pp. 251–267.
- Pap, M. and Mahler, A. (2019). 'Comparison of different empirical correlations to estimate permeability coefficient of quaternary Danube soils'. In: *Periodica Polytechnica Civil Engineering* 63.1, pp. 25–29.
- Powrie, W. (1997). *Soil Mechanics: Concepts and Applications*. 2nd ed. London: Taylor and Francis.
- Pye, K. (1994). *Sediment Transport and Depositional Processes*. Oxford, Blackwell.
- Reddi, L. N., Lee, I-M. and Bonala, M. V. S. (2000). 'Comparison of internal and surface erosion using flow pump tests on a sand-kaolin mixture'. In: *Geotechnical Testing Journal* 23 (1), pp. 116–122.
- Rochim, A., Marot, D., Sibille, L. and Le, V. T. (2017). 'Effects of hydraulic loading history on suffusion susceptibility of cohesionless soils'. In: *Journal of Geotechnical and Geoenvironmental Engineering* 143.7, p. 04017025.
- Sail, Y., Marot, D., Sibille, L. and Alexis, A. (2011). 'Suffusion tests on cohesionless granular matter: Experimental study'. In: *European Journal of Environmental and Civil Engineering* 15.5, pp. 799–817.
- Sato, M. and Kuwano, R. (2015). 'Suffusion and clogging by one-dimensional seepage tests on cohesive soil'. In: *Soils and Foundations* 55 (6), pp. 1427–1440.
- Sellmeijer, J. B. (1988). 'On the mechanism of piping under impervious structures'. PhD thesis. TU Delft.
- Shire, T. and O'Sullivan, C. (2013). 'Micromechanical assessment of an internal stability criterion'. In: *Acta Geotechnica* 8.1, pp. 81–90.
- Shire, T., O'Sullivan, C., Hanley, K. J. and Fannin, R. J. (2014). 'Fabric and effective stress distribution in internally unstable soils'. In: *Journal of Geotechnical and Geoenvironmental Engineering* 140 (12), pp. 1–11.
- Skempton, A. W. and Brogan, J. M. (1994). 'Experiments on piping in sandy gravels'. In: *Géotechnique* 44.3, pp. 449–460.
- Slangen, P. (2015). 'On the influence of effective stress and micro-structure on suffusion and suffosion'. PhD thesis. University of British Columbia.

- Slangen, P. and Fannin, R. J. (2017). 'A flexible wall permeameter for investigating suffusion and suffosion'. In: *Geotechnical Testing Journal* 40.1.
- Taylor, R.N. (1994). *Geotechnical centrifuge technology*. Cambridge: CRC Press.
- Terzaghi, K. (1939). 'Soil mechanics: a new chapter in engineering science'. In: *Journal of the Institution of Civil Engineers* 12, pp. 106–141.
- Thevanayagam, S., Shenthan, T., Mohan, S. and Liang, J. (2002). 'Undrained fragility of clean sands, silty sands, and sandy silts'. In: *Journal of Geotechnical and Geoenvironmental Engineering* 128.10, pp. 849–859.
- Thusyanthan, N. I. and Madabhushi, S. P. G. (2003). *Scaling of Seepage flow velocity in centrifuge models*. CUED/D-SOILS/TR326.
- Tian, D., Xie, Q., Fu, X. and Zhang, J. (2020). 'Experimental study on the effect of fine contents on internal erosion in natural soil deposits'. In: *Bulletin of Engineering Geology and the Environment* 79, pp. 4135–4150.
- To, H., Scheuermann, A. and Galindo-Torres, S. (2016). 'Probability of transportation of loose particles in suffusion assessment by self-filtration criteria'. In: *Journal of Geotechnical and Geoenvironmental Engineering* 2.142, p. 04015078.
- Tomlinson, S. S. and Vaid, Y. P. (2000). 'Seepage forces and confining pressure effects on piping erosion'. In: *Canadian Geotechnical Journal* 37.1, pp. 1–13.
- Wan, C. and Fell, R. (2008). 'Assessing the Potential of Internal Instability and Suffusion in Embankment Dams and Their Foundations'. In: *Journal of Geotechnical and Geoenvironmental Engineering* 134, pp. 401–407.
- Wautier, A. (2018). 'Micro-inertial analysis of mechanical instability in granular materials with application to internal erosion'. PhD thesis. Aix-Marseille Université.
- Wautier, A., Bonelli, S. and Nicot, F. (2019). 'DEM investigations of internal erosion: Grain transport in the light of micromechanics'. In: *International Journal for Numerical and Analytical Methods in Geomechanics* 43.1, pp. 339–352.
- Yang, J., Yin, Z. Y., Laouafa, F. and Hicher, P. Y. (2019). 'Analysis of suffusion in cohesionless soils with randomly distributed porosity and fines content'. In: *Computers and Geotechnics* 111, pp. 157–171.
- Zhang, L. and Chen, Q. (2006). 'Seepage failure mechanism of the Gouhou rockfill dam during reservoir water infiltration'. In: *Soils and Foundations* 45 (5), pp. 557–568.
- Zhong, C., Le, V. T., Bendahmane, F., Marot, D. and Yin, Z. Y. (2018). 'Investigation of spatial scale effects on suffusion susceptibility'. In: *Journal of Geotechnical and Geoenvironmental Engineering* 144.9, p. 014018067.

Zou, Y., Chen, C. and Zhang, L. (2020). 'Simulating Progression of Internal Erosion in Gap-Graded Sandy Gravels Using Coupled CFD-DEM'. In: *International Journal of Geomechanics* 20.1, p. 014019135.